

Propositions to the thesis

'Time-dependent Behaviour of Polymers and Unidirectional Polymeric Composite'

by Li Zhang

November 1995

1. *In the literatures it is implicitly assumed that the power-law is the only suitable kernel function for the Schapery model. This assumption is not correct.*
2. *Pure viscoelastic matter does not exist. But all matter exhibits viscoelastic properties at a certain temperature level and after a certain period of time.*
3. *'Material constants' are never constant.*
4. *The micro-mechanical modelling of the global behaviour of composites shows many similarities to attempting to explain the human behaviour by means of genetics.*
5. *Ugliness may become beauty when it grows up.*
6. *The meaning of life can only be hidden in its evolution.*
7. *In a family with two children, one looks like the father and the other like the mother.*
8. *The previous statement does not apply to a family with a twin.*
9. *It is potentially dangerous for a human society to rely solely upon a centralized supply system, especially for food and energy. A solution is to adopt varieties of supply sources in an independent way.*
10. *Consequently, the scale of a building or a city should be limited.*
11. *If people ate the same food, there would be no conflict/war in this world.*

Stellingen bij het proefschrift

"Time-dependent Behaviour of Polymers and Unidirectional Polymeric Composites"

door Li Zhang

november 1995

1. *In de literatuur wordt impliciet verondersteld dat de machtsfunctie de enige geschikte kernfunctie voor het Schapery-model zou zijn. Deze veronderstelling is niet juist.*
2. *Een zuiver viscoelastisch materiaal bestaat niet. Maar alle materialen vertonen viscoelastische eigenschappen bij een zeker temperatuurniveau en na een zekere tijdsduur.*
3. *"Materiaal constanten" zijn nooit constant.*
4. *Het micromechanisch modelleren van het globale gedrag van composieten vertoont veel overeenkomsten met het pogen om met behulp van de genetica het menselijk gedrag te verklaren.*
5. *Lelikhheid kan uitgroeien tot schoonheid.*
6. *De betekenis van het leven kan alleen zijn verborgen in zijn evolutie.*
7. *In een gezin met twee kinderen lijkt het een op de vader en het ander op de moeder.*
8. *De vorige stelling is niet van toepassing op een gezin met een tweeling.*
9. *Het is een potentieel gevaar voor een menselijke samenleving volledig te steunen op een gecentraliseerd bevoorradingsstelsel, in het bijzonder voor voedsel en energie. Een oplossing ligt in het toelaten van meerdere van elkaar onafhankelijke bevoorradingsbronnen.*
10. *Dientengevolge zou de schaal van een gebouw of een stad beperkt moeten blijven.*
11. *Er zou geen conflict/oorlog in deze wereld zijn, indien alle mensen het zelfde voedsel zouden eten.*

Time-Dependent Behaviour of Polymers and Unidirectional Polymeric Composites

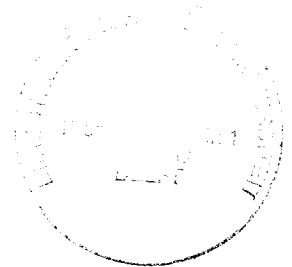
PROEFSCHRIFT

ter verkrijging van de graad van doctor aan
de Technische Universiteit Delft, op gezag van de
Rector Magnificus Prof. ir. K. F. Wakker, in het
openbaar te verdedigen ten overstaan van een
commissie, door het College van Dekanen aange-
wezen, op maandag 6 november 1995 te 13.30 uur

door

LI ZHANG

master of science in engineering
at Shanghai Jiao Tong University
geboren te Shanghai



Dit proefschrift is goedgekeurd door de promotoren:

Prof. dr. ir. L. J. Ernst

en

Prof. dr. ir. H. R. Brouwer

Samenstelling promotiecommissie:

Rector Magnificus, voorzitter

Prof. dr. ir. L.J. Ernst, Technische Universiteit Delft, promotor

Prof. dr. ir. H. R. Brouwer, Vrije Universiteit van Brussel, promotor

Prof. dr. ir. A. Bakker, Technische Universiteit Delft

Prof. dr. ir. R. de Borst, Technische Universiteit Delft

Prof. dr. ir. R. Marissen, Technische Universiteit Delft

Prof. dr. ir. A. Posthuma de Boer, Technische Universiteit Delft

Prof. ir. J. L. Spoormaker, Technische Universiteit Delft

CIP-DATAKONINKLIJK BIBLIOTHEEK, DEN HAAG

Zhang, Li

Time-Dependent Behaviour of Polymers and Unidirectional Polymeric Composites /

Zhang, Li. - Delft: Delft University of Technology.

Dissertation Delft University of Technology. - With ref. - With summary in Dutch.

ISBN 90-74445-22-5

Subject headings: polyester / viscoelasticity / creep / unidirectional composite / micromechanics

Druk: Wibro dissertatiedrukkerij, Helmond

Copyright © 1995 by Li Zhang

All rights reserved.

No part of the material protected by this copyright notice may be reproduced or utilized in any form or by any means, electronic, magnetic, optical or mechanical, including photocopying, recording or by any information storage and retrieval system without written permission from the copyright owner.

To Zhen-zhen

To my parents

Contents

Acknowledgements	viii
Summary	ix
Introduction	1
1.1 Foreword	1
1.2 Objectives	3
1.3 Outline of the Thesis	4
Time Dependent Constitutive Modelling	5
2.1 Viscoelastic Theories	5
2.1.1 Linear Viscoelasticity	5
2.1.2 Nonlinear Viscoelasticity	7
2.2 Schapery's Model	7
2.2.1 Kernel Functions	8
2.2.2 Limitation in Unloading Behaviour	9
2.3 Ageing Effects	10
2.3.1 Introduction	10
2.3.2 Physical Ageing	11
2.3.3 Chemical Ageing	11
2.3.4 Basic Physical Ageing Phenomena	12
2.3.5 Struik's Theory of Physical Ageing	14
2.4 Ageing Implementation	16
2.5 Restrictions on the Model Parameters	17
2.5.1 A General Multi-Step Loading Case	18
2.5.2 Single-Step Stress-Input	20
2.5.3 Simplification	23
Material Characterization and Experiments	25
3.1 Characterization of Physical Ageing	25
3.1.1 Specimen and Equipment	26
3.1.2 Single Specimen Method	26
3.1.3 Rejuvenation by Large Stresses and Specimen Conditioning	28
3.1.4 Testing Procedure for Ageing Creep Tests	29
3.1.5 Shifting of Creep Curves	30
3.1.6 Shifting Rate	33
3.1.7 Long-Term Creep Prediction	35
3.1.8 Conclusions and Discussions	38
3.2 Material Characterization for the Model	39
3.2.1 Experimental	39
3.2.2 Formulation for Data Fitting	40
3.2.3 Model Parameter Determination	41
3.2.4 Unloading Behaviour	47
3.2.5 Ageing Effects on the Exponent n	48
3.2.6 Validation of Theories	50
3.2.7 Conclusions	50

3.3 Prediction of Cyclic Loading	52
3.3.1 Experimental	53
3.3.2 One/Two Cycles up to a Maximum Stress of 30MPa	53
3.3.3 Cyclic loading with increasing amplitudes of stress	56
3.3.4 Five-Cycle Loading	58
3.3.5 Conclusions	59
Three Dimensional Model	61
4.1 Introduction	61
4.2 3-D Model	61
4.3 Poisson's Ratio of a Viscoelastic Material	63
4.3.1 Overall Poisson's Ratio	63
4.3.2 Creep Poisson's Ratio	65
4.3.3 Determination of Poisson's Ratios	66
4.3.4 Test Results	67
4.3.5 Aging Influence	69
4.3.6 Temperature Influence	70
4.4 Discussion on Poisson's Ratio Measurements	71
4.4.1 Thermal Influence in the Overall Poisson's Ratio	71
4.4.2 Loading Imperfection Influence	71
4.4.3 Thermal Expansion and Contraction Influence	72
4.4.4 Stability of Signal Amplifiers and the Correction Method	74
4.4.5 Conclusions	76
Numerical Algorithm and DIANA Implementation	77
5.1 Introduction	77
5.2 Formulation and Discretisation	78
5.2.1 Theory	78
5.2.2 Discretisation	79
5.2.3 The Procedure of Stress Evaluation in DIANA	82
5.2.4 Tangential Stiffness Matrix	82
5.3 Numerical Testing	83
5.3.1 Accurate Result from the Theory	84
5.3.2 FEM Test by DIANA	85
5.4 Conclusions	94
2D Stress States	95
6.1 Introduction	95
6.2 A Plate with a Circular Hole	96
6.2.1 Experimental	96
6.2.2 Numerical Simulation	97
6.2.3 Results	98
6.3 Polyester Tubes - Biaxial Loading	104
6.3.1 Experimental	104
6.3.2 Numerical Model	105
6.3.3 Results and Comparison	106
6.3.4 Difference between Linear Theory and Nonlinear Theory	107
6.4 Conclusions	108
Unidirectional Composite Creep	109
7.1 Introduction	109

7.2	Experiment on the Transverse Creep of UD Composites	112
7.3	Constitutive Relations for Fibres and Matrix	114
7.4	Rectangular and Hexagonal Fibre Packing	116
7.4.1	Rectangular Fibre Packing	116
7.4.2	Hexagonal Fibre Packing	118
7.4.3	Discussion	121
7.5	Modified Hexagonal Fibre Packing - Type 1 and Type 2	121
7.5.1	Fibre Distribution in Samples	122
7.5.2	A Special Regular Fibre Packing	124
7.5.3	Boundary Conditions for the Numerical Calculation	125
7.5.4	57% Fibre Volume Fraction, 10MPa Global Load	125
7.6	Stress and Strain Redistribution	128
7.6.1	Y-direction global loading case (mid-CPD)	128
7.6.2	X-direction global loading case (CPD)	131
7.6.3	Conclusions	134
7.7	Random Packing of Fibres	135
7.8	Shrinkage and Prestress State	138
7.8.1	Shrinkage due to polyester curing	138
7.8.2	Prestress state due to matrix shrinkage	139
7.8.3	Relaxation and creep in the matrix without external loading	141
7.8.4	Influence of prestress on composite creep	143
7.8.5	The Influence of Matrix Initial Strains	150
7.8.6	Global Loading Level Influence on the Stress Distribution Patterns	153
7.8.7	Stress Fields in the Model Cell	154
7.9	Interphase Influence	158
7.10	Conclusions	162
Conclusions		163
8.1	General Conclusions	163
8.1.1	A constitutive model for an unsaturated polyester resin	163
8.1.2	Numerical implementation of the model into an FEM package	164
8.1.3	Transverse creep of a unidirectional polyester/glass fibre composite	164
8.2	Limitation and Recommendation	165
References		167
Appendix		170
Samenvatting		173
Curriculum Vitae		174

Acknowledgments

The research reported in this dissertation has been carried out at the Laboratory for Engineering Mechanics and Fibre Technology, Faculty of Mechanical Engineering and Marine Technology, Delft University of Technology, The Netherlands. It was financed by the university under the technology stimulation project M5.

First of all the author wishes to express his sincere gratitude to the promoter, Prof. dr. ir. L. J. Ernst, for his giving me this opportunity to pursue my doctorate education in The Netherlands, for his continuous encouragements, valuable suggestions and stimulating discussions during the whole period of study.

The author would like to express his thanks to the co-promoter, Prof. dr. ir. H. R. Brouwer, for his surveillance to my work, especially the thesis construction. His suggestions and comments are extremely valuable to the completion of the thesis.

The long-term creep tests were conducted in Laboratory for Material Science, Delft University of Technology. The kind and efficient support from Prof. dr. ir. A. Bakker is gratefully acknowledged.

The other experimental work as done in the Laboratory for Engineering Mechanics and Fibre Technology. The author is indebted to many colleagues in the laboratory, especially to Mr. J. C. Sterk, Mr. L. Th. van der Drift and Mr. W. T. M. Ruygt for their technical assistance.

The author is greatly indebted to Ir. A. ten Busschen for the pleasant cooperation. His early introducing assistance was crucial for the author to start this research very quickly. Without his help, this work would not be carried out in such a pace. My Dutch speaking has been greatly improved through his help.

The author would also like to express his gratitude to MSc. J. Booy for his hardware and software support; to Ir. A. H. van den Boogaard (TNO-bouw) for his patient instruction in the modification of the DIANA package.

The beneficial discussions with Prof. dr. ir. L. C. E. Struik (DSM), Prof. dr. ir. R. Marissen (DSM), Dr. S. Turner (Queen Mary and Westfield College) and Ir. A. H. J. Nijhof are gratefully acknowledged.

The assistance from Mr. H. de Boer, Mr. J. J. G. Vermaas and Mr. V. Toutenhoofd, in experiment preparation and/or numerical processing work, is highly appreciated.

Summary

In order to analyse the long-term time-dependent behaviour of unidirectional polymeric matrix composites micromechanically, a constitutive model for the matrix material, polyester, is necessary. It should be able to describe the matrix behaviour adequately. A 3D model based on nonlinear viscoelastic theory has been set up and the aging effect and the creep Poisson's effect have been taken into account. This model is then implemented into an FEM package. A series of experiments have been done such as biaxial and cyclic loading tests. Excellent agreement between experiment and theory is obtained.

Further this matrix material model is employed to simulate the composite creep by means of finite element calculations. The fibre packing geometry has been found to be important for both the local stress field and the global deformation. The traditional uniform hexagonal and rectangular geometry of fibre packing have been found to be inappropriate for simulating the real unidirectional composite behaviour. To take into account the non-uniformity of the fibre packing, such as the fibre-rich area and matrix-rich area, the global creep deformation can be modelled in a better way. As an improved approach, two special periodic packing geometries have been proposed. These contain the local non-uniform fibre array but are still periodic. These packing geometries can provide cell models which are convenient for numerical analysis. Compared with the test data and the traditional method, the new cell models have demonstrated to yield a better agreement. In this thesis, the phenomenon of stress redistribution in the matrix and fibres due to time-dependent deformation has been exhibited for the first time. The matrix shrinkage induced prestressed state and its influence on both the local stress field and the global creep deformation has been considered as well.

Chapter 1

Introduction

1.1 Foreword

Plastics are nowadays a key part of our daily life. From packaging material to automobile parts, the industry can provide a range of engineering plastics with a unique balanced combination of properties tailored exactly to meet new demanding applications. Moreover plastics enable the designer's expertise to be exploited to the full.

Plastics have been developed with a well-deserved reputation for good performance through properties such as low density, toughness, corrosion resistance and electrical insulation, which are all inherent to the polymer. It is possible to achieve those special properties required by demanding applications.

The history of using composites dates back very early from about 1000 BC in the Middle East, where people started to make mud and straw bricks. The application of polymeric composites began in this century. In the beginning, it was common to add fillers into the basic resins, such as chalk, mostly because it made the resin cheaper. Later fillers were added to improve various properties of plastics, such as processability or reduced shrinkage, electrical resistivity, lubricity, elevated temperature stability, fire and smoke control. But fillers are generally referred to as reinforcements only, when their main objective is to improve the mechanical properties, such as strength, stiffness and toughness.

Polymer based composites or reinforced plastics comprise a group of materials, generally reinforced with fibrous or high aspect ratio particulate fillers. Continuous fibre reinforced materials contain less

polymer and therefore are dominated by the fibre. This is in contrast to thermoplastics with particulate fillers, which usually contain more polymer than filler and therefore their mechanical properties are dominated by the polymer component.

Three major forms of reinforcement are used continuous filaments, discontinuous filaments and particulate reinforcement. The reinforced plastics may be separated into two sub-categories, commodity composites and advanced composites. The commodity composites are based on E-glass-fibre and particulate reinforcement with the cheaper thermosetting and thermoplastic matrix materials. They are mostly used in marine, construction, land transportation and many other industries. These materials account for the most of the total composite market. The advanced composites are based on the higher performance fibres, *e.g.*, carbon (graphite), high performance glass, aramid, high performance thermoplastics and ceramics. They are often combined with higher performance polymeric matrices, their cost is up to 100 times greater than the commodity composites and their application is largely in the military, aerospace and sports equipment markets.

The unidirectional continuous fibre reinforced polymeric composites are polymers reinforced with continuous and straight fibres which are laid parallel to each other in a chosen direction. The polymeric matrix is a continuous phase which supports the fibre and provides adequate environmental protection. The interface controls the transfer of stress from matrix to fibre and also has a strong influence on the toughness and on damage tolerance. In the fibre direction, mechanical properties are dominated by the stiff and strong fibres. Transversely, however, the matrix and interface play dominant roles in the deformation.

For the E-glass/unsaturated polyester system, a commodity composite, the mechanical properties of E-glass may determine the longitudinal properties of the composite, while those of the polyester material determine the transverse properties. The unsaturated polyester resin used for the present research is a liquid when supplied, and has a low viscosity which suggests a good processability. During the curing process, the molecular weight increases and an infusible and insoluble cross-linked polymeric network is formed. The possible fast curing property enables a high efficiency in mass production. Variations in formulation allow a wide range of viscosities, cure rates and final properties to be achieved. Unsaturated polyester resin is dominant in the commodity composites market. It is manufactured in much greater quantities and is cheaper than all alternatives.

The resin used in the present research is an unsaturated polyester, resin: Synolite 593-A-2, produced by DSM, The Netherlands. This unsaturated resin is a liquid with a viscosity of about 2000 cp. It appears as slightly straw coloured. The crosslinking can be initiated by adding 0.5% (in weight) of Cobalt Octoate, an accelerator, and 1.5% (in weight) of MEK (Methyl Ethyl Keton), a catalyst. The resin then cures within one to three hours. For obtaining a more chemically stable material, a postcuring procedure is necessary at elevated temperatures, 24 hours at 60°C and 24 hours at 80°C. The post-cured polyester is a brittle plastic with a high E-modulus of 4–5 GPa.

The E-glass fibre is a composition called aluminium-boro-silicate glass^[39], which is a stable solid material with an E-modulus of 73 GPa. The diameter of the fibre is about 15 μm . This size determines, to a large extent, the processing characteristics of the glass fibre products and the conditions at the glass-matrix interface in the composite material.

The unidirectional composite was manufactured by the filament winding technique, the details can be found in Chapter 7. This technique is ideal for mass production of simple axially symmetric components, e.g. tubes, but is adaptable for more complex forms too. It is amenable to complete computer control.

In a unidirectional fibrous composite, the interface between the matrix and the fibres, or even an interphase, may play an important role in its fracture behaviour. In the present research however this interface is assumed as a perfect bonding surface. No special properties are defined on the interface. The reason for this assumption is the fact that evidence is lacking either about a mechanically important thickness of the interface or about the mechanical properties of such an interphase and therefore only the bonding strength may be special and different from both the matrix and the fibre strength. But the bonding strength will be useful in a fracture analysis of the composite. The objectives of this research are limited to the time-dependent behaviour of this sort of composite when loaded in the direction transverse to the fibres.

1.2 Objectives

In order to investigate the time-dependent composite behaviour, the matrix constitutive behaviour must first be studied. Therefore this work deals with two major objectives,

1. *A time-dependent nonlinear theory for unsaturated polyester matrix material;*
2. *The transverse behaviour of unidirectional fibrous composites.*

These two studies will establish a foundation for the further research of the fracture or cracking behaviour of unidirectional composites under a transverse loading condition and of laminates with different layer arrangement. In this thesis, only the two parts of work mentioned above are presented.

It is of great interest to study the UD composite behaviour in the transverse direction. In practice, laminates which consist of several layers of UD composite are often used. Although the laminates are generally designed in such a way that the reinforcing fibres take the majority of the loads, failure often starts in the layers which are loaded in the transverse direction to the fibres, simply because the UD composite has a much higher strength in the fibre direction than in the transverse direction.

For the constitutive law of the matrix material, the time-dependence basically concerns the creep/relaxation behaviour, which can be accurately depicted by a viscoelastic theory due to its feature of recoverable deformation. However, for the long-term behaviour, polymers age and become stiffer and more compact in volume. In this case, the age of the material affects the rule of the time-dependence which manifests itself not only in its stiffness but also in the creep law of the composite.

A good description of the stress-strain relation for a general loading situation, needs a three-dimensional interpretation where the coupling between different features needs more attention to be paid.

The applicability is often prior to all others. The theory must be finally installed into a finite element computing code and only then, a three-dimensional analysis is made possible.

Finite element computations are needed to be carried out on the purpose of composite analysis. The inclusions or fillers in the composite cause the stresses which are concentrated in some places where the matrix material undergoes a local large deformation and eventually may develop a local failure. The fibre packing geometry plays an important role in the stress and strain distribution under loading. In the extreme case, when two fibres contact each other, this contacting area is a defect in the composite. This area can cause a premature local failure or the initiation of cracks. More generally, the random pattern of the fibre packing always constructs the areas where fibres are close to each other, although the fibre volume fraction is not high. These areas contribute to the building-up of the stress concentration, which is much more severe than in the case of a uniform pattern, such as it occurs in the hexagonal case of fibre arrangement.

The shrinkage of the matrix will alter the stress field built up by the loading. On the other hand, the shrinkage induced prestress field will fade away itself due to the relaxation process because of the viscoelastic nature of the matrix. Therefore the age of the composite works in two directions. One is the physical aging effect on the polymer, and the other is the relaxation effect on the prestressed state of the composite.

1.3 Outline of the Thesis

The thesis comprises seven chapters. In the second chapter, a theoretical basis is set up for the research of the matrix material. Most of nonlinear viscoelastic theories are not new. However, when a specific material is proposed to be modelled, many of them can not be adapted to the application. Actually most of these theories only have their academic significance but are not applicable in practice. The rest have their deficiencies here and there, and must be improved and modified before any application may take place. Among different possibilities, Schapery's theory was adopted in Chapter 2 in which, improvements, modifications and simplifications are performed. Finally the model parameters have been characterized by simple step load test data and are afterwards compared to other test data. With the data of the cyclic loading case, the comparison has approved the model accuracy.

Chapter 3 presents the aging phenomena of polyester. The theory has been established according to the test data. Chapter 4 deals with the development of a three-dimensional model. A creep Poisson's ratio (which remains a constant) is introduced. In Chapter 5 a numerical scheme has been developed as it was implemented into a commercial finite element software package. By means of this finite element code, the three-dimensional model has been applied to simulate the stress distribution in a plate with a circular hole as well as that of the biaxial loading case in Chapter 6. The calculated results have been found to agree quite well with the test data. Finally, in Chapter 7, the nonlinear composite creep behaviour has been analysed by using a micromechanical model. A cell model is developed based on a special fibre packing geometry and the effects of the shrinkage of the matrix material has been considered.

Time Dependent Constitutive Modelling

In this chapter, the constitutive framework, used to describe time dependent material behaviour, is briefly described. Time dependent behaviour is assumed to follow a single integral nonlinear viscoelastic model, which is due to Schapery. The model is modified in order to include physical ageing. This is accomplished by implementing the effective-time theory of Struik into the nonlinear viscoelastic model. Some important ensuing restrictions on the model parameters are discussed.

2.1 Viscoelastic Theories

2.1.1 Linear Viscoelasticity

Linear viscoelastic theory is considered to be a useful approximation of the time dependent behaviour of materials at small strains. Viscoelasticity manifests itself through features like creep under constant load or stress relaxation at constant deformation. Linear viscoelastic models, such as the Maxwell

model, the Voigt model and the standard linear solid or Kelvin model, are composed of combinations of linear springs and dashpots. More general models may be composed by adding more elements to the Kelvin model. One of the most general uniaxial expressions for a linear viscoelastic material behaviour is given by

$$p_0 \sigma + p_1 \frac{\partial \sigma}{\partial t} + p_2 \frac{\partial^2 \sigma}{\partial t^2} + \dots + p_m \frac{\partial^m \sigma}{\partial t^m} = q_0 \epsilon + q_1 \frac{\partial \epsilon}{\partial t} + q_2 \frac{\partial^2 \epsilon}{\partial t^2} + \dots + q_n \frac{\partial^n \epsilon}{\partial t^n} \quad (2.1)$$

where ϵ and σ are strain and stress respectively, and p_i and q_j are material constants ($i = 0, 1, \dots, m; j = 0, 1, \dots, n$).

An explicit expression between strain and stress for one dimensional linear viscoelasticity is due to Boltzmann (1844-1906). Boltzmann's superposition principle uses a convolution integral with an integration limit over the whole stress or strain history.

The superposition principle is given by either

$$\epsilon(t) = J_0 \sigma(t) + \int_0^t J(t-\tau) \dot{\sigma}(\tau) d\tau \quad (2.2)$$

in the case of a creep formulation, or

$$\sigma(t) = E_0 \epsilon(t) + \int_0^t E(t-\tau) \dot{\epsilon}(\tau) d\tau \quad (2.3)$$

when stress relaxation is considered. Here, J and E are the compliance function and the modulus function respectively, both functions are independent of stress and strain. The superposition principle, or the Boltzmann superposition theorem, states that if $\epsilon_1 = f(t, \sigma_1)$ and $\epsilon_2 = f(t, \sigma_2)$, then $\epsilon_1 + \epsilon_2 = f(t, \sigma_1 + \sigma_2)$. Within the framework of linear viscoelasticity therefore, "time invariance" of the creep or relaxation function must hold. These functions only depend on the difference between the present time t and the time τ of integration, but do not change with time.

For a more detailed description of the superposition principle, reference is made to standard text books, such as Arridge (1985).

Linear viscoelastic theory is well developed and has been widely used to describe the mechanical behaviour of polymeric materials. However the concept of linearity is only applicable in the situation of relatively low stress or strain levels. At moderate to high levels of stress the behaviour of polymers can become highly nonlinear. Moreover, for composite materials, the micro-structural geometry consisting of fibres and a polymeric matrix, having different stiffnesses, will cause high stress concentrations on a local level, even when the material is only lightly loaded on the macroscopic level.

2.1.2 Nonlinear Viscoelasticity

The type of nonlinearity mostly encountered at higher levels of stress and/or strain manifests itself through stress (or deformation) dependencies of the creep compliance or stress relaxation function. Other forms of nonlinear behaviour frequently encountered are stress coupling effects (nonlinear interaction in multi-axial stress fields) and time dependence of mechanical properties of the material.

In this thesis, stress dependence and stress coupling will be discussed as sources of nonlinear behaviour. Time dependence in the form of physical ageing will also be addressed.

The superposition principle does not hold in the nonlinear regime. Several extensions to the linear theory have been proposed. One of the most general approaches considers a series of multiple integrals based on the Green-Rivlin theory (Green & Rivlin 1957^[21], 1960^[22]; Green *et al.* 1959^[23]) and was given by Lockett^[30] (1965) for homogeneous isotropic materials. Although potentially very accurate, a multiple integral formulation is rather cumbersome to use. A large test program is needed to evaluate all kernel functions.

Another approach to nonlinear modelling is to modify the Boltzmann superposition integral in some way. Examples of this approach are given by Leaderman (1943)^[29] and Schapery (1969)^[38].

2.2 Schapery's Model

In this thesis, nonlinear viscoelastic modelling will be carried out using Schapery's theory. Schapery's model is originally based on a thermodynamic theory (Schapery 1969)^[38] which gives it a theoretical background for modelling nonlinear viscoelasticity. Its one-dimensional creep formulation is given by

$$\varepsilon(t) = g_0 J_0 \sigma(t) + g_1 \int_0^t \Delta J(\psi - \psi') \frac{d(g_2 \sigma)}{d\tau} d\tau \quad (2.4)$$

where the kernel function (compliance function) $\Delta J = \Delta J(\psi - \psi')$ depends on two shifted times

$$\psi = \int_0^t \frac{dt'}{a_\sigma} \quad \text{and} \quad \psi' = \int_0^\tau \frac{dt'}{a_\sigma} \quad (2.5)$$

J_0 represents the initial elastic compliance, g_0 , g_1 , g_2 and a_σ are nonlinearizing model parameters which are at least stress dependent functions. They describe the nonlinear nature of the material response and can be determined experimentally. When the four nonlinearizing functions are equal to unity, Schapery's creep formulation Eq (2.4) reduces to Boltzmann's superposition integral, Eq (2.2). When g_0 , g_1 and a_σ are unity, the nonlinearity is modelled entirely by g_2 which reduces the expression to that of Leaderman's MSM (modified superposition Method, H. Leaderman^[29] 1943).

Schapery's model seems to be especially attractive because it has the advantage of retaining a single integral form at all load levels. Also the nonlinearizing functions can in principle be determined quite easily by a number of creep-recovery experiments at different load levels. Schapery's model has been used successfully for a large number of material types.

2.2.1 Kernel Functions

The kernel function of Eq (2.4) can, in principle, be any form of function, as long as it increases monotonously with time. It should be appropriately chosen for a specific material. Because creep of many materials can be represented by a power-law function of time, Schapery has chosen the following form of the kernel function ΔJ (Schapery 1969)^[38],

$$\Delta J(\psi) = C\psi^n \quad (2.6)$$

where the material properties C and n are independent of the stress level and of time. Constancy of C and n is required to preserve superposition at small stress levels.

The only thermodynamic restriction to the model parameters, g_0 , g_1 , g_2 and a_σ , is that these should be positive for stable materials (Schapery 1969)^[38]. Several functional dependencies of g_0 , g_1 , g_2 and a_σ on the stress level have been proposed. Schapery obtained the following expressions in a study on creep of a fibre-reinforced phenolic resin (Schapery 1969)^[38],

$$\begin{cases} g_0 = \frac{\sinh(\sigma/\sigma_e)}{\sigma/\sigma_e} \\ \frac{g_1 g_2}{a_\sigma^n} = \frac{\sinh(\sigma/\sigma_m)}{\sigma/\sigma_m} \\ \Delta J(\psi) = C\psi^n \end{cases} \quad (2.7)$$

where σ_e and σ_m are two material constants. The function $g_1 g_2 / a_\sigma^n$ is the so-called creep coefficient.

A generalized Kelvin model consisting of springs and dashpots in series has also been used as a representation of the kernel function. Its functional form is given by

$$\Delta J(\psi) = \sum_{i=1}^N J_i \left(1 - e^{-\psi/\tau_i}\right) + J_s \psi \quad (2.8)$$

where J_i , J_s and τ_i are positive constants; τ_i are the so-called 'retardation times'. The factor $J_s \psi$ represents a steady-flow component, which leads to irrecoverable or residual strain in a creep experiment after removal of the stress. The coefficient J_s is negligible for most polymers, far below their glass-transition temperatures. Un-cross-linked amorphous polymers above their glass-transition temperature may however exhibit steady flow.

Another representation of the creep compliance consists of an infinite sum of fractional exponential functions (Rabotnov 1980)^[33]. This representation has been used widely in the Russian school for predicting long-term behaviour from short-term tests. Fractional exponentials have been incorporated in Schapery's model (Brouwer 1986). The fitting procedure for this type of function however is very elaborate (Brouwer 1986)^[11], since fitting has to be carried out in the Laplace-domain.

Finally an exponential-law has been proposed as an appropriate description for long time creep deformation for the master curve when the physical ageing effect is taken into account (long-term creep behaviour, see Chapter 3). The kernel function of the exponential-law can be expressed as

$$\Delta J(\psi) = C[\exp(\psi^n) - 1] \quad (2.9)$$

where C and n are two constants, or so-called *creep parameters* (Zhang 1993c).

Schapery's model as given by Eq (2.4) & Eq (2.5) has four *nonlinearizing parameters*, g_0, g_1, g_2 and a_G , one material constant to describe the initial response, J_0 , and two or more creep parameters contained in the kernel function ΔJ . Here the term, *model parameters*, stands for all these constants and parameters.

2.2.2 Limitation in Unloading Behaviour

Schapery's model has been successfully used in polymer materials and polymer based composites. The model has many advantages, such as the fact that the model parameters can easily be determined by simple tests; the model can also be conveniently extended into a three-dimensional constitutive relation. However, some limitations of this model have been revealed.

Hadley and Ward (1975)^[25] concluded that Schapery's model was quite appropriate when applied for cases with increasing loading situations, such as constant-strain-rate loading. It however turned out to be very inadequate for unloading situations. The conclusion was based on the original discussion by Ward and Onat (1963)^[44] about the limited ability of the simple Boltzmann superposition integral to describe recovery behaviour. Their study revealed that the nonlinear activity in recovery spoiled the superposition rule in both Boltzmann's expression and Leaderman's nonlinear representation. Rendell *et al.* (1987)^[34] reached the same conclusion in their work. There is no detailed research available being described in the literature about this restriction of Schapery's model. Some recent implementation and application of the model (e.g. Brouwer 1986^[11] and Rooijackers 1988^[36]) did not consider the unloading problem.

In Section 2.5, a remedy, based on the concept of history-dependent or loading-status-dependent parameters is proposed. By introducing this concept, the flexibility of Schapery's model is largely enhanced and, theoretically, there is no restriction of this modified model to describe unloading situations within the short-term range. The idea of history-dependent or loading-status-dependent parameters is based on the premise that these parameters may change at any moment during loading. After a certain loading period, a polymeric material may change its mechanical properties even if all the loading conditions and other environmental conditions are regained.

For long-term behaviour, however, the model parameters have to meet the requirement of convergence in recovery (see Section 2.5). Technically, the enhanced method requires additional loading sta-

tus-dependent tests to characterize these extra model parameters and, furthermore, a mathematical description for the separate unloading parameters is needed when the loading and unloading status switches frequently (Zhang 1992)^[47]. These requirements make the method less applicable in practice. Nevertheless, this loading-status-dependent-parameter-method may be useful in some specific cases, especially when the unloading behaviour needs to be modelled accurately.

The model parameter properties will be discussed and the unloading behaviour of polyester will be examined in Chapter 3.

2.3 Ageing Effects

2.3.1 Introduction

To characterize the long-term behaviour of polymers, an adequate method is needed for practical purposes, in the sense that it must be effective in performance and relatively simple in application for most engineering materials. Using short-term test data to predict the long-term behaviour of materials is certainly the most economic way and, therefore, the most appealing method to obtain this long term information. Schapery's model has been used for this purpose by a number of research groups, especially, from Virginia Polytechnic Institute (Tuttle and Brinson 1986)^[45]. Indeed, the nonlinearizing function, a_t , shifts the viscoelastic response with respect to time, making the model, at least in principle, a possible tool for long term prediction. An extremely important aspect of the long-term behaviour of polymers is however the influence of ageing. Neglecting ageing may lead to large errors, *e.g.*, Sterrett & Miller (1988)^[41] have found that without taking the ageing effect into account a large over-estimation occurred, when extrapolating one day creep data for the prediction of a one-year-creep case.

The polymeric material considered in the present work is an *unsaturated polyester resin*, *i.e.*, a thermosetting polymer. For such polymers, two different ageing phenomena can in principle be distinguished. These are rooted in completely different structural changes of the polymer with time. Physical ageing corresponds to a thermodynamic process which concerns only the molecular chain configuration of polymers. Chemical ageing, on the other hand, can be described as the continuation of a chemical reaction, *i.e.* a cross-linking reaction.

The influence of ageing on the time-dependent behaviour of polymers is larger than most people expect. In the case of creep loading, not taking ageing effects into account has caused either large extrapolation errors in the long term prediction or has resulted in a poor fitting quality of the fitting functions. Results from the present study show that neglecting the ageing effect can cause an error of more than 200% in the strain when extrapolating a 24-day-creep strain over 3 decades. Even during short-term creep, ageing may well be important. Deviations from linear viscoelastic behaviour in recovery or general unloading may well be caused by a partial erasure of ongoing ageing due to high imposed stress levels (Struik 1978)^[42].

In this chapter, a brief review of ageing concepts will be given. A possible implementation of the ageing effect into the viscoelastic model will be proposed later. The aim of the implementation is an attempt to consider ageing influences to predict long-term nonlinear viscoelastic behavior with the use of short-term data. Specifically, the work aims to characterize the effect of physical ageing on the nonlinear creep deformation of polymers and to provide the necessary parameter(s) for a 3D nonlinear viscoelastic model (Zhang & Ernst 1993)^[52].

2.3.2 Physical Ageing

The physical ageing phenomenon, which has been studied extensively by Struik and coworkers originally for amorphous polymers, is due to a general continuation of the glass formation that sets in around the glass transition temperature T_g . Ageing is therefore a basic feature of the glassy state and it affects all those temperature-dependent properties which change drastically and abruptly at T_g . During ageing these properties change in the same direction as during cooling through the T_g range; the material becomes stiffer and embrittles, its damping decreases, and so do its creep- and stress-relaxation rates (Struik 1978)^[42].

It is hard to obtain a reliable creep curve over a long period of time through an experiment, due to the limited stability of available test equipment and disturbances from the surrounding environment. A technique has therefore been presented to 'construct' such a long-time creep curve from a series of short-time creep tests, carried out at different temperatures under the assumption that a time-temperature superposition rule holds for the material under investigation. In this manner, a so-called 'master curve' is constructed (see, e.g., Findley *et al.*^[18], page 107, for the procedure to obtain a master curve). Fig. 2.1(b) shows that ageing effects cause the experimentally obtained long-term creep curves to deviate from the master curve. Generally speaking the long-term creep curve will be much flatter and will become straight and will even change in curvature.

Amorphous solids are not in thermodynamic equilibrium at temperatures below their glass transition temperature (Struik 1978^[42], page 1). Such materials are to be regarded as solidified supercooled liquids whose volume, enthalpy and entropy are larger than in a final equilibrium state. Polymers will however reach a thermodynamic equilibrium immediately when they are heated to above T_g , and any previous ageing will then be erased. Its thermal-reversibility is an important aspect of physical ageing. Use can be made of this in setting up an experimental program. A material can be rejuvenated quite conveniently by a short excursion above its T_g .

Physical ageing can be explained at least qualitatively by the free-volume concept (see Struik 1978^[42], Chapter 2).

2.3.3 Chemical Ageing

Chemical ageing of polymers is due to phenomena such as additional cross-linking, chemical degradation and photo-oxidation. For the unsaturated polyester under investigation in this study, additional cross-linking turns out to be the most important part of chemical ageing. Additional cross-linking gives a significant reduction in molecular mobility. In order to reduce the influence of chemical age-

ing on experimental data, the material is usually subjected to a postcuring process. Postcuring is necessary to make an unsaturated polyester and its composite products stable in a long-term sense. An essential difference with physical ageing is that chemical ageing, in the sense of additional cross-linking, can only be accumulated and is therefore not reversible without damage (degradation). Under much higher temperatures above T_g and close to the degradation temperature of the polymer, chemical degradation will be triggered. Chemical bonds between molecules are then permanently disrupted and the original material no longer exists. Since the tests performed in this study are all carried out at room temperature, degradation is not an issue in this work. Other possible sources of chemical ageing, like UV radiation etc., are not studied in this work either.

2.3.4 Basic Physical Ageing Phenomena

Struik (1978)^[42] has shown that all polymers (physically) age in a similar way. Physical ageing persists for a very long period of time and, therefore, should be considered when characterizing the long-term behaviour of polymer materials.

1. Creep and Relaxation

Ageing affects material properties primarily by changing the relaxation times. These relaxation times turn out to increase proportional to the ageing time (Struik 1978)^[42]. Ageing effects will cause a creep curve of a polymer to shift over the time-scale in a short-term creep case (Fig. 2.1 (a)).

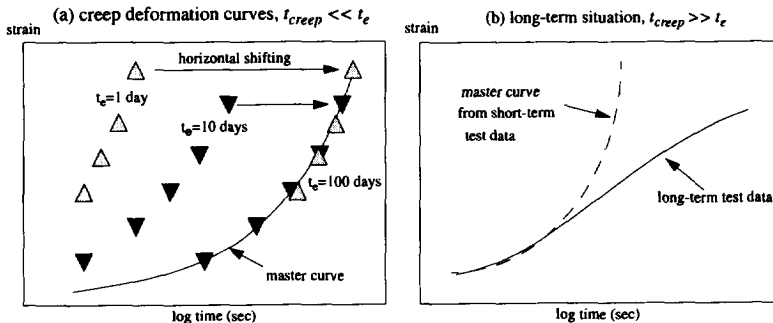


Figure 2.1. (a) Tensile creep curves (artificial). The creep curves were obtained for various ageing times, t_e . The master curve gives the result of a superposition of data; the shifting direction is indicated by the arrow. (b) Long-term test (artificial). The dashed line is the master curve derived by time-temperature superposition.

Besides, because of physical ageing, it is generally incorrect to predict long-term creep behaviour from short-term data simply by time-temperature superposition (see, for example, Findley *et al.* 1976^[18], page 105). Time-temperature superposition results in a creep curve which strongly overestimates the actual long-term creep behaviour, since ageing induced gradual stiffening has been neglected. This also affects the definition of 'long-term' and 'short-term' behaviour.

The definitions of short-term and long-term material behavior should be based on the ageing time of a material as was pointed out by Struik (1978)^[42]. It is incorrect to say that one hour is a short-term period and two years a long-term period. If the ageing time of a material is t_e , and the test duration is t , long-term and short-term are defined by:

$$t \gg t_e, \text{ long-term test} \quad (2.10)$$

$$t \ll t_e, \text{ short-term test} \quad (2.11)$$

Therefore, for a new material (*i.e.*, just after rejuvenating the material by raising its temperature to above T_g for a certain period of time, to remove its physical ageing history) with an ageing time of several minutes, an one-hour-creep test is a long-term test. On the other hand, for a ten-year-old specimen, a two-year-creep test is considered to be a short-term test.

2. Frozen Strain

Not only a small excursion to a temperature above T_g is able to rejuvenate a polymeric material, the same effect can be obtained by large deformations (or stresses). Struik has shown that stresses (at least partly) erase some of the previous ageing (Struik 1978)^[42]. The interaction between deformation and ageing is an interesting phenomenon and leads to surprising results.

For the unsaturated polyester studied in the present work, experiments have been performed, which clearly show this interaction phenomenon (de Boer 1993)^[1].

A partly cured unsaturated polyester bar having a rectangular cross section was subjected to a large twist. The angle of twist during the test was measured in order to record the difference between the set angle of twist during loading and the remaining angle of twist after the load had been released.

After removal of the load, a non-negligible remaining deformation was found which turned out to be permanent. Both physical ageing and chemical ageing (additional cross-linking) can catch and freeze the deformation at least partially if the material is kept in a deformed situation for a long-term period ($\log t \gg \log t_e$). The physical ageing induced part of frozen deformation can, however, be removed totally by raising the temperature above T_g (rejuvenation). The additional cross-linking induced part on the contrary is a permanent part which is due to an ongoing build-up of the molecular structure by new chemical bonds during the period of deformation. It was found in a test on a postcured sample that there did not exist permanent frozen deformation since it turned out that all the frozen deformation was removed by raising the temperature above T_g .

The interaction phenomenon might be one of the reasons why in a creep-recovery test on some polymers at high stress levels, the recovery data show some permanent strain after very long times of recovery. An other example of possible ageing effects is found in the so-called recovery abnormality phenomenon. It reveals a slower decreasing recovery curve than what the superposition law would suggest. This recovery abnormality was mentioned very early S. Turner around 1960.

The relaxation tests on the twisted partly cured unsaturated polyester test bars have also shown that the recovery process following unloading does not always exists. If the 'loading' time is long enough, almost all the deformation is frozen in (after removal of the loading, only less than 1% recovered tor-

sional deformation was found for a 'loading' period up to one month). It suggests that the stresses have been almost fully relaxed during the interaction process of relaxation and ageing.

The phenomenon of frozen-in deformation due to physical ageing was extensively studied by Struik (1990) for thermoplastic materials by twisting tests by thermoplastic materials. Our tests on a thermo-setting material have revealed that a large amount of permanent frozen-in deformation occurs. This permanent deformation is attributed to the ongoing chemical ageing.

2.3.5 Struik's Theory of Physical Ageing

Struik's theory has been given and documented extensively in his book on physical ageing (Struik 1978)^[42]. It will be summarized in this section.

For short-time creep of polymers, the creep curves often have the same shape for different ageing times and temperatures and can be described by one single 'universal' creep compliance function (the Kohlrausch-Williams-Watts exponential function) given by,

$$J(t)_{T, t_e} = J_0 \exp \left[\left(\frac{t}{t_0} \right)^n \right], \quad (2.12)$$

where T is the temperature, t_e the ageing time, $t_0 = t_0(T, t_e)$ the mechanical retardation time, $J_0 = J_0(T, t_e)$ the initial compliance ($= J_0(T)$ if a small vertical shift due to ageing can be neglected), J the creep compliance and n a material constant.

1. Shifting Rule

Shifting of short-term creep curves (for $t \ll t_e$) on a logarithmic time scale may be interpreted as a change of all mechanical retardation times, t_0 , with one factor. Creep is accelerated by shifting towards shorter ageing times (Lamers 1989)^[28],

$$at_0(t_{e1}) = t_0(t_{e2}), \quad t_{e1} < t_{e2}, \quad (2.13)$$

$$bJ(t_{e1}) = J(t_{e2}), \quad t_{e1} < t_{e2}, \quad (2.14)$$

where a and b are positive acceleration factors or shifting factors in the horizontal (*i.e.* time) and the vertical (*i.e.* creep compliance) directions respectively.

2. Effective-Time Theory

For the prediction of long-term creep ($t \gg t_e$), the acceleration factors become time dependent and the change of ageing times should be taken into account. The regularity of the ageing shifting behavior in Fig. 2.1(a) suggests that two constants, α and β , for horizontal and vertical shifting respectively exist, such that

$$\alpha = \frac{d \log a}{d \log t_e}, \quad (2.15)$$

$$\beta = \frac{d \log b}{d \log t_e}. \quad (2.16)$$

α and β are the so-called horizontal (time) and vertical (creep compliance) shifting rates. Integrating Eq (2.15) and Eq (2.16) in the domain $(t_e, t+t_e)$ one obtains

$$a(t+t_e) = \left(\frac{t+t_e}{t_e} \right)^\alpha, \quad (2.17)$$

$$b(t+t_e) = \left(\frac{t+t_e}{t_e} \right)^\beta. \quad (2.18)$$

where t_e is the initial ageing time and $(t+t_e)$ the current ageing time.

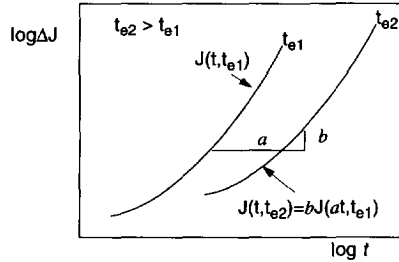


Figure 2.2. Shifting of a creep curve due to the ageing influence

The short-term creep compliances of a material at different ageing times t_{e1} and t_{e2} are related as follows:

$$J(t, t_{e2}) = bJ(at, t_{e1}) \quad t_{e1} < t_{e2}. \quad (2.19)$$

In other words, if the ageing time is changed from t_e to t_e+dt , from Eq (2.19), the creep compliance is

$$J(t, t_e) = \frac{1}{b(t_e+dt)} J\left(\frac{t}{a(t_e+dt)}, t_e+dt\right). \quad (2.20)$$

The effective time interval $d\tau$ is now introduced as

$$d\tau = \frac{dt}{a(t+t_e)} \quad (2.21)$$

Its physical meaning is clear: within the time interval between t and $t+dt$ the same amount of creep will occur as within the effective time interval $d\tau$, which refers to a short-term creep process where the case of (physical) ageing is too slow to be detected. Combining Eq (2.17) and Eq (2.21) gives

$$\frac{d\tau}{dt} = \left(\frac{t_e}{t+t_e} \right)^\alpha \quad (2.22)$$

Further, with the initial condition $\tau(t=0) = 0$, one derives, starting from Eq (2.22),

$$\text{for } \alpha = 1, \quad \tau = t_e \ln\left(1 + \frac{t}{t_e}\right) \quad (2.23)$$

$$\text{for } \alpha \neq 1, \quad \tau = \frac{t_e}{1-\alpha} \left(\left(1 + \frac{t}{t_e}\right)^{1-\alpha} - 1 \right). \quad (2.24)$$

Note that no ageing occurs for $\alpha = 0$. For most polymers, $\alpha = 1$ only holds near the glass transition temperature. In principle the relation between short-term creep and long-term creep is solved and the mathematical expressions for long-term creep curves can readily be calculated. The long-term creep compliance for a given temperature and a given initial ageing time is easily derived from Eq (2.19),

$$J^{longterm}(t, T, t_e) = \frac{1}{b(t)} J^{shortterm}(\tau, T, t_e). \quad (2.25)$$

When the creep compliance J is an exponential function as defined in Eq (2.12), one obtains

for $\alpha = 1$:

$$J^{longterm}(t, T, t_e) = \left(\frac{t_e}{t+t_e} \right)^B J_0 \exp \left[\left[\frac{t_e}{t_0} \ln \left(1 + \frac{t}{t_e} \right) \right]^n \right], \quad (2.26)$$

for $\alpha \neq 1$:

$$J^{longterm}(t, T, t_e) = \left(\frac{t_e}{t+t_e} \right)^B J_0 \exp \left[\left[\frac{t_e}{(1-\alpha)t_0} \left(\left(1 + \frac{t}{t_e} \right)^{1-\alpha} - 1 \right) \right]^n \right]. \quad (2.27)$$

In this manner it is possible to make satisfactory predictions of the long-term creep behaviour of amorphous linear macromolecular glasses (Lamers 1989)^[28]. Measurements have shown that predictions differ less than 10% for extrapolations up to $t/t_e \approx 3000$ (Lamers 1989)^[28].

2.4 Ageing Implementation

In the previous section, the ageing phenomenon and the way physical ageing is dealt with by using a physical ageing dependent shifting rule were discussed. In this section a possible way to introduce ageing into the nonlinear viscoelastic model of Schapery, given by Eq (2.4) and Eq (2.5) is proposed. Although chemical ageing is not important for the present purpose and can be limited if not excluded by postcuring as was discussed in the previous section, both physical ageing and chemical ageing will be included in the model. This will allow the presentation of a more general nonlinear viscoelastic model for implementation in a finite-element-method package.

Physical and chemical ageing effects can be implemented into Schapery's model by shifting the kernel function, ΔJ , horizontally and vertically on logarithmic time scales (see Fig. 2.2).

The continuing ageing during loading will deviate the long-term creep curve from its original course. According to Struik's theory (Struik 1978)^[42] and Lamers' work (Lamers 1989)^[28], the ageing-

induced shifting factor a (along the time axes) and b (along the ΔJ axes) obey the rules, given by Eq (2.17) and Eq (2.18) respectively. To take this effect into account, it is proposed here to replace the variable ψ , from Eq (2.5), and the compliance function ΔJ of the Schapery model by a long-term shifted time (or so-called effective-time), $\bar{\psi}$, and a long-term parameter, $\bar{\Delta J}$, respectively:

$$\bar{\psi} = \int_0^t \frac{dt'}{\bar{a}_\sigma} \quad \text{and} \quad \bar{\psi}' = \int_0^\tau \frac{d\tau'}{\bar{a}_\sigma}. \quad (2.28)$$

Considering Eq (2.19), the long term kernel function is taken as follows,

$$\bar{\Delta J} = \left(\frac{t_e}{t_e + \tau} \right)^\beta \Delta J, \quad (2.29)$$

where t_e is the reference (or initial) ageing time, while $t_e + t$ is the current ageing time. If there is no coupling effect between stress-induced and ageing-induced shifting, the relation between the shifting factors \bar{a}_σ and a_σ is given by

$$\frac{1}{\bar{a}_\sigma} = \frac{a_{\text{aging}}}{a_\sigma}. \quad (2.30)$$

With the aid of Eq (2.17), \bar{a}_σ can then be written as

$$\bar{a}_\sigma = a_\sigma \left(\frac{t_e + \tau}{t_e} \right)^\alpha. \quad (2.31)$$

Here a_σ is the stress-induced shifting factor as originally defined in the Schapery model, Eq (2.5).

2.5 Restrictions on the Model Parameters

Nonlinear behaviour occurs when the viscoelastic functions become deformation (or stress) dependent. In general therefore these functions may be dependent on both stress and stress history. If a constitutive equation within the framework of viscoelasticity is to be formulated, the consistency requirement must be met. This requirement prescribes a return to the original 'material state' after a loading-unloading excursion, *i.e.*, complete recoverability of deformation. If a viscous flow is included in order to take unrecoverable (permanent) deformation into account, the model is extended to a viscoelasto-plastic theory. Such a viscous flow effect, or plastic deformation will not be considered in the present model. Therefore the present model is viscoelastic and does not include plastic deformation (viscous flow).

A mathematical model however will not satisfy this recoverability automatically. The analysis in this section concerns an assessment of the stress dependence and stress history dependence of the model parameters taking into account the consistency requirement of the viscoelastic assumption.

2.5.1 A General Multi-Step Loading Case

In order to add a possibility for the model to describe unloading behaviour more accurately (see Section 2.2.2), it is assumed here that the polymer changes its mechanical properties when it is under a mechanical or thermal load for a period of time. The material changes can be reflected in changes of the kernel function of the model, ΔJ with real time.

Evaluating the strain given by the Schapery model in Eq (2.4), for a general multi-step stress-input loading case, some specific loading cases such as a single-step and a two-step stress-input, can be easily described.

For a multi-step stress input (see also Zhang 1992)^[47], as depicted in Fig. 2.3,

$$\sigma(t) = \sum_{j=1}^i (\sigma_j - \sigma_{j-1}) H(t - t_j), \quad (2.32)$$

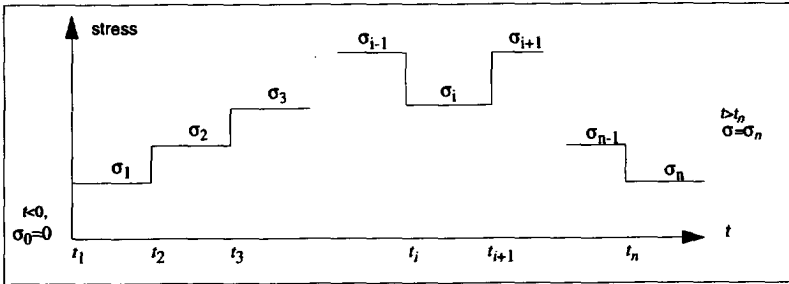


Figure 2.3. *n*-step stress input

where $H(t-t_j)$ is the unit step function. If $\sigma_j - \sigma_{j-1} < 0$, an unloading step is given. The most general expression for the kernel function ΔJ , being stress history dependent, is now assumed. Thus ageing effects can be induced, for instance, directly into the kernel function ΔJ . ΔJ is thus written in a form corresponding to expression Eq (2.32) for a multi-step loading,

$$\Delta J(t) = \sum_{j=0}^i (\Delta J_{j-1}^j - \Delta J_{j-1}^{j-1}) H(t - t_j), \quad (2.33)$$

with $\Delta J_{-1} = 0$. In this expression, the subscripts indicate the stress-dependence and the superscripts the time step, (see Fig. 2.4). Different subscripts and superscripts suggest a different value of the kernel function ΔJ , which corresponds to a material change with either stress or real time, or both.

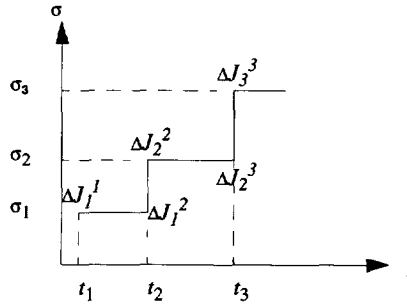


Figure 2.4. Definition of superscripts and subscripts of the kernel function

In Eq (2.33), the kernel function value for the i th time-step ΔJ_i^j is given by $\Delta J_i^j(\psi - \psi_j)$, where the argument ψ is evaluated for the i th time-step, while ψ_j is evaluated for the stress level corresponding to the j th time-step. Hence, following expression is obtained (Zhang 1992^[47]),

$$g_2\sigma = \sum_{j=1}^i \left(g_2\sigma_j - g_2\sigma_{j-1} \right) H(t-t_j), \quad (2.34)$$

where the superscript j preceding g_2 stands for a different value of g_2 , which value is step-dependent and corresponds to the stress level σ_j during the j th step in time. It follows that

$$\frac{d(g_2\sigma)}{dt} = \sum_{j=1}^i \left(g_2\sigma_j - g_2\sigma_{j-1} \right) \delta(t-t_j), \quad (2.35)$$

where $\delta(t)$ is the delta function. The kernel of the integral in Eq (2.4) is therefore

$$\Delta J_i^d \frac{d}{dt} (g_2\sigma) = \left\{ \sum_{j=0}^i \left[\Delta J_i^j(\psi - \psi_j) - \Delta J_{i-1}^j(\psi - \psi_{j-1}) \right] H(t-t_j) \right\} \left\{ \sum_{j=1}^i \left(g_2\sigma_j - g_2\sigma_{j-1} \right) \delta(t-t_j) \right\}, \quad (2.36)$$

and the strain ϵ^i (the superscript i preceding a symbol indicates the strain in the i th step period) becomes

$$\begin{aligned} \epsilon^i &= g_0^j(0)\sigma_i + \\ &+ g_1^i \int_0^t \left\{ \sum_{j=0}^i \left[\Delta J_i^j(\psi - \psi_j) - \Delta J_{i-1}^j(\psi - \psi_{j-1}) \right] H(\tau-t_j) \right\} \left\{ \sum_{j=1}^i \left(g_2\sigma_j - g_2\sigma_{j-1} \right) \delta(\tau-t_j) \right\} d\tau, \end{aligned} \quad (2.37)$$

where $i = 1, 2, \dots, n$ and

$$\psi = \frac{t-t_i}{a_\sigma} + \sum_{m=1}^{i-1} \frac{(t_{m+1}-t_m)}{a_\sigma}, \quad (2.38)$$

and

$$\psi_j = \sum_{m=1}^{j-1} \frac{(t_{m+1}-t_m)}{a_\sigma}. \quad (2.39)$$

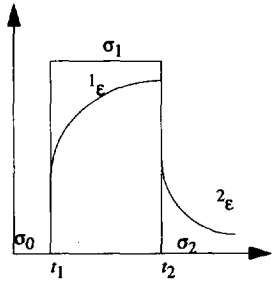


Figure 2.5. Single-step case

2.5.2 Single-Step Stress-Input

The particular case of a single creep-recovery experiment is then considered. It will now be shown that if a viscoelastic requirement must be met for the recovery deformation, some important conditions for the creep parameters, C and n must be ensured.

For a single-step case (see Fig. 2.5), $\sigma_0 = 0$, $\sigma_1 = \sigma$ and $\sigma_i = 0$ for $i \geq 2$, the second term on the right hand side of Eq (2.36) becomes,

$$\{\Delta J_0 + (\Delta J_1 - \Delta J_0)H(t-t_1) + (\Delta J_2 - \Delta J_1)H(t-t_2)\} \{({}^1g_2\sigma_1 - {}^0g_2\sigma_0)\delta(t-t_1) + ({}^2g_2\sigma_2 - {}^1g_2\sigma_1)\delta(t-t_2)\}, \quad (2.40)$$

in which, $\sigma_0 = 0$ and $\sigma_2 = 0$, so that the following terms are obtained after integration,

$$\begin{aligned} \int_0^t \Delta J_0 \{({}^1g_2\sigma_1 - {}^0g_2\sigma_0)\delta(t-t_1) + ({}^2g_2\sigma_2 - {}^1g_2\sigma_1)\delta(t-t_2)\} d\tau &= (\Delta J_0^1 - \Delta J_0^2){}^1g_2\sigma, \\ \int_0^t (\Delta J_1 - \Delta J_0)H(t-t_1){}^1g_2\sigma_1\delta(t-t_1) d\tau &= \frac{1}{2}(\Delta J_1^1 - \Delta J_0^1){}^1g_2\sigma, \\ \int_0^t (\Delta J_1 - \Delta J_0)H(t-t_1)({}^2g_2\sigma_2 - {}^1g_2\sigma_1)\delta(t-t_2) d\tau &= (\Delta J_1^2 - \Delta J_0^2)(-{}^1g_2\sigma), \end{aligned}$$

$$\int_0^t (\Delta J_2 - \Delta J_1) H(t-t_2) {}^1g_2 \sigma_1 \delta(t-t_1) d\tau = 0 ,$$

$$\int_0^t (\Delta J_2 - \Delta J_1) H(t-t_2) \left({}^2g_2 \sigma_2 - {}^1g_2 \sigma_1 \right) \delta(t-t_2) d\tau = \frac{1}{2} (\Delta J_2^2 - \Delta J_1^2) \left(-{}^1g_2 \sigma \right) .$$

Together with all the terms above, the integration in Eq (2.37) becomes

$$\int_0^t \Delta J \frac{d}{d\tau} (g_2 \sigma) d\tau = \frac{1}{2} \left({}^1g_2 \sigma \right) \left[\left(\Delta J_0^1 - \Delta J_2^2 \right) + \left(\Delta J_1^1 - \Delta J_1^2 \right) \right] , \quad (2.41)$$

and the strain

$${}^2\varepsilon = \frac{1}{2} \left({}^2g_1 {}^2g_2 \sigma \right) \left[\left(\Delta J_0^1 - \Delta J_2^2 \right) + \left(\Delta J_1^1 - \Delta J_1^2 \right) \right] , \quad (2.42)$$

where the superscripts on ΔJ^j indicate the step time, ($t_1 = 0$ and $t_2 = t_a$), and

$$\Delta J_0^1 = \Delta J_0 \left(\frac{t_a}{1 a_\sigma} + \frac{t-t_a}{2 a_\sigma} \right) ,$$

$$\Delta J_2^2 = \Delta J_2 \left(\frac{t-t_a}{2 a_\sigma} \right) ,$$

$$\Delta J_1^1 = \Delta J_1 \left(\frac{t_a}{1 a_\sigma} + \frac{t-t_a}{2 a_\sigma} \right) ,$$

$$\Delta J_1^2 = \Delta J_1 \left(\frac{t-t_a}{2 a_\sigma} \right) .$$

Finally the recovery strain for the single-step stress input case is,

$${}^2\varepsilon = \frac{1}{2} \left({}^2g_1 {}^2g_2 \sigma_2 \right) \left\{ C_2 - C_0 + C_0 \exp \left(\frac{t_a}{1 a_\sigma} + \frac{t-t_a}{2 a_\sigma} \right)^{n_0} - C_2 \exp \left(\frac{t-t_a}{2 a_\sigma} \right)^{n_2} + C_1 \exp \left(\frac{t_a}{1 a_\sigma} + \frac{t-t_a}{2 a_\sigma} \right)^{n_1} - C_1 \exp \left(\frac{t-t_a}{2 a_\sigma} \right)^{n_1} \right\} , \quad (2.43)$$

where the exponential law Eq (2.9) has been applied. Rearranging Eq (2.43) yields ($\sigma_2 = 0$),

$${}^2\varepsilon = \frac{1}{2} {}^2g_1 {}^2g_2 \sigma C_1 \left\{ \frac{C_2 - C_0}{C_1} + \frac{C_0}{C_1} \left[\exp \left(\frac{t_a}{1 a_\sigma} + \frac{t-t_a}{2 a_\sigma} \right)^{n_0} - \frac{C_2}{C_0} \exp \left(\frac{t-t_a}{2 a_\sigma} \right)^{n_2} \right] + \left[\exp \left(\frac{t_a}{1 a_\sigma} + \frac{t-t_a}{2 a_\sigma} \right)^{n_1} - \exp \left(\frac{t-t_a}{2 a_\sigma} \right)^{n_1} \right] \right\} . \quad (2.44)$$

Assuming that the consistency requirement of viscoelasticity holds for the material, a convergent strain expression for the recovery period must be obtained. Therefore

$$\lim_{t \rightarrow \infty} {}^2\varepsilon = 0 , \quad (2.45)$$

In Eq (2.44)

$$\lim_{t \rightarrow \infty} \left[\exp \left(\frac{t_a}{1/a_\sigma} + \frac{t-t_a}{2/a_\sigma} \right)^{n_1} - \exp \left(\frac{t-t_a}{2/a_\sigma} \right)^{n_1} \right] = 0, \quad (2.46)$$

Condition Eq (2.45) therefore requires that the limit for $t \rightarrow \infty$ of the remaining terms in Eq (2.46) also vanishes. This is the case if

$$\lim_{t \rightarrow \infty} \left[\exp \left(\frac{t_a}{1/a_\sigma} + \frac{t-t_a}{2/a_\sigma} \right)^{n_0} - \frac{C_2}{C_0} \exp \left(\frac{t-t_a}{2/a_\sigma} \right)^{n_2} \right] = \frac{C_0 - C_2}{C_0} = a, \quad (2.47)$$

or, equivalently

$$\lim_{t \rightarrow \infty} \exp \left(\frac{t-t_a}{2/a_\sigma} \right)^{n_2} \left\{ \exp \left[\left(\frac{t_a}{1/a_\sigma} + \frac{t-t_a}{2/a_\sigma} \right)^{n_0} - \left(\frac{t-t_a}{2/a_\sigma} \right)^{n_2} \right] - \frac{C_2}{C_0} \right\} = a, \quad (2.48)$$

where a is a constant. Eq (2.48) further requires that

$$\lim_{t \rightarrow \infty} \left\{ \exp \left[\left(\frac{t_a}{1/a_\sigma} + \frac{t-t_a}{2/a_\sigma} \right)^{n_0} - \left(\frac{t-t_a}{2/a_\sigma} \right)^{n_2} \right] - \frac{C_2}{C_0} \right\} = 0, \quad (2.49)$$

or alternatively,

$$\lim_{t \rightarrow \infty} \left[\left(\frac{t_a}{1/a_\sigma} + \frac{t-t_a}{2/a_\sigma} \right)^{n_0} - \left(\frac{t-t_a}{2/a_\sigma} \right)^{n_2} \right] = \ln \frac{C_2}{C_0}. \quad (2.50)$$

Finally

$$\lim_{t \rightarrow \infty} \left(\frac{t-t_a}{2/a_\sigma} \right)^{n_2} \left[\frac{\left(\frac{t_a}{1/a_\sigma} + \frac{t-t_a}{2/a_\sigma} \right)^{n_0}}{\left(\frac{t-t_a}{2/a_\sigma} \right)^{n_2}} - 1 \right] = \ln \frac{C_2}{C_0}. \quad (2.51)$$

Since $\lim_{t \rightarrow \infty} \left(\frac{t-t_a}{2/a_\sigma} \right)^{n_2} = \infty$, because $n_2 > 0$, a finite value of the above limit, Eq (2.51), requires that

$$\lim_{t \rightarrow \infty} \left[\frac{\left(\frac{t_a}{1/a_\sigma} + \frac{t-t_a}{2/a_\sigma} \right)^{n_0}}{\left(\frac{t-t_a}{2/a_\sigma} \right)^{n_2}} - 1 \right] = 0. \quad (2.52)$$

The first part of the above limit is assumed to be a constant b ,

$$\lim_{t \rightarrow \infty} \frac{\left(\frac{t_a}{1} + \frac{t-t_a}{2a_\sigma} \right)^{n_0}}{\left(\frac{t-t_a}{2a_\sigma} \right)^{n_2}} = b. \quad (2.53)$$

L'Hospital's rule for a $\frac{\infty}{\infty}$ type of limit is applied to evaluate this limit, b .

$$\lim_{t \rightarrow \infty} \frac{\left(\frac{t_a}{1} + \frac{t-t_a}{2a_\sigma} \right)^{n_0}}{\left(\frac{t-t_a}{2a_\sigma} \right)^{n_2}} = \lim_{t \rightarrow \infty} \frac{2a_\sigma n_0 \left(\frac{t_a}{1} + \frac{t-t_a}{2a_\sigma} \right)^{n_0-1}}{2a_\sigma n_2 \left(\frac{t-t_a}{2a_\sigma} \right)^{n_2-1}} = \lim_{t \rightarrow \infty} \frac{\left(\frac{t_a}{1} + \frac{t-t_a}{2a_\sigma} \right)^{n_0}}{\left(\frac{t-t_a}{2a_\sigma} \right)^{n_2}} \left(\frac{n_0}{n_2} \right) \left(\frac{\frac{t-t_a}{2a_\sigma}}{\frac{t_a}{1} + \frac{t-t_a}{2a_\sigma}} \right) = b \left(\frac{n_0}{n_2} \right). \quad (2.54)$$

Comparing with Eq (2.53), yields the conclusion that $n_0 = n_2$. When $n_0 = n_2$, it is not difficult to prove that the limit of Eq (2.50) is zero, hence $C_0 = C_2$. These results suggest that the creep pattern should not change after a step loading history and only then the strain can be fully recovered if the recovery time is long enough. It confirms that, within the framework of viscoelasticity, the creep parameters C , and the exponent n of the exponential creep rule should NOT be stress/strain history dependent and ageing dependent. These parameters may only be stress dependent. While there is no such restriction on the nonlinearizing parameters, g_0 , g_1 , g_2 and a_σ .

2.5.3 Simplification

The following simplifying picture emerges from the previous assumptions made above. J_0 is a material constant which is independent of the stress and strain history. From a theoretical point of view, the creep parameters C and n may only be stress dependent. The nonlinear parameters g_0 , g_1 , g_2 and a_σ are generally both stress state and stress history dependent.

For the material studied, it will be demonstrated in Chapter 3 that the nonlinearity can be primarily reflected by the parameter g_2 . If only one of the nonlinear parameters, g_2 , remains, the model is actually simplified to the MSM, Modified Superposition Method (Leaderman 1943)^[29].

Starting out from the MSM, and adopting one more nonlinear parameter g_0 to account for a nonlinear elastic behavior (the instantaneous part of the deformation), a simplified model is obtained which, as it will be proved later, is accurate enough for the material under consideration. The model equations in Eq (2.4) & Eq (2.5) are then simplified to

$$\epsilon(t) = g_0 J_0 \sigma(t) + \int_0^t C [\exp(t-\tau)^n - 1] \frac{d(g_2 \sigma)}{d\tau} d\tau, \quad (2.55)$$

wherein $g_0 = g_0(\sigma; t)$; $g_2 = g_2(\sigma; t)$; n , C , J_0 are constants.

In Chapter 3 it will be shown that for relatively low stress levels, the simplified model is accurate enough and eventually it is adopted for further study instead of applying a more complicated model

with load-history dependent model parameters. A motivation for the adaptation of the model Eq (2.55) for the material studied will be given again in Chapter 3.

Material Characterization and Experiments

In this chapter the uniaxial nonlinear viscoelastic model, including ageing effects, which has been developed in Chapter 2 (consists of Eq (2.4), Eq (2.9), Eq (2.28), Eq (2.29) and Eq (2.31)), will be applied to the time-dependent behaviour of an unsaturated polyester.

Ageing behaviour of the unsaturated polyester material will be discussed first, whereafter the nonlinearizing parameters of the Schapery model will be determined. Finally, the obtained model will be verified by cyclic loading tests.

3.1 Characterization of Physical Ageing

In this section the ageing properties of the unsaturated polyester will be studied. The characterization will be restricted to determination of the ageing shifting rate α in Eq (2.31). Other model parameters in the model will be characterized in Section 3.2.

3.1.1 Specimen and Equipment

Creep-recovery tests have been used for characterizing the physical ageing behaviour of the unsaturated polyester.

The specimen used in the tests was designed for a creep test machine which can provide a maximum load of 7,000 N. The geometry of the dog-bone plate specimen is shown in Fig. 3.1.

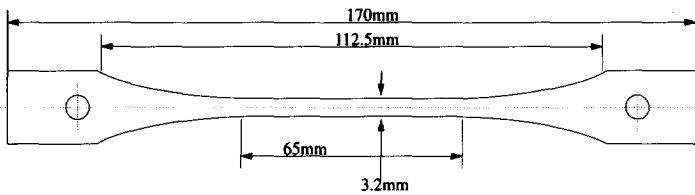


Figure 3.1. Specimen geometry (thickness is 3.5 mm)

The material used for characterization is an unsaturated polyester obtained from DSM Resins and denoted Synolite 593-A-2. This resin is an amorphous cross-linked polymer with a glass transition temperature around 116°C, see Table 3.1. The procedure of specimen preparation is the same as in ten Busschen *et al.* (1989)^[15]. All specimens, after being moulded, were postcured according to the following cycle: 60°C for 24 hours and 80°C for 24 hours. To obtain a zero reference ageing time all specimens were rejuvenated at 130°C for 20 min. An extensometer was used to measure the strain data. The strain signal was recorded with the aid of a personal computer.

Table 3.1. Unsaturated polyester resin, Synolite 593-A-2

Young's modulus, E	5.0 GPa
tensile strength, σ_t	87 MPa
compression strength, σ_c	120 MPa
glass transition temperature, T_g	116°C

All tests were carried out on the creep test machine in the laboratory of Material Science, Delft University of Technology.

3.1.2 Single Specimen Method

Preliminary creep test results on different specimens have shown that the variation of the test data from specimen to specimen is quite large. Typically a 10% difference in creep strains is obtained (Zhang 1992^[47]). The reasons for this variation are due to induced variability in the manufacture of the specimens and in loading preparation. During specimen fabrication, variability is introduced in, *e.g.*, the volume fractions of chemical components, impurities and entrapped air (visible and invisible). Also the curing conditions, such as thermal history and moisture conditions can vary appreciably from specimen to specimen. It is costly to try to improve the preparation procedure in order to obtain a better repeatability of specimen preparation. A second source of variability occurs in the loading

procedure. Also the loading weights of the test machine itself have about 3% error. All these factors suggest that the poor repeatability of the creep test is inevitable. A simple way to minimize these problems is to use one single sample for a series of tests instead of using many different samples. The same method was adopted by Struik^[42] and Lamers^[28] in their tests. One example of even failing to reveal shifting due to ageing when using different samples can be found in Zhang (1993c, Fig. 8)^[50],

Some tests have been carried out to check the reliability of the single-specimen-method for the unsaturated polyester material and to determine the necessary recovery period between two tests (see Section 3.1.3). In order to avoid additional cross-linking which may be accelerated at higher temperatures and thus might interfere with the normal creep process, all tests were performed at room temperature. No rejuvenating procedure was performed during the tests. This is a much simplified method which may cause some minor errors in the results.

When performing repeating creep tests on a single specimen, the main source of errors occurs when the loading levels are all beyond the linear creep range of the material. In this range, the Boltzmann superposition principle no longer holds. Between two creep tests, there is always some not-yet-recovered deformation and the next creep strains actually superpose on this deformation. The remaining strain in a creep-recovery cycle can not simply be subtracted from the creep strain in the next cycle because the superposition principle does not hold in the nonlinear range of the material response.

We thus have designed a particular test which repeats the loading and unloading cycle a large number of times in order to check the possible error induced by the subtraction method. A typical deformation history is shown in Fig. 3.2 for a eight-month-old specimen. The series of tests mostly consist of creep-recovery-recovery tests with a loading period (1 hour), a partial loading period (1 hour) and an unloading period (22 or 70 hours). After subtracting the not-yet-recovered strain from every creep curve the creep curves, as shown in Fig. 3.3, are obtained.

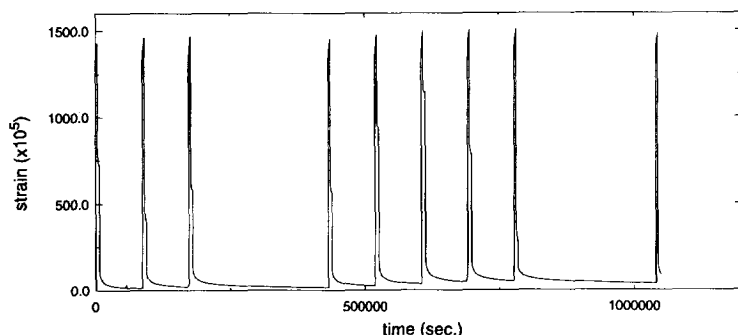


Figure 3.2. Deformation History (for the repeating creep test). For the first eight creep tests, the stress levels of the first step are 40 MPa, the stress levels for the first recovery step are different, ranging from 5 MPa to 35 MPa, the load is released for the second recovery step. The last test is a simple creep-recovery test.

Apart from the first creep curve which shows lower strains than all the other subsequent creep curves, all subsequent curves show little differences in strain values. The difference is smaller than 1%. It should be noted that the creep stress is 40 MPa in this case, which is higher than the applied stresses for the ageing tests. According to these results this method was accepted for further application within the present research.

3.1.3 Rejuvenation by Large Stresses and Specimen Conditioning

Another interesting phenomenon, which was first found by Struik (1978)^[42], is that a stress loading far beyond the linear loading range obviously can partially and temporarily erase prior ageing. This phenomenon is used here to explain the observed difference in creep strains between subsequent creep curves discovered in the repeating tests. The first creep curve shows the lowest strain values because after the first creep load (40 MPa), the amount of previous physical ageing was partially erased and consequently the material became more compliant resulting in larger strains. The ageing is however gradually recovered during the unloading period. A recovery period of 70 hours seems to be long enough for subsequent creep curves to allow to recover, at least partially. Indeed two creep curves (the 4th and 9th) show lower strains than the others (except for the first one). The results obtained also suggest that physical ageing erasure by high stresses (or deformation) is limited for a certain stress level. Once this limit is reached, further loading cycles with the same maximum stress level will not further erase the ageing and the creep curves will start to have repeatability.

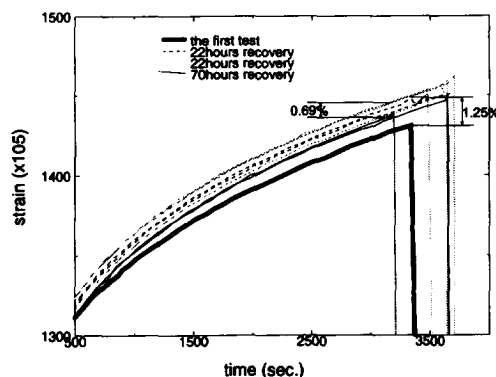


Figure 3.3. Subtraction Method applied to the series of creep tests of Fig. 3.2 (specimen # 046, creep stress: 40 MPa).

This limited rejuvenation capacity at a certain stress level can be used to explain the so-called well-known "conditioning" procedure for test specimens. Specimen conditioning was suggested by Leaderman (1943)^[29]. The sample should be subjected to successive creep and recovery cycles before the formal tests are carried out. Ward & Onat (1963)^[44] explained that by this procedure the "long-time memory" of the sample obviously can be removed. After the conditioning procedure, only the effects of the loads applied in the very recent history are remembered by the specimen.

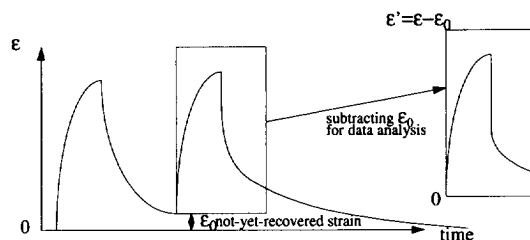


Figure 3.4. Subtraction Method to obtain a creep-recovery curve from the raw data

Their test results show an apparently different first cycle of strain response, being smaller than the responses of other cycles. The same phenomenon was found here. The explanation offered for this phenomenon, *i.e.* the prior ageing erasing at high stress levels, seems however more appropriate. Partial rejuvenation at high stresses is, however, only a minor effect of physical ageing. It will therefore not be included in the model being used later.

3.1.4 Testing Procedure for Ageing Creep Tests

The test procedure used and the ageing times for all creep curves are given in Table 3.2. The subsequent creep strains are shown in Fig. 3.5.

Table 3.2. The testing procedure for a single specimen

test state	clock time t = ageing time t_e (from ~ to)	creep time t_c	recovery time t_r	t_c/t_e	t_r/t_c
rejuvenating	-20min ~ 0 min at a temperature of 130°C				
resting	0 min ~ 22.5 min				
1st creep	22.5 min ~ 30 min	7.5 min		1/4 ~ 1/3	
recovery	30 min ~ 1.5 hr		60 min		8
2nd creep	1.5 hr ~ 2 hr	30 min		1/4 ~ 1/3	
recovery	2 hr ~ 6 hr		240 min		8
3rd creep	6 hr ~ 8 hr	120 min		1/4 ~ 1/3	
recovery	8 hr ~ 24 hr		960 min		8
4th creep	24 hr ~ 32 hr	480 min		1/4 ~ 1/3	
recovery	32 hr ~ 96 hr (4 day)		3840 min		8
5th creep	96 hr ~ 128 hr	1920 min		1/4 ~ 1/3	

The advantages of the specific testing procedure are:

(1) Since no refreshing or rejuvenating of samples was performed by raising the temperature above T_g before starting a novel creep test, the test programme is considerably shortened and possible additional cross-linking (chemical ageing) caused by raising the temperature is avoided.

(2) There is no variation of material data occurring due to specimen to specimen differences

The disadvantages are:

(1) The creep tests are not strictly short-term tests, since Eq (2.11) is not strictly satisfied, due to the fact that $t_c/t_e < 1/3$ instead of $t_c/t_e \ll 1$ (the creep testing times are not absolutely small compared to the physical ageing times for various cycles);

(2) The interaction between ageing and creep deformation will cause some remaining strain which is accumulated with the increase of the number of creep tests (see Fig. 3.5);

(3) Not yet recovered creep strain will also be accumulated (see Fig. 3.5) because of limited recovery duration.

Except where indicated, all specimens were first cured free standing at 60°C for 24 hours and at 80°C for 24 hours. In a special case, extra postcuring was applied at 130°C for 120 hours.

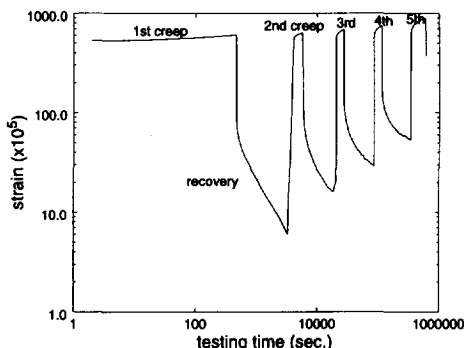


Figure 3.5. Strain output from a repeating creep test (specimen # 150, creep load: 20MPa)

3.1.5 Shifting of Creep Curves

Fig. 3.6 gives an overview of the shifting of creep curves over the time scale, due to physical ageing. The curves are taken at 4 different stress levels. Four different specimens have been used, one for each stress level. It is clear from Fig. 3.6 that ageing affects the creep strains at all stress levels tested, the highest level being 40MPa, corresponding to about half the tensile strength of the unsaturated polyester resin.

Fig. 3.7, Fig. 3.8 and Fig. 3.9 show a series of creep curves for different ageing times, obtained at stress levels of respectively 30MPa, 20MPa and 10MPa.

Moreover Fig. 3.7 shows the possible effect of chemical ageing on creep strains at different ageing times. The solid lines in this figure represent the creep strains of a specimen, which had been additionally postcured for 120 hours at 130°C, prior to the start of the testing procedure.

In Fig. 3.9 four creep curves have been shifted horizontally to the fifth curve corresponding to an ageing time of 4 days. The resulting shifting factors for three stress levels are given in Fig. 3.10. The shifting rates are obtained by measuring the slopes of the curves in Fig. 3.10 and the results are listed in Table 3.3 and depicted graphically in Fig. 3.11.

Table 3.3. Shifting Rate α

creep stress	10 MPa	20 MPa	30 MPa
postcured	0.4806	0.5417	0.4489
postcured	0.4579	0.5187	0.4251
extra-postcured	0.4490	0.4390	0.4489

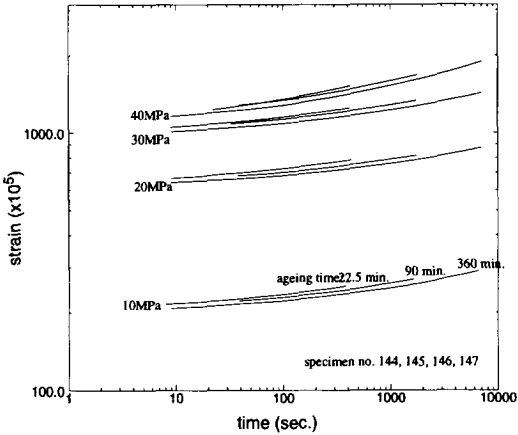


Figure 3.6. Physical Ageing Effect on Creep (Synolite 593-A-2)

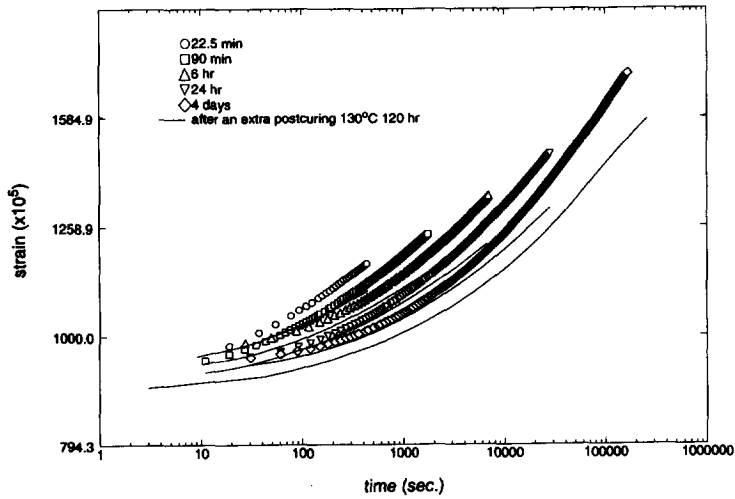


Figure 3.7. Physical Ageing (specimen # 149, creep load: 30MPa)

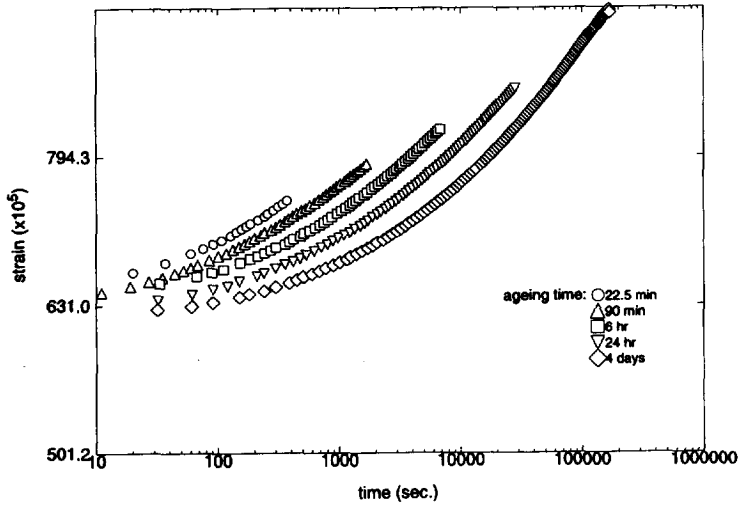


Figure 3.8. Physical Ageing (specimen # 150, creep stress: 20MPa)

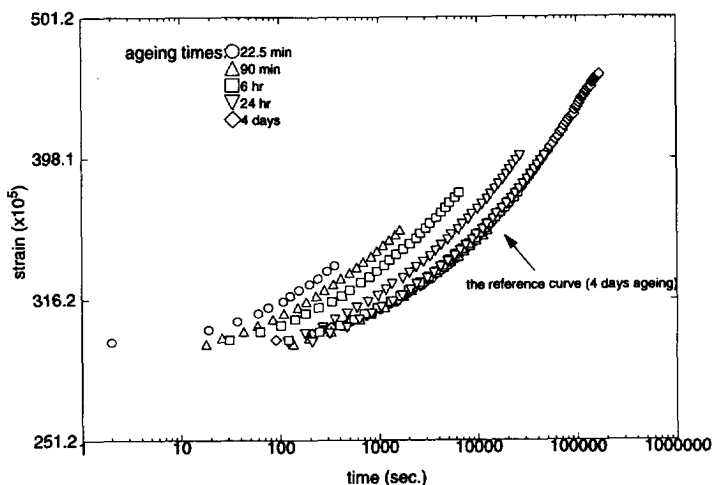


Figure 3.9. Horizontal Shifting (specimen # 153, creep stress: 10MPa). The data for different ageing times are shifted horizontally onto the data (curve) corresponding to 4 days ageing time.

3.1.6 Shifting Rate

The shifting factor was measured directly from the creep curves as shown in Fig. 3.6~Fig. 3.9. The results obtained for the shifting factor are shown in Fig. 3.10. The solid lines stand for creep data of specimens with a postcure (60°C/24hr and 80°C/24hr), the dotted lines for specimens with an extra postcure (130°C/120hr). The obtained shifting rates, defined as the slopes of the curves in Fig. 3.10, are depicted in Fig. 3.11.

The results show that the physical ageing induced horizontal shifting rate is not apparently stress dependent, nor does it seem to be influenced by additional cross-linking or chemical ageing. If the shifting rate is not creep stress dependent, the curves in Fig. 3.11 should be horizontal. Considering the scatter in the data, this is assumed to be correct at least for stress levels up to 30MPa. The computed averaged shifting rate for all stress levels is then $\alpha = 0.45$. This value will be used in the analysis of the data, although probably a range for the shifting rate, 0.40~0.55, is more correct for the unsaturated polyester material tested.

It should be noted that for most amorphous thermoplastic polymers within the ageing range, the shifting rate is about equal to 1 (see Fig. 3.12). The obtained shifting rate for the unsaturated polyester material is considerably lower than unity. Several factors might be responsible such as, *e.g.*, a broad glass transition. Another possibility is that the stresses are sufficiently high to erase a part of the previous ageing. This also results in a lower shifting rate, although in this case one would expect a gradual decrease of the shifting rate with the stress level and not a constant value, such as obtained here.

Due to a lack of additional supportive data, no conclusive explanation can be given here, nor was this aimed at in this study.

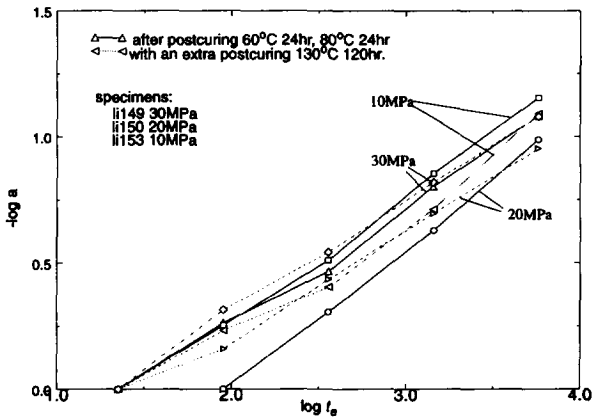


Figure 3.10. Shifting Factor a , horizontal shifting in creep due to physical ageing

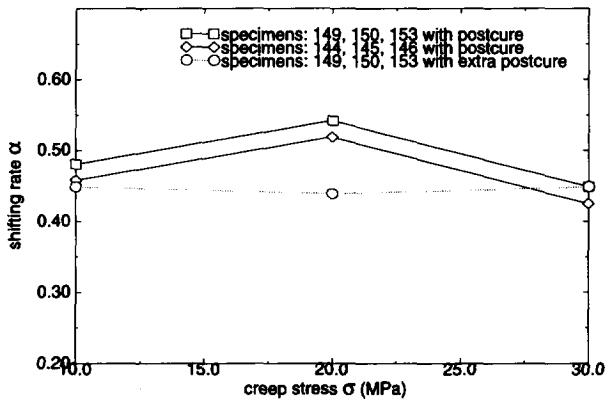


Figure 3.11. Shifting Rate α , horizontal shifting of creep curves due to physical ageing (a point in this figure can be obtained from the average slope of a curve in Fig. 3.10).

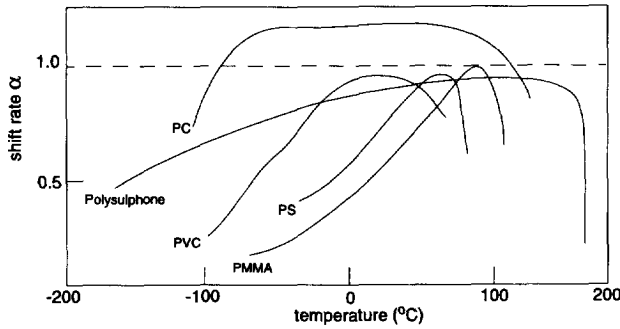


Figure 3.12. The shifting rate α vs. temperature for various polymers (remade from Struik 1978^[42], page 20)

3.1.7 Long-Term Creep Prediction

Three long-term creep tests have been done for different initial ageing times and loading levels, as specified in Table 3.4.

specimen number	#106	#117	#156
initial ageing time	45 minutes	12 minutes	40 minutes
testing time	24 days	12 days	96 days
creep stress	30 MPa	20 MPa	10 MPa

Table 3.4. Experiment conditions for the long-term creep tests

Short-term creep tests of one to fifteen minutes duration were used for curve fitting to define exponential creep rules for these specimens. The creep rules were subsequently corrected for the ageing effect by assuming shifting rates $\alpha = 0.45$ and $\beta = 0$ in Eq (2.27). For the case of a 30MPa creep stress, the following exponential creep rule was obtained

$$\epsilon = 0.0075638 + 0.00037888 \exp \left[(1.4424t)^{0.11557} \right]. \quad (3.1)$$

After the ageing effect correction, according to Eq (2.27), the following long-term prediction results

$$\epsilon_{longterm} = 0.0075638 + 0.00037888 \exp \left[2.7858 \left\{ \left(1 + \frac{t}{2700} \right)^{0.55} - 1 \right\}^{0.11557} \right]. \quad (3.2)$$

Fig. 3.13 shows a comparison of the model prediction Eq (3.2) with an experimental creep curve of 24 days.

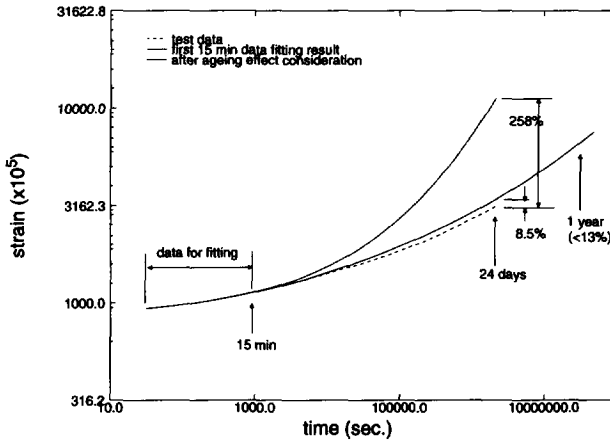


Figure 3.13. Ageing Influence on Long-Term Creep (specimen # 106, creep stress: 30MPa)

With the correction of ongoing ageing, the creep strain is overestimated by about 8.5% after 24 days of creep ($t/t_e = 768$). Using 15 min. data for a 24-day-creep prediction corresponds to an extrapolation over about three decades (~ 2300 times). Similarly, for the case of a 20MPa creep stress, following creep strain expressions were found (see Fig. 3.14). Here a fitting period of 1 minute was used.

$$\epsilon = 0.0046173 + 0.0003966 \exp[(1.1012t)^{0.10952}], \quad (3.3)$$

$$\epsilon_{longterm} = 0.0046173 + 0.0003966 \exp\left[2.218 \left\{\left(1 + \frac{t}{720}\right)^{0.55} - 1\right\}^{0.10952}\right]. \quad (3.4)$$

The expressions for 10MPa creep strain are (see Fig. 3.15),

$$\epsilon = 0.002025 + 0.00020136 \exp[t^{0.093252}], \quad (3.5)$$

$$\epsilon_{longterm} = 0.0017536 + 0.001815 \exp\left[1.0925 \left\{\left(1 + \frac{t}{2400}\right)^{0.55} - 1\right\}^{0.093252}\right]. \quad (3.6)$$

Here a fitting period of 1.9 hours was used. In the 10MPa creep stress case, the strain after about 90 days was underestimated by about 15.7% after the ageing effect correction. This was due to the fact that the momentary creep rule Eq (3.3) was obtained by fitting data up to 1.9 hour of creep. This was needed because with less data points no reliable fitting results could be obtained. However using a momentary creep time of 1.9 hours on a specimen with an age of 40 minutes violates the definition of short-term creep data. It is therefore likely that in this case the 'short-term' creep data were considerably influenced by ongoing ageing. The long-term prediction therefore underestimates the real long-term strains.

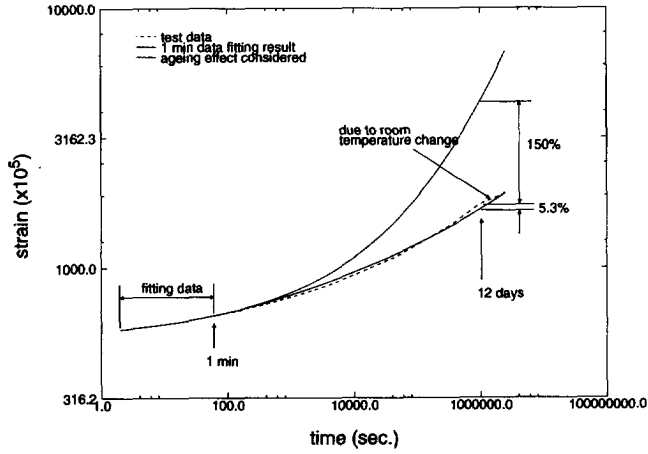


Figure 3.14. Ageing Influence on Long-Term Creep (specimen # 117, creep stress: 20MPa)

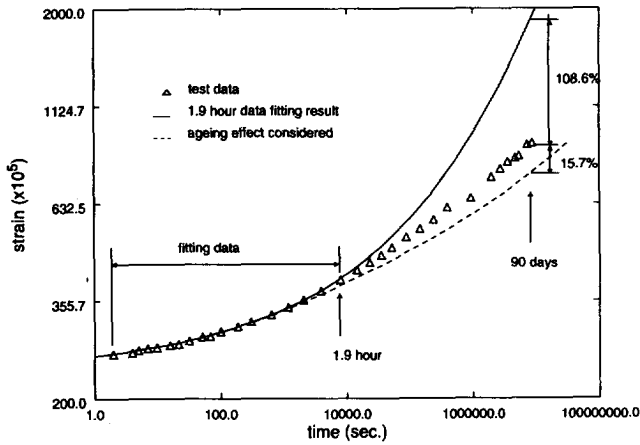


Figure 3.15. Ageing Influence on Long-Term Creep (specimen # 156, creep stress: 10MPa)

3.1.8 Conclusions and Discussions

The following conclusions for the unsaturated polyester material studied can be formulated. The conclusions are only valid for the material at room temperature.

(1) *The effect of physical ageing on the creep behaviour of the unsaturated polyester can be approximated by a horizontal shifting of the creep curves only.*

This approximation reduces two shifting factors to only one. This simplifies the effects of ageing. In the model presented here, only one parameter accounts for the ageing effect and is needed to be characterized.

(2) *Physical ageing of the unsaturated polyester is independent of the stress level up to 30MPa. Its shifting rate averages 0.45.*

The horizontal shifting rates for many polymers at room temperatures were reported (Struik 1978)^[42] between 0.5 and 1.0 (see Fig. 3.12). The present results show a rate of 0.45 for polyester.

(3) *Physical ageing shifting is independent of the cross-linking level.*

The shifting rate of physical ageing, α , remains unaffected by a prolonged cure of the tested specimens. It can therefore be concluded that extra postcuring does not change the shifting rule of physical ageing.

This result suggests that coupling between physical ageing and chemical ageing is not present. This decoupling property represents a great convenience in dealing with the ageing behaviour of the unsaturated polyester material studied.

(4) *Additional cross-linking causes both horizontal and vertical shifting, but only to a negligible extent.*

Fig. 3.7 shows a difference in two sets of creep curves, corresponding to different cross-linking levels. The difference may be explained by both the horizontal and the vertical shifting level. However, the tests were not carried out under a strict moisture level control. Part of the observed difference in creep may be due to different moisture levels in the specimens, and due to the extra postcure given. Furthermore, after a postcure at 60°C for 24 hours and 80°C for 24 hours, the material is quite chemically stable. An additional curing at 130°C for 120 hours may cause extra cross-linking in the material but only to a limited extent. Therefore the effect of the additional curing (chemical ageing) was expected to be small.

Even if the difference of creep curves in Fig. 3.7 is totally due to the effect of the cross-linking level, this effect is not large. For simplicity, this effect will be neglected so that there is no cross-linking level induced shifting in the model. Due to the fact that a possible moisture level decrease during additional ageing will cause a similar effect as shown in Fig. 3.7, the simplicity reached in this manner is believed to be appropriate.

A translation relation between the real time for chemical ageing and the postcuring procedure has not been established here. Hence no effort was made to determine the shifting factors for chemical ageing. In this thesis, the polyester under study is always prepared by a postcuring procedure which can warrant a much more stable material. The chemical ageing influence on creep is therefore neglected in the further chapters.

(5) *There is a temporary stress influence in physical ageing.*

Experimental data have shown that a tensile stress can erase a part of the physical ageing temporarily, see Fig. 3.3. A successive application of a certain level of stress can only erase a certain amount of physical ageing and reaches some limit. A possible reason of this erasing effect is that a tensile load may create some additional free volume in the material.

(6) *Long-term creep prediction is made possible by considering physical ageing.*

Using Struik's effective-time theory, good predictions of the long-term creep behaviour of the unsaturated polyester are obtained, see Fig. 3.13, Fig. 3.14 and Fig. 3.15.

3.2 Material Characterization for the Model

In this section, the creep parameters C and n , the nonlinearizing parameters g_0 , g_1 , g_2 and a_g , and the initial compliance J_0 will be characterized. The verification of the model for the uniaxial loading case will be presented in Section 3.3, and for biaxial loading cases in Chapter 6.

Lou & Schapery (1971)^[31] have developed a graphical method to determine the model parameters from experimental data. This method uses a power-law kernel function. It has been demonstrated in great detail in Zhang (1992)^[47] and that this method is inaccurate and time consuming. The inaccuracy directly stems from the choice of a power law as kernel function in the Schapery equations. The power-law provides linear creep curves on a logarithmic time scale, and is not able to model all the experimentally obtained creep curves, especially not for the long time creep cases. Hence in this work, the exponential creep-law will be adopted, as has been described in Chapter 2 (Section 2.3.1). A concept of history dependent model parameters which was meant to deal with significant changes of certain model parameters with time and loading direction was suggested in Section 2.5. The material change of unsaturated polyester with time under a deformed state was later confirmed in the laboratory (De Boer 1993^[1]) and was explained by introducing the ageing concept, as has been discussed in Section 2.4.

3.2.1 Experimental

The creep-recovery test method was used here for determination of the parameters of the viscoelastic model. The tests were carried out at room temperature on plate dog-bone specimens under a uniaxial constant tensile load. The same type of dog-bone specimens was used as for the ageing characterization. A series of tests at different loading levels provide data for the characterization of the stress dependence of the creep deformation of the material.

The experimental technique has already been discussed in Section 3.1. No conditioning procedure was applied however. Moreover the age of the specimen was held constant (seven months). The creep

testing time was one hour, followed by twenty three hours of recovery. The creep load was varied between 3MPa and 40MPa.

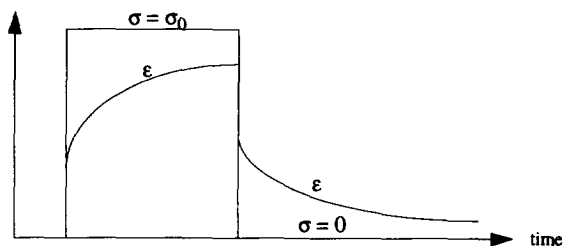


Figure 3.16. Stress input (σ) and strain output (ϵ) of the experiment

3.2.2 Formulation for Data Fitting

If a series of single-step creep-recovery tests is carried out for model parameters determination, the ongoing ageing effect can be neglected since the testing time is short with respect to the chosen specimen age of 7 months. Therefore J_0 , C and n are assumed to be constant. The exponential creep law for the kernel function is adopted. This has shown to give a better description of long-time creep behaviour of unsaturated polyester than the power law. This has especially been the case, when physical ageing is involved.

The choice of the exponential creep law causes a different procedure for model parameter determination. Here a procedure is presented which differs from the procedure originally used by Schapery (1969) which was subsequently adopted by a large number of other researchers. The fitting functions for different loading cases and their relations to the model parameters are easily derived from the Schapery equations, Eq (2.4) and Eq (2.9). In the single-step stress input situation, the strain during creep is

$$^1\epsilon = g_0 J_0 \sigma + ^1g_2 \sigma C [\exp(t^n) - 1], \quad (3.7)$$

and the strain during recovery is

$$^2\epsilon = ^2g_2 C \sigma [\exp(t^n) - \exp(t - t_a)^n]. \quad (3.8)$$

For a two-step stress input situation, the strain in the first step is the same as given by Eq (3.7).

$$^1\epsilon = ^1g_0 J_0 \sigma_1 + ^1g_2 \sigma_1 C [\exp(t^n) - 1]. \quad (3.9)$$

In the second step and the third step, the strains are

$$^2\epsilon = ^2g_0 J_0 \sigma_2 + ^2g_2 \sigma_2 C [\exp(t - t_1)^n - 1] + ^1g_2 \sigma_1 C [\exp(t^n) - \exp(t - t_1)^n], \quad (3.10)$$

and

$$^3\varepsilon = {}^1g_2\sigma_1C[\exp(t^n) - \exp(t-t_1)^n] + {}^2g_2\sigma_2C[\exp(t-t_1)^n - \exp(t-t_2)^n] \quad (3.11)$$

For a one-step creep experiment, the creep compliance ($J = \varepsilon/\sigma$) is given by,

$$f_a(t) = a_1 + a_2 \left[\exp\left(\frac{t}{a_3}\right)^{a_4} - 1 \right], \quad (3.12)$$

where Eq (3.7) has been used. For recovery data the following function is obtained from Eq (3.8),

$$f_b(t) = b_1 [\exp(t-t_a+b_2)^{b_3} - \exp(t-t_a)^{b_3}], \quad (3.13)$$

The fitting variables, a_1 to a_4 and b_1 to b_3 , are defined as

$$\begin{cases} a_1 = g_0 J_0 \\ a_2 = {}^1g_1 {}^1g_2 C \\ a_3 = {}^1a_\sigma \\ a_4 = n \end{cases}, \quad (3.14)$$

$$\begin{cases} b_1 = ({}^2g_1 {}^1g_2) C \\ b_2 = t_a / {}^1a_\sigma \\ b_3 = n \end{cases}. \quad (3.15)$$

Since at sufficiently small strains linear viscoelastic behaviour must ensue, following initial values are used,

$$\begin{cases} {}^1g_0|_{\sigma=0, t=0} = 1 \\ {}^1g_1|_{\sigma=0, t=0} = 1 \\ {}^1g_2|_{\sigma=0, t=0} = 1 \\ {}^1a_\sigma|_{\sigma=0, t=0} = 1 \end{cases} \quad (3.16)$$

3.2.3 Model Parameter Determination

The procedure used to obtain the model parameters from the creep-recovery data is described in subsequent paragraphs.

1. exponent n

To determine the exponent only creep data have been used. Due to the large strain signal (with respect to typical recovery strains), it was found that this procedure yielded the best accuracy. The fitting results for n using the fitting function Eq (3.12) are shown in Fig. 3.17 for a number of creep tests with various stress levels, ranging from 3MPa to 40MPa. Most of the tests have been per-

formed using one specimen. No clear linear range could be identified in the tests (in the linear range, the curves of the creep compliances at different stress levels are coincident), therefore the lowest load level applied was assumed to correspond to the linear range (3MPa load).

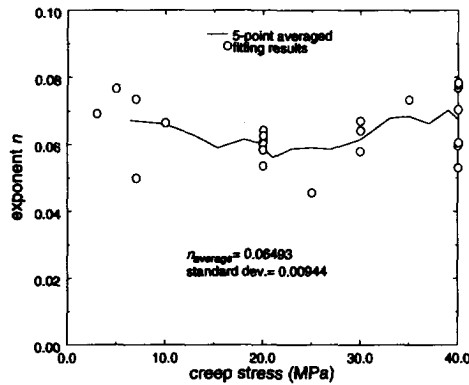


Figure 3.17. Fitting results for the exponent n from tests on one specimen (# 46)

It is clear from Fig. 3.17 that the exponent n is independent of the creep stress. The average of the fitting data in Fig. 3.17 is 0.065 with a standard deviation of 0.009.

2. shifting factor a_0

When using the exponential creep law, the fitting results yield a constant shifting factor a_0 , independent of the stress level, and on the average equal to 1.0. The values obtained at different stress levels are given in Table 3.5.

Table 3.5. Creep data fitting results for a_0 (specimen #46, Table A1, Zhang 1993c)

3 MPa	5 MPa	7 MPa	10 MPa	20 MPa	25 MPa	35 MPa	40 MPa
1.0436	1.009	0.99403	1.0047	0.93428	0.79104	0.96536	0.95862

The obtained values for a_0 close to 1 suggest that a higher stress level does not accelerate the viscoelastic rate process for the unsaturated polyester studied. This means that no horizontal shift of creep curves occurs for different stress levels. The effect of the creep stress actually manifests itself as a rotation of the creep curves. A higher creep stress causes a faster creep rate. This rotation is accounted for by the nonlinearizing parameter g_2 .

3. initial compliance J_0

The fitting results for the initial compliance, again using Eq (3.12) are shown in Fig. 3.18. A slight stress dependence of the fitting parameter a_1 can be seen in Fig. 3.18. As a first approximation, the fitting variable a_1 can be assumed to be a constant. g_0 and J_0 are therefore constants, given by $g_0 = 1$ and $J_0 = 22.4 \times 10^{-11} \text{ (Pa)}^{-1}$.

Creep data from different specimens were also used to determine J_0 by fitting with Eq (3.12). The results are listed in Zhang (1993c, Table A3)^[50] and are shown here in Fig. 3.19.

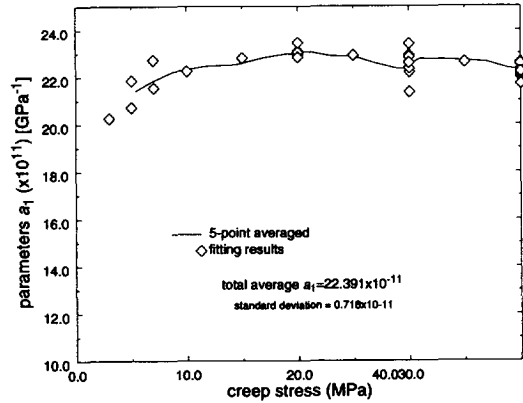


Figure 3.18. Fitting Parameter $a_1 = g_0 J_0$ (specimen # 46)

Since the creep data used for Fig. 3.19 are obtained from different specimens (of the same material) the fitting results of J_0 scatter in a larger range than those obtained from a single specimen (as in Fig. 3.18). The average of J_0 is $21.66 \times 10^{-11}(\text{Pa})^{-1}$ with a standard deviation of $1.786 \times 10^{-11}(\text{Pa})^{-1}$. The scatter reflects the differences in material properties, storage and testing conditions, etc.

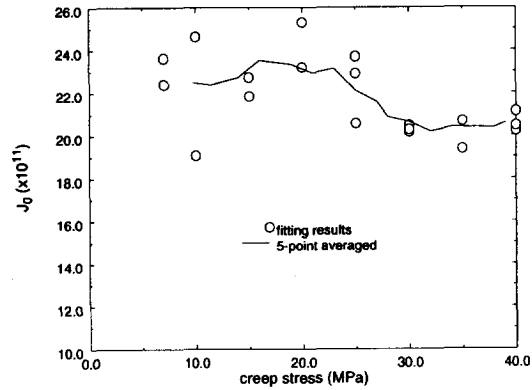


Figure 3.19. Fitting Results for J_0 (from tests on different specimens)

A better approximation is obtained if the parameter a_1 is not assumed to be constant, but is taken to be slightly stress dependent according to Fig. 3.18. In this case, the nonlinear parameter g_0 is taken to be slightly stress dependent. In doing this a more appropriate model is obtained. This more appropriate model, referred to as the 'two-nonlinear-parameter model', has shown to be more accurate than the MSM, especially in describing the response to cyclic loading (see next section).

4. model parameters g_1 and g_2

The fitting parameter a_2 for the creep data contains the product $(g_1 g_2)$ while the parameter b_1 for the recovery data contains the product $(^2 g_1 g_2)$. Except for the superscript '2', which indicates the stress level σ_2 , the other superscripts of g_1 and g_2 (corresponding to the creep stress σ_1), are omitted for writing convenience. By using $n = 0.065$, $J_0 = 21.66 \times 10^{-11} \text{GPa}^{-1}$, $g_0 = 1$ and $a_\sigma = 1$, the creep data are refitted for $(g_1 g_2)$. The fitting results of a_2 are shown in Fig. 3.20 (Zhang 1993c)^[50].

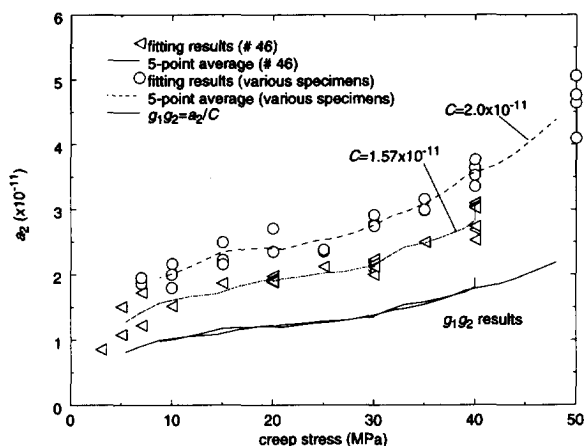


Figure 3.20. Fitting Parameter a_2 (results from different tests and specimens)

Because C is a material constant, it can be determined by scaling the curves in Fig. 3.20. Doing so it was found to be different for two sets of data. The scaled results of the two curves however coincide very well (see $(g_1 g_2)$ results in Fig. 3.20). The existing difference in the creep parameter C can, just as in the parameter n , be explained by the variation of material properties and testing conditions from specimen to specimen.

Using recovery data parameter b_1 was subsequently fitted. The results at different stress levels are shown in Fig. 3.21 and are listed in Table A4, Zhang (1993c)^[50]. By vertically shifting the b_1 data by an amount of C , the $(^2 g_1 g_2)$ data are obtained. Fig. 3.22 gives a comparison between $g_1 g_2$ data and $^2 g_1 g_2$ data. The coincidence of the three curves suggests that $g_1 = ^2 g_1 = 1$. Moreover since $^2 g_1$ represents the nonlinearizing function $g_1(\sigma)$, evaluated at a stress level $\sigma_2 = 0$ (recovery) this

parameter should be equal to one. Therefore the curves in Fig. 3.21 & Fig. 3.22 represent g_2 only. An analytical expression for g_2 is graphically shown in Fig. 3.23. An exponential function, selected as

$$g_2 = e^{(2.07 \times 10^{-14} \sigma^{1.77})}, \quad (3.17)$$

represents the stress dependency of g_2 reasonably well. Here the stress σ is given in Pa. In Fig. 3.23 a curve according to this function is drawn.

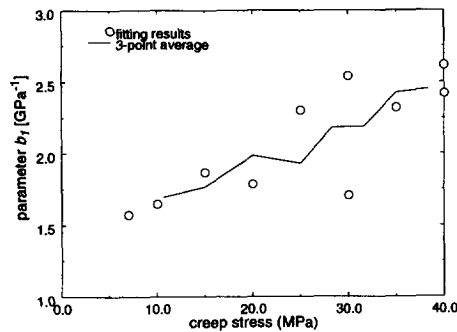


Figure 3.21. Fitting Parameter b_1 (specimen # 46)

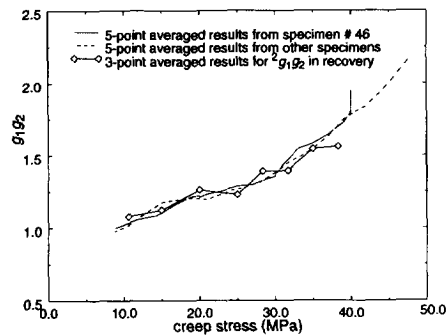


Figure 3.22. Model Parameter $g_1 g_2$ (comparison between $g_1 g_2$ from creep and $^2 g_1 g_2$ from recovery data)

If it is assumed that the parameter $g_0 = 1$, it follows from the described fitting procedure that three of the four nonlinearizing parameters are constant and equal to unity. Only g_2 shows a stress-dependency. The model is then actually simplified to MSM, Leaderman's modified superposition method (Leaderman 1943)[29].

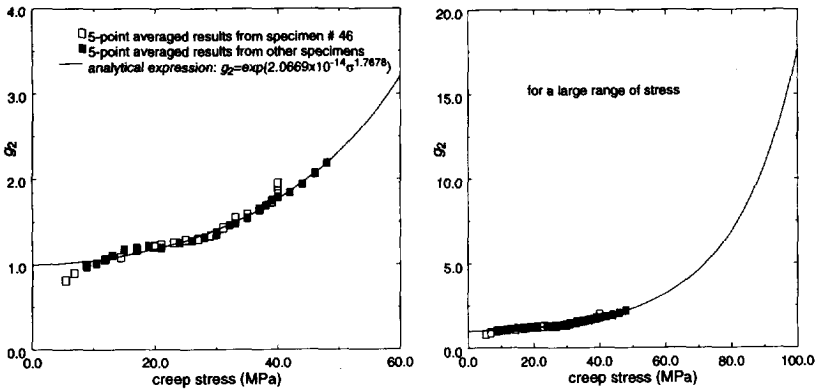


Figure 3.23. Model Parameter g_2

5. Two-nonlinear-parameter-model

The parameter g_2 plays a major role in the nonlinear stress dependence. Since it varies considerably with the stress level, only g_2 in fact could be determined satisfactorily from the test data. The scatter in the data overshadows a possible minor stress dependence of the other parameters. A possible slight stress dependence might be present in the parameter g_0 .

When viewing the data for g_0 in Fig. 3.18 especially at low stress levels between about 4MPa to 10MPa such a stress dependence can be observed. By considering the data between 4MPa and 10MPa, these data can be fitted quite well by Eq (3.18) when using a value of $J_0 = 21.66 \times 10^{-11} \text{Pa}^{-1}$.

$$g_0 = \begin{cases} 1.0 & \sigma \leq 4.9 \text{ MPa} \\ 0.5\sigma^{0.045} & \sigma > 4.9 \text{ MPa} \end{cases} \quad (3.18)$$

This choice for the stress dependence of g_0 is not unique. From the data gathered it is clear that other combinations of J_0 and g_0 are possible. However, it is found that when choosing g_0 as given in Eq (3.18), the quality of the prediction in cyclic loading is drastically improved. Summarizing the fitting effort, a 'two-nonlinear-parameter-model' appears to fit the creep-recovery data, obtained on the unsaturated polyester material, very well. The variation of the two parameters with stress is given in Fig. 3.24. Although there is little to discriminate between the present model and a MSM model for creep loading, the present model is superior for simulation of cases with a cyclic loading.

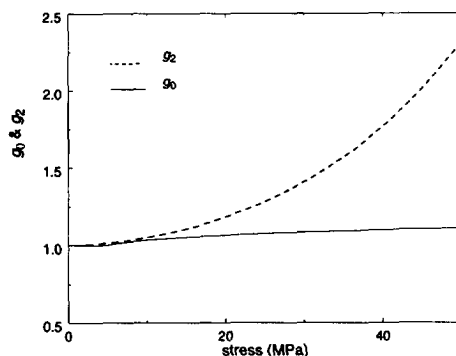


Figure 3.24. Model Parameters g_0 , Eq (3.18), and g_2 , Eq (3.17), ($g_1 = a_\sigma = 1$)

3.2.4 Unloading Behaviour

It has been found that creep-recovery tests are generally not able to provide sufficient information for establishing a model to describe higher stress level loading and unloading behaviour (Zhang 1992^[47] and Zhang 1993c^[50]). Unloading behaviour can be significantly different from loading behaviour, especially when the imposed stresses are high, *e.g.* larger than 70% of the strength of the material. However little difference is usually found. Fig. 3.25 shows an example of the underestimation of the strains by a power-law theory as well as by an exponential theory during the second creep period of a two-step-test. In such a two-step test the sample is loaded up to a first stress level, whereafter complete unloading occurs. In this case the first stress level was 40MPa, while for the second stress level stresses ranging from 5MPa to 30MPa have been used. In Fig. 3.25 the simple (MSM) model with only one non-unity parameter g_2 has been used. For unloading stresses less than about 60% of the strength (the strength of unsaturated polyester = 87 MPa), the simple model established by creep-recovery tests has sufficient accuracy for both loading and unloading behaviour. However at higher unloading stress levels considerable deviation is observed between theoretical prediction and experiment. Note that by introducing the exponential creep law, instead of the widely used power law, for the kernel function in the Schapery model, the prediction is improved.

In Section 3.3 where cyclic loading is considered, comparison between the theoretical model with only two nonlinear parameters (the 'two-nonlinear-parameter model') and experiments will be shown to be excellent. Although for higher stress levels, the model can still be improved by applying other stress-history dependent model parameters too, we did not consider this in this work, since it was very difficult to obtain reliable data at high stress levels (close to the strength). Consequently the 'two-nonlinear-parameter model' has been established according to the data from tests in a mild stress region (0 ~ 50 MPa). This model will therefore be adopted for further calculations.

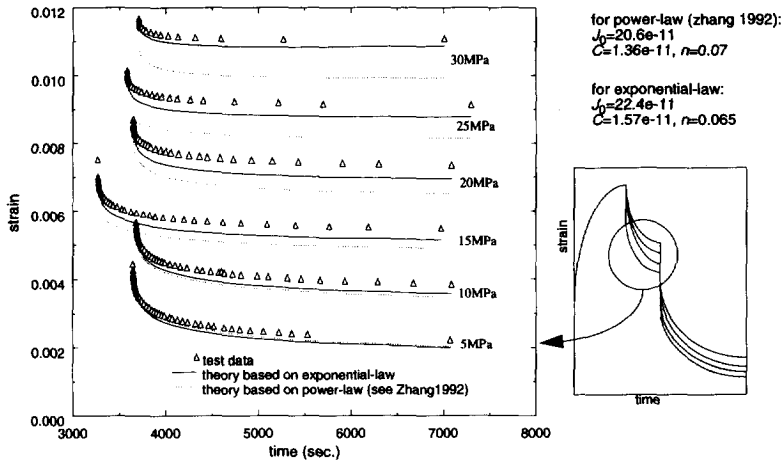


Figure 3.25. Comparison between theoretical and experimental results, the stress level of the first creep step is 40MPa, the figure shows the results for the second (recovery) step strains, different stress levels are applied in the second step, specimen #46)

3.2.5 Ageing Effects on the Exponent n

In the case of long-term creep and relaxation, the coupling effect between deformation and ongoing (physical and chemical) ageing will definitely cause permanent deformation. Evidence for this was found in the laboratory (De Boer 1993)^[11]. Therefore the long-term viscoelastic behaviour is actually not likely to be modelled accurately for a polymer, when disregarding physical as well as chemical ageing. The relative contribution of both types of ageing depends on the nature of the polymer studied. Chemical ageing may cause a change in the creep parameter C to a certain degree during several stages of creep (see Chapter 3 and also Zhang 1993a^[48], Fig. 6a). However, for the unsaturated polyester studied here, a suitable postcuring procedure makes the chemical ageing effect on the creep behaviour negligible.

Creep (elongation) data for different physical and chemical (cross-linking) ageing times were obtained by the author (Zhang 1993a)^[48]. The data were fitted by an exponential creep law. The fitting results for the exponent n of the creep law for a number of sets of creep data are summarized in Fig. 3.26.

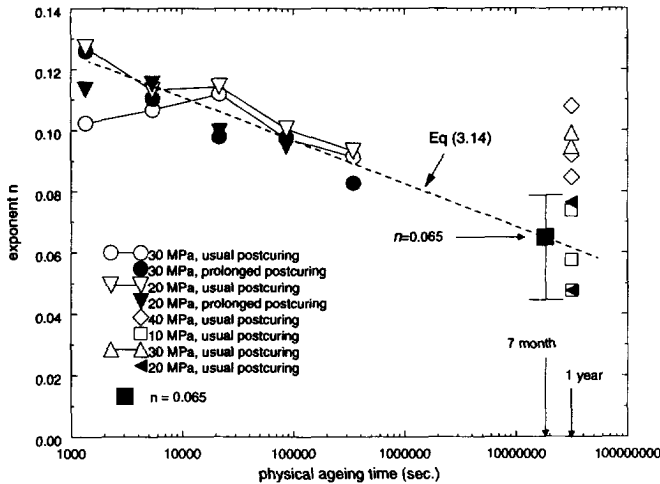


Figure 3.26. Ageing effect on the exponent n (20°C), the data at the physical ageing time of one year are obtained from various specimens, the point at the ageing time of seven months is from Fig. 3.16

A series of creep tests with different curing levels and corresponding to small physical ageing times ($< 1,000,000$ sec. = 11.5 days) were performed by using single-specimen method as previously described. Five different physical ageing times were chosen. The results of these experiments are shown in Fig. 3.26 as those points with physical ageing times less than 1,000,000 sec. Some tests were performed on a 7 month old specimen. The results indicate a range of variation of n . This variation is larger than the variation for n found for specimens with the same age (see also Fig. 3.17). Additional tests were carried out with four one-year old specimens. For these specimens a larger variation of n was found. Although there are some contradictory points (30 MPa and 40 MPa) located at one year physical ageing time, the tendency of the exponent can be presented by the dashed line in Fig. 3.26. It agrees well with the average exponent, $n = 0.065$, obtained for the seven month physical aged specimens (Fig. 3.17). The variation of the exponent n with ageing time t_e can be expressed analytically as (t_e in sec.)

$$n = 0.1673 - 0.04141 \log t_e. \quad (3.19)$$

In order to observe a possible effect of chemical ageing, some samples were given a prolonged postcuring. The usual postcuring consists of two periods of curing, at 60°C for 24 hours and at 80°C for 24 hours. A prolonged postcuring corresponds to an additional curing at 130°C for 120 hours.

The results obtained (Fig. 3.26) show that there is hardly any chemical ageing effect on the exponent n . The effect of physical ageing in fact remains the same whether the unsaturated polyester material is given an additional postcuring or not.

3.2.6 Validation of Theories

Although the data scatter is large, as can be observed in Fig. 3.26, it seems that there is an influence of the physical ageing time on the creep parameter n . If the ageing dependence of the exponential law generally exists (which means that the creep parameters C and n are ageing time dependent), both Schapery's viscoelastic theory and Struik's ageing theory may at least not be very accurate.

In Section 2.5 it has been proven that the introduction of a stress dependence of the creep parameters of the exponential creep law does not contradict the basic viscoelastic assumption, *i.e.*, full recoverability of the viscoelastic strains. But introduction of ageing dependent creep parameters, C and n , will indeed conflict this assumption and lead to irrecoverable deformation. In this sense, a viscoelastic theory may not be suitable to predict long-term behaviour at all.

Struik's theory assumes that the physical ageing effects on the creep deformation can be described simply by shifting creep curves over the time scale, which is based on the superimposability of creep curves with different physical ageing times (see Chapter 2). But if the shape of the creep curves is changing with ageing time as exemplified by changing the creep parameters C and n with ageing time, then the ageing effect can not be described by solely changing relaxation times, *i.e.*, a simple shift over the time scale.

On the other hand, the change of the exponent n is very limited given the large physical ageing times considered. Table 3.6 lists some physical ageing times and the corresponding exponent n obtained from Eq (3.19) (the dashed line in Fig. 3.26). When physical ageing is between one year and thirty

Table 3.6. The relation between the physical ageing time and the exponent of exponential law

t_e	6 hours	1 day	10 days	3 months	7 months	1 year	10 years	30 years
n	0.1062	0.0977	0.0836	0.0701	0.0650	0.0616	0.0475	0.0407

years, the averaged exponent n has an extrapolated value between about 0.04 and 0.06. This range of the exponent is within the scatter of data being obtained from the tests when using different specimens (*e.g.*, the data at one year, in Fig. 3.26). In other words, for the unsaturated polyester material studied, the scatter in the test data is usually large enough to overwhelm the change of the exponent due to physical ageing. Considering the scatter in the data, the fitting result of the exponent has a range even for a certain ageing time. In order to avoid the conflict with the consistency requirement discussed in Chapter 2, a constant value for n of 0.065 (at 7 months ageing time) is chosen for the numerical simulation in the later part of this thesis.

3.2.7 Conclusions

The following conclusions regarding the time-dependent characterization of the unsaturated polyester material (DSM Resins Synolite 593-A-2) can be formulated.

1. The nonlinear viscoelastic model able to characterize the material contains three kinds of parameters: material constants, creep parameters and nonlinearizing model parameters. The material constant, J_0 (the creep compliance in the linear range), is independent of the stress level and of the ageing time. According to the consistency analysis in Chapter 2, both creep parameters C and n can only be stress dependent. Limited experimental evidence suggests, however, that the creep

parameter, C , may depend on chemical ageing if any vertical shift in creep data due to chemical ageing occurs (for the unsaturated polyester material this dependence is negligible after postcuring). The creep exponent n indeed is related to ongoing physical ageing (see Fig. 3.26). The nonlinearizing parameters, g_0 , g_1 , g_2 and a_σ , are generally stress level, stress state and stress history dependent. The dependency of the nonlinearizing parameters upon stress state and stress history will assure the capability of the theory of modelling unloading behaviour.

2. It is found that to use the exponential kernel function gives more accurate prediction of the stress-strain relation of the unsaturated polyester studied. It has shown that the exponential law is better than the traditional power law for this material. To use the exponential kernel function, the theory for the material studied can be simplified to have only two nonlinearizing parameters.
3. The nonlinearizing parameter g_2 plays a major role in describing the nonlinearity of the unsaturated polyester. Therefore an MSM (modified superposition model), which has only one nonlinear parameter g_2 , is an acceptable simplified model for the unsaturated polyester in the case of short-term loading and for moderate stress levels.
4. According to Struik's theory, the effect of physical ageing can be accounted for by a shift of the creep strains over the time scale (see Chapter 3 and Struik 1978)^[42] as has been formulated in Eq (2.30). The nonlinearizing parameters, g_0 , g_1 , g_2 and a_σ , are assumed to be independent of ageing time.
5. The theory described in this chapter is capable of describing the short-term time dependent behaviour of unsaturated polyester very accurately. Due to variation in the material properties from specimen to specimen, an accurate model set up in terms of one specimen may however be in error when trying to describe the behaviour of another specimen. The unavoidable scatter in mechanical properties of the material will result in an error band for practical modelling.
6. Viscoelastic models are intrinsically not capable of predicting the long-term behaviour of a thermoset material in a general sense because of the existence of permanent deformation due to chemical ageing or extra cross-linking. In other words, these effects will change the creep parameters, C and n in a long term sense, which in turn conflicts the consistency requirement of viscoelasticity. However, for the unsaturated polyester studied, after postcuring treatment, the material is chemically stable and the error of applying a viscoelastic theory is considerably small.

For all practical purposes, Schapery's model and Struik's theory are very useful for long-term behaviour modelling since the errors brought about by these theories are small, most specifically, much smaller than the errors introduced by variability in the material mechanical properties.

The scatter in material properties is reflected in a range of variation of all model parameters. This scatter in the creep parameter data, n , overwhelms the range of the change caused by the physical ageing (at 7 months and 1 year in Fig. 3.26).

The scatter of strain in elongation creep among different specimens can be as large as 10% (see Zhang 1992^[47], Fig. 9) and even increases under higher stress levels or/and longer creep times (Fig. 3.27). The scatter of model parameters determined by fitting of test data can be always larger than 10% (see Fig. 3.17~Fig. 3.21 and Fig. 3.26).

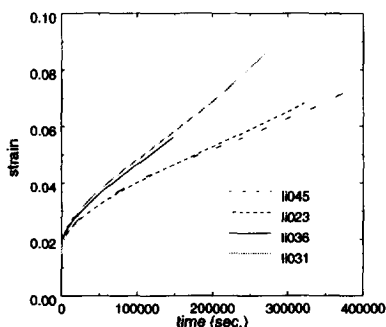


Figure 3.27. Creep Rupture Tests (creep stress = 50 MPa, 20°C, t_c = 5 months) showing typical scatter in the creep data.

All these scatters of the material properties can overwhelm the error brought by the viscoelastic theories for the long-term behaviour prediction. Henceforth, the viscoelastic theories can still be adopted for the practical use of modelling.

7. Unloading behaviour may be completely different from loading behaviour when the imposed stress is very high, close to the ultimate tensile strength of the material (Zhang 1993c^[50], Fig. 29 and Zhang 1992^[47], Fig. 26).

For moderate stresses (up to 70% of the ultimate tensile strength) not much difference in deformation behaviour can be expected between loading and unloading. Without considering this difference in the model parameters, the theory works quite well and shows excellent agreement with test data for a uniaxial tensile cyclic loading case, although there are some small underestimations.

But generally, the nonlinearizing parameters, g_0 , g_1 , g_2 and a_σ , are deformation history dependent, which may be more important for a higher stress level loading. Fortunately, in this study, the loading stress was always less than 70% of the ultimate tensile strength. The history-independent nonlinearizing parameters are sufficiently accurate. For the further calculations in this work, the 'two-nonlinear-parameter model' will be chosen instead of using a model with more nonlinear parameters or stress-history dependent parameters.

3.3 Prediction of Cyclic Loading

In Section 3.1 and Section 3.2, the model parameters were determined on the basis of step loading (with constant stresses) experiments. Now the validity of the model will be checked by considering more complicated loading situations. In this section this check will be carried out by comparing the model prediction to experimentally obtained cyclic loading strains. Biaxial testing will be presented

in Chapter 6, to further ensure a simple-test-determined model being able to predict the response under a more general loading situation.

3.3.1 Experimental

The specimens used were slightly different from those used in the creep experiments (Fig. 3.1). The plate dog-bone specimens have a larger width (Fig. 3.28). The test machine used was a Zwick-1484 with which the changing load could be controlled automatically. Strain gauges were used for strain measurements. All tests were stress-rate controlled.

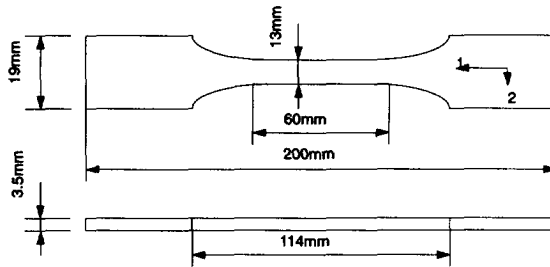


Figure 3.28. Specimen geometry

The cyclic loading tests were performed using three different loading speeds of 0.5, 2 and 10MPa/sec. The model employed for comparison is the two-nonlinear-parameter-model (g_0 and g_2 stress-dependent), with an exponential-law kernel function. Only in one case the MSM model has been used in order to compare its predictive quality with that of the two-parameter nonlinear model (Fig. 3.29). Possible different model parameters for the unloading situation have not been considered. In other words, g_0 is defined by Eq (3.18) and g_2 by Eq (3.17). Due to the variation of the test data between tests, and from specimen to specimen, the constant J_0 has been adjusted (within 2%) in order to obtain a good comparison between theory and test result.

All theoretical predictions are obtained by numerical integration of Eq (2.4). The method of numerical integration adopted here is a usual one (since there is no singularity or sharp peaks in the integrand function) which automatically updates the number of sub-domains and adds up the value of the integrand in a sequence of sub-domains within the range of integration until a certain criteria of accuracy is satisfied. Specifically, the trapezoidal rule (Press *et al.* 1989^[32], p. 110) was used here. Accuracy is obtained by comparing two recent results of integration and letting the relative error be less than 0.001.

3.3.2 One/Two Cycles up to a Maximum Stress of 30MPa

The stress input is controlled at a constant stress-rate. Fig. 3.29 shows a result for a stress rate of 0.5MPa/sec.

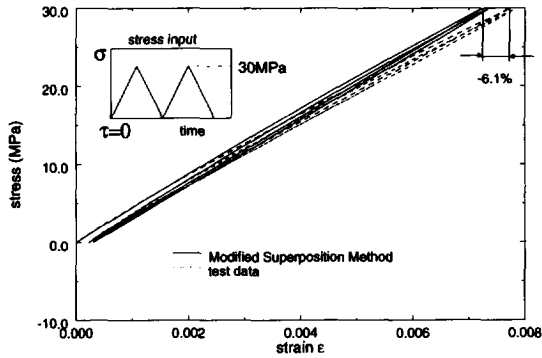


Figure 3.29. Comparison between MSM and the test data (stress rate: 0.5MPa/sec; model parameters: $g_0=g_1=a_0=1$, g_2 defined in Eq (3.17), $J_0=19.071 \times 10^{-11} \text{ Pa}^{-1}$, $C=1.727 \times 10^{-11}$, $n=0.065$)

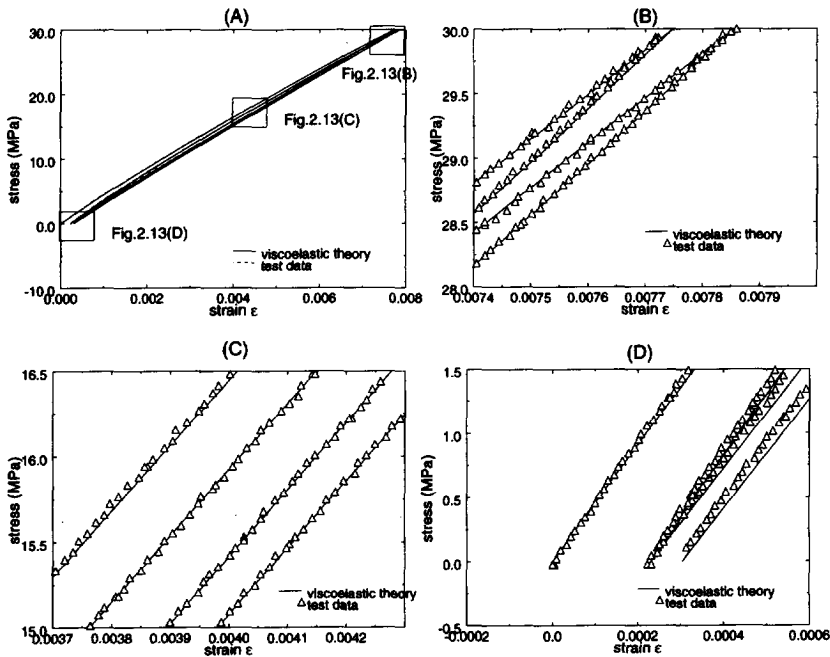


Figure 3.30. A comparison between the two-parameter model prediction and the test data (stress rate: 0.5MPa/sec)

Here theoretical prediction is from the simplest theory, the MSM (Modified Superposition Method). The model parameters are all constant and equal to 1, except g_2 which is defined in Eq (3.17). There is a 6.1% underestimation of the strain at the maximum stress of 30 MPa. The error can be expected to be more than 10% if the stress is higher than 30 MPa (see the deviation of the dash lines from the test data in Fig. 3.29).

By admitting a slight stress dependency of the nonlinearizing parameter g_0 , according to Eq (3.18) and shown in Fig. 3.24, the prediction improves considerably. This is shown in Fig. 3.30 where an excellent agreement between theory and test data can be observed (for the 'two-nonlinear-parameter model').

The details in Fig. 3.30(B)~(D) exhibit the quality of the coincidence. For stress rates of 1, 2 and 10MPa/sec respectively, the comparison between model and data is shown in Fig. 3.31~Fig. 3.33. The error has been found to be less than 1% for all cases considered.

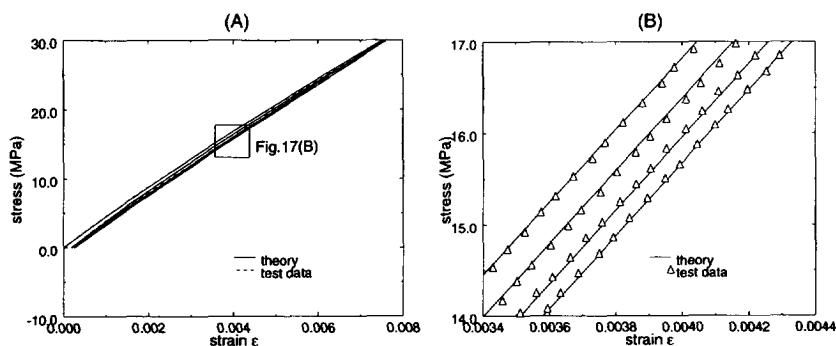


Figure 3.31. A comparison between the two-parameter model and the test data (stress rate: 2MPa/sec)

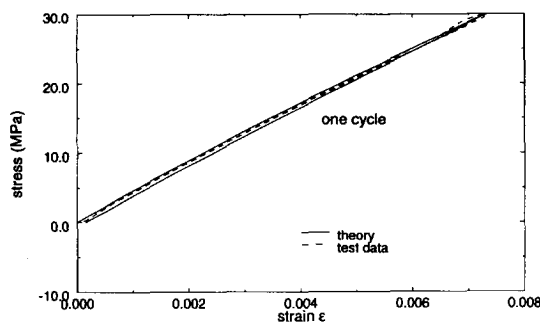


Figure 3.32. A comparison between the two-parameter model prediction and the test data (stress rate: 10MPa/sec), the experimental data show some disturbance at the minimum and maximum stresses, due to the inability of the test machine to follow the rapid changes in loading speed.

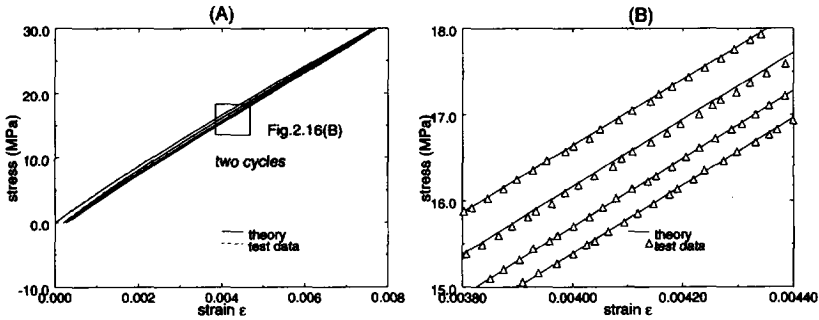


Figure 3.33. A comparison between the two-parameter model and the test data (stress rate: 1MPa/sec)

3.3.3 Cyclic loading with increasing amplitudes of stress

The stress input and strain output are shown in Fig. 3.34. The comparisons between experimental data and theoretical results are shown in detail in Fig. 3.35~Fig. 3.37 for different loading conditions. All parameters are the same as in the previous section, except for a small adjustment of J_0 to a value $J_0 = 19.452e-11 \text{ GPa}^{-1}$ (1% difference with the J_0 value in Section 3.3.2). Again excellent agreement is obtained.

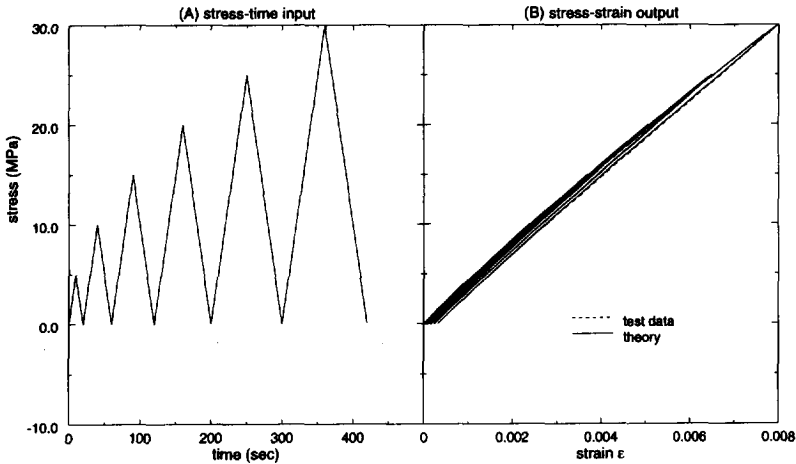


Figure 3.34. Cyclic Loading; stress rate: 0.5MPa/sec

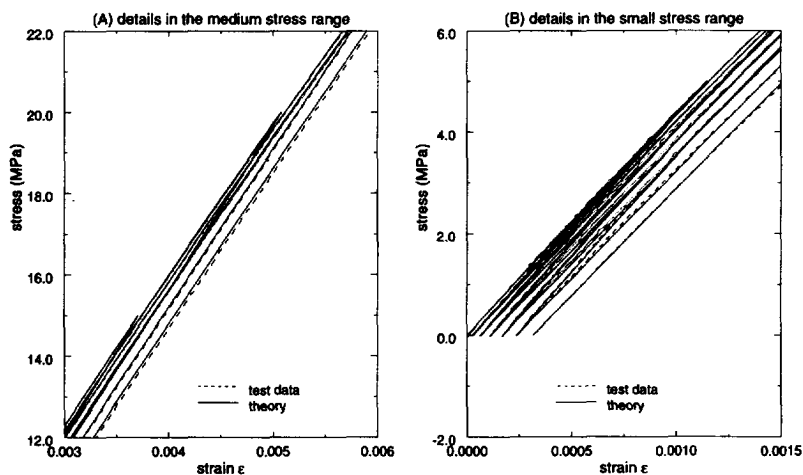


Figure 3.35. Cyclic Loading; stress rate: 0.5MPa/sec

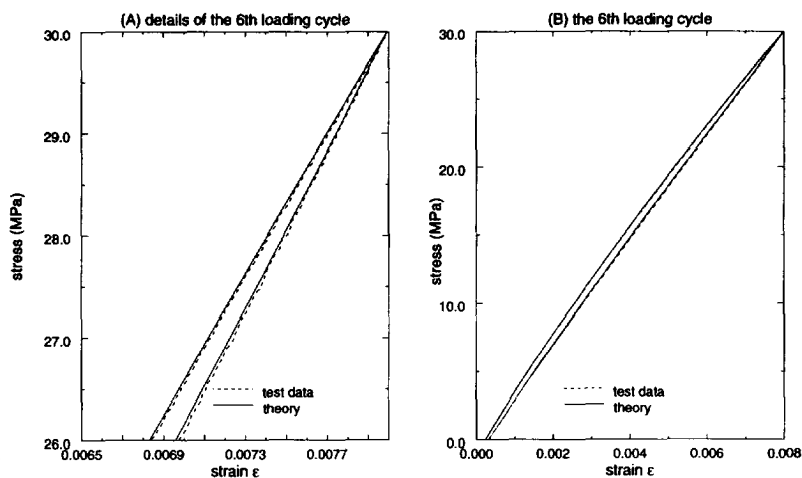


Figure 3.36. Cyclic Loading; stress rate: 0.5MPa/sec

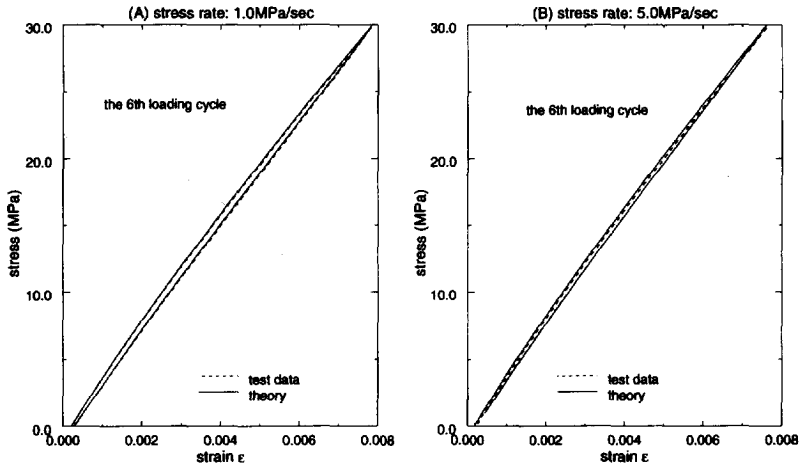


Figure 3.37. Cyclic Loading, two different loading speeds

3.3.4 Five-Cycle Loading

The stress input is shown in Fig. 3.38(A). The elastic compliance J_0 is adjusted to a value of $19.643 \times 10^{-11} \text{GPa}^{-1}$ (1.03% of difference compared to $19.071 \times 10^{-11} \text{GPa}^{-1}$). Using the value of Section 3.3.2 for J_0 yields a 2.55% error in the maximum strain (Fig. 3.38B).

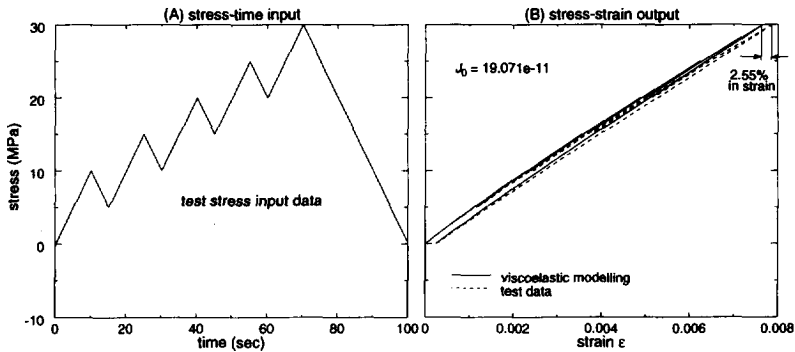


Figure 3.38. A cyclic case (stress rate: 1MPa/sec)

The results for the adjusted initial compliance J_0 are shown in Fig. 3.39. The small adjustment of J_0 yields an excellent agreement.

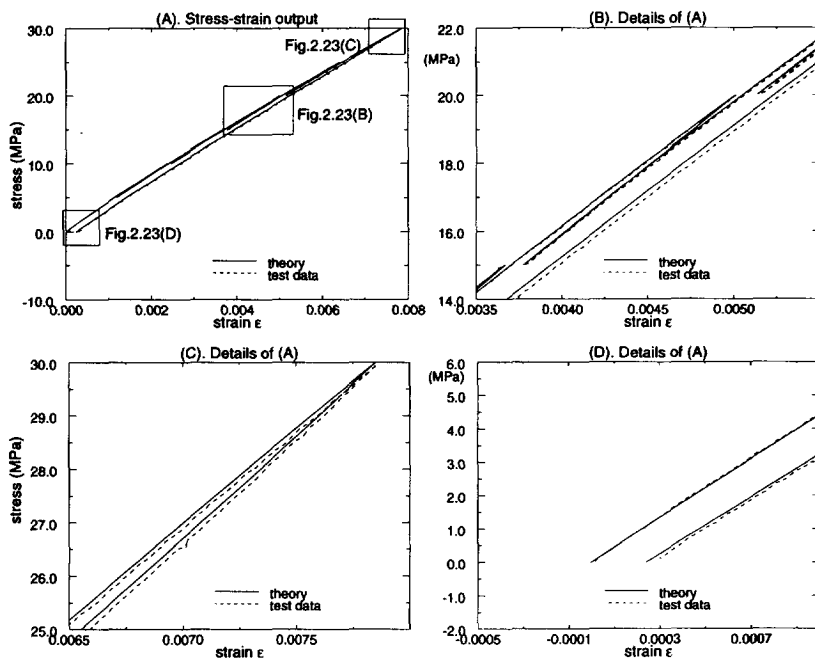


Figure 3.39. Cyclic Loading; stress rate: 0.5MPa/sec; $J_0=19.643e-11$)

The predictions using the two-nonlinear-parameter model in this sub-section and in the previous two sub-sections show a good description of the creep and cyclic behaviour of the unsaturated polyester material. Using a slight adjustment of the parameter J_0 , different cyclic loading behaviour can be modelled excellently. The adjustment of J_0 can be viewed upon as an adaptation to the theory to account for the data scatter which is inherent to the experimental procedure. It most probably results from slight variations in experimental conditions such as *e.g.* the load application, *etc.*, between tests.

3.3.5 Conclusions

1. The use of two nonlinear parameters, g_0 and g_2 in Schapery's model, is sufficient to establish an accurate model for the unsaturated polyester material studied.

For various cyclic loading conditions, the strains predicted with this simplified theory, have small relative errors, less than 1%. This confirms that the history-independent nonlinearizing parameters are sufficiently accurate. For the further calculations in this work, the 'two-nonlinear-parameter model' will be chosen instead of using a model with more nonlinear parameters or stress-history dependent parameters.

2. *The model is correct for relaxation behaviour*

Because of the difficulties in doing relaxation tests, that there is no appropriate method for the brittle materials in our laboratory, the relaxation case has not been checked directly. However, the successful prediction of cyclic loading cases ensures in a certain degree that the relaxation behaviour can be described appropriately. In the cyclic loading case, the loading speed is limited and therefore, both creep and relaxation occur.

3. *The simple-test determined model can be used for describing cyclic loading behaviour*

The model established will be used to simulate the micromechanical behaviour of a fibre reinforced composite with the unsaturated polyester as matrix. The model is then expected to be able to describe the constitutive behaviour of the material under a complicated loading history. It is encouraging that the cyclic loading behaviour can be successfully simulated by a model which is characterized by simple creep-recovery tests.

Three Dimensional Model

4.1 Introduction

It has been shown in the previous chapters that the short-term time-dependent behaviour of the unsaturated polyester resin under study can be described very well by a single-integral nonlinear viscoelastic model, due to Schapery. The model was extended by including the physical ageing shifting effect in order to describe long-term time-dependent behaviour of the resin.

The ultimate goal of this work is to build a numerical model which is able to predict time-dependent behaviour of glass fibre reinforced unsaturated polyester composites. In these materials, the polyester matrix will generally experience multi-axial stresses, even when the global (macroscopic) stress field is uniaxial. Therefore an extension of Schapery's model to a general 3D formulation is necessary.

4.2 3-D Model

The uniaxial stress-strain relation which results from Schapery's model has been given in Chapter 2, Eq (2.4). The Poisson effect is of main concern when the expansion of a model from a uniaxial for-

mulation to a three-dimensional formulation is considered. A viscoelastic material will generally show a time or strain rate dependent Poisson effect. In order to prevent a complicated time or strain rate dependent Poisson's ratio function, however, two constants are introduced instead, a so-called instantaneous Poisson's ratio, ν , and a creep Poisson's ratio, ν_c . With the aid of these constants, the Poisson effect can be described successfully, as will be shown hereinafter.

One of the possible three-dimensional representations of the Schapery model for isotropic materials is given by

$$\epsilon_i = g_0 J_0 S_{ij} \sigma_j + g_1 \int_0^t \Delta J (\psi - \psi') \frac{d}{d\tau} (g_2 S_{ij}^c \sigma_j) d\tau, \quad (4.1)$$

where

$$\begin{cases} (\epsilon_1, \epsilon_2, \epsilon_3, \epsilon_4, \epsilon_5, \epsilon_6) = (\epsilon_{11}, \epsilon_{22}, \epsilon_{33}, \epsilon_{12}, \epsilon_{23}, \epsilon_{13}) \\ (\sigma_1, \sigma_2, \sigma_3, \sigma_4, \sigma_5, \sigma_6) = (\sigma_{11}, \sigma_{22}, \sigma_{33}, \sigma_{12}, \sigma_{23}, \sigma_{13}) \end{cases}, \quad (4.2)$$

$$S_{ij} = \begin{bmatrix} 1 & -\nu & -\nu & 0 & 0 & 0 \\ -\nu & 1 & -\nu & 0 & 0 & 0 \\ -\nu & -\nu & 1 & 0 & 0 & 0 \\ 0 & 0 & 0 & 1+\nu & 0 & 0 \\ 0 & 0 & 0 & 0 & 1+\nu & 0 \\ 0 & 0 & 0 & 0 & 0 & 1+\nu \end{bmatrix}, \quad (4.3)$$

and

$$S_{ij}^c = \begin{bmatrix} 1 & -\nu_c & -\nu_c & 0 & 0 & 0 \\ -\nu_c & 1 & -\nu_c & 0 & 0 & 0 \\ -\nu_c & -\nu_c & 1 & 0 & 0 & 0 \\ 0 & 0 & 0 & 1+\nu_c & 0 & 0 \\ 0 & 0 & 0 & 0 & 1+\nu_c & 0 \\ 0 & 0 & 0 & 0 & 0 & 1+\nu_c \end{bmatrix}. \quad (4.4)$$

The kernel function ΔJ is defined as

$$\Delta J (\psi - \psi') = C \{ \exp [(\psi - \psi')^n] - 1 \} \quad (4.5)$$

where the shifted times are given by

$$\psi = \int_0^t \frac{dt'}{\bar{a}_\sigma} \quad \text{and} \quad \psi' = \int_0^\tau \frac{dt'}{\bar{a}_\sigma}, \quad (4.6)$$

and

$$\bar{a}_\sigma = a_\sigma \left(\frac{t_c + \tau}{t_c} \right)^\alpha, \quad (4.7)$$

In these equations, t_e and α are the initial physical ageing time and the shifting rate of physical ageing respectively.

For uniaxial loading, the nonlinearizing functions g_0 , g_1 , g_2 and α_0 of the model are functions of the uniaxial stress only. For a multiaxial formulation, these functions in general will depend on some measure of the multiaxial stress field. This measure must of course be invariant. Several approaches have been proposed (Brouwer 1986^[11], etc.). One of the most cited invariants is the effective stress (or von Mises stress), σ_e , defined by

$$\sigma_e = \sqrt{I_1^2 - 3I_2}, \quad (4.8)$$

where I_1 and I_2 are the first and second stress invariants which are defined as

$$\begin{cases} I_1 = \sigma_1 + \sigma_2 + \sigma_3 \\ I_2 = \sigma_1\sigma_2 + \sigma_2\sigma_3 + \sigma_1\sigma_3 - \left(\sigma_4^2 + \sigma_5^2 + \sigma_6^2 \right) \end{cases} \quad (4.9)$$

A simplification of the model Eq (4.1) results when assuming a single Poisson's ratio for both instantaneous and creep deformations, i.e. $\nu_c = \nu$. This was done by Henriksen (1984)^[27] for plane stress and plane strain cases but there was no experimental evidence given for this assumption. For the present material it was found from experiments that these Poisson's ratio's are not equal. The results of these experiments are presented in Section 4.3.

4.3 Poisson's Ratio of a Viscoelastic Material

For a viscoelastic material, the Poisson's ratio in general is not a constant but varies with time. It is a function of the strain, stress, time, etc. In this section, it is hypothesized that two constant parameters are sufficient to describe the Poisson effect in a 3D stress-strain relation. These two parameters are the instantaneous Poisson's ratio, which describes the instantaneous elastic deformation, and the creep Poisson's ratio, which is related to the time-dependent deformation part.

The major objective of this section is to apply these two parameters and determine experimentally that these two parameters can be considered as two material constants. It will bring us a great convenience in 3-D modelling if they are constants instead of functions.

4.3.1 Overall Poisson's Ratio

If ν_c in Eq (4.4) is assumed to be a constant, Eq (4.1) can be rewritten as

$$\epsilon_i = g_0 J_0 S_{ij} \sigma_j + S_{ij}^c g_1 \int_0^t \Delta J \frac{d}{d\tau} (g_2 \sigma_j) d\tau. \quad (4.10)$$

But this assumption is not apparently true and proof for it is required. If ν_c is a function of stress and/or time, the determination of ν_c according to Eq (4.1) is not possible.

The first three components of strain in Eq (4.1) are

$$\epsilon_1 = g_0 J_0 S_{1j} \sigma_j + g_1 \int_0^t \Delta J \frac{d}{d\tau} (g_2 S_{1j}^c \sigma_j) d\tau, \quad (4.11)$$

$$\epsilon_2 = g_0 J_0 S_{2j} \sigma_j + g_1 \int_0^t \Delta J \frac{d}{d\tau} (g_2 S_{2j}^c \sigma_j) d\tau, \quad (4.12)$$

$$\epsilon_3 = g_0 J_0 S_{3j} \sigma_j + g_1 \int_0^t \Delta J \frac{d}{d\tau} (g_2 S_{3j}^c \sigma_j) d\tau. \quad (4.13)$$

Under a uniaxial loading situation (Fig. 4.1), only σ_1 is different from zero, while all other stress components are zero, $\sigma_2 = \sigma_3 = \sigma_4 = \sigma_5 = \sigma_6 = 0$. Above expressions can in this case be written as

$$\epsilon_1 = g_0 J_0 \sigma_1 + g_1 \int_0^t \Delta J \frac{d}{d\tau} (g_2 \sigma_1) d\tau, \quad (4.14)$$

$$\epsilon_2 = \epsilon_3 = -\nu g_0 J_0 \sigma_1 - g_1 \int_0^t \Delta J \frac{d}{d\tau} (g_2 \nu_c \sigma_1) d\tau, \quad (4.15)$$

where relations Eq (4.3) and Eq (4.4) have been used for the components of S_{ij} and S_{ij}^c . The creep Poisson ratio ν_c is for now assumed to be in general a function of time.

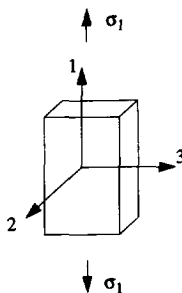


Figure 4.1. Loading Direction

On the other hand, the viscoelastic strain can always be divided into two parts, the elastic strain and the creep strain, i.e.,

$$\begin{cases} \epsilon_1^{elastic} = g_0 J_0 \sigma_1 \\ \epsilon_1^{creep} = g_1 \int_0^t \Delta J \frac{d}{d\tau} (g_2 \sigma_1) d\tau \end{cases} \quad (4.16)$$

The coefficient of lateral contraction (overall Poisson's ratio), defined by the negative ratio of lateral to axial strain for each instant of time, is then given by

$$\eta(\sigma_1, t) = \frac{\epsilon_2}{\epsilon_1} = \frac{v_{g_0} \int_0^t \sigma_1 + g_1 \int_0^t \Delta J \frac{d}{d\tau} (g_2 v_c \sigma_1) d\tau}{g_0 \int_0^t \sigma_1 + g_1 \int_0^t \Delta J \frac{d}{d\tau} (g_2 \sigma_1) d\tau} \quad (4.17)$$

An approximation of Eq (4.17) for an almost constant v_c is

$$\eta(\sigma_1, t) \approx \frac{v_{\epsilon_1}^{elastic} + v_c \epsilon_1^{creep}}{\epsilon_1^{elastic} + \epsilon_1^{creep}} \quad (4.18)$$

The equality only holds exactly when v_c is a constant. Apparently, the overall Poisson's ratio is not a material constant. It is generally both stress and time dependent for viscoelastic materials (Findley *et al.* 1976^[18], p. 189).

4.3.2 Creep Poisson's Ratio

In the same fashion as above, the lateral strain, ϵ_2 , can be separated into an elastic strain and a creep strain,

$$\epsilon_2 = \epsilon_2^{elastic} + \epsilon_2^{creep} \quad (4.19)$$

If v_c is constant then according to Eq (4.15)

$$\epsilon_2^{creep} = -v_c g_1 \int_0^t \Delta J \frac{d}{d\tau} (g_2 \sigma_1) d\tau = -v_c \epsilon_1^{creep} \quad (4.20)$$

Lateral and axial strains are proportional to each other. The creep Poisson's ratio is then by definition

$$v_c = -\frac{\epsilon_2^{creep}}{\epsilon_1^{creep}} \quad (4.21)$$

Generally, v_c is both time and stress dependent, $v_c = v_c(\sigma, t)$. In order to fully determine v_c , therefore, the test program should include different stress levels and creep-recovery times.

Probably because of the fact that the experimental determination of the creep Poisson's ratio is extremely difficult, little information is available about the creep Poisson's ratio in the literature and even some opinions about this Poisson's ratio conflict each other due to the difference of the materials. Ross (1964)^[37] reported that creep in the direction of the major principal stress appeared to be unaffected by the presence of stresses in the other principal directions, thus suggesting that the creep Poisson's ratio was zero for concrete material. While most people believe that creep is essentially a shear-dominated process. Boyle and Spence (1983^[9], p. 41) in a study on metals, concluded that changes in hydrostatic pressure had no influence on the creep behaviour and the observation showed

that creep deformations appeared as distortions. There was a change in shape without a change in volume. They therefore suggested a creep Poisson's ratio of 0.5 for metal. Some other researchers suggested a creep Poisson's ratio similar in magnitude to the instantaneous elastic Poisson's ratio (e.g. Henriksen 1984^[27] for polymers and Gopalakrishnan *et al.* 1969^[20] for concrete materials). Due to the sparse and unreliable literature data, a test program was set up to evaluate the creep Poisson's ratio of the unsaturated polyester.

4.3.3 Determination of Poisson's Ratios

A uniaxial creep-recovery test is considered here. The uniaxial stress is given by $\sigma(t) = \sigma_1 H(t)$. For this one-step stress input, the strain in the loading direction is given (from Eq (4.14)) by

$$\epsilon_1 = g_0 J_0 \sigma_1 + g_1 g_2 \sigma_1 \Delta J \left(\frac{t}{a_\sigma} \right). \quad (4.22)$$

In the transverse direction, the strain ϵ_2 becomes, according to Eq (4.15)

$$\epsilon_2 = -\nu g_0 J_0 \sigma_1 - g_1 g_2 \nu_c \sigma_1 \Delta J \left(\frac{t}{a_\sigma} \right). \quad (4.23)$$

The overall Poisson's ratio is then obtained from Eq (4.17)

$$\eta(\sigma_1, t) = \frac{\epsilon_2}{\epsilon_1} = \frac{\nu \epsilon_1^{elastic} + \nu_c \epsilon_1^{creep}}{\epsilon_1^{elastic} + \epsilon_1^{creep}}, \quad (4.24)$$

where

$$\epsilon_1^{creep} = g_1 g_2 \sigma_1 \Delta J \left(\frac{t}{a_\sigma} \right). \quad (4.25)$$

Note that, under a step stress input, Eq (4.24) is an exact relation without the assumption of a constant ν_c , whereas Eq (4.18) only holds exactly when ν_c is constant under a general stress input.

In the beginning of the loading, the creep time is very small, $\epsilon_{1,2}^{elastic} \gg \epsilon_{1,2}^{creep} \approx 0$. From Eq (4.24) we obtain

$$\frac{\epsilon_2}{\epsilon_1} = \frac{\nu \epsilon_1^{elastic} + \nu_c \epsilon_1^{creep}}{\epsilon_1^{elastic} + \epsilon_1^{creep}} \approx \nu. \quad (4.26)$$

During recovery, the strain in the loading direction is

$$\epsilon_1 = g_2 \sigma_1 [\Delta J(\psi) - \Delta J(\psi - \psi_1)]. \quad (4.27)$$

Similarly Eq (4.15) provides the transverse strain

$$\epsilon_2 = g_2 (-\nu_c \sigma_1) [\Delta J(\psi) - \Delta J(\psi - \psi_1)], \quad (4.28)$$

and thus the overall Poisson's ratio (without an assumption of a constant ν_c) can be derived by dividing Eq (4.28) by Eq (4.27),

$$\frac{-\epsilon_2}{\epsilon_1} = \nu_c. \quad (4.29)$$

An experimental method to determine both the instantaneous Poisson's ratio, ν , and the creep Poisson's ratio, ν_c , is then established by Eq (4.26) and Eq (4.29).

Fig. 4.2(C) shows this graphically. At the point P in Fig. 4.2(C), the value of $-\epsilon_2/\epsilon_1$ at short times equals the elastic Poisson's ratio, since creep deformation has not got enough time to become visible (there is a difficulty to measure this ν accurately, see Section 4.3.4). Along the path PQ , $-\epsilon_2/\epsilon_1$ increases because of the increase of the creep strain in Eq (4.17). But it will not reach the creep Poisson's ratio (here assume $\nu_c > \nu$) unless the creep strains are much larger than the elastic strains. At the points Q and R , when the load is released, the elastic strains are recovered immediately, while the creep strains remain. According to Eq (4.29), the measured value $-\epsilon_2/\epsilon_1$ is exactly the creep Poisson's ratio ν_c .

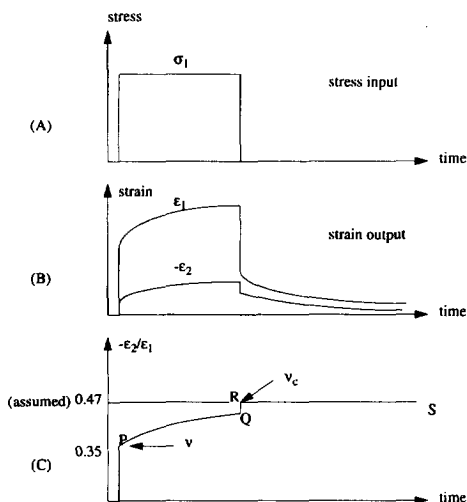


Figure 4.2. Creep-recovery test and overall Poisson's ratio

4.3.4 Test Results

Uniaxial tensile creep tests were performed on dog-bone specimens. A uniaxial tensile load was applied in the '1' direction (which is along the specimen, see Fig. 4.1 and Fig. 4.2). Both strains in the

'1' and the '2' direction were measured and were divided by each other to obtain the overall Poisson's ratio.

The tests were carried out in an air-conditioned room with a constant temperature of $23^{\circ}\text{C} \pm 0.5^{\circ}\text{C}$ and a relative humidity of $52\% \pm 2\%$. A temperature chamber was used for several cases when lower and higher temperatures were required. Specimens used were the same as those presented in Figure 3.28 on page 53. The test machine (Zwick-1484) could provide automatic loading control in tension as well as in compression. Strain gauges were used for strain measuring.

Different test conditions were chosen in order to examine the dependence of the creep Poisson's ratio on factors like stress/strain level, aging time, creep time and temperature.

A fundamental difficulty of these tests originates from the small strains during the recovery period. These strains are so small that any slight change in temperature due to the air flow around the strain gauges may spoil the data for the Poisson's ratio measurement. Some discussions about this problem are presented in Zhang (1993b).

1. Stress Level Influence

Fig. 4.3 shows the creep Poisson's ratio against different stress levels.

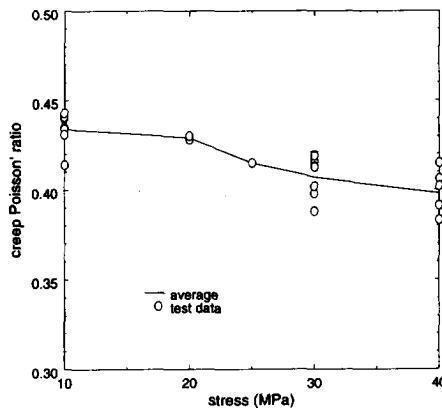


Figure 4.3. Creep Poisson's Ratio

Fig. 4.4 gives three results for different creep stresses and creep times. It can be observed that there is a slight stress dependence of the creep Poisson's ratio. The averaged creep Poisson's ratios are listed in Table 4.1. As a first approximation, it can still be assumed that there is a constant creep Poisson's ratio which equals 0.417 (according to the data obtained in a stress range of 10–40 MPa). The ultimate error is defined as the half of the maximum of the difference of any two data.

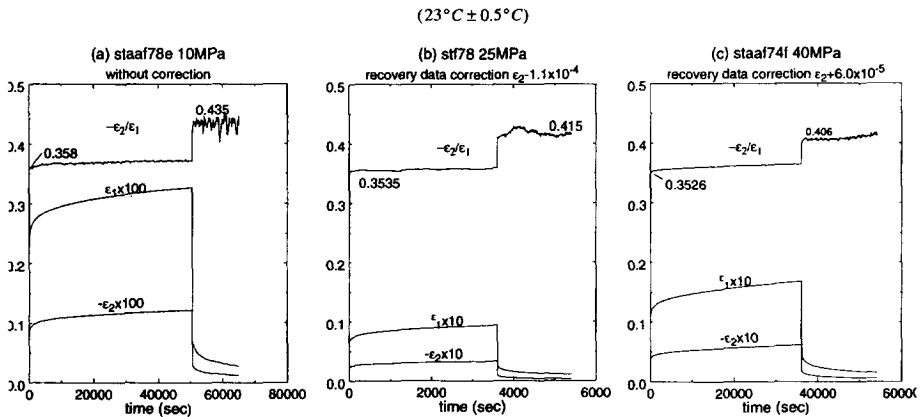


Figure 4.4. Test Results for Different Creep Stresses

Table 4.1. Averaged Creep Poisson's Ratio (23°C ± 0.5°C)

creep stress	10 MPa	20 MPa	25 MPa	30 MPa	40 MPa
creep Poisson's ratio	0.434	0.429	0.415	0.407	0.398
ultimate error	±0.020	±0.001		±0.019	±0.017
(number of data)	(7)	(2)	(1)	(7)	(6)

2. Creep Time Dependence

From the test results it can be concluded that the creep Poisson's ratio is not time dependent. Table 4.2. shows the results of averaged creep Poisson's ratios from different creep times and stresses.

Table 4.2. Creep Time Influence (23°C ± 0.5°C)

creep stress	10 MPa		30 MPa		40 MPa	
creep time	14 hours	1 hour	12 hours	4 hours	10 hours	1 hour
creep Poisson's ratio	0.435	0.442	0.419	0.410	0.404	0.395
ultimate error	±0.005	±0.001		±0.008	±0.002	±0.020
(number of data)	(4)	(2)	(1)	(3)	(2)	(4)

Due to the scatter of the data (Table 4.2) the differences between creep times can not be attributed to a time dependence since the scatter in the data is of the same order of magnitude.

4.3.5 Aging Influence

The aging times of samples are recorded in Zhang (1993b^[49], Appendix). A comparison between creep Poisson's ratios for samples with different physical aging times is given in Table 4.3. Again a

slight influence on the creep stress level can be observed, but there is no evidence of a dependence on the physical aging time.

Table 4.4. shows the results for a sample which did not undergo postcuring. Without postcuring, the cross-linking level of molecules is lower. This causes a softer material behaviour and a larger instantaneous Poisson's ratio. This suggests that, on the other hand, the increase of the cross-linking level will reduce the instantaneous Poisson's ratio while the creep Poisson's ratio remains constant. The results from the case with a 20 MPa creep stress are not reliable. More details about this are described in Zhang (1993b)^[49]. It can not be concluded from Table 4.4 that there is a dependence of the creep Poisson's ratio on the chemical aging or on the creep stress level. The thermal influence will be discussed in the Section 4.3.6

Table 4.3. Physical Aging Time Influence ($23^{\circ}\text{C} \pm 0.5^{\circ}\text{C}$)

creep stress	10 MPa		30 MPa			40 MPa	
aging time	10 mon.	2 mon.	10 mon.	2 mon.	55 min.	10 mon.	2 mon.
test results of creep Poisson's ratio	0.440	0.435	0.398	0.416	0.4127	0.391	0.415
	0.434	0.414	0.402	0.413		0.391	0.402
	0.431	0.441	0.388	0.419		0.406	0.383
	0.443						
averaged	0.437	0.430	0.396	0.416	0.4127	0.396	0.400

Table 4.4. Results from Samples without Postcuring ($23^{\circ}\text{C} \pm 0.5^{\circ}\text{C}$)

creep stress	10 MPa	20 MPa
instantaneous Poisson's ratio/creep Poisson's ratio	0.386/0.439	0.381/0.408*
	0.388/0.434	0.378/0.388*
	0.3834/0.434	
	0.391/0.435	
averaged	0.3871/0.4355	
ultimate error	$\pm 0.004 / \pm 0.0035$	

* poor data quality

4.3.6 Temperature Influence

The results for different temperatures are listed in Table 4.5. Table 4.6 shows the instantaneous Poisson's ratio.

There is a large deviation of the results of the instantaneous Poisson's ratio due to a 'zero-point' shifting of the electronic instruments after a sudden increase of the displacement. This phenomenon will be discussed later. The occurrence of this problem suggests that for the measurement of time dependent material behaviour, a long-term stable measuring system is crucial for a good data quality.

There were three tests done for a higher temperature (40°C). The results showed a severe zero-point shifting influence (see Section 4.4.4). Due to the difference of thermal expansion between the polyester and the base material of the strain gauges, an initial strain of the same order of magnitude as the creep strain was observed. Besides, under a higher temperature than the room temperature, a period of

time is needed for the polymer to reach a new thermodynamic equilibrium, during which the physical aging may be partially removed.

A temperature independence of both Poisson's ratios is required in order to be able to apply the acceleration method for general 3-D creep-relaxation tests by increasing the temperature. If the independence is not true, the acceleration method can only be adopted for uniaxial testing and modelling. The experiments have proved the temperature independence within a range of 10°C ~ 23°C, for both Poisson's ratios.

Table 4.5. Tests for Different Temperatures (creep stress: 10 MPa)

temperature	10°C ± 1°C		23°C ± 0.5°C	
physical aging time	10 months	2 months	10 months	2 months
creep Poisson's ratio (from various samples)	0.427	0.430	0.440 0.434	0.435 0.414
	0.417		0.431 0.443	0.441
averaged & ultimate error	0.422±0.05	0.430	0.437±0.06	0.430±0.16

Table 4.6. Instantaneous Poisson's Ratio (creep stress: 10 MPa)

temperature	10°C ± 1°C	23°C ± 0.5°C
instantaneous Poisson's ratio	0.371	0.362
ultimate error	±0.002	±0.009

4.4 Discussion on Poisson's Ratio Measurements

4.4.1 Thermal Influence in the Overall Poisson's Ratio

Eq (4.17) and Eq (4.18) are obtained under the assumption of a viscoelastic material behaviour. For a more general situation, other strains might be involved during the measurement too. Here the influence of possible thermal strain is considered. In this case, the overall Poisson's ratio under a uniaxial load can be written as follows

$$\frac{\epsilon_2}{\epsilon_1} = \frac{\epsilon_2^{therm} + \nu \epsilon_1^{elastic} + \nu_c \epsilon_1^{creep}}{\epsilon_1^{therm} + \epsilon_1^{elastic} + \epsilon_1^{creep}}.$$

(4.30)

Here $\epsilon_{1,2}^{therm}$ are thermal strains, where $\epsilon_2^{therm} / \epsilon_1^{therm} = 1$ due to the assumed isotropy; Elastic strains are instantaneously recoverable and creep strains are typically time dependent but recoverable.

4.4.2 Loading Imperfection Influence

In the experiments, the loading rate was about 20MPa/sec. for the first 90% of loading. For 40MPa creep stress, it took the test machine about 2.5 seconds to finish a loading or an unloading step (99%)

without overshoot. Fig. 4.5 shows a case with a loading step of 30MPa creep stress. The strain data at the beginning of the loading step and at the start of the unloading step are not accurate.

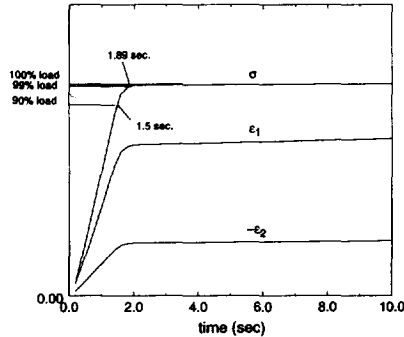


Figure 4.5. Loading imperfection, creep stress: 30MPa, specimen # 745

It was found that, however, the loading imperfections have just minor influences on the creep and recovery data compared with the influences due to temperature effects and due to stability of the instruments.

4.4.3 Thermal Expansion and Contraction Influence

Dealing with temperature influences, two different aspects have to be considered: heat generation by the strain gauge and heat transfer between strain gauge and specimen, and consequently thermal expansion/contraction of the testing material.

If a strain gauge is used for testing, the electrical resistance of the strain gauge will create heat, hence the temperature of the material will be raised locally and the material can be expected to undergo a volume change according to the local temperature. On the other hand, the heat is partly transferred to the surrounding air. This transfer is sensitive to the air flow around the specimen. Although a dummy sample was used for temperature compensation, the air current around the samples changed locally and randomly and caused a difference in heat diffusion efficiencies between the specimen gauge and the dummy gauge, and consequently a temperature discord between them. Thus a temperature induced strain variation occurs. This can in turn spoil small strain data (see Fig. 4.6). For lower stress levels and short creep times, the recovery data are extremely small, of the order of 10^{-4} , which is compatible with the order of magnitude of the variations caused by the above-mentioned temperature changes.

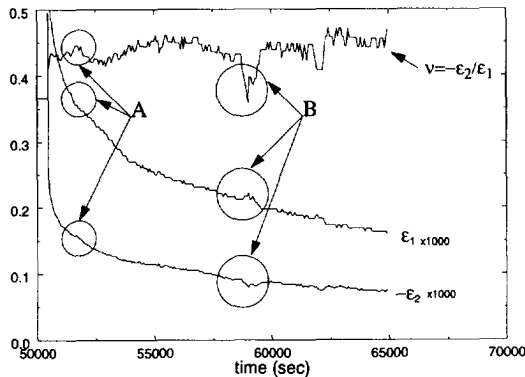


Figure 4.6. Recovery Data & Poisson's Ratio, creep stress: 10MPa

The thermal expansion and contraction can distort the overall Poisson's ratio data considerably as can be observed in Fig. 4.6. The arrows marked with A show a thermal contraction influence (in a short period of time) on the overall Poisson's ratio, while those marked with B indicate an expansion effect.

The environmental temperature will have an influence on the heat transmission efficiency from the strain gauge to the surrounding air. If the air flows along the strain gauge, the heat transmission efficiency between the gauge and the air will be influenced by the air temperature. A relatively high air temperature will cause a larger part of the generated heat to remain on the sample and cause a raise of the local temperature. An analysis of the air flow influence has been done in Zhang (1993b)^[49] and the disturbances of the strains as shown in Fig. 4.6 have been well explained.

The variation of strain will change the electrical resistance of the strain gauge, hence the electric power and eventually change the amount of heat generated by the strain gauge. An unloading will reduce the strain significantly in a short period of time, and hence reduce the resistance of the strain gauge too. This causes a corresponding increase of the electric power or the heat generated by the strain gauge. This in turn further raises the local temperature and thus produces an extra thermal strain. An analysis of this second thermal effect is given in Zhang (1993b)^[49]. The results show that there is 1~2% of relative strain error existing in the beginning of the recovery data due to a sudden change of load. According to Fig. 4.7, the relative errors of the peak disturbances in the overall Poisson's ratio (10MPa) can be calculated. They are 2.7% and 7% at the beginning of creep and of recovery respectively. The division of strains doubles the error, hence the errors in the individual strains are 1.35% (at the beginning of creep) and 3.5% (at the beginning of recovery). They are of the same order of magnitude as those calculated in Zhang (1993b)^[49].

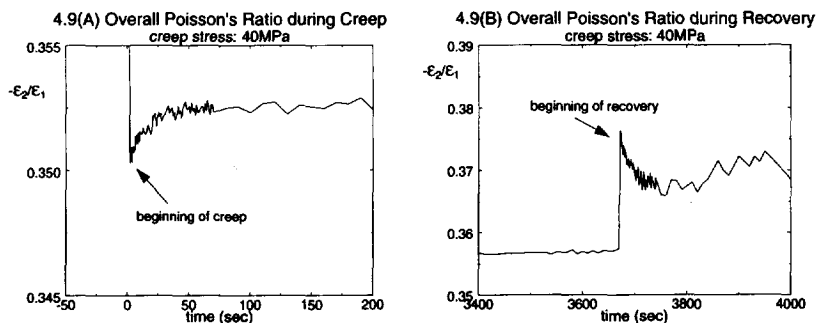


Figure 4.7. Overall Poisson's ratio at the beginning of creep and recovery

Because of the small strain situation during recovery, the thermal strain exhibits as an inseparable part of the strain data due to the application of the strain gauge. To avoid the temperature influence, it is better to use other measuring means instead of strain gauges. But to pursue a higher accuracy will finally lead to a complicated and expensive measurement method.

4.4.4 Stability of Signal Amplifiers and the Correction Method

It has been found that the measuring system can cause 1% error in creep and recovery data including zero-point floating during large amplitude signal changes and zero-point variations during a long time measurement under room temperature. The floating of data generated by creep step jumping will shift the creep data and cause an inaccuracy of the result for the Poisson's ratio even at the very beginning of creep. But the variation during creep will possibly not bring large errors for creep data, neither the variation from the recovery period for recovery data will do. But there may be a large error transportation from the creep period to the recovery period. Since the strain in the creep period is usually large, its 1% floating and variation can be as large as the strain in the recovery period. When the test is transferred into the recovery stage, the remaining variation error from the creep stage will shift the strain data in recovery unanimously.

This influence is hard to be observed from strain data, but can easily be reduced from overall Poisson's ratio data. If there is no permanent deformation and thermal deformation, the overall Poisson's ratio in the recovery period is the same as the creep Poisson's ratio. The overall Poisson's ratio keeps then a constant value and will not increase or decrease with time during recovery (see Section 4.3.3). On the $(-\epsilon_2/\epsilon_1)$ vs. time figure, a horizontal line during the recovery period should be seen. The position of this horizontal line thus determines the creep Poisson's ratio. The test results, however, often show that the data curve tends to deviate from a horizontal line.

It is easy to make a correction by shifting the strain data until the Poisson's ratio curve becomes horizontal. Fig. 4.8 shows how to perform this method: adding or subtracting a constant from the strain data in recovery until the overall Poisson's ratio curve becomes horizontal. This constant is hence considered to be the accumulated zero-point shifting in the creep period. This method is usually valid

if there is no thermal deformation involved. It was found that there is little difference whether ϵ_1 or ϵ_2 is corrected, as long as the correction is not larger than 10% of the total strain in the recovery period. In the data processing, usually the strain data, ϵ_2 , were shifted because ϵ_2 is smaller than ϵ_1 and more sensitive to a correction.

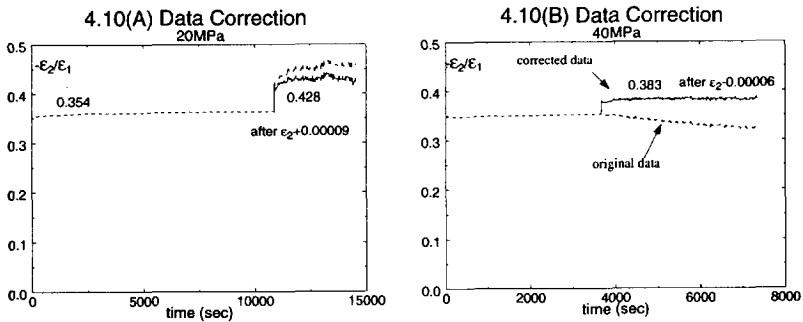


Figure 4.8. Data correction by a translation of strain

Fig. 4.8(A) shows a result where 0.00009 was added to the recovery data of ϵ_2 . In Fig. 4.8(B) 0.00006 was subtracted from the recovery data of ϵ_2 (the dot lines are the original data, the solid lines are the corrected data).

Some results show a zero-point shifting of the strain signal which is too large to be corrected by this method. The data then seem to be useless. In Fig. 4.9 some data of a higher temperature experiment (40°C) are presented. The correction of the recovery data by the above mentioned method required a correction beyond the above-mentioned 10% limit. It results in creep Poisson's ratio's above 0.5. The high zero-point shifting here probably may also be attributed to a thermal influence, to the creep of the base material of the strain gauge and to clamping imperfections.

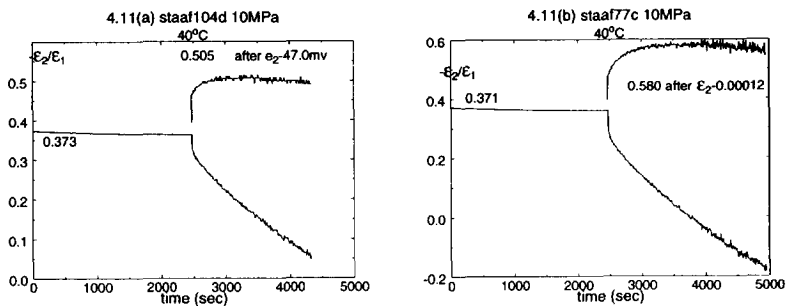


Figure 4.9. Thermal volume change influence

4.4.5 Conclusions

1. *An accurate description of 3D behaviour is observed when considering two constant Poisson's ratio's: an instantaneous and a creep Poisson's ratio.*
2. *The creep Poisson's ratio remains constant for different creep times, aging times (both physical and chemical aging) and temperatures (10°C ~ 23°C).*
3. *The creep Poisson's ratio slightly varies with the creep stress level from 0.398 for 40 MPa to 0.434 for 10 MPa, the average being 0.417. This suggests that there is a hydrostatic pressure effect on the creep deformation (volume creep). On the other hand, the creep Poisson's ratio is apparently larger than the instantaneous creep Poisson's ratio, which suggests that if a single Poisson's ratio is used a large error will be introduced in the 3D time-dependent analysis;*
4. *The instantaneous Poisson's ratio decreases with an increase of the cross-linking level. It is also possibly dependent on temperature;*
5. *The proposed method for determination of the creep Poisson's ratio is easily and economically to be used, especially the data correction method is simple to carry out and can avoid the requirement of extraordinary stable electronic instruments for long time small strain measurements;*
6. *Thermal strain caused by strain gauges has various influences in small strain measurements, and can distort the creep data and recovery data significantly.*

In the composite creep analysis, Chapter 7, an example will be given of the fact that neglecting the creep Poisson's ratio by equalizing it to the instantaneous Poisson's ratio will lead to a 10% error in the strain for a creep time longer than one month, see Fig. 7.13. In the direction perpendicular to the remote load, there is a 6% error. Due to the fact that the remote load is not large (10MPa) when a 10% error has been found, a larger error is expected at higher load levels. It is therefore necessary to consider the creep Poisson's ratio in the composite creep calculation.

Numerical Algorithm and DIANA Implementation

5.1 Introduction

In Chapter 4, a 3D constitutive relation has been established. In order to apply the finite element method to analyse the composite material, this 3D model is needed to be implemented into a finite element package, and hence the numerical scheme for this model is required. This is the subject of this chapter.

The integral representation of the viscoelastic constitutive relations straightforwardly reveals the hereditary property of polymer materials, *i.e.*, the time dependence or the memory of the stress history. However, to evaluate this integral, all the information of the stress history from time zero to the present time is necessary. This is due to the fact that the kernel of the integral is a function of current time which is the integration limit of the convolution integral (see Eq (5.1)). The kernel thus changes with current time and consequently the integral is needed to be repeatedly evaluated for different current times. This suggests that if a numerical evaluation is adopted, as the observing time increases, the computing time of the integral becomes longer and longer and, at the same time, more and more evaluated stress data from every time step are needed to be stored for later calculation of the integral.

In this Chapter, we use an exponential function series to approximate the kernel function. A numerical scheme in which only the data of the previous time increment are involved in the current time calculation thus has been developed. Hence only the data of the previous time step are required to be stored. Therefore no large data storage is required and the computing time is also reduced. A similar method, using an exponential series kernel, was developed by Henriksen (1984)^[27] for plane strain and plane stress cases. Here the general 3-D formulation is presented with the physical aging effects and a creep Poisson's ratio being included.

This material model will be particularly used for the modelling of the matrix behaviour of fibre-reinforced polymers in the micromechanical analysis of composites.

DIANA software is a finite element method package developed by TNO, the Netherlands. The implementation of the constitutive model has been done in this package and has been tested by several examples including creep with an aging influence, cyclic loading and shear deformation. The results have shown a good accuracy of the numerical scheme. Especially, for a uniaxial creep simulation, a large time step for the calculation is possible and brings very limited errors, hence a several years creep calculation, whatever for pure polymer or composite, can be done with merely several time steps. The numerical scheme can successfully deal with the strong nonlinearities at high stress rates and high stress levels although these situations may cause a low convergent speed and hence require either smaller time increments or more iterations.

5.2 Formulation and Discretisation

In this section, the formulation is focused on setting up a numerical scheme which can avoid a large storage for all old stress information.

5.2.1 Theory

Under the assumption of a constant creep Poisson's ratio, the three-dimensional representation Eq (4.1) becomes

$$\varepsilon_i = g_0 J_0 S_{ij} \sigma_j + S_{ij}^c g_1 \int_0^t \Delta J \frac{d}{d\tau} (g_2 \sigma_j) d\tau \quad (5.1)$$

and g_0 , g_1 , g_2 (will appear later) and a_σ (in Eq (5.3) and Eq (5.4)) are nonlinear parameters being functions of the effective stress $\Sigma(t)$ (defined in Eq (5.19)). The kernel function, ΔJ , can be generally approximated by a certain number of terms of the exponential series

$$\Delta J = \sum_{p=1}^{\infty} J_p \left(1 - e^{-\lambda_p (\psi - \psi')} \right), \quad (5.2)$$

where the reduced times, in which the physical aging effect is included (see Chapter 4 for details), are

$$\psi = \psi(t) = \int_0^t \frac{d\tau'}{{}_0a_\sigma(\Sigma(\tau')) \left(\frac{t_e + \tau'}{t_e} \right)^\alpha}, \quad (5.3)$$

$$\psi' = \psi(\tau) = \int_0^\tau \frac{d\tau'}{{}_0a_\sigma(\Sigma(\tau')) \left(\frac{t_e + \tau'}{t_e} \right)^\alpha}. \quad (5.4)$$

Here t_e is the physical aging time of the material at $\tau = 0$ and α the shifting rate of physical aging (see Chapter 3). Compared to Eq (4.9), the bar over ψ is dropped for writing convenience. Breaking of the series expansion Eq (5.2) at a chosen value of p , an adequate approximation of the power law or exponential law kernel function within a certain time domain is obtained (see, e.g., Figure 5.1 on page 86). The participation factors can be determined by a usual curve fitting procedure. Generally a limited number of terms will be sufficient for a required accuracy. If more terms are used in the same time domain, the accuracy of the series may be improved extensively. If a certain accuracy is chosen, the use of more terms can extend the time domain. The stresses and strains will be written as follows, see Eq (4.2),

$$\begin{cases} (\epsilon_1, \epsilon_2, \epsilon_3, \epsilon_4, \epsilon_5, \epsilon_6) = (\epsilon_{11}, \epsilon_{22}, \epsilon_{33}, \epsilon_{12}, \epsilon_{23}, \epsilon_{13}) \\ (\sigma_1, \sigma_2, \sigma_3, \sigma_4, \sigma_5, \sigma_6) = (\sigma_{11}, \sigma_{22}, \sigma_{33}, \sigma_{12}, \sigma_{23}, \sigma_{13}) \end{cases} \quad (5.5)$$

and S_{ij} , S_{ij}^c are copied from Eq (4.3) and Eq (4.4):

$$S_{ij} = \begin{bmatrix} 1 & -\nu & -\nu & 0 & 0 & 0 \\ -\nu & 1 & -\nu & 0 & 0 & 0 \\ -\nu & -\nu & 1 & 0 & 0 & 0 \\ 0 & 0 & 0 & 1+\nu & 0 & 0 \\ 0 & 0 & 0 & 0 & 1+\nu & 0 \\ 0 & 0 & 0 & 0 & 0 & 1+\nu \end{bmatrix}, \quad (5.6)$$

$$S_{ij}^c = \begin{bmatrix} 1 & -\nu_c & -\nu_c & 0 & 0 & 0 \\ -\nu_c & 1 & -\nu_c & 0 & 0 & 0 \\ -\nu_c & -\nu_c & 1 & 0 & 0 & 0 \\ 0 & 0 & 0 & 1+\nu_c & 0 & 0 \\ 0 & 0 & 0 & 0 & 1+\nu_c & 0 \\ 0 & 0 & 0 & 0 & 0 & 1+\nu_c \end{bmatrix}, \quad (5.7)$$

5.2.2 Discretisation

Substitution of Eq (5.2) into Eq (5.1) yields

$$\epsilon_i = g_0 J_0 S_{ij} \sigma_j + S_{ij}^c g_1 \int_0^t \sum_p \left(J_p - J_p e^{-\lambda_p(\psi(t) - \psi(\tau))} \right) \frac{d}{d\tau} (g_2 \sigma_j) d\tau, \quad (5.8)$$

or

$$\varepsilon_i = g_0 J_0 S_{ij} \sigma_j + S_{ij}^c g_1 \int_0^t \left(\sum_p J_p \right) \frac{d}{d\tau} (g_2 \sigma_j) d\tau - S_{ij}^c g_1 \int_0^t \sum_p J_p e^{-\lambda_p (\psi(t) - \psi(\tau))} \frac{d}{d\tau} (g_2 \sigma_j) d\tau. \quad (5.9)$$

The second term of the right hand side of Eq (5.9) is

$$S_{ij}^c g_1 \int_0^t \left(\sum_p J_p \right) \frac{d}{d\tau} (g_2 \sigma_j) d\tau = S_{ij}^c g_1 \sum_p J_p \int_0^t \frac{d}{d\tau} (g_2 \sigma_j) d\tau = S_{ij}^c g_1 \left(g_2 \sigma_j - g_2 \sigma_j^0 \right) \sum_p J_p \quad (5.10)$$

where the initial stress $\sigma_j^0 = \sigma_j(0)$ and $g_2^0 = g_2[\Sigma(0)]$. The third term of the right hand side of Eq (5.9) is

$$-S_{ij}^c g_1 \int_0^t \left(\sum_p J_p \right) e^{-\lambda_p (\psi(t) - \psi(\tau))} \frac{d}{d\tau} (g_2 \sigma_j) d\tau = -S_{ij}^c g_1 \sum_p J_p \left\{ \int_0^{t-\Delta t} + \int_{t-\Delta t}^t \right\} e^{-\lambda_p (\psi(t) - \psi(\tau))} \frac{d}{d\tau} (g_2 \sigma_j) d\tau \quad (5.11)$$

and, by the use of the basic properties of logarithms, the first integral of the right hand side can be as follows:

$$\int_0^{t-\Delta t} e^{-\lambda_p (\psi(t) - \psi(\tau))} \frac{d}{d\tau} (g_2 \sigma_j) d\tau = e^{-\lambda_p \Delta \psi(t)} \theta_j^p(t - \Delta t), \quad (5.12)$$

where

$$\theta_j^p(t - \Delta t) = \int_0^{t-\Delta t} e^{-\lambda_p (\psi(t) - \Delta \psi(t) - \psi(\tau))} \frac{d}{d\tau} (g_2 \sigma_j) d\tau. \quad (5.13)$$

Here according to the definition of ψ in Eq (5.3), $\psi(t - \Delta t) = \psi(t) - \Delta \psi(t)$ and

$$\Delta \psi(t) = \int_{t-\Delta t}^t \frac{d\tau'}{\left(\frac{t_\varepsilon + \tau'}{t_\varepsilon} \right)^\alpha a_\sigma(\tau')}. \quad (5.14)$$

The second integral of the right hand side of Eq (5.11) can approximately be integrated by assuming that $g_2 \sigma_j(\tau)$ varies linearly over the time step $(t - \Delta t, t)$, for small Δt

$$\begin{aligned} \int_{t-\Delta t}^t e^{-\lambda_p (\psi(t) - \psi(\tau))} \frac{d}{d\tau} (g_2 \sigma_j) d\tau &= \int_{\psi(t-\Delta t)}^{\psi(t)} e^{-\lambda_p (\psi(t) - \psi(\tau))} \frac{d}{d\psi} (g_2 \sigma_j) d\psi = \\ &= \frac{\Delta(g_2 \sigma_j(t))}{\lambda_p \Delta \psi(t)} \left[e^{-\lambda_p (\psi(t) - \psi(\tau))} \right]_{t-\Delta t}^t = \frac{\Delta(g_2 \sigma_j(t))}{\lambda_p \Delta \psi(t)} \left[1 - e^{-\lambda_p \Delta \psi(t)} \right] \end{aligned} \quad (5.15)$$

Therefore, by introducing

$$\Gamma \Lambda_p(t) = \frac{1 - e^{-\lambda_p \Delta \Psi(t)}}{\lambda_p \Delta \Psi(t)}, \quad (5.16)$$

and

$$\theta_j^p(t) = \int_0^t e^{-\lambda_p(\Psi(t) - \Psi(\tau))} \frac{d}{d\tau} (g_2 \sigma_j) d\tau, \quad (5.17)$$

following relation is found by considering Eq (5.11), Eq (5.12) and Eq (5.15),

$$\theta_j^p(t) = e^{-\lambda_p \Delta \Psi(t)} \theta_j^p(t - \Delta t) + \Delta (g_2 \sigma_j(t)) \Lambda_p(t), \quad (5.18)$$

where $\Delta (g_2 \sigma_j(t)) = g_2(\Sigma(t)) \sigma_j(t) - g_2(\Sigma(t - \Delta t)) \sigma_j(t - \Delta t)$ and the effective stress Σ is

$$\Sigma = \sqrt{I_1^2 - 3I_2} = \frac{1}{\sqrt{2}} \sqrt{(\sigma_1 - \sigma_2)^2 + (\sigma_2 - \sigma_3)^2 + (\sigma_3 - \sigma_1)^2 + 6(\sigma_4^2 + \sigma_5^2 + \sigma_6^2)}. \quad (5.19)$$

Here I_1 and I_2 are the first and the second stress invariants.

Eq (5.9) can now be written as

$$\begin{aligned} \epsilon_i &= g_0 J_0 S_{ij} \sigma_j + S_{ij}^c g_1 (g_2 \sigma_j - g_2^0 \sigma_j^0) \sum_p J_p \\ &\quad - S_{ij}^c g_1 \sum_p J_p \{ e^{-\lambda_p \Delta \Psi(t)} \theta_j^p(t - \Delta t) + \Delta (g_2 \sigma_j(t)) \Lambda_p(t) \} \\ &= \{ g_0 J_0 S_{ij} + g_1 S_{ij}^c \sum_p J_p (1 - \Lambda_p) \} \sigma_j(t) \\ &\quad + g_1 S_{ij}^c \sum_p J_p \{ (g_2 \sigma_j) |_{t=t-\Delta t} \Lambda_p(t) - (g_2 \sigma_j) |_{t=0} \} - e^{-\lambda_p \Delta \Psi(t)} \theta_j^p(t - \Delta t) \} \end{aligned} \quad (5.20)$$

Introducing

$$J_{ij}(t) = g_0 J_0 S_{ij} + g_1 S_{ij}^c \sum_p J_p (1 - \Lambda_p), \quad (5.21)$$

and

$$E_i(t) = g_1 S_{ij}^c \sum_p J_p \{ g_2(t - \Delta t) \sigma_j(t - \Delta t) \Lambda_p(t) - g_2(0) \sigma_j(0) - e^{-\lambda_p \Delta \Psi(t)} \theta_j^p(t - \Delta t) \}. \quad (5.22)$$

Eq (5.20) becomes

$$\epsilon_i(t) = J_{ij}(t) \sigma_j(t) + E_i(t), \quad (5.23)$$

or

$$\sigma_i(t) = J_{ij}^{-1}(t) \epsilon_j(t) - J_{ij}^{-1}(t) E_j(t). \quad (5.24)$$

5.2.3 The Procedure of Stress Evaluation in DIANA

The nonlinear viscoelastic model has been implemented in the nonlinear internal force part of DIANA. The subroutine is named as SCHPRY.F, and is meant to calculate new stresses at an integration point by using the data of the previous time step and the previous iteration. It contains the following parts:

1. basic data input:

$^{k-1}\sigma_i(t)$, $\sigma_i(t-\Delta t)$, $\sigma_i(0)$, $\theta_i^p(t-\Delta t)$, $\Sigma(t-\Delta t)$ and $\Sigma(t-2\Delta t)$; k denotes iteration

2. evaluate S_{ij} and S_{ij}^c , Eq (5.6) & Eq (5.7)

3. evaluate $^k\Sigma(t)$, Eq (5.19), and nonlinear parameters $^k g_i(t)$; g_0 , g_1 , g_2 and $g_3 = a_\sigma$ are listed, for the present case, in Table 5.1 on page 85 and Table 5.2 on page 85

4. evaluate $^k\Delta\psi(t)$, Eq (5.14)

5. evaluate $^k\Lambda_p(t)$, Eq (5.16), applying Simpson's rule by using four sub-domains

6. evaluate $^k J_{ij}(t)$, Eq (5.21); $^k E_i(t)$, Eq (5.22); and $^k \sigma_i(t)$, Eq (5.24)

7(a). (optional for faster convergence) back to step 4 only once, and define the new stresses: $^k \sigma_i(t) = 0.3 \ ^{k-1} \sigma_i(t) + 0.7 \ ^k \sigma_i(t)$

7. evaluate $\theta_i^p(t)$, Eq (5.18)

8. store the data: $^k \Sigma(t)$, $\Sigma(t-\Delta t)$ and $\theta_i^p(t)$

5.2.4 Tangential Stiffness Matrix

The total differential of the strains is derived in Appendix 1. It can be simply written as

$$d\epsilon_i = D_{ij}^{-1} d\sigma_j - \left(D_{ij}^{-1} C_j \right) dt, \quad (5.25)$$

where D_{ij} is the tangential stiffness matrix

$$D_{ij}^{-1} = T_1 + T_2 + T_3 + T_4 \quad (5.26)$$

$$T_1 = g_0 J_0 S_{ij} + \frac{S_{ij}^c g_1 dt}{\left(\frac{t_\sigma + t}{t_\sigma} \right)^\alpha a_\sigma(t)} g_2 \left(\sum_p J_p \Lambda_p \Gamma_p(t) \right) \quad (5.27)$$

$$T_2 = J_0 S_{ik} \sigma_k \frac{\partial g_0}{\partial \sigma_j} \quad (5.28)$$

$$T_3 = S_{ik}^c \left[\left(g_2 \sigma_k - g_2^0 \sigma_k^0 \right) \sum_p J_p - \sum_p J_p \theta_k^p \right] \frac{\partial g_1}{\partial \sigma_j} \quad (5.29)$$

$$T_4 = \frac{S_{ij}^c g_1 dt}{\left(\frac{t_e + t}{t_e}\right)^\alpha a_\sigma(t)} \sigma_j \left(\sum_p J_p \lambda_p \Gamma_p(t) \right) \frac{\partial g_2}{\partial \sigma_j} \quad (5.30)$$

and

$$D_{ij}^{-1} C_j = \frac{S_{ij}^c g_1}{\left(\frac{t_e + t}{t_e}\right)^\alpha a_\sigma(t)} \sum_p J_p \lambda_p e^{-\lambda_p d\Psi(t)} \theta_j^p(t - dt) dt \quad (5.31)$$

where

$$\frac{\partial g_0}{\partial \sigma_i} = \left(\frac{dg_0}{d\Sigma} \right) \frac{\partial \Sigma}{\partial \sigma_i}, \quad (5.32)$$

$$\frac{\partial g_1}{\partial \sigma_i} = \left(\frac{dg_1}{d\Sigma} \right) \frac{\partial \Sigma}{\partial \sigma_i}, \quad (5.33)$$

$$\frac{\partial g_2}{\partial \sigma_i} = \left(\frac{dg_2}{d\Sigma} \right) \frac{\partial \Sigma}{\partial \sigma_i}. \quad (5.34)$$

and

$$\frac{\partial \Sigma}{\partial \sigma_i} = \begin{cases} \frac{3\left(\sigma_i - \frac{1}{3}I_1\right)}{2\Sigma}, & normal \\ \frac{3\sigma_i}{\Sigma}, & shear \end{cases} \quad (5.35)$$

$dg_0/d\Sigma$, $dg_1/d\Sigma$ and $dg_2/d\Sigma$ are input data.

During the numerical tests, it was found that some economization of the computing time usage can be performed by letting $D_{ij}^{-1} = T_1$ combined with the computing step 7(a) in the stress evaluation (Section 5.2.3 on page 82). Some comparisons have been made in Section 5.3. This method will be referred to as *the improved method*. It can remarkably reduce the number of iterations and the computing time. *The original method* is a method without step 7(a) in the stress evaluation and with all four terms in Eq (5.26).

5.3 Numerical Testing

Among other methods, the Newton-Raphson method is used in DIANA, for the iterative process of solving the nonlinear equations. The convergence is then controlled by setting a relative criterion for the norm of the "out-of-balance force" term of the Newton-Raphson equation. When during iteration,

the norm of the "out-of-balance force" vector decreases until it becomes less than 0.01% of the first calculated norm value (before iterations), the calculation is considered as convergent for this loading or time step. The calculation then continues, with a next loading step.

The numerical tests were carried out under two uniaxial loading situations and one pure shear loading situation (in Section 5.3.2). The solution obtained by a direct numerical integration of the uniaxial model provides the *accurate* result for comparison. The results from DIANA are always related to the use of the *improved method* mentioned above except when particularly specified.

5.3.1 Accurate Result from the Theory

The *accurate results* are based on a numerical integration of the uniaxial model. This uniaxial model has been completely established through an experimental procedure of model parameter determination (see Chapter 3). This uniaxial model has the following simple representation, (from Eq (2.55) combined with the aging effect, Eq (5.3) and Eq (5.4))

$$\epsilon_1 = g_0 J_0 \sigma_1 + C \int_0^t \{ \exp[(\psi - \psi')^n] - 1 \} \frac{d}{d\tau} (g_2 \sigma_1) d\tau \quad (5.36)$$

where

$$\left\{ \begin{array}{l} \psi = \psi(t) = \int_0^t \frac{d\tau'}{\left(\frac{t_e + \tau'}{t_e} \right)^\alpha} \\ \psi = \psi(\tau) = \int_0^\tau \frac{d\tau'}{\left(\frac{t_e + \tau'}{t_e} \right)^\alpha} \end{array} \right. \quad (5.37)$$

$$\left\{ \begin{array}{l} J_0 = 2.0 \times 10^{-10} \\ C = 1.727 \times 10^{-11} \\ n = 0.065 \\ t_e = 7 \text{ month} = 1.8 \times 10^7 \\ \alpha = 0.45 \end{array} \right. \quad (5.38)$$

$$g_0 = \begin{cases} 1.0 & \Sigma \leq 4.9 \times 10^6 \text{ MPa} \\ 0.5 \Sigma^{0.045} & \Sigma > 4.9 \times 10^6 \text{ MPa} \end{cases} \quad (5.39)$$

$$g_2 = \exp(2.0669 \times 10^{-14} \Sigma^{1.7678}) \quad (5.40)$$

$g_1 = a_\sigma = 1$, and the effective stress Σ is defined in Eq (5.19). These basic data have been determined in Chapter 3 and will be used for all the numerical tests. The numerical integration divides the time domain into more than 2^{10} sub-domains and hence provides us with a very accurate result. For every specific time, the integration in Eq (5.36) is calculated independently.

This model is simple to use for uniaxial analysis, especially, for creep deformation because then the integral can be calculated directly without numerical approximation. For other cases, e.g. the 3-D case, the computing is too complicated or even not possible. But the restriction is that the 3-D stress state situation and the relaxation process can not be solved by this method, therefore, the numerical testing here is restricted to the uniaxial stress-strain states in a creep situation.

5.3.2 FEM Test by DIANA

For the DIANA implementation, the model parameters are required in an alternative form. First, an initial elastic modulus is introduced:

$$E = \frac{1}{J_0} = 5.0 \times 10^9. \quad (5.41)$$

Next, the kernel function for the exponential creep law, according to Eq (2.9) and Eq (5.2), is replaced by an exponential series expansion:

$$C[\exp(t^n) - 1] = \sum_{p=1}^N J_p (1 - e^{-\lambda_p t}) \quad (5.42)$$

The number of terms of this series depends on the required accuracy and the time domain. Different series are used for different time domains. Fig. 5.1 shows the parameters J_p and λ_p for different time domains.

The nonlinear parameters g_0 and g_2 are given by two tables according to Eq (5.39) & Eq (5.40), see Table 5.1 and Table 5.2.

Table 5.1. g_0 vs. Σ

Σ (MPa)	0.0	4.9	10.0	15.0	20.0	30.0	50.0	70.0	100.0
g_0	1.0	1.0	1.03	1.051	1.065	1.084	1.110	1.126	1.145

Table 5.2. g_2 vs. Σ

Σ (MPa)	0.0	5.0	10.0	20.0	30.0	40.0
g_2	1.0	1.0106	1.0500	1.1800	1.4000	1.7600
Σ (MPa)	50.0	60.0	70.0	80.0	90.0	100.0
g_2	2.3200	3.2000	4.6100	6.9000	10.700	17.500

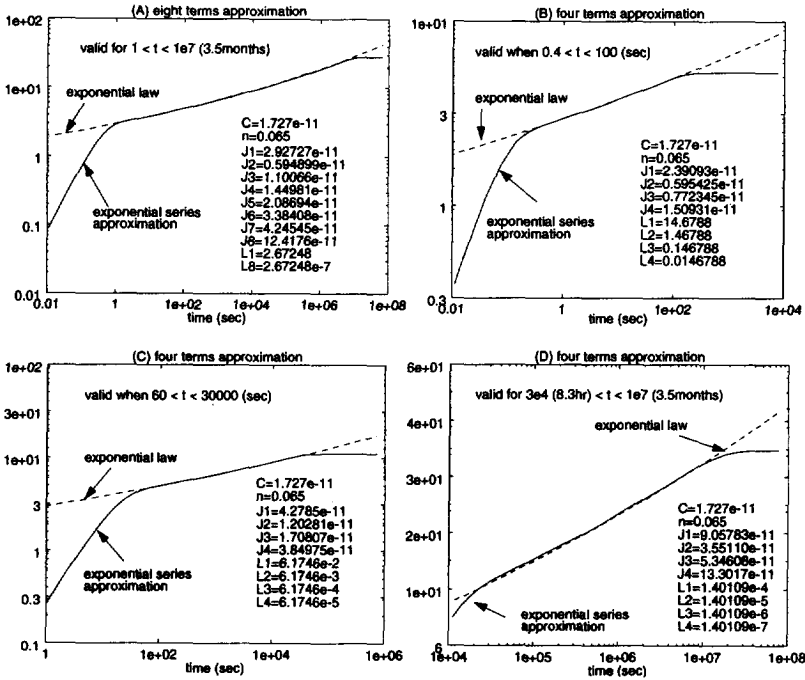


Figure 5.1. Exponential Series Approximation to the Kernel Function (A) Eight terms of the exponential series; (B)-(D) Four terms of the exponential series for different time domains

Case 1.Creep Test

Three different types of membrane elements (plane stress) are used for creep testing. The meshes being used are shown in Fig. 5.2.

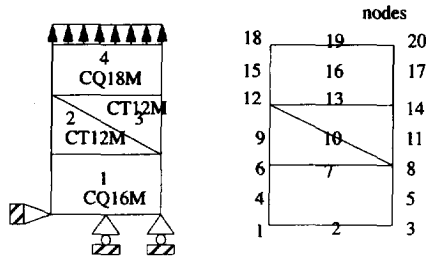


Figure 5.2. Elements and nodes

The data-file and command-file are given in Zhang (1993d^[51], Appendix). Under a creep loading situation, Eq (5.36) becomes (*i.e.* Eq (2.34))

$$\varepsilon_1 = g_0 \int_0^{\sigma_1} + g_2 C [\exp(t^n) - 1] \sigma_1 \quad (5.43)$$

In this test, a creep stress of 40 MPa was chosen. Using the parameters given in Eq (5.38) ~ Eq (5.40), the exact strain data can be easily expressed by the formula

$$\varepsilon_1 = 8.793 \times 10^{-3} + 1.2189 \times 10^{-3} [\exp(t^{0.065}) - 1] \quad (5.44)$$

The comparison between the DIANA calculation and the "exact results" is shown in Table 5.3.

Table 5.3. Creep Test

creep time (sec)	exact strain	DIANA results				
		$\Delta t=5$ sec N=4 Fig. 5.1(B)	$\Delta t=10$ sec N=4 Fig. 5.1(B)	$\Delta t=50$ sec N=4 Fig. 5.1(B)	$\Delta t=100$ sec N=4 Fig. 5.1(A)	$\Delta t=1000$ sec N=4 Fig. 5.1(A)
0.0	8.793e-3	8.776e-3	8.776e-3	8.776e-3	8.776e-3	8.776e-3
5.0	11.27e-3	11.06e-3				
10.0	11.47e-3	11.43e-3	11.23e-3			
15.0	11.59e-3	11.56e-3				
20.0	11.68e-3	11.65e-3	11.65e-3			
25.0	11.76e-3	11.72e-3				
30.0	11.82e-3	11.79e-3	11.79e-3			
35.0	11.87e-3	11.84e-3				
40.0	11.92e-3	11.89e-3	11.88e-3			
45.0	11.96e-3	11.93e-3				
50.0	12.00e-3	11.97e-3	11.97e-3	11.66e-3		
100	12.27e-3	12.24e-3	12.23e-3	12.22e-3	11.88e-3	
200	12.57e-3				12.52e-3	
500	13.02e-3				12.99e-3	
1000	13.41e-3				13.39e-3	12.70e-3
5000	14.52e-3				14.48e-3	14.46e-3
10000	15.09e-3				15.08e-3	15.07e-3
50000	16.77e-3					16.76e-3
100000	17.66e-3					17.66e-3

In Table 5.3, the series parameters of four terms were chosen based on Fig. 5.1(B) for the time increments $\Delta t = 5, 10$ and 50 sec. The parameters of eight terms (Fig. 5.1A) were used for the time increments $\Delta t = 100$ and 1000 sec. In Table 5.4, a comparison of creep strains for different numbers of terms in the series expansion is given. As can be seen in Table 5.4, the errors are always less than 3%

of the "exact results". These errors are mainly due to the quality of the series expansion approximation of the exponential law.

The conclusion that the time increment can be chosen as large as 10^6 seconds without introducing a large error in strain ($<3\%$) has been reached from these tests. It is found that even if a larger time step is chosen, mostly no extra iteration is needed for convergence. For both $\Delta t = 10^5$ and $\Delta t = 10^6$, the number of iterations is 8 (nominal force convergence criterium); but using the *original method* (Section 5.2.3 on page 82) the numbers of iteration are 20 and 30 respectively. In the long-term creep calculation using the *improved method*, a large amount of computing time can be saved by using relatively large time increments.

The error at $t = 1.e7$ sec. (Table 5.4) shows that the accuracy of the series expansion approximation of the kernel function plays a major role in the accuracy of the long-term creep modelling. Smaller time increments and more terms of the series will not always be necessary for a more accurate simulation in DIANA in this case. Table 5.5 shows two very large time-step cases.

Table 5.4. A comparison between the numbers of terms of the series

creep time (sec)	accurate strain	DIANA results $\Delta t = 1.0e5$ sec		DIANA results $\Delta t = 1.0e6$ sec		DIANA results $\Delta t = 1.e5$ & $1.e6$ sec	
		N=8 Fig. 5.1(A)	N=4 Fig. 5.1(D)	N=8 Fig. 5.1(A)	N=4 Fig. 5.1(D)	N=8 Fig. 5.1(A)	N=4 Fig. 5.1(D)
0.0	8.793e-3	8.776e-3	8.776e-3	8.776e-3	8.776e-3	8.776e-3	8.776e-3
1.e5	17.66e-3	17.67e-3	17.66e-3			17.64e-3	17.64e-3
1.e6	21.77e-3	21.74e-3	21.71e-3	21.74e-3	21.42e-3	21.74e-3	21.71e-3
2.e6	23.47e-3	23.50e-3	23.48e-3	23.50e-3	23.42e-3	23.50e-3	23.47e-3
3.e6	24.59e-3	24.71e-3	24.57e-3	24.71e-3	24.55e-3	24.71e-3	24.57e-3
4.e6	25.46e-3	25.63e-3	25.42e-3	25.63e-3	25.40e-3	25.63e-3	25.42e-3
5.e6	26.18e-3	26.34e-3	26.13e-3	26.34e-3	26.12e-3	26.34e-3	26.13e-3
6.e6	26.79e-3	26.88e-3	26.74e-3	26.88e-3	26.73e-3	26.88e-3	26.74e-3
7.e6	27.33e-3	27.29e-3	27.27e-3	27.29e-3	27.26e-3	27.29e-3	27.27e-3
8.e6	27.82e-3	27.60e-3	27.73e-3	27.61e-3	27.72e-3	27.60e-3	27.73e-3
9.e6	28.26e-3	27.85e-3	28.13e-3	27.85e-3	28.12e-3	27.85e-3	28.13e-3
1.e7	28.67e-3	28.03e-3	28.48e-3	28.03e-3	28.47e-3	28.03e-3	28.48e-3

Table 5.5. 8 terms series expansion for the kernel, EP is the accuracy criterion

creep time (sec)	strains from DIANA analysis (N=8)			
	EP = 1.e-4 $\Delta t = 5.e6$	EP = 1.e-2 $\Delta t = 5.e6$	EP = 1.e-4 $\Delta t = 1.e7$	EP = 1.e-2 $\Delta t = 1.e7$
0.0	8.776e-3 (5)	8.776e-3 (5)	8.776e-3 (5)	8.776e-3 (5)
5.e6	26.34e-3 (8) (>50)*	26.26e-3 (5) (41)*		
1.e7	28.03e-3 (7) (>50)*	28.02e-3 (4) (32)*	28.03e-3 (8)	28.02e-3 (6) (47)*

- the numbers in parentheses indicate the iteration numbers, with asterisks refer to the *original method*

The iteration numbers are indicated within parentheses, the parentheses with asterisks refer to the original method (Section 5.2.3 on page 82).

case 2. Uniaxial Cyclic Tensile Loading

The 'accurate results' were based on the numerical integration method as mentioned in Section 5.3.1. A comparison is presented in Table 5.6 for a single-cycle loading case. The parentheses with asterisks in Table 5.6 refer to the *original method* (Section 5.2.3 on page 82). Table 5.7 shows two results of different time increments. It is found that the accuracy is quite good even though the time step is large.

Table 5.8 gives a check on convergent speed. Here a higher stress, 80 MPa, is reached in one-cycle loading situation. Larger time increments will lead to more iterations and even divergence for higher stress levels. The idealized tensile strength of polyester (DMS Resins Synolite 593-A-2) is 87 MPa. The lower convergent speed for higher stress levels is due to the strong nonlinearity of the material.

Table 5.6. Tensile loading, stress rate: 5 MPa/sec, $\Delta t = 1$ sec.

time (sec)	stress (MPa)	strain accurate	strain DIANA (N=8)	iteration number	error %
0	0.0	0.0	0.0		
1	5.0	1.1376e-3	1.131e-3	4 (5)*	0.580
2	10	2.3680e-3	2.357e-3	5 (7)*	0.465
3	15	3.6514e-3	3.647e-3	5 (8)*	0.121
4	20	4.9868e-3	4.978e-3	5 (8)*	0.176
5	25	6.3809e-3	6.369e-3	6 (9)*	0.186
6	30	7.8455e-3	7.824e-3	6 (9)*	0.274
7	35	9.3988e-3	9.381e-3	7 (7)*	0.189
8	40	11.063e-3	11.02e-3	7 (9)*	0.389
9	45	12.870e-3	12.87e-3	8 (14)*	0.0
10	50	14.864e-3	14.84e-3	9 (14)*	0.161
11	45	13.212e-3	13.26e-3	6 (15)*	0.363
12	40	11.535e-3	11.53e-3	7 (15)*	0.043
13	35	9.9321e-3	9.938e-3	6 (11)*	0.059
14	30	8.4028e-3	8.401e-3	6 (9)*	0.021
15	25	6.9396e-3	6.948e-3	5 (7)*	0.121
16	20	5.5319e-3	5.547e-3	5 (8)*	0.289
17	15	4.1753e-3	4.197e-3	5 (7)*	0.520
18	10	2.8635e-3	2.881e-3	5 (7)*	0.611
19	5.0	1.5968e-3	1.619e-3	4 (6)*	1.390
20	0.0	0.4050e-3	0.4277e-3	4 (4)*	5.605

Table 5.7. Single-cycle loading with 5 MPa/sec, the same as in Table 5.6

time (sec)	stress (MPa)	strain accurate	strain results (DIANA) (N=8)			
			$\Delta t = 5$ sec	iteration	$\Delta t = 10$ sec	iteration
5	25	6.3809e-3	6.389e-3	6		
10	50	14.864e-3	14.92e-3	9	15.05e-3	10
15	25	6.9396e-3	7.045e-3	7		
20	0	0.4050e-3	0.4810e-3	4	0.6497e-3	11

Table 5.8. The convergent speed and the stress level, stress rate = 5 MPa/sec

time (sec)	stress (MPa)	analytical strains	strains from DIANA	
			$\Delta t = 2.0$ sec	
2	10	2.368e-3	2.358e-3 (5)	
4	20	4.987e-3	4.980e-3 (5)	
6	30	7.846e-3	7.827e-3 (6)	
8	40	11.06e-3	11.03e-3 (7)	
10	50	14.86e-3	14.85e-3 (9)	
12	60	19.67e-3	19.64e-3 (10)	
14	70	26.25e-3	26.22e-3 (>30)	
16	80	36.05e-3	divergent	
	since 70		$\Delta t = 0.2$ sec	$\Delta t = 0.4$ sec
14.2	71	27.05e-3	27.03e-3 (16)	
14.4	72	27.88e-3	27.93e-3 (21)	27.94e-3 (21)
14.6	73	28.75e-3	28.86e-3 (21)	
14.8	74	29.66e-3	29.80e-3 (21)	29.81e-3 (>30)
15.0	75	30.61e-3	30.77e-3 (21)	
15.2	76	31.60e-3	31.76e-3 (21)	31.76e-3 (27)
15.4	77	32.64e-3	32.77e-3 (21)	
15.6	78	33.72e-3	33.80e-3 (11)	33.80e-3 (27)
15.8	79	34.86e-3	34.85e-3 (21)	
16.0	80	36.05e-3	divergent	divergent
	since 79.00		$\Delta t = 0.05$ sec	
15.85	79.25	35.15e-3	35.11e-3 (7)	
15.90	79.50	35.45e-3	35.38e-3 (8)	
15.95	79.75	35.75e-3	35.65e-3 (8)	
16.00	80.00	36.05e-3	35.92e-3 (10)	
16.05	79.75	35.94e-3	35.98e-3 (7)	unloading period
16.10	79.50	35.77e-3	35.92e-3 (6)	
16.15	79.25	35.59e-3	35.81e-3 (8)	
16.20	79.00	35.42e-3	35.67e-3 (8)	

The numbers within parentheses in Table 5.8 indicate the iterations required in the calculation. The iteration number increases with the increase of the stress level, but it can be reduced if a smaller time step is chosen.

Table 5.9 shows a two-cycle loading case. The total error was found mostly less than 0.5% when the stress is close to zero. In Table 5.9, after the first cycle and after the second cycle, the errors in the strain are 3.5% and 4.2% respectively (compared to the accurate results). In Table 5.9, larger errors have also been found in the lower loading level situations, about 1% when $\sigma = 5$ MPa and 5.6% when $\sigma = 0$. The parentheses with asterisks in all the tables refer to the *original method* (Section 5.2.3 on page 82).

Table 5.9. Two cycles, stress rate: 5 MPa/sec, $\Delta t = 1$ sec.

time (sec)	stress (MPa)	accurate strain	DIANA strain	iteration number	error %
0	0.0	0.0	0.0		
1	5.0	1.1376e-3	1.131e-3	4 (5)*	0.580
2	10	2.368e-3	2.357e-3	5 (7)*	0.465
3	15	3.651e-3	3.647e-3	5 (8)*	0.120
4	20	4.987e-3	4.978e-3	5 (8)*	0.180
5	25	6.381e-3	6.369e-3	6 (9)*	0.188
6	30	7.846e-3	7.824e-3	6 (9)*	0.280
7	25	6.519e-3	6.526e-3	5 (9)*	0.107
8	20	5.179e-3	5.182e-3	5 (8)*	0.058
9	15	3.867e-3	3.871e-3	5 (7)*	0.103
10	10	2.588e-3	2.586e-3	5 (7)*	0.077
11	5.0	1.347e-3	1.351e-3	3 (6)*	0.297
12	0.0	0.1762e-3	0.1823e-3	3 (3)*	3.462
13	5.0	1.277e-3	1.273e-3	4 (5)*	0.313
14	10	2.488e-3	2.482e-3	5 (7)*	0.241
15	15	3.758e-3	3.760e-3	5 (8)*	0.053
16	20	5.083e-3	5.080e-3	5 (8)*	0.059
17	25	6.469e-3	6.463e-3	6 (9)*	0.093
18	30	7.927e-3	7.909e-3	6 (9)*	0.227
19	35	9.474e-3	9.495e-3	7 (7)*	0.222
20	40	11.13e-3	11.10e-3	7 (10)*	0.270
21	35	9.677e-3	9.660e-3	6 (11)*	0.176
22	30	8.206e-3	8.207e-3	6 (10)*	0.012
23	25	6.778e-3	6.780e-3	5 (7)*	0.030
24	20	5.396e-3	5.399e-3	5 (9)*	0.056
25	15	4.057e-3	4.065e-3	5 (7)*	0.197
26	10	2.795e-3	2.763e-3	5 (7)*	1.145
27	5.0	1.502e-3	1.513e-3	4 (6)*	0.732
28	0.0	0.3184e-3	0.3319e-3	3 (3)*	4.240

case 3. Shear Cyclic Loading

In this case, a single element was used for testing. Fig. 5.3 shows the element and the loading condition.

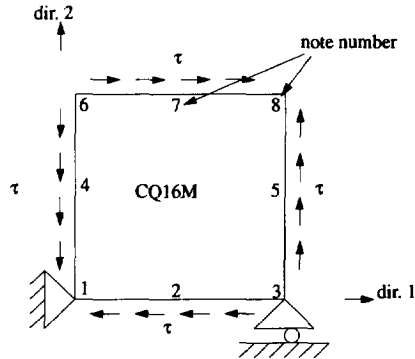


Figure 5.3. Element and loading for shear test

Table 5.10 shows the results of the shear test.

Table 5.10. Shear test, $\Delta t = 1 \text{ sec}$

shear stress τ (MPa)	accurate result Eq (5.36)	accurate result (N=4)	DIANA results (N=4)	iteration number	iteration number*
5	1.584e-3	1.575e-3	1.573e-3	7	10*
10	3.312e-3	3.302e-3	3.318e-3	7	11*
15	5.146e-3	5.133e-3	5.184e-3	7	11*
20	7.111e-3	7.093e-3	7.223e-3	8	7*
25	9.263e-3	9.236e-3	9.526e-3	9	13*
30	11.696e-3	11.65e-3	12.24e-3	9	16*
25	9.564e-3	9.587e-3	9.980e-3	7	20*
20	7.491e-3	7.498e-3	7.724e-3	6	11*
15	5.543e-3	5.542e-3	5.671e-3	6	7*
10	3.697e-3	3.698e-3	3.775e-3	6	9*
5	1.939e-3	1.944e-3	1.991e-3	5	9*
0	0.2969e-3	0.3067e-3	0.3474e-3	4	5*

• numbers with an asterisks refer to the original method (see Section 5.2.3)

The approximation of the kernel with an exponential series expansion may produce some error which can be seen in the different results between column 2 and column 3 in Table 5.10. The error is usually

smaller than 2.5%, except an error of 13% when the stress is almost zero. The iteration number with asterisk refers to the original method.

case 4. Physical Aging

The influence of physical aging is tested in a case of creep deformation (same conditions as in Case 1). When the aging effect is taken into account, the creep formula Eq (5.44) becomes (for details see Chapter 3)

$$\epsilon_1 = g_0 A_0 \sigma_1 + g_2 C \sigma_1 \left\{ \exp \left(\frac{t_e}{1-\alpha} \left[\left(1 + \frac{t}{t_e} \right)^{1-\alpha} - 1 \right] \right)^n - 1 \right\} \quad (5.45)$$

$$\epsilon_1 = 8.793 \times 10^{-3} + 1.2189 \times 10^{-3} \left\{ \exp \left(\frac{1.8 \times 10^7}{0.55} \left[\left(1 + \frac{t}{1.8 \times 10^7} \right)^{0.55} - 1 \right] \right)^{0.065} - 1 \right\} \quad (5.46)$$

Eq (5.46) is based on the seven months old material. In order to consider the aging effects to be reasonably pronounced, a long-term creep case must be considered. Hence a three years creep was chosen. An exponential series expansion covering a time domain from 10^6 to 10^8 seconds is used (Fig. 5.4A). The creep results both with and without the physical aging effect are listed in Table 5.11. Fig. 5.4(B) shows the difference between the curves with and without the aging effect. The DIANA

Table 5.11. Aging Effect on Long-Term Creep Elongation (initial aging $t_e = 1.8e7$ sec)

creep time (sec)	without physical aging effect			with physical aging effect		
	accurate strain	DIANA (N=6) $\Delta t = 5e6$	DIANA (N=6) $\Delta t = 2e7$	accurate strain	DIANA (N=6) $\Delta t = 5e6$	DIANA (N=6) $\Delta t = 2e7$
0	8.793e-3	8.776e-3 (5)	8.776e-3 (5)	8.793e-3	8.776e-3 (5)	8.776e-3 (5)
1e7	28.67e-3	28.66e-3 (6)		28.26e-3	28.24e-3 (9)	
2e7	31.63e-3	31.55e-3 (7)	31.54e-3 (9)	30.79e-3	30.74e-3 (7)	30.69e-3 (9)
3e7	33.62e-3	33.49e-3 (7)		32.38e-3	32.26e-3 (7)	
4e7	35.17e-3	35.06e-3 (7)	35.06e-3 (7)	33.55e-3	33.41e-3 (7)	33.36e-3 (7)
5e7	36.46e-3	36.40e-3 (7)		34.48e-3	34.34e-3 (8)	
6e7	37.57e-3	37.54e-3 (8)	37.54e-3 (8)	35.26e-3	35.14e-3 (7)	35.10e-3 (7)
7e7	38.56e-3	38.52e-3 (10)		35.92e-3	35.83e-3 (8)	
8e7	39.44e-3	39.38e-3 (11)	39.38e-3 (8)	36.51e-3	36.44e-3 (8)	36.40e-3 (8)
9e7	40.25e-3	40.13e-3 (12)		37.03e-3	36.98e-3 (8)	
1e8	41.00e-3	40.79e-3 (12)	40.79e-3 (8)	37.50e-3	37.46e-3 (11)	37.43e-3 (8)

input data-file for this case can be found in Zhang (1993d^[51], Appendix). Again the iteration number in Table 5.11 suggests that applying a large time increment can reduce the computing time enormously. If the aging effect is taken into account, the accuracy tends to become poor for a larger time increment. This can be observed by comparing the last two columns in Table 5.11.

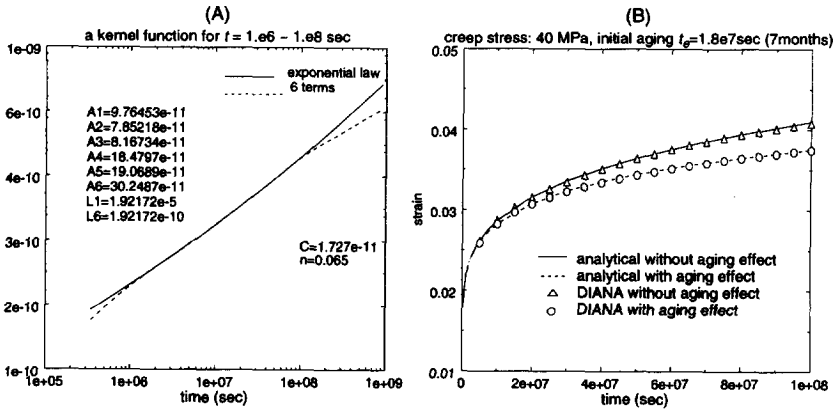


Figure 5.4. Physical aging influence on creep (A) Six terms of exponential series; (B) Long-Term Creep

5.4 Conclusions

1. The implementation of the nonlinear viscoelastic constitutive relation in DIANA is successful for creep loading. For a long period of creep as well as for a cyclic loading situation in a short period of time, the DIANA simulation has sufficient accuracy;
2. For static loading situations, the time increment can be chosen larger than 10^7 seconds without having to increase the number of iterations for the same accuracy;
3. For cyclic loading situations with relatively high stress levels, the convergent speed is sensitive to the time increment. Small time increments can reduce the number of iterations while large time increments require more iterations and may even lead to divergence;
4. The effect of physical aging on a long-term loading situation is taken into account by the effective-time theory (see Chapter 3). Its implementation in DIANA is simple and has been found to be adequate.

2D Stress States

6.1 Introduction

The intention of the work in this Chapter is to evaluate the 3D model as presented in Chapter 4 and Chapter 5. The parameters in this model were obtained from simple uniaxial creep tests.

In Chapter 3, the validity of the uniaxial model has been demonstrated by comparison with experiments for creep and for cyclic loading cases. Due to the difficulty of doing relaxation tests (a step deformation is obstructed by the brittleness of the material), the relaxation property was checked indirectly by cyclic loading tests.

The implementation of the theory into a finite element package in Chapter 5 facilitates the examination of the performance of the theory in a 3D stress state. However, in order to reduce the complexity of the experiments, some tests of two-dimensional stress states have been carried out. In this chapter, the results from the tests of a plate with a circular hole and of biaxial tests on polyester tubes will be shown. The tests, for a plate with a hole, can be done under a simple tensile loading. But, around the hole, there exists a two-dimensional stress field which results into a more complicated stress-strain response than in the uniaxial case. Both creep and relaxation occur in this case. The biaxial tests can produce a relatively higher effective stress compared to the applied normal stress. A relatively higher effective stress will lead to a highly nonlinear stress-strain response, which may challenge the accuracy of the nonlinear theory.

The comparison between the experiment and the theory showed an excellent agreement. This gave confidence for the application of the model to more complicated cases, such as in composite micro-mechanical analysis (Chapter 7).

6.2 A Plate with a Circular Hole

6.2.1 Experimental

The size of the specimen is shown in Fig. 6.1. Two kinds of tests have been carried out with two different series of measuring points (see Fig. 6.2). The loading direction corresponds to the y-axis.

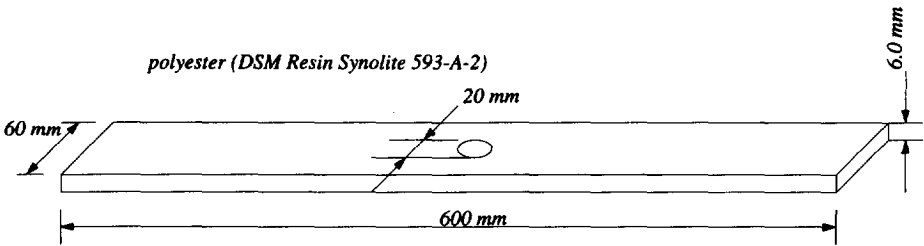


Figure 6.1. Specimen

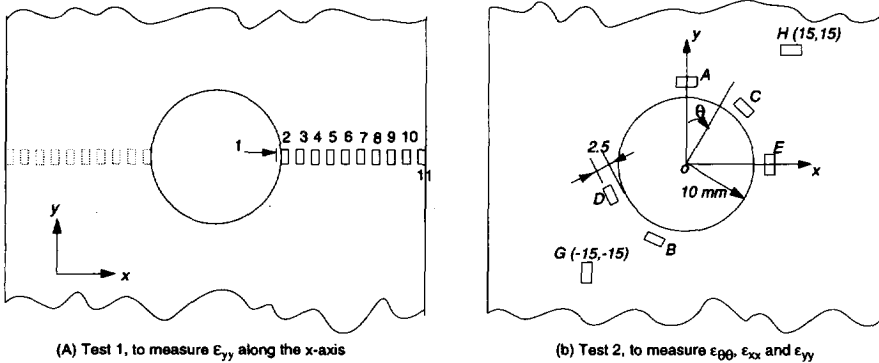


Figure 6.2. Test 1. and Test 2 for different strain measurements (positions and directions)

In test 1, only ϵ_{yy} along the x-axis was measured and the strain gauges were placed on both surfaces of the plate, symmetrically about the centre of the hole. Gauge no. 1 (see Fig. 6.2) was placed on the inner side of the hole. The averaged strain data of symmetry positions were recorded by a PC in order to eliminate the possible bending influence from the clamping system of the test machine. In test 2, the strain gauges were placed along the edge of the hole with a distance of 2.5 mm to the hole. Only the strains in the circumferential direction were measured. There are two gauges, *G* and *H* in Fig. 6.2, measuring the strains in x-direction, ϵ_{xx} , and y-direction, ϵ_{yy} , respectively. At these places, a more general two-dimensional stress state exists.

The specimens were postcured at 60°C, 24 hours and 80°C, 24 hours successively. The physical aging times were recorded starting from the end of the postcuring, and listed in Table 6.4 for three different specimens. The details of the specimen preparation can be found in Toutenhoofd (1993)^[44].

6.2.2 Numerical Simulation

The numerical simulation was performed by means of the finite element package, DIANA, in which the constitutive relation was implemented as described in Chapter 5. The mesh creation and the post-processing were performed by means of the finite element package I-Deas.

1. Material Properties

The physical aging is only considered according to the age of the specimen. The ongoing aging effect is not considered for this short-term test. The material properties used for the simulation are listed in Table 6.1, Table 6.2 and Table 6.3.

$E \text{ (N/m}^2\text{)}$	ν	ν_c
5.0e9	0.353	0.417

Table 6.1. Material constants: tensile modulus (experimental data in Chapter 3), instantaneous Poisson's ratio (experimental data in Chapter 3) and creep Poisson's ratio (experimental data in Chapter 4)

eff. stress	0.0	4.9e6	1.0e7	1.5e7	2.0e7	3.0e7	5.0e7	7.0e7	1.0e8
g_0	1.0	1.0	1.03	1.051	1.065	1.084	1.11	1.126	1.145

eff. stress	0.0	1.0e8
g_1	1.0	1.0

eff. stress	0.0	5.0e6	1.0e7	2.0e7	3.0e7	4.0e7	5.0e7	6.0e7	7.0e7	8.0e7	9.0e7	1.0e8
g_2	1.0	1.0106	1.05	1.18	1.40	1.76	2.32	3.20	4.61	6.90	10.7	17.5

eff. stress	0.0	1.0e8
a_σ	1.0	1.0

Table 6.2. Model nonlinear parameters (according to Eq (2.44) and Eq (2.45))

p	1	2	3	4	5	6	7	8
J_p	2.92727 e-11	.594899 e-11	1.10066 e-11	1.44981 e-11	2.08694 e-11	3.38408 e-11	4.24545 e-11	12.4176 e-11
λ_p	2.67248	2.67248 e-1	2.67248 e-2	2.67248 e-3	2.67248 e-4	2.67248 e-5	2.67248 e-6	2.67248 e-7

Table 6.3. Exponential-Law parameters (according to Eq (5.2))

2. Mesh and Boundary Conditions

One eighth of the specimen was chosen to be the calculation model and 318 solid elements were applied with a varied density from the edge of the hole to the end of the specimen (see Fig. 6.3).

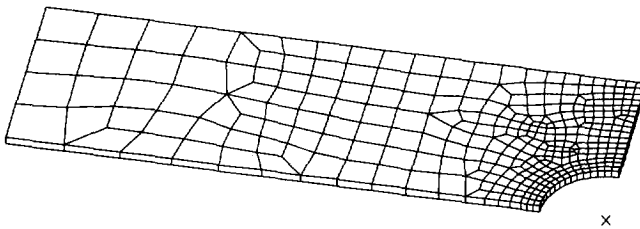


Figure 6.3. Mesh for FEM analysis (318 linear hexahedron elements)

The boundary conditions are shown in Fig. 6.4. The plate was supported on three surfaces. A tying for the axial displacement was subjected on the surface where the load was exerted.

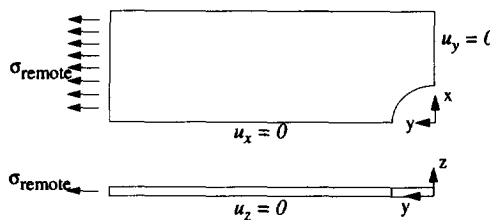


Figure 6.4. Boundary Conditions, u_x , u_y and u_z are the components of the displacement vector of the nodes

6.2.3 Results

The comparison between experiment and theory has been done for three cases, ϵ_{yy} along the x-axis, the hoop strain $\epsilon_{\theta\theta}$ along the edge of the hole and ϵ_{xx} and ϵ_{yy} at chosen points H (15, 15) and G (-15, -15) (see Fig. 6.2). The hoop strain along the edge was considered at an average distance of 2.5 mm from the edge. Therefore the measuring points A~E (see Fig. 6.2) are actually under a 2D stress state.

A model which was characterized by uniaxial creep tests is used here to predict a 2D stress state mechanical response. In this 2D stress state, both creep and relaxation occur, the Poisson's effect exists and stress coupling contributes to the nonlinear response. Stress coupling means that more stress components contribute to the nonlinear response in a general 3D stress state.

After the numerical discretisation, the model was employed for a 2D simulation by means of the DIANA package. Errors could originate from the extension of the uniaxial model to a 3D model, see Chapter 4, and could come from the numerical discretisation with the finite element method including the series expansion of the kernel function. However, a good agreement between experimental data and the theoretical calculation confirms that the 3D extension of the uniaxial model is accurate enough and the assumed effective stress dependent nonlinear model parameters are correct. Finally, the numerical discretisation procedure has also shown to be sufficiently accurate.

1. ϵ_{yy} along the X-Axis

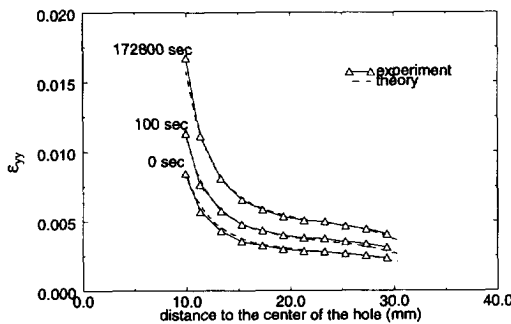


Figure 6.5. ϵ_{yy} along the x-axis (see Fig. 6.2). Remote creep stress: 11.667MPa, specimen no. 85 with an age of 111 days, temperature: $23 \pm 0.2^\circ\text{C}$

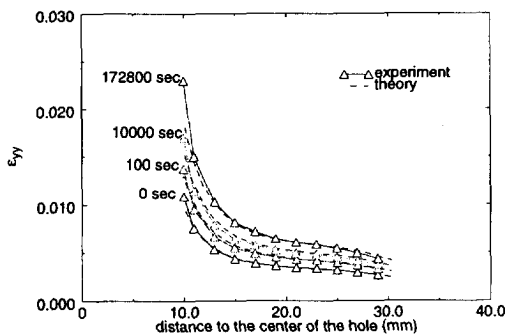


Figure 6.6. ϵ_{yy} along the x-axis (see Fig. 6.2). Remote creep stress: 13.333MPa, specimen no. 64 with an age of 111 days, temperature: $23 \pm 0.2^\circ\text{C}$

Fig. 6.5, Fig. 6.6 and Fig. 6.7 have generally demonstrated an excellent agreement between the experiment and the theory. A finer mesh has been used to check the accuracy of the numerical method. Fig. 6.7 demonstrates an excellent strain prediction even for a relatively high stress level ($\sigma_{yy} = 38\text{--}40\text{ MPa}$ at the edge of the hole, see Fig. 6.10(A)).

However, there is some difference at the edge of the hole. The strain gauge no. 1 has measured apparently larger strains than those of the calculation, if the remote stress is large (Fig. 6.6). The possible reasons are the following: the theory is not accurate enough for high stress levels. This has not been checked, even not in the uniaxial case, due to the difficulty of testing; the accuracy of the experimental results is limited due to the error introduced, *e.g.* by placing the strain gauges on to the specimen; the material difference between the tests here and the tests for model characterization.

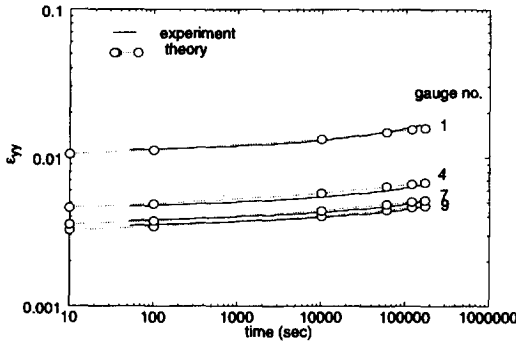


Figure 6.7. ϵ_{yy} on four measuring points (see Fig. 6.2), same case as in Fig. 6.5

2. Hoop Strain along the Edge of the Hole

The hoop strains being measured originate from positions with a distance of 2.5 mm from the edge of the hole.

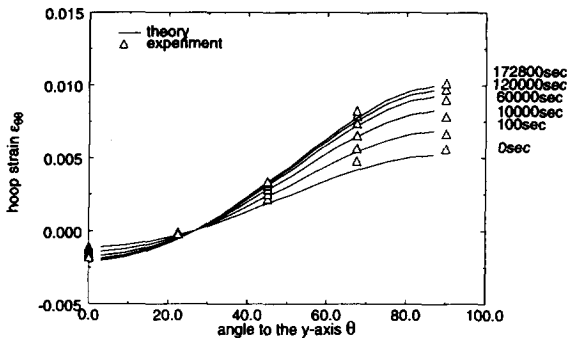


Figure 6.8. Hoop strains along the edge of the circular hole with a distance of 2.5 mm, specimen no. 93 with a month of age, remote constant stress: 11.667 MPa, room temperature $23 \pm 0.2^\circ\text{C}$.

Generally, the comparison of hoop strains is satisfactory.

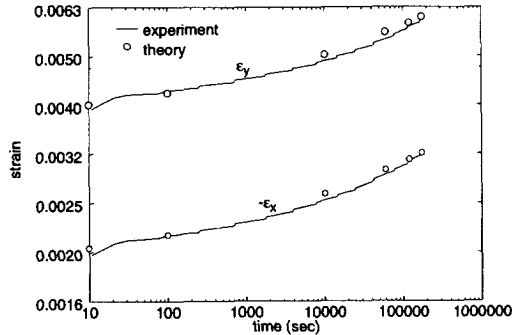


Figure 6.9. Strains at the location (15mm, 15mm). The test data represent the mean values from the points G and H (see Fig. 6.2). The same specimen and the test conditions as in Fig. 6.8.

Fig. 6.9 shows the strains for a 2D stress state case. At the point (15, 15) (see Fig. 6.2(B), G and H), the stress state is slightly changing with time. When $t = 0$, the stress state in this point is given by: $\sigma_{xx} = -2.52$ MPa, $\sigma_{yy} = 14.41$ MPa, $\sigma_{xy} = -1.09$ MPa. The agreement of strains between experiment and theory can be observed from the figure.

3. Stress Distribution

Redistribution of the normal stress σ_{yy} as calculated with the theory, can be found in Fig. 6.10 and Fig. 6.11. Some stress and strain fields are presented in Fig. 6.12 and Fig. 6.13. The maximum shear stress, which is related to the Tresca criterion of failure, is defined as half the difference of the maximum principal stress and the minimum principal stress.

The maximum stresses decreasing during the creep process suggest a relaxation of the stress concentration.

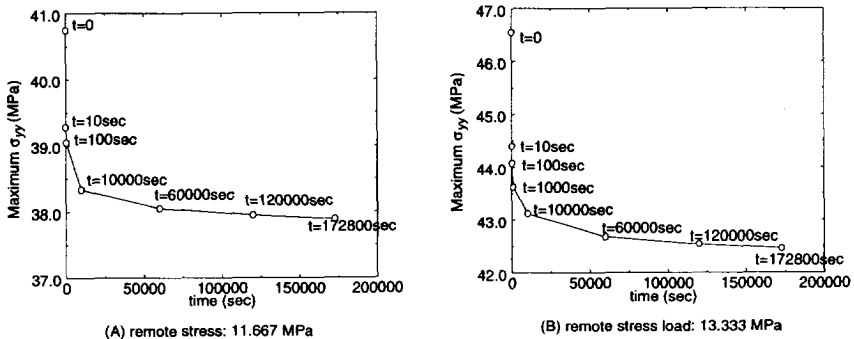


Figure 6.10. Calculated maximum σ_{yy} (on the edge of the hole) for two load cases

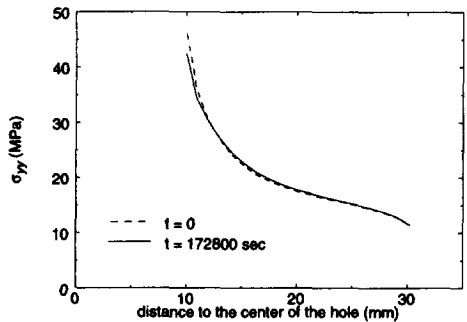


Figure 6.11. Calculated σ_{yy} redistribution along the x-axis, remote stress load: 13.333 MPa

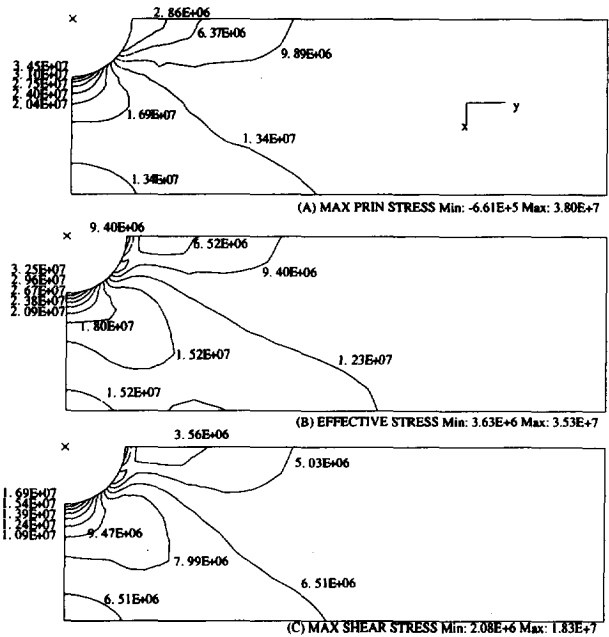


Figure 6.12. Calculated maximum principal stress, effective stress and maximum shear stress at $t = 0$, the same load conditions as in Fig. 6.8

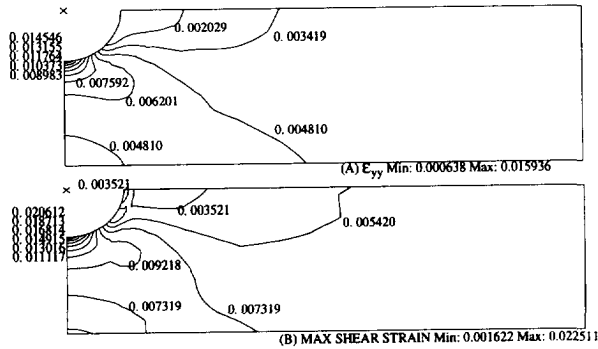


Figure 6.13. Calculated ϵ_{yy} and maximum shear strain at $t = 0$, the same load conditions as in Fig. 6.8

4. Aging Influence

The specimens had different aging times when the tests were performed. The model parameters originally have been determined (in Eq (2.43) and Eq (2.44)) for a 7 months old specimen, therefore, the basic theory is applicable for the material with a seven-month age. In the calculations for specimens with other ages, the aging time influence was taken into account according to the theory as presented in Section 4.3.

The shifting rate and the reference aging time are chosen as $\alpha = 0.45$ (see Section 3.5.2 on page 48) and $t_{er} = 7$ months. The shifting factor $a_\sigma a$ has been determined for the different aging times, and are listed in Table 6.4.

specimen	#9	#8	#6 & #8	
aging time t_e	30 days	55 days	111 days	7 months
$a_\sigma a$	0.4166	0.5472	0.7507	1.0

Table 6.4. Aging influence was considered in the model parameter a_σ

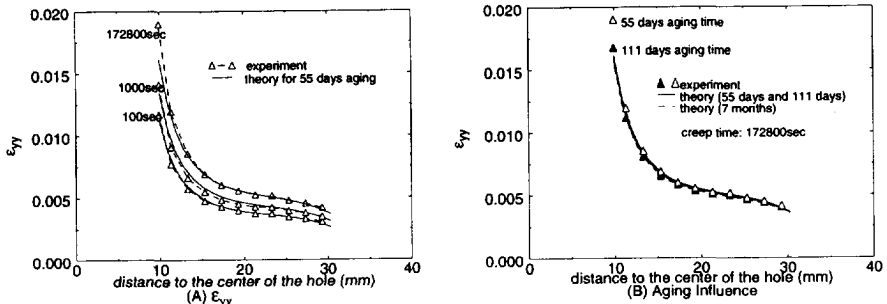


Figure 6.14. ϵ_{yy} from specimen #8 with 55 days aging time, remote stress: 11.667 MPa

According to the theory there is only a small difference in the deformation due to the initial aging time difference. But the experimental results show a slightly larger difference.

6.3 Polyester Tubes - Biaxial Loading

Another evaluation of the accuracy of the model in a 2D loading case is done by using a biaxial loading test. The stress coupling effect will play a role in the nonlinear response of the material in a tension and torsion loading situation. The purpose of this experimental work is to verify this role.

6.3.1 Experimental

Aging information of the specimen is given below. The test conditions are listed in Table 6.6. The geometry of the specimen is shown in Fig. 6.15. Manufacturing of these specimens is described in Ten Busschen (1995). Due to the possible unstable state in compression, only tensile loading has been applied in combination with torsion.

making date	Nov.9, 1989
postcuring date (60°C 24 hours, 80°C 24 hours)	Apr.13, 1993

Table 6.5. Specimen information

test condition	σ - σ & τ		τ - σ & τ		σ - τ		τ - σ		σ - σ & $\tau_1\tau_2$
test no.	2211	2212	2221	2222	2231	2232	2241	2242	2251
testing date	20/10/93	29/10/93	21/10/93	27/10/93	22/10/93	01/11/93	25/10/93	28/10/93	2/11/93
aging time	190 days	199 days	191 days	197 days	192 days	201 days	195 days	198 days	202 days

Table 6.6. Testing Conditions (σ - tension state, τ - torsion state)

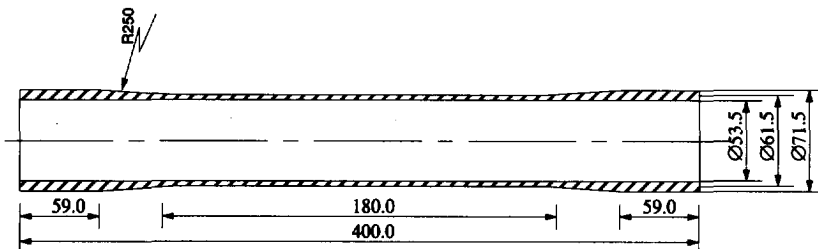


Figure 6.15. Specimen Geometry

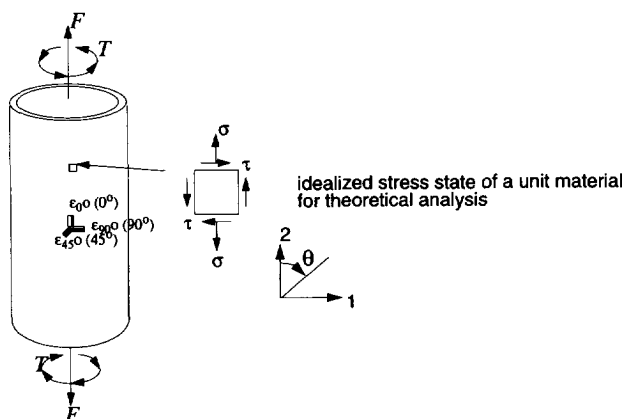


Figure 6.16. Loading, Measurement and Calculation

On the specimen, two metal ends were glued. These in turn were clamped in the testing machine. The torsion stress $\tau \approx T/A$ (thin shell assumption), tensile stress $\sigma = F/A$, where A is the cross-sectional area of the tube. Using this method of clamping, the load level to be applied is limited (Ten Busschen 1995). Two specimens were broken at the tube ends during testing.

In the experiments, the stress levels for tension and torsion were both chosen to be 10 MPa. The effective stress is then 20 MPa (see Eq (5.19)). Hence the material behaves under a moderate range of nonlinearity (see Fig. 2.11).

6.3.2 Numerical Model

The calculation was performed by using a single element (linear hexahedron element). This choice is based on a thin shell assumption. The calculated strains are ϵ_{11} , ϵ_{22} and ϵ_{12} . Their directions are indicated in Fig. 6.16. The theoretical relationships between the calculated strains and the measured strains are

$$\epsilon_{0^\circ} = \epsilon_{22} \quad \epsilon_{45^\circ} = \epsilon_{12} + \frac{1}{2}(\epsilon_{11} + \epsilon_{22}) \quad \epsilon_{90^\circ} = \epsilon_{11} \quad (6.1)$$

The general expression of the strain in a chosen direction (parallel to the tube surface) is

$$\epsilon_{\theta\theta} = \epsilon_{11} \sin^2 \theta + \epsilon_{22} \cos^2 \theta + \epsilon_{12} \sin 2\theta \quad (6.2)$$

The material parameters and model parameters are those as listed in Table 6.1~Table 6.3.

6.3.3 Results and Comparison

1. Torsion first, tension next

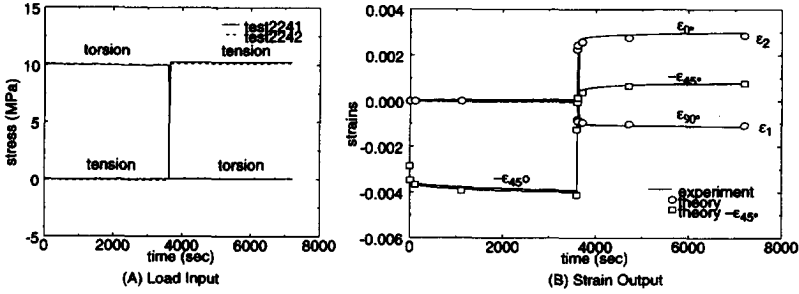


Figure 6.17. Results from tests 2241 & 2242, two tests for a constant torsional load first and after one hour switched over to a constant tensile load

2. torsion first, tension & torsion next

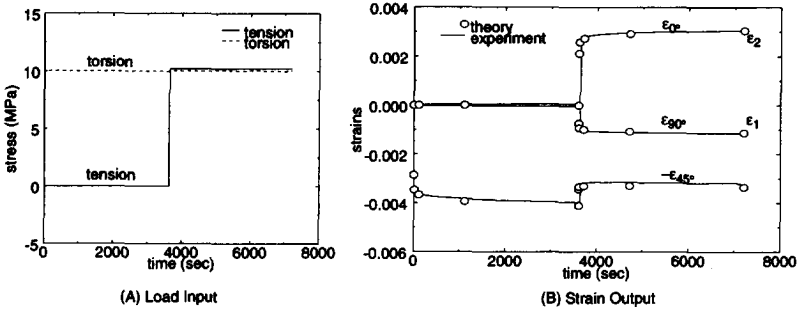


Figure 6.18. Test 2221, a constant torsional load and, after one hour, combined with a constant tensile load

3. Tension first, torsion next

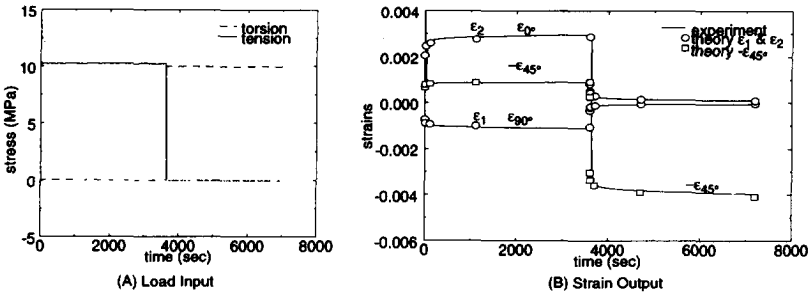


Figure 6.19. Test 2231, first a constant torsion load and then a constant tension load

4. tension first, tension & torsion next

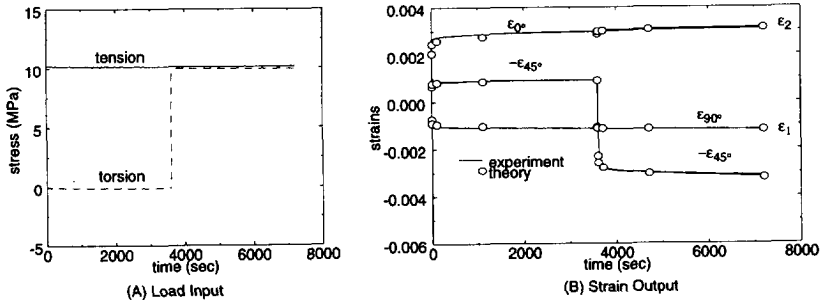


Figure 6.20. Test 2211 & 2212, two tests for a constant tension load and after one hour combined with a constant torsion load

5. Tension first, tension & increasing torsion next, finally tension & opposite torsion

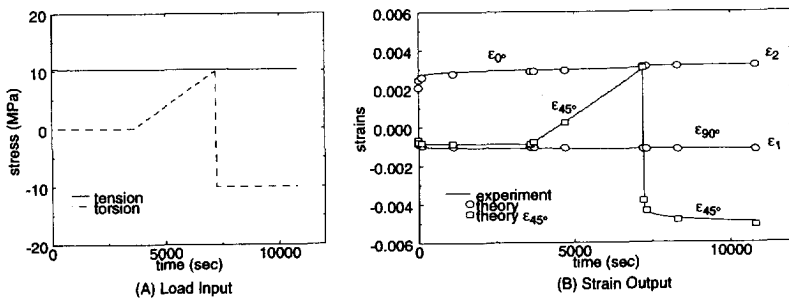


Figure 6.21. Test 2251, a constant tension load combined with a linearly increasing torsion load, which finally is reversed abruptly

6.3.4 Difference between Linear Theory and Nonlinear Theory

When the stresses are small, as an approximation, one could try to apply the linear viscoelastic theory by assuming all the nonlinear parameters, g_0 , g_1 , g_2 and a_0 , to be unity. This has been proven to be inaccurate for this case even when the maximum effective stress was only 20 MPa, see Fig. 6.22.

Comparing with the experimental data, the linear theory brings 9.05% error in ϵ_{0° and 5.84% error in ϵ_{45° , while the nonlinear theory only brings 0.28% and 3.26% errors in ϵ_{0° and ϵ_{45° respectively. In Fig. 6.23, for the plate with a hole (as discussed in Section 6.2), it is shown that the error from the linear theory is further pronounced if the stress level is higher and when the creep time is larger.

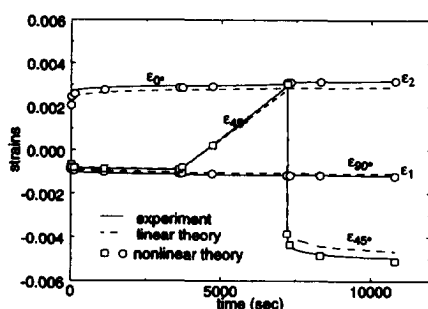


Figure 6.22. Comparison between the experimental data, the linear viscoelastic theory and the nonlinear viscoelastic theory for a biaxial loading case. The data are taken from Fig. 6.21

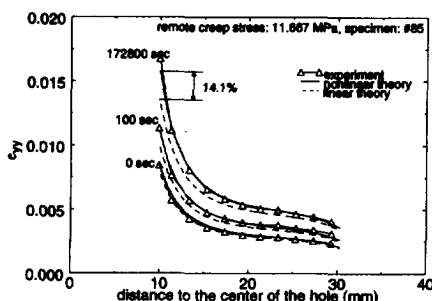


Figure 6.23. Comparison between the experimental data, the linear theory and the nonlinear theory. The data of the nonlinear theory and the experiment are taken from Fig. 6.5

6.4 Conclusions

In the previous chapters, a nonlinear viscoelastic model has been established and characterized by simple tensile creep tests. The model has been applied in this chapter to simulate 2D stress state cases. Here both creep and relaxation occur while stress coupling and strain coupling (Poisson's effect) exist. The successful prediction of creep and relaxation behaviour, found here for biaxial stress states, leads to confidence in the capability of the theory to simulate a general time-dependent behaviour for a complicated stress state and history.

It is concluded that a simply established theory (through uniaxial tests) can indeed be applied to simulate more complicated stress states such as cyclic loading in Section 2.6 and the 2D stress situation in this chapter. Both the time-dependence and the stress-dependent nonlinearity can be modelled successfully. This conclusion will lead us to employ the theory for the simulation of general 3D stress situations, i.e., the micromechanical analysis of unidirectional glass fibre/polyester composites in the next chapter.

Unidirectional Composite Creep

7.1 Introduction

In this chapter, the nonlinear viscoelastic model, developed in the previous chapters, will be applied to the micromechanical study of a unidirectional composite, a glass-fibre reinforced polyester system. For such a composite, the polyester matrix will generally be in a 3D stress state and will creep and relax with time under the action of this 3D stress field. Therefore even if we want to describe composite mechanical behaviour under a uniaxial load, a general 3D model for the matrix material is needed.

The matrix behaviour depends also on the fibre packing geometry of the composite. For a unidirectional composite (see Fig. 7.4), the fibres are embedded in the matrix material all in one direction. To simplify the real random fibre distribution, the simplest idealization for analytical and or numerical approaches is to adopt so-called hexagonal and rectangular patterns of fibre packing geometry (see Fig. 7.7, Fig. 7.9 and Fig. 7.10). These are based on assumptions of uniform distribution and periodic packing of the fibres. These assumptions have brought a great convenience since models of limited size can be used. Moreover the boundary conditions for both analytical and numerical analyses can be constructed in a simple way.

Foye was probably the first to apply simple cell models and the finite element method to estimate the transverse properties of unidirectional composites (1966). Both a square packing and a hexagonal packing geometry of fibres were considered to predict the Poisson's ratios, elastic moduli and stress concentrations. The results also included the stress distributions around the fibre for two different fibre packing cases (Foye 1966)^[19]. Recently, simple cell models are still used to study the interface effects of metal matrix composites; Ronald *et al.* (1991) for rectangular arrays of fibres and Achenbach and Zhu (1990) for hexagonal arrays of fibres are typical examples of such studies.

Adams and his colleagues have started to use the cell model for a rectangular array of fibres in the early 70's. They used a finite element method to simulate the subsequent propagation of failure in a cell (Adams 1973, 1987). Their method is capable of modelling many aspects, including matrix non-linear stress-strain response, fibre anisotropy and fibre-matrix interface degradation (Adams 1987).

The ability to model longitudinal shear loading in combination with normal stress loading was originally developed by Crane and Adams (1981). Achenbach and his colleagues have improved the method by a spring layer interface model and obtained more reasonable results for their material (Achenbach and Zhu 1989). While Ronald *et al.* (1991) assumed an infinitely strong interface as well as an interface without tensile strength for unidirectional silicon-carbide fibre within titanium aluminide as an elasto-plastic matrix system. The results suggest that large thermally-induced residual stresses and weak fibre/matrix interface conditions are both significant issues for metal-matrix composites being used and the differences between experiment and model are due to the regularity of the model fibre array in contrast to the local variability in fibre location (While Ronald *et al.* 1991).

Aboudi (1982) applied a doubly periodic array arrangement, the simplest geometry shown in Fig. 7.1, on which an analytically micromechanical analysis was performed. The analysis consists of the application of the continuity of displacements and tractions at the interfaces between the subcells and between neighbouring cells on an average base, as well as considerations on equilibrium.

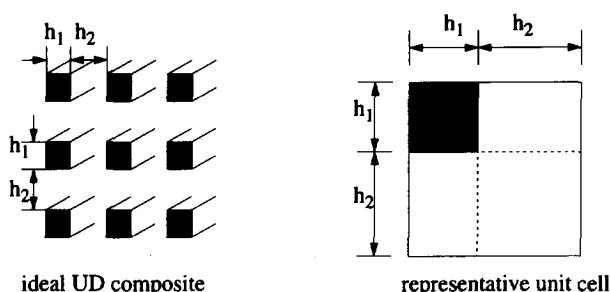


Figure 7.1. Aboudi's cell model (Aboudi 1989)

For a UD-composite, there are three aspects that play important roles in both the local and the global load-deformation response. These aspects are the mechanical model of components (fibres and matrix), the interfacial properties and the fibre packing geometry. To simplify the problems, many

researchers have adopted choices for the above aspects to perform numerical simulations. These simulations thus can only provide qualitative results.

Various studies about UD-composites (for polymeric matrix or metal matrix) have been done with emphasis on, *e.g.*, thermal stress (Zywicz 1986) and interface influences (Achenbach and Zhu 1990, Sottos *et al.* 1989). However, this work was restricted by using a regular type of fibre packing geometry. Analytical or numerical models of UD-composites based on uniform and regularly periodic distributions of fibres provide erroneous predictions of the behaviour of real composites. Therefore, non-uniform packing cases have been presented to perform more accurate simulations, *e.g.*, a random fibre packing case was adopted by Brockenbrough *et al.* (1990) for an aluminium alloy reinforced with boron fibres.

In this thesis, not only a carefully characterized constitutive model is used for the matrix material, but also two types of local non-uniform fibre packing geometry are presented. The models used yield a more accurate simulation of local stress fields and global deformation of a UD-composite. Initial strain effects have also been considered in the calculation. An experiment on the transverse creep behaviour of a unidirectional composite has been carried out. The test data were used to evaluate and select an appropriate numerical model for further examination of the local details of the stress state of the composite. These local details can not be measured directly through experiments. These details may illustrate the reason and the patterns of the early failure of the composite in the transverse direction. But for small loads, the interfacial influence was considered negligible, hence a perfect bonding interface has been adopted in the present simulation. The comparison with the experiment shows a good agreement.

The experiment was suitable to measure the overall stress-strain-time response and provides the data for a comparison and evaluation of the quality of the numerical models. Various numerical models have been tested upon the experiment data. The modelling provided us the detailed pictures of the local stress distribution and redistribution as well as the strain accumulation due to the time-dependent properties. The details of stress distribution can not be measured through experiments, however, the stress concentration and redistribution are crucial for the crack initiation and crack growth, which in turn determine the transverse strength of the composite. In this work, efforts are made to examine the level of the stress concentration which is reached under different loading conditions.

The basic material properties for the glass-fibre reinforced polyester are listed in Table 7.1.

	E-glass fiber	unsaturated polyester	composite longitudinal (<75% fvf)	composite transverse (57-62% fvf)
stiffness	73 GPa*	5.0 GPa**	42 GPa*	15-20 GPa**
tensile strength	1900 MPa*	85 MPa*	1150 MPa*	24 MPa**

Table 7.1. Basic material properties for the glass-fiber reinforced polyester system; fvf stands for the fiber volume fraction; * from Silenka Manual (1990)^[39]; ** from experiment.

One can see from the table that the transverse strength of the UD composite is very low, even lower than that of the matrix. The stress concentration in the matrix, defects in the matrix and on the interface and a possible lower strength of the interface are all possible candidates to contribute to the low

overall strength of the composite in the transverse direction. More explanation can be found in Ten Busschen (1995). For the long-term behaviour, the tensile transverse strength will be even lower, due to creep strain accumulation which reaches its limitation at the stress concentration area.

7.2 Experiment on the Transverse Creep of UD Composites

The experiment was carried out in the Laboratory for Engineering Mechanics, Delft University of Technology. The specimens were dog-bone tubes which were made on a continuous winding machine (see Fig. 7.2).

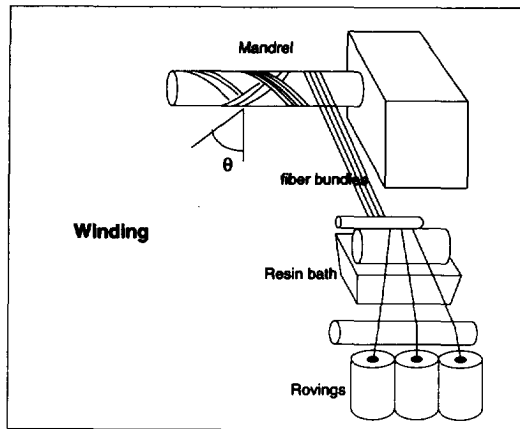


Figure 7.2. Winding machine

The winding angle θ was kept less than 1 degree (see the definition of θ in Fig. 7.2) in order to achieve an almost unidirectional composite tube. Fig. 7.3 demonstrates the specimen size.

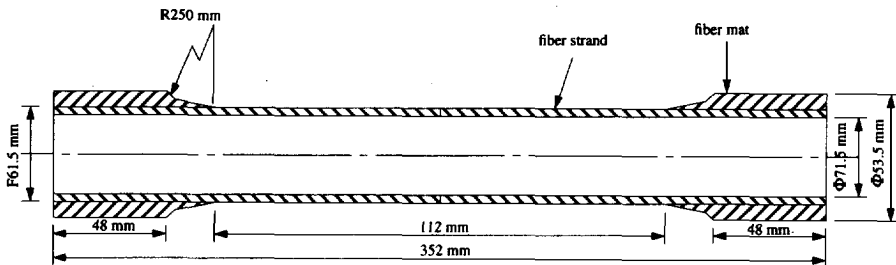


Figure 7.3. Specimen

The fibre volume fraction varies from 56% to 63% for different specimens. It is roughly controlled through changing the winding force. The circumferential direction of the tube is the longitudinal direction of the fibres, while the centre line of the tube is the transverse direction of the fibres, see Fig. 7.4.

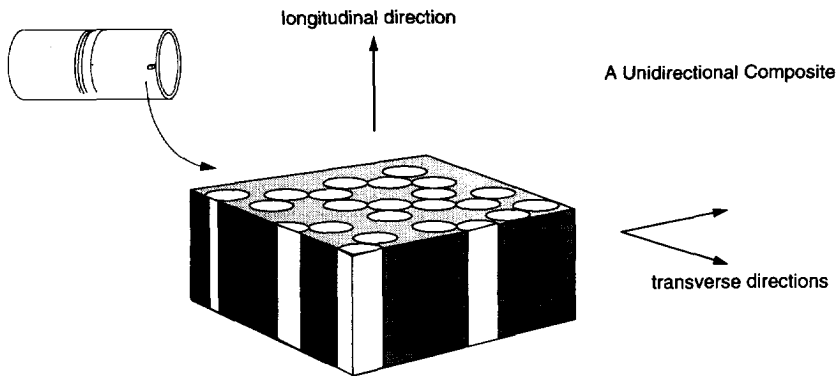


Figure 7.4. A UD composite

The tests were performed at room temperature under a constant load in order to obtain creep data. The principle of the testing machine is illustrated in Fig. 7.5. The possible tensile force varies from 0 to 120 kN. The force is applied by means of a semidead weight system and remains constant by adjusting the position of the lower end of the specimen. The beam ratio is 1:75 (Fig. 7.5), which provides a precise control to keep the beam horizontal. Fig. 7.6 reveals a band of creep data due to the variation of the fibre volume fraction and other influences on the specimens. The fibre volume fraction was obtained from a measuring procedure as described in Ten Busschen (1995).

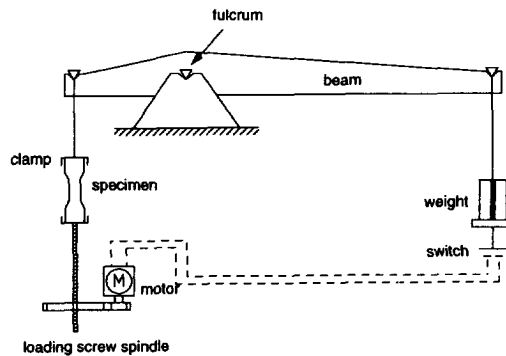


Figure 7.5. Testing equipment

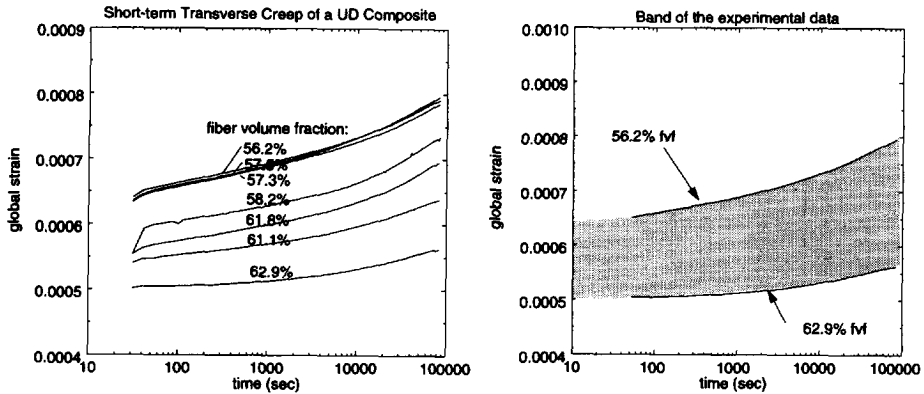


Figure 7.6. Test result, one-day short-term creep experiment under room temperature 20.5°C ; constant load 10MPa ; from the top curve to the bottom curve: specimen no. 710, 910, 010, 310, 510, 810, 610; their aging times (days): 48, 50, 51, 62, 62, 49 and 44 respectively

7.3 Constitutive Relations for Fibres and Matrix

For the later calculations it is assumed that the fibres are linear elastic while the matrix is the nonlinear viscoelastic material as described before in Chapters 2–6. Both materials are isotropic.

For the matrix material, the stress-strain relation as given in Chapter 2 has been adopted, *i.e.*, Eq (2.55). The finite element approach is based on its three-dimensional representation as described in Chapter 5.

Material constants as used are given in subsequent tables.

	fibres	polyester
Young's modulus	$E_f \approx 73\text{e9}$	$E_m = 5\text{e9}$
Poisson's ratio	$\nu_f = 0.18$	$\nu_m = 0.353$
creep Poisson's ratio		$\nu_{cm} = 0.417$
parameter of exponential creep law		$C = 1.727\text{e-11}$
exponent of exponential creep law		$n = 0.065$
physical aging shifting rate		$\alpha = 0.45$

Table 7.2. Material constants for two components of a UD composite

The parameters in the exponential function series are given below

i	J_i	λ_i
1	2.92727e-11	2.67248
2	0.594899e-11	2.67248e-1
3	1.10066e-11	2.67248e-2
4	1.44981e-11	2.67248e-3
5	2.08694e-11	2.67248e-4
6	3.38408e-11	2.67248e-5
7	4.24545e-11	2.67248e-6
8	12.4176e-11	2.67248e-7

Table 7.3. Parameters in the exponential function series

The model nonlinear parameters are presented in the next table,

σ_e	0.0	4.9e6	1.0e7	1.5e7	2.0e	3.0e7	5.0e7	7.0e7	1.0e8				
g_0	1.0	1.0	1.03	1.05	1.065	1.084	1.11	1.126	1.145				
σ_e	0.0	5.0e6	1.0e7	2.0e7	3.0e7	4.0e7	5.0e7	6.0e7	7.0e7	8.0e7	9.0e7	1.0e8	
g_1	1.0	1.011	1.05	1.18	1.4	1.76	2.32	3.2	4.61	6.9	10.7	17.5	

Table 7.4. Model nonlinear parameter vs. the effective stress (Zhang 1993b)

Two kinds of output from the calculation are presented. One represents physical values within an element averaged from the integration point values. The other is a post-processed output, the contour picture. In the contour pictures, the curves are calculated by interpolation of integration point values. This interpolation process always results into continuous curves. In some cases these should be discontinuous, *e.g.*, in the case of a normal strain across the interface between the matrix and the fibres. The confusion is due to the post-processing program, *e.g.*, I-Dias, which was used to deal with large amounts of data through the easiest way. We will accept these unreality in the contour pictures when the distortion is not too large to lead to any wrong conclusions. On the other hand, the contour pictures are only meant to provide a qualitative view on the distributions of those physical quantities. Any values listed in the tables are obtained directly from the output-files and have only an averaged sense over all integration points in one element.

The numerical results include the distributions and redistribution of various stresses and strains, such as normal stresses and strains, principal stresses and strains, effective stress and strain and maximum shear stress and strain. The effective stress and strain and maximum shear stress and strain are defined as follows:

If σ_I , σ_{II} and σ_{III} are the principal stresses ($\sigma_I > \sigma_{II} > \sigma_{III}$) the effective stress is defined as

$$\sigma_e = \frac{1}{\sqrt{2}} \sqrt{(\sigma_I - \sigma_{II})^2 + (\sigma_{II} - \sigma_{III})^2 + (\sigma_{III} - \sigma_I)^2} . \quad (7.1)$$

σ_I is the maximum principal stress and σ_{III} is the minimum principal stress. The maximum shear stress then is

$$\tau_{max} = (\sigma_I - \sigma_{III}) / 2. \quad (7.2)$$

If ϵ_I , ϵ_{II} and ϵ_{III} are the principal strains, and $\epsilon_I > \epsilon_{II} > \epsilon_{III}$, the effective strain is defined as

$$\epsilon_e = \frac{1}{\sqrt{2}} \sqrt{(\epsilon_I - \epsilon_{II})^2 + (\epsilon_{II} - \epsilon_{III})^2 + (\epsilon_{III} - \epsilon_I)^2}. \quad (7.3)$$

The maximum shear strain is

$$\epsilon_{max} = (\epsilon_I - \epsilon_{III}) / 2. \quad (7.4)$$

In this chapter, results of maximum principal stress and strain, effective stress and strain and the maximum shear stress and strain will be presented.

7.4 Rectangular and Hexagonal Fibre Packing

The periodic packing geometry reduces the mechanical analysis of a unidirectional composite to the solution of a set of boundary problems for a repeating cell. According to this method in an infinite medium a surface isolates a volume composed of one or several fibres, and assumes that the structure of the remaining part is obtained by means of repetition of the cell, see, *e.g.*, Fig. 7.7 and Fig. 7.9.

The boundary condition for this rectangular cell is such that any of two parallel edges remain straight and parallel during deformation (or all edges are symmetry planes). The load is applied on two parallel edges in the normal directions (see, *e.g.*, Fig. 7.18).

The fibres and matrix are assumed perfectly contacted (perfect bonding condition). When the loading is small, this assumption is realistic. In a study of time-independent behaviour of the same material (Busschen 1995), a friction interfacial model has been proposed, and combined with initial strains. The comparison with tests shows a good agreement (Busschen 1995). In this thesis, a softer interphase layer and a faster creep interphase layer are examined in Section 7.11. The purpose of using these two cases is to know how the influences of different interphases on the global creep behaviour of a cell exhibit.

7.4.1 Rectangular Fibre Packing

Assuming a periodic array of fibres as shown in Fig. 7.7, a typical repeating unit can be isolated and the computation will be carried out for this unit cell.

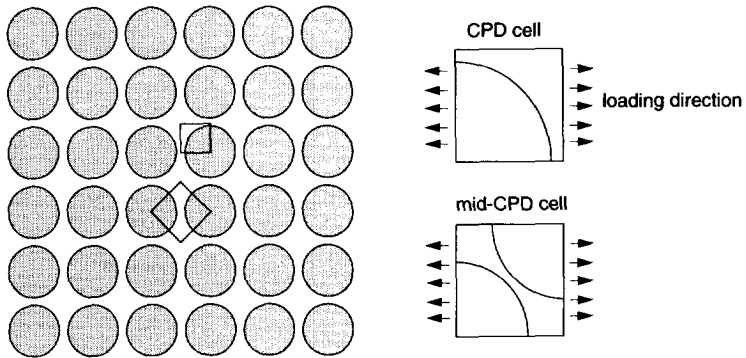


Figure 7.7. Unit cells of square packing geometry of fibres

The unit cell can be obtained through drawing four closest symmetry axes, two parallel axes perpendicular to another two parallel axes. In Fig. 7.7, there are two different packing directions depending on the loading direction on this square packing geometry. One is called the closest packing direction (CPD), and the other one the mid closest packing direction (mid-CPD).

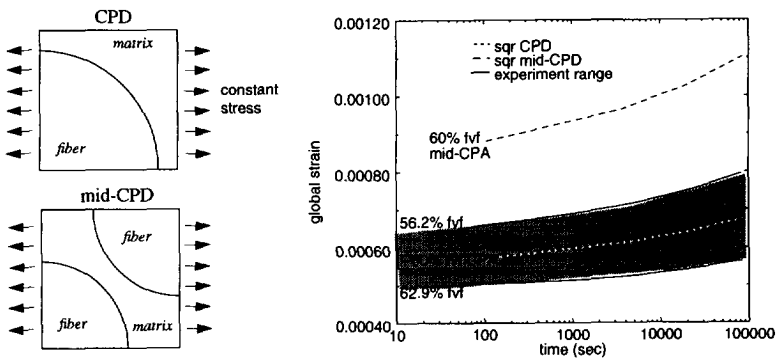


Figure 7.8. The theoretical prediction by a square cell overestimates the transverse creep of a UD composite, global load 10MPa

The square cell shows an anisotropic property in global stress-strain behaviour. Fig. 7.8 demonstrates an overestimation of the creep deformation in mid-CPD. This anisotropic property is not only unrealistic, but also may bring difficulties in the numerical simulation of the overall composite creep behaviour. For the convenience of further analysis, this anisotropic cell case was abandoned. Furthermore,

in further analysis, the isotropic property will always be considered as a favourite property of chosen cell models.

For a more general rectangular packing geometry, only one unit cell exists with a CPD packing and a mid CPD packing, see Fig. 7.9. This rectangular packing geometry gives even a worse global isotropic property.

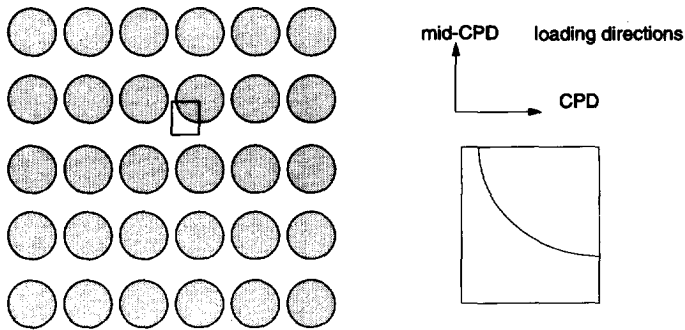


Figure 7.9. Rectangular packing

7.4.2 Hexagonal Fibre Packing

A most uniform packing geometry is the so-called hexagonal array packing, which is almost an isotropic packing case. In this packing geometry, there are also two packing directions, see Fig. 7.10, i.e., CPD and mid-CPD. Both will be used as loading directions. A finite element mesh (3D brick elements) is shown in Fig. 7.11. Some numerical results at different tensile loading levels and directions are demonstrated. Fig. 7.11 shows two contour pictures of stress distributions.

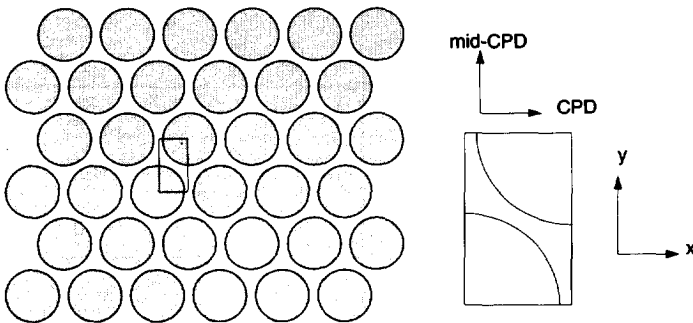


Figure 7.10. Hexagonal packing and its numerical cell model

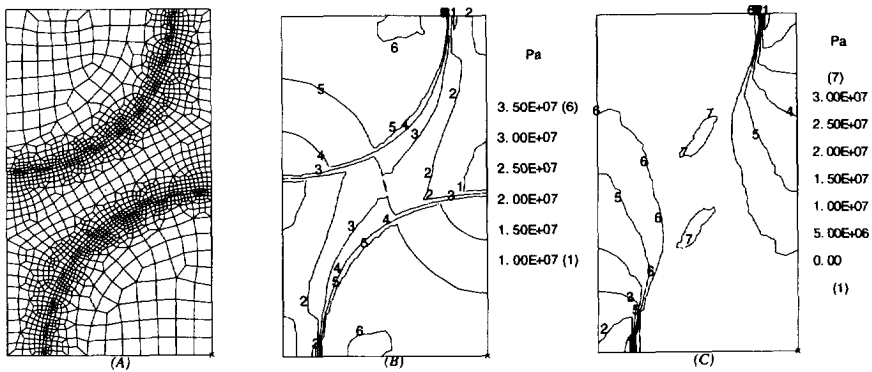


Figure 7.11. (A) mesh, (B) effective stress and (C) maximum principal stress, after 3 month, loaded in y -direction (see Fig. 7.10) with global stress 24MPa, 60% fibre volume fraction

An evidence of the stress redistribution can be found in Fig. 7.12 even though the remote load is low, 10MPa. The influence of the creep Poisson's ratio has been found to be quite large in Fig. 7.13. When the creep time is more than one month, the error in the global strain due to the neglect of this ratio can be as large as 10%, for a small remote load, 10MPa. The differences of global Poisson's ratio between fibres and matrix can result in interfacial stresses similar to thermal stresses. When a fibre has a lower global Poisson's ratio than the matrix, upon application of axial tension (in the fibre direction) to the composite the matrix shrinks to a greater extent than the fibre, that results in radial compressive stresses. Conversely, upon compression, the mismatch of the global Poisson's ratios can contribute to fibre-matrix debonding.

The global creep deformation in Fig. 7.14 illustrates a less anisotropic property of this fibre packing geometry compared with the square packing case (Fig. 7.7). However an overestimation of the global creep strain is still formed.

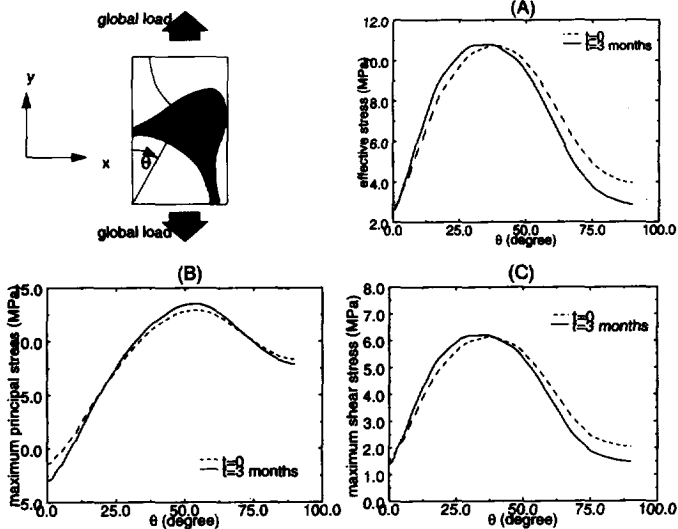


Figure 7.12. Data points, (A) effective stress, (B) maximum principal stress and (C) maximum shear stress, loaded in y-direction with global stress 10MPa, 60% fibre volume fraction

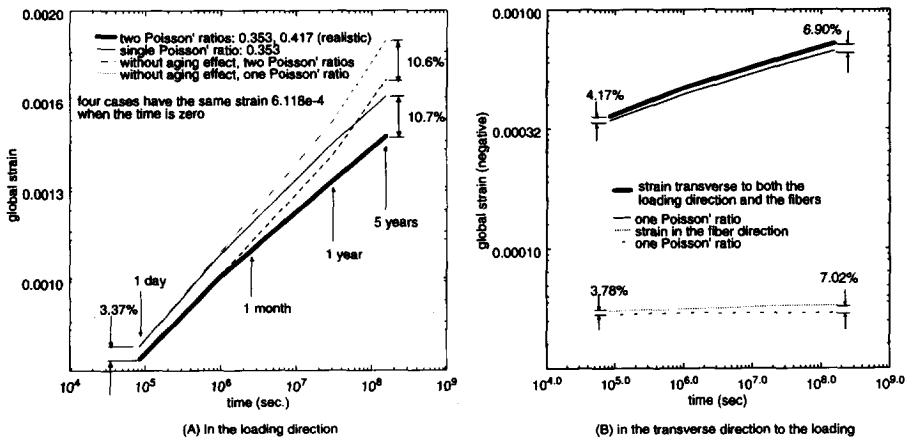


Figure 7.13. Influence of the creep Poisson's ratio on the creep strain, calculated results from the hexagonal cell model, creep stress: 10MPa; initial aging time: 3.9e6 sec. (1.5 months); (A) The strains in the loading direction; (B) The strains transverse to both the loading direction and the fibre direction

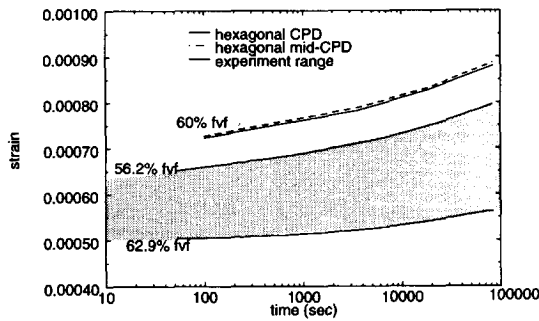


Figure 7.14. The theoretical prediction by the hexagonal cell model overestimates the transverse creep of a UD composite, global load 10MPa

7.4.3 Discussion

The result of the hexagonal cell model in Fig. 7.14 demonstrates an overestimation of the global creep deformation. This overestimation suggests a fundamental incorrectness of the uniform cell models. In the real situation, fibres are packed non-uniformly but it has been observed that globally the composite still behaves transversely isotropic.

In general, the rectangular fibre packing is not appropriate due to its anisotropy. The hexagonal fibre packing is better than the rectangular packing, but both are not realistic due to their too uniform fibre distribution, which suggests a more uniform stress distribution and hence a more efficient matrix material use than in reality.

To overcome these problems, modification is necessary. Ten Busschen (1995) has tried to use an effective volume fraction, which is higher than the global fibre volume fraction, in order to compensate the application of a uniform fibre packing geometry. Among other possibilities, two special cases of fibre packing geometry have been proposed in the following sections. Different kinds of packing geometry meet in some sense the non-uniformity of the real fibre packing geometry.

7.5 Modified Hexagonal Fibre Packing - Type 1 and Type 2

The overestimation of the creep deformation is due to the oversimplification of the real fibre distribution, which is always of a random form. The photos in Fig. 7.15 demonstrate that in the realistic fibre distribution, there apparently exist two different kinds of regions, so-called fibre-rich regions and matrix-rich regions. The traditional regular fibre packing approximations, both rectangular and hexagonal packing forms, fail to simulate the transverse deformation of UD composites since these provide the models with too much unrealistic uniformity. These models imply a more efficient usage of

matrix material. This is not true in reality because the non-uniform distribution of fibres in the matrix may cause severe non-uniform stress and strain distributions. A fibre-rich area will show a relatively higher stress level compared to a matrix-rich area.

To take into account the influence of fibre-rich regions and matrix-rich regions, a modified regular distribution pattern will be used. This again results into a lot of convenience in the numerical work. A simple calculation cell with a local non-uniform distribution of fibres will be used for this purpose.

7.5.1 Fibre Distribution in Samples

According to the revelation of the photos (*e.g.* Fig. 7.15), the winding fibre reinforced composite has a very particular fibre distribution pattern. Almost all the fibres are distributed close to each other forming fibre clusters where the distance between two neighbouring fibres is usually much smaller than the scale of the fibre radius. These fibre-rich areas are dominant in the cross-section of the composite tubes. While between the fibre clusters, there exist some narrow and long matrix-rich regions, mostly parallel to the axis of the sample tube. The difference of the global fibre volume fraction of samples can hardly change the compactness of the fibre clusters, but can indeed change the total area of the matrix-rich regions.

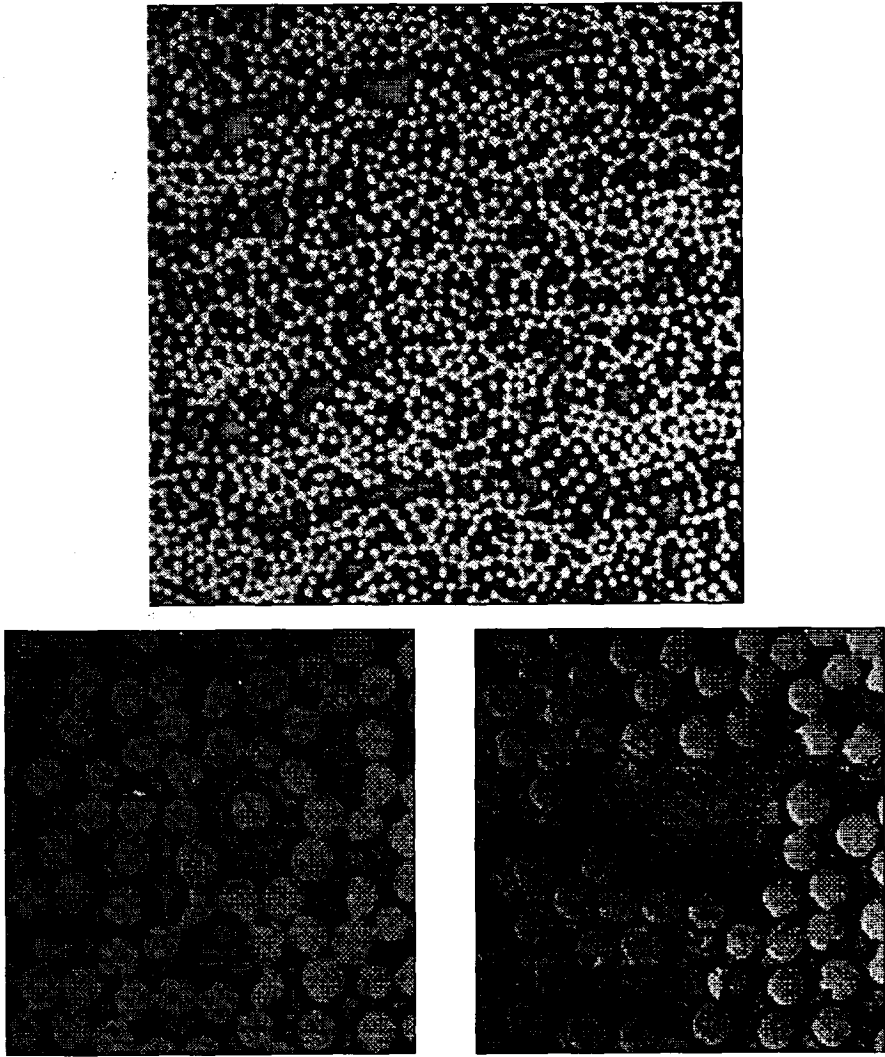


Figure 7.15. Video-photos by a microscope, the fibre distribution in a composite tube (tube no. 13)

7.5.2 A Special Regular Fibre Packing

In order to consider the non-uniformity of the fibre distribution, in the present research two different periodic fibre packing geometry patterns have been developed, *i.e.*, type 1 and type 2 packing forms, as shown below. Globally they are transversely isotropic.

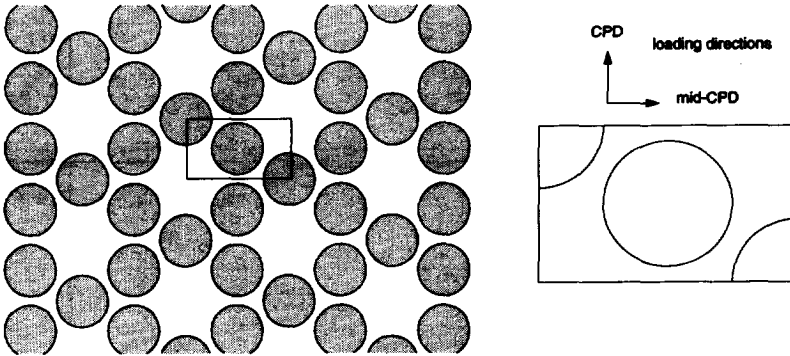


Figure 7.16. Type 1 regular non-uniform packing

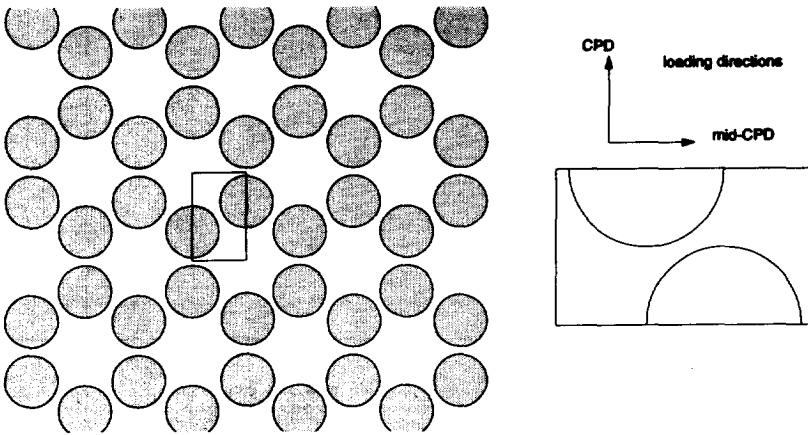


Figure 7.17. Type 2 regular non-uniform packing

In these cases, the concentrated fibres and matrix are still periodically arranged but with a local variation of the fibre density. Therefore these packing forms will be referred to as the "locally non-uniform geometry". One interesting property of these packing forms is the highest volume fraction these can reach. These are 68.02% and 60.46% for type 1 and type 2 respectively. The highest fibre volume

fraction of the specimens which could be performed in the laboratory, by means of the winding technique, were never larger than 65%. In industry, this technique can reach a maximum fibre volume fraction of about 75%. The ideal hexagonal geometry can have a maximum fibre volume fraction of 90.69%. This suggests that the severe non-uniformity of the fibre distribution prevents a higher compactness of the fibres, resulting in a lower fibre volume fraction. Consequently this will bring more distributed fibre-rich regions and matrix-rich regions.

7.5.3 Boundary Conditions for the Numerical Calculation

The numerical cell model for a periodic packing geometry with symmetry properties has an advantage of simple boundary conditions. As shown in Fig. 7.18, three surfaces are supported in three different directions: the surface $EFGH$ is supported in the z -direction, the surface $ABFE$ in the y -direction and the surface $AEHD$ in the x -direction. According to the symmetric property, the surface $ABCD$ is forced to remain plane and parallel to the surface $EFGH$. A tying of an equal displacement in the z -direction is hence applied on the surface $ABCD$. Similarly, the surface $DCGH$ is kept parallel to the surface $ABFE$ and the surface $BFGC$ parallel to the surface $AEHD$. The tensile load in the x -direction or in the y -direction is then applied on the node C as a concentrated force.

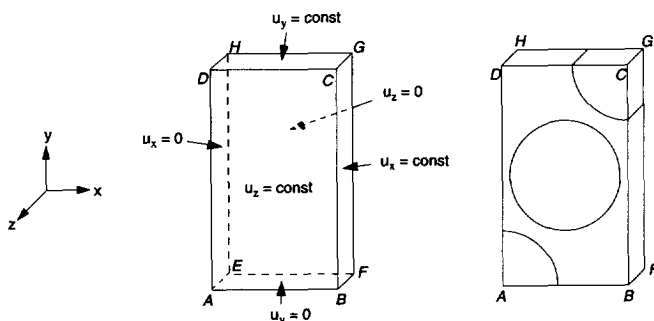


Figure 7.18. Boundary conditions for a numerical cell model

7.5.4 57% Fibre Volume Fraction, 10MPa Global Load

The FEM analysis result shows that the stress is concentrated in the fibres and in the matrix region where two fibres are close to each other (see Fig. 7.21). The corresponding strains then situate dominantly in the same matrix region (Fig. 7.19). But most importantly, the creep curves for different load levels are very close to the experimental results (Fig. 7.20). One sample is used to perform a series of creep tests with increasing loads from test to test until the sample failed. It is assumed that the fibre and matrix are perfectly bonded and that during the deformation no damage occurs. Therefore, the underestimation of the numerical results in Fig. 7.19 suggests a reasonable modelling due to the fact that in reality, before the failure of the composite, the damage at the interface and in the matrix has contributed to a larger global deformation. Hence the composite showed a larger strain for the global

creep elongation than the theoretical prediction, especially, when the global stress was relatively high, see Fig. 7.21.

The initial strain is excluded in this section. This will be considered later in Section 7.8.

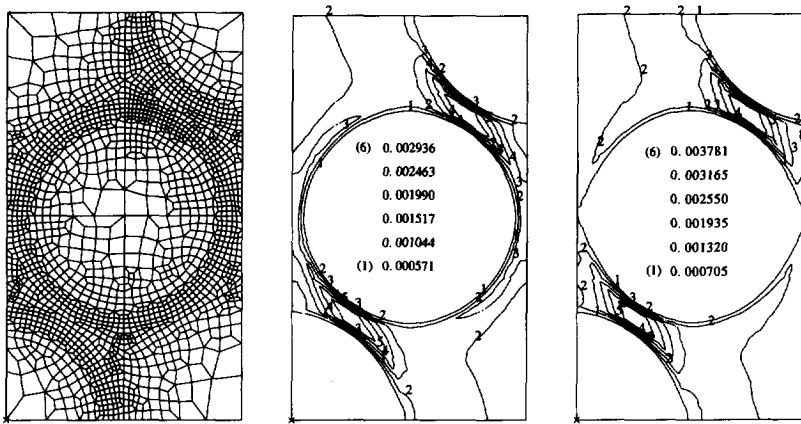


Figure 7.19. Mesh, maximum principal strain and effective strain distributions, type 1 fibre packing form, fibre volume fraction 57%, global creep stress load 10mpa in y-direction

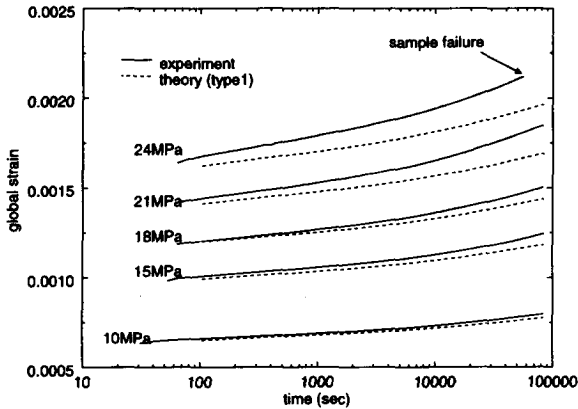


Figure 7.20. Transverse creep of a UD composite, specimen #9, fvf 57.5%, cell model (type 1) loaded in y-direction

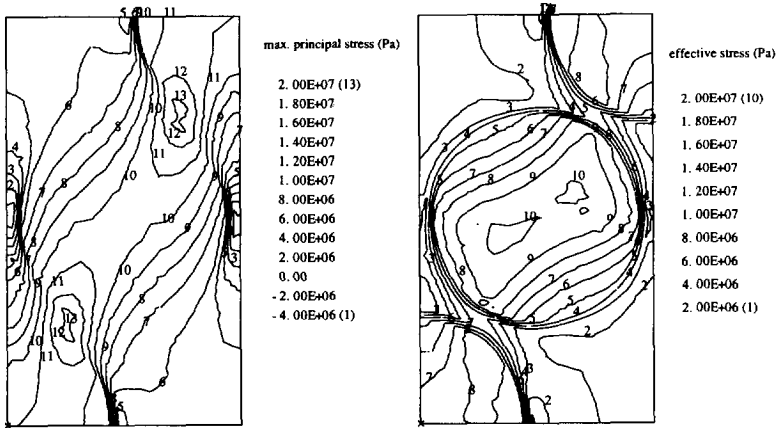


Figure 7.21. Principal stress and effective stress distributions for type 1 fibre packing, volume fraction 57%, global creep stress load 10mpa in y-direction

Fig. 7.22 demonstrates the creep curves of the largest global stress (24MPa) being applied in the experiment. All the four specimens fractured after some time. Both type 1 and type 2 models give an underestimation in the strain for the case of 57% fibre volume fraction.

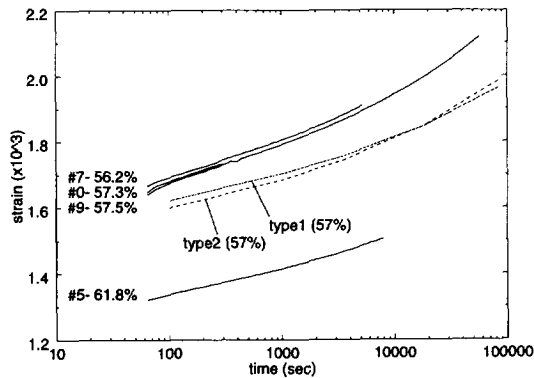


Figure 7.22. Composite creep, 24MPa in y-direction, specimen no. (from top to bottom) #7, #0, #9 and #5, the fibre volume fractions are depicted in the figure

7.6 Stress and Strain Redistribution

Due to the viscoelastic behaviour of the matrix, under a stressed and deformed state, the matrix starts to creep and relax. After a period of time, one can expect a redistribution of stresses in both matrix and fibres. This will not only change the stress concentration level, but also its location

The type 1 model cell can be loaded in two different directions, *i.e.*, the x-direction (CPD) and the y-direction (mid-CPD), and consequently has two different stress and strain distributions within the cell.

In this section, the calculation has been done for a cell model with a fibre volume fraction of 57%.

7.6.1 Y-direction global loading case (mid-CPD)

The loading direction is in mid-CPD, see the following figure. The effective stresses along the “central fibre” in the matrix and in the “corner fibre” are different.

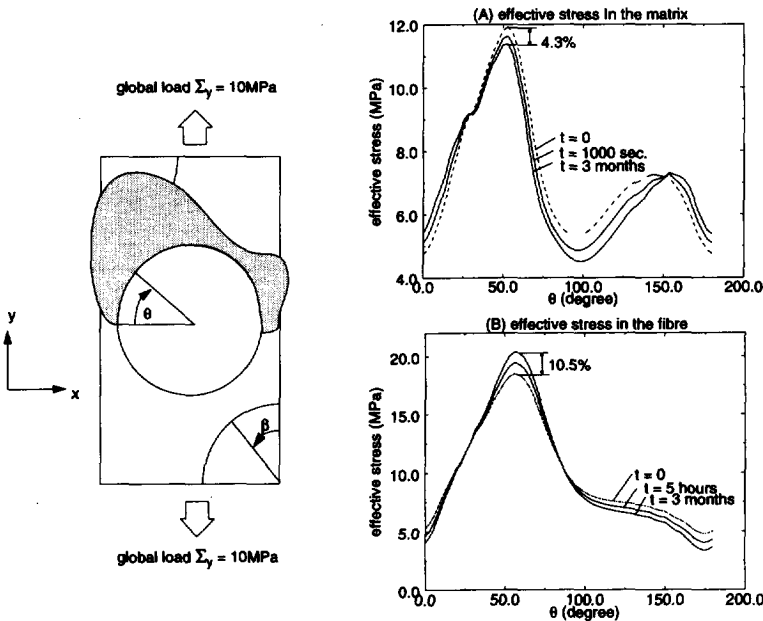


Figure 7.23. Effective stress in the matrix and in the fibre region along the interface of the central fibre

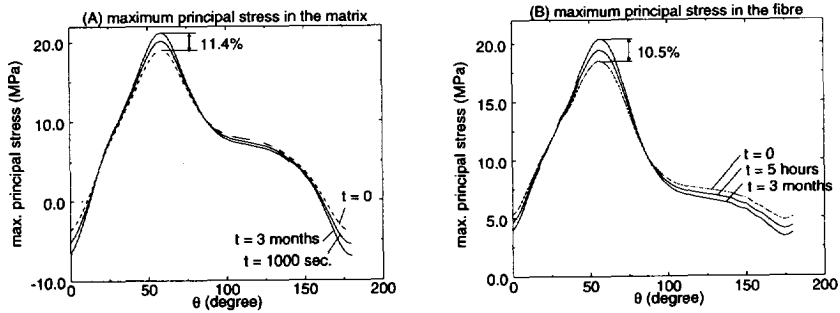


Figure 7.24. Maximum principal stresses in the matrix and in the fibre along the interface of the centre fibre, $\Sigma_y = 10 \text{ MPa}$

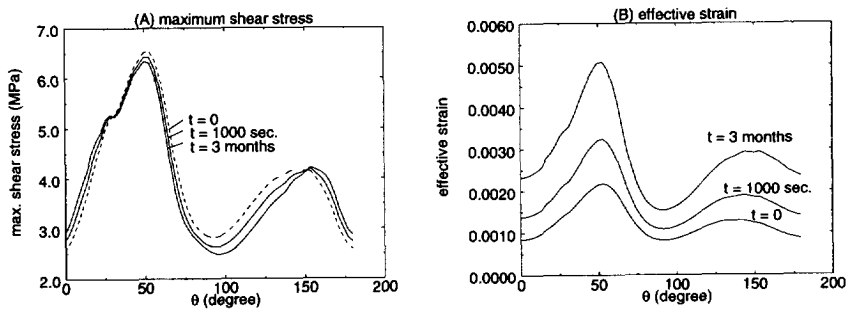


Figure 7.25. Maximum shear stress and effective strain in the matrix along the interface of the centre fibre, creep loading $\Sigma_y = 10 \text{ MPa}$

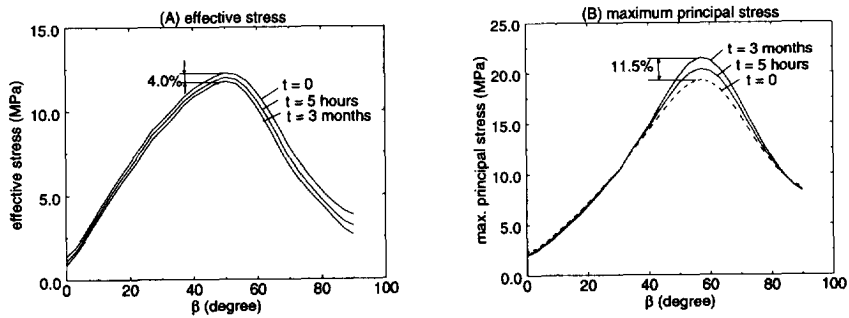


Figure 7.26. Stresses in the matrix along the interface of the corner fibre, $\Sigma_y = 10 \text{ MPa}$

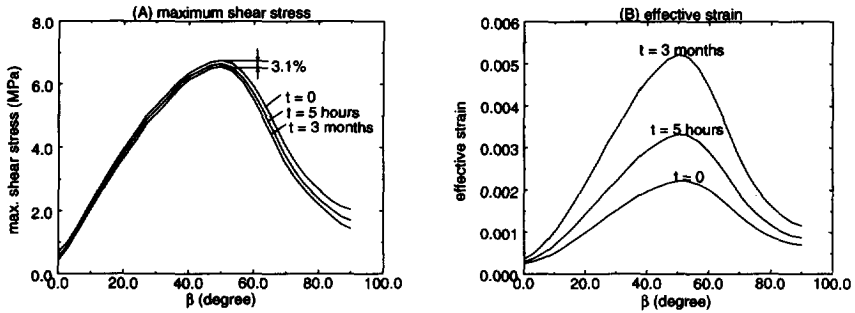


Figure 7.27. Maximum shear stress and effective strain in the matrix along the interface of the corner fibre, creep loading $\Sigma_y = 10 \text{ MPa}$

Fig. 7.28 shows the path where the stress and strain distributions as presented in Fig. 7.29 and Fig. 7.30 are considered.

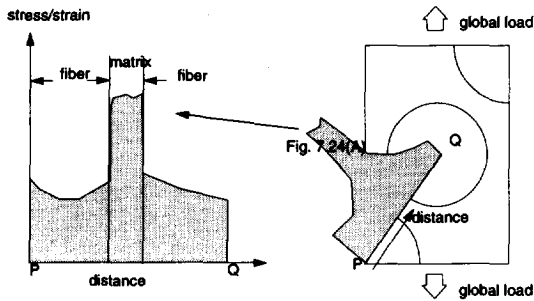


Figure 7.28. The stress/strain distribution along the line PQ, for Fig. 7.29 ~ Fig. 7.31

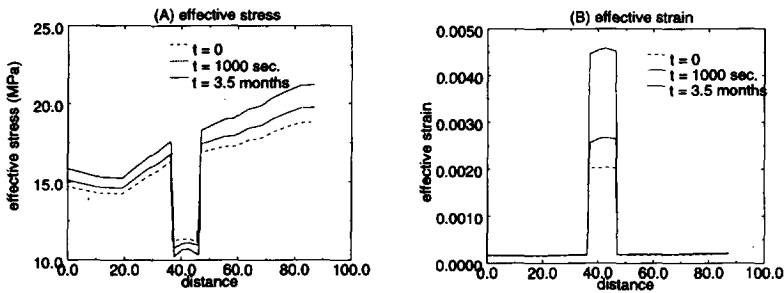


Figure 7.29. Effective stress and effective strain along the path PQ, in Fig. 7.28, fibre volume fraction 57%, global load 10 MPa in y-direction

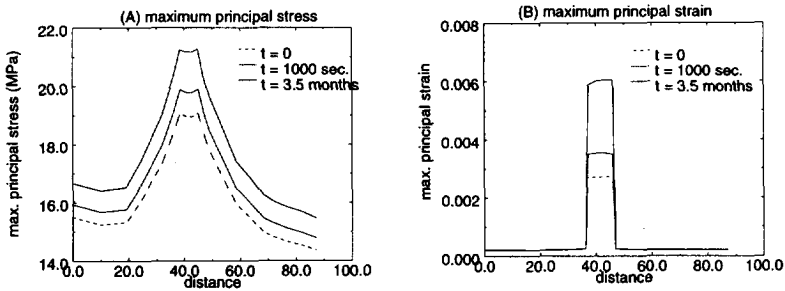


Figure 7.30. Maximum principal stress and maximum principal strain along the path PQ, in Fig. 7.28, fibre volume fraction 57%, global load 10MPa in y-direction

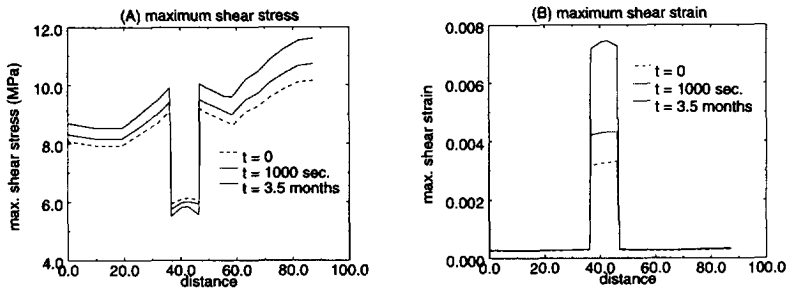


Figure 7.31. Maximum shear stress and maximum shear strain along the path PQ, in Fig. 7.28, fibre volume fraction 57%, global load 10MPa in y-direction

7.6.2 X-direction global loading case (CPD)

When the “local non-uniform geometry” model is loaded in x-direction, the stress distribution pattern will be completely different from the results as presented in the latter section for loading in the y-direction.

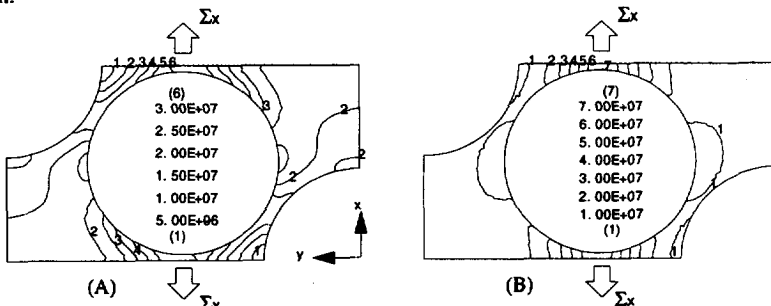


Figure 7.32. (A) effective stress and (B) maximum principal stress distribution, type 1 fibre packing geometry, global load 24 MPa in x-direction

The stress and the strains also show different distributions along the interface.

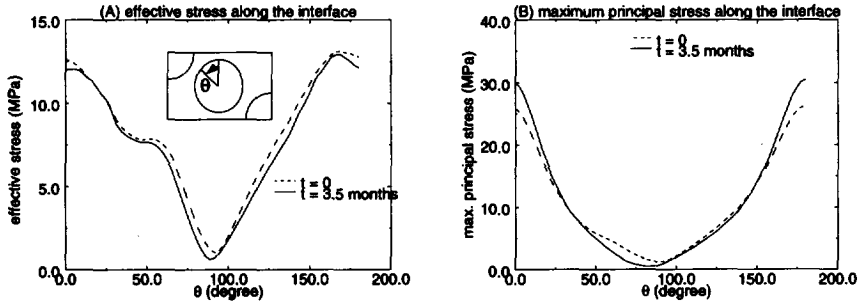


Figure 7.33. Stress distributions in the matrix along the interface of the centre fibre, fibre volume fraction 57%, global load 10MPa in x-direction

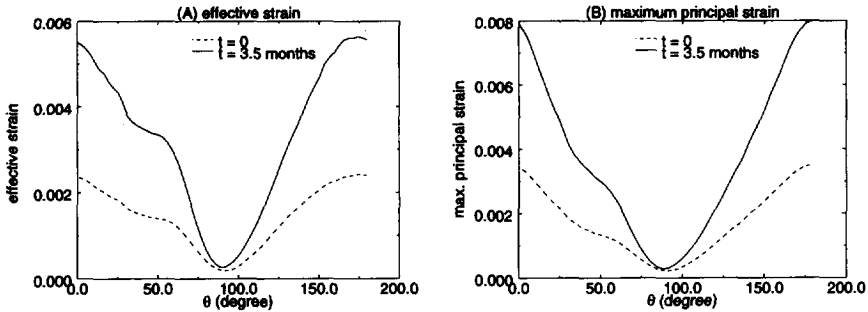


Figure 7.34. Strain distributions in the matrix along the interface of the centre fibre, fibre volume fraction 57%, global load 10MPa in x-direction

The stress and strain redistribution around the corner fibre have been illustrated in Fig. 7.35 and Fig. 7.36.

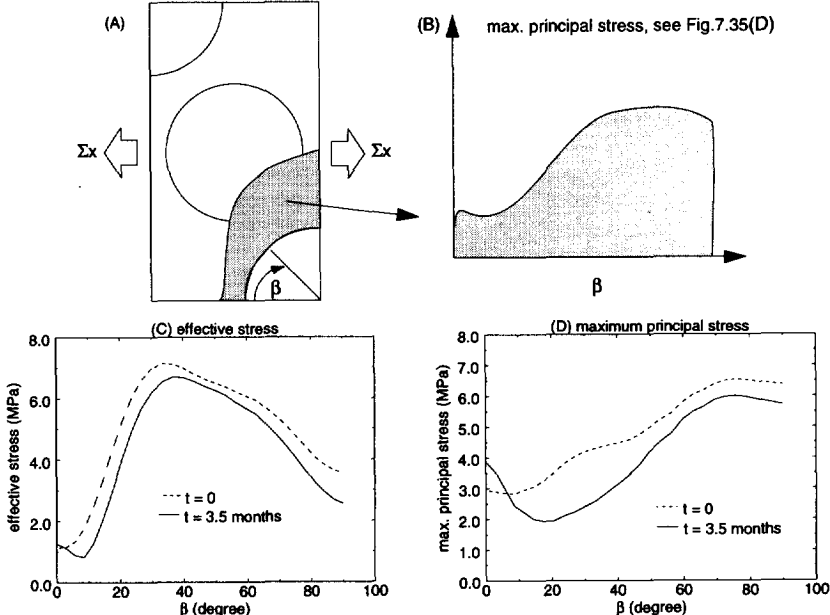


Figure 7.35. Stress distributions in the matrix along the interface of the corner fibre, fibre volume fraction 57%, global load 10MPa in x-direction

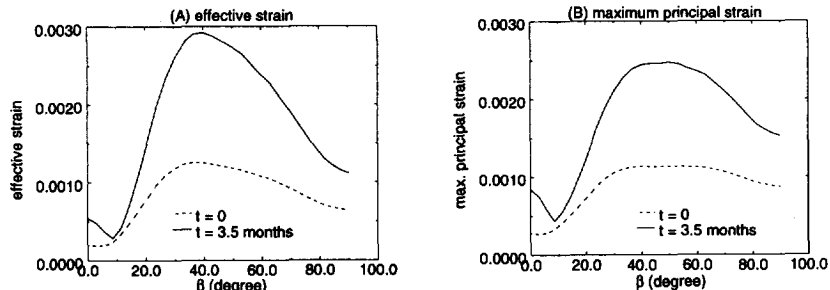


Figure 7.36. Strain distributions in the matrix along the interface of the corner fibre, fibre volume fraction 57%, global load 10MPa in x-direction

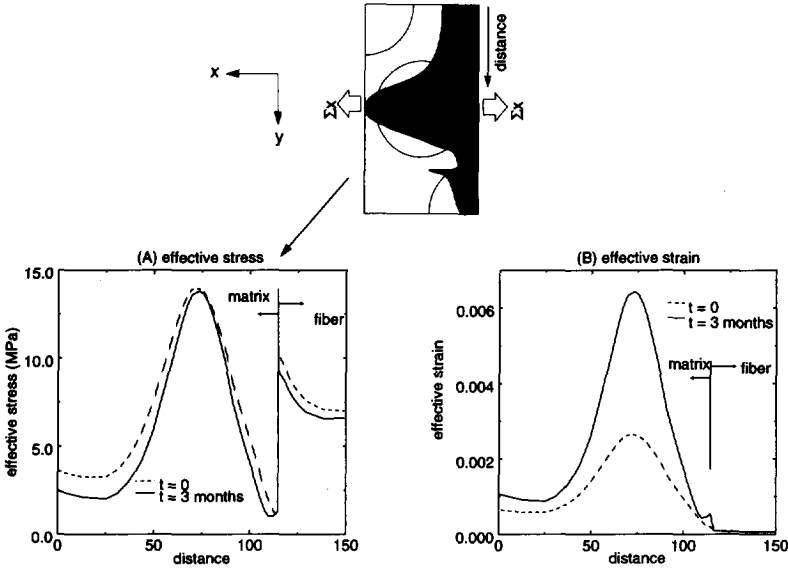


Figure 7.37. Effective stress and effective strain along an edge of the model cell as defined above

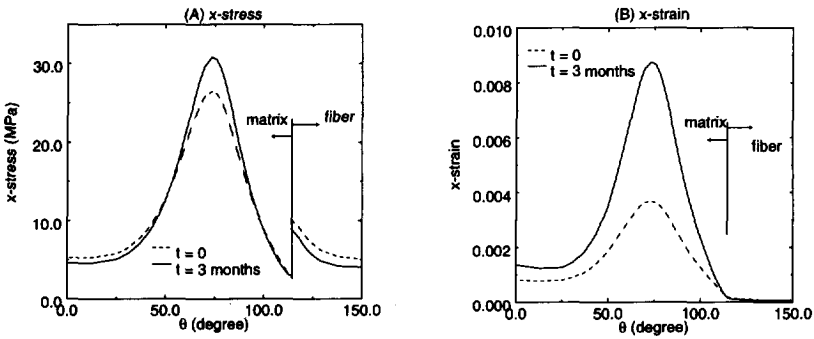


Figure 7.38. x-stress and x-strain along the left-edge of the model cell

7.6.3 Conclusions

The figures have shown that the stresses and strains along the interface and other paths change with time. The locations of the maxima also change slightly. Therefore the stress redistribution is insignif-

icant. The new types of fibre packing geometry show almost isotropic properties. Stress concentration in the matrix occurs at the areas where the distance between two fibres is the smallest.

7.7 Random Packing of Fibres

The geometry in Fig. 7.39 was artificially made for the simulation of a case with a random fibre distribution. The fibre volume fraction was chosen to be 60%.

A coarse mesh (not shown here) was first made for initial calculation. According to the stress distribution found, especially, for the area with the largest stress gradients, a relatively finer mesh with 2636 linear solid elements was made (Fig. 7.39). It was observed that the load transfer follows a band of relatively closely spaced fibres, where the matrix between those fibres shows a relatively high stress level (compared to the matrix-rich areas).

The mesh used here, however, is still a coarse mesh. It was adopted due to the limitation of the computer capacity. Errors are inevitable when a coarse mesh is used for stress calculation. Especially, between some fibres, the matrix only has one element thickness. The goal of using this mesh is to examine the relative relation of the stress pattern to the mutual distance of fibres.

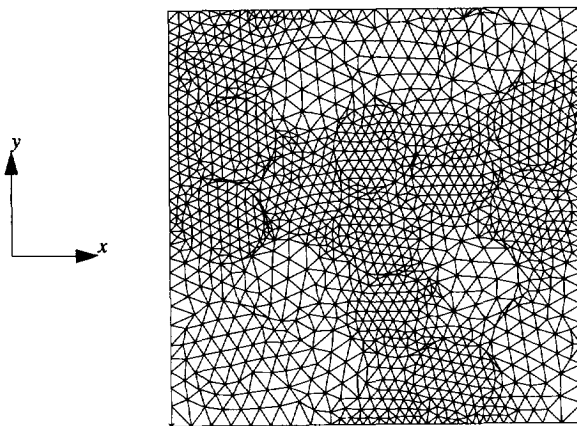


Figure 7.39. A mesh for a random fibre packing form, fvf 60%

The stress distribution is illustrated in Fig. 7.40 and Fig. 7.41. In Fig. 7.43 ~ Fig. 7.45 irregular stress and strain patterns around a fibre in the matrix are observed. Some of the fibres are close to each

other, so that both the effective stress and the maximum principal stress have higher peaks after a period of creep time.

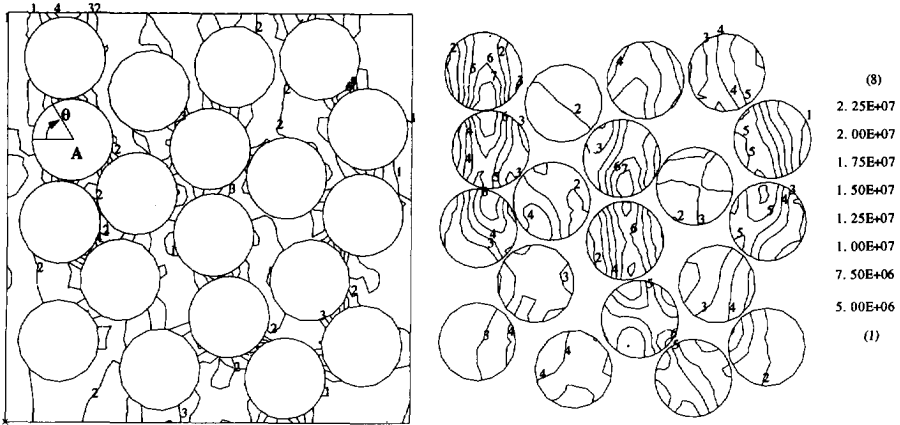


Figure 7.40. Distribution of effective stress, 10mpa global creep stress in y-direction

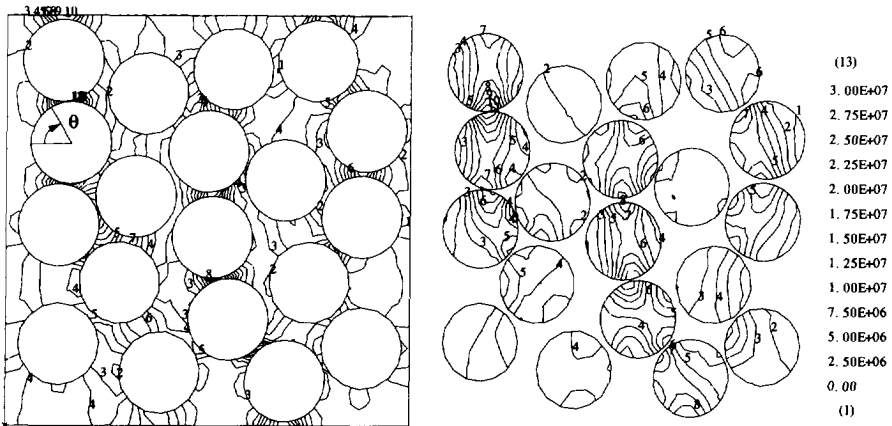


Figure 7.41. Maximum principal stress, 10mpa global creep stress in y-direction

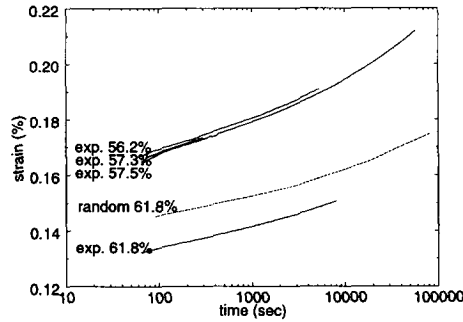


Figure 7.42. Composite creep, 24MPa, experimental data stop when specimens fail, their fibre volume fractions are shown in the figure. The random fibre-packing model provides an overestimated result.

The global strains obtained from the simulation with the random fibre-packing model are slightly higher than the experimentally obtained strains. In the calculation, the matrix volume was adjusted in order to obtain a fibre volume fraction of 61.8%. The overestimation suggests that this artificial "random" case is not appropriate to present the reality. In reality, fibre-rich regions are connected to each other while the matrix-rich regions are relatively isolated. In the present case, see Fig. 7.40, the fibre-rich region is surrounded by a matrix-rich region.

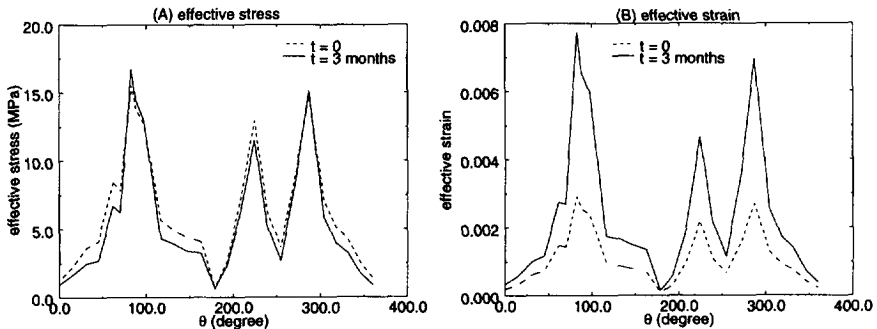


Figure 7.43. Effective stress and effective strain in the matrix along the interface of the fibre 'A' (see Fig. 7.40), global stress load 10MPa, fibre volume fraction 60%

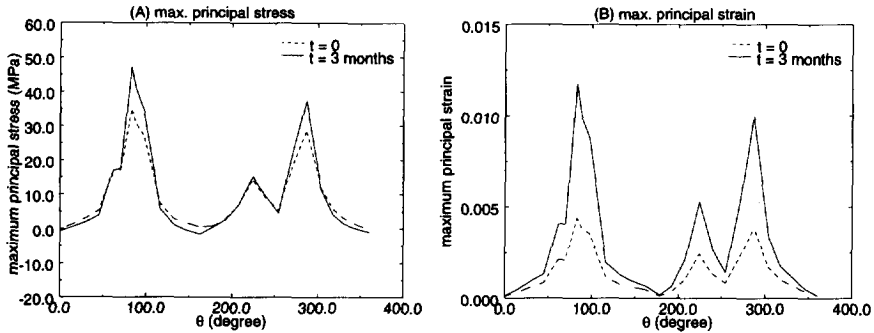


Figure 7.44. Maximum principal stress and maximum principal strain in the matrix along the interface of the fibre 'A' (see Fig. 7.40), global stress load 10MPa, fibre volume fraction 60%

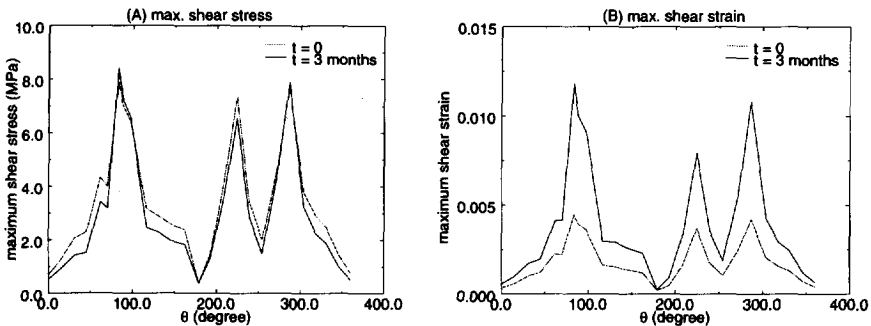


Figure 7.45. Maximum shear stress and maximum shear strain in the matrix along the interface of the fibre 'A' (see Fig. 7.40), global stress load 10MPa, fibre volume fraction 60%

7.8 Shrinkage and Prestress State

7.8.1 Shrinkage due to polyester curing

Shrinkage occurs during the chemical reaction of the reactants where the polymerization and accompanied temperature changing are the reasons of a volume change. This volume change is a continuous phenomenon when the chemical reaction continues. In the beginning, the curing starts and the polymerization causes a volume shrinkage but the raising of the temperature due to the heat generation because of the chemical reaction causes an expansion. Differences in heat conductivity in the mould lead to a varied temperature distribution, which may in turn accelerate the reaction in a local higher temperature region. This accelerated reaction causes more curing shrinkage compared to the shrink-

age within other relatively lower temperature areas. When the material still is in the liquid state, no stress will be built up. Even when the material in one region first is solidified, the surrounding material can still flow and shrinkage induced stress is limited. However, when the whole material turns into the solid state, due to a different thermal history and consequently different curing stages, the volume shrinkage may vary from region to region. This finally introduces a stress distribution even without inclusions such as fibres. In the later curing stage, the chemical reaction slows down and little heat is generated, the temperature drops which causes a corresponding thermal shrinkage too. The thermal shrinkage may introduce an extra stress value on the stress field built up by the curing shrinkage, especially, when inclusions exist.

The total volume change for cast polyester (DSM Resins Synolite 593-A-2) after postcuring (60°C 24hours and 80°C 24hours) is 9.3% ($\Delta V/V$) with a standard deviation of 0.2% (Ten Busschen 1995). However, since a description of the relation of the curing stage, the physical phase (liquid or solid), the heat creation and the volume shrinkage rate is not yet available, a quantitative determination of the stresses build-up during the curing procedure can not be obtained.

The test results have shown (Ten Busschen 1995) that, among the total volume shrinkage 9.3%, about 2.7% (linear shrinkage 0.9%) occurs in the solid state and 6.6% (linear shrinkage 2.2%) in the liquid state. When the polyester changes in phase from the liquid state into the solid state, the material firstly behaves quite soft and then gradually becomes harder. Hence only a part of the shrinkage contributes to the stress built up in the composite. Ten Busschen (1995) has introduced an equivalent initial strain to provide an initial stress state of a UD composite for time independent analysis of the ultimate strength of this composite.

In this report, a volume reduction of 1.05% (equivalent to a linear initial strain -0.35%) was chosen for investigation of possible influences of shrinkage on the time dependent composite behaviour. The distributions and redistribution of stress and strain fields due to the viscoelastic property of the matrix and the influences on the loading situations are considered. The above volume reduction of 1.05% is in some sense arbitrarily chosen, however, it was found that higher initial strain values resulted in too large stresses (above the strength of the material).

A calculation for an initial strain of 0.9% (as used by Ten Busschen for the time independent case) resulted in quite unrealistic stress levels, using the "time-dependent" material data. Computational results for different initial strain levels are presented in Section 7.8.5. The major reason of this is due to the fact that before the material is cured to a certain degree, its relaxation time is considerably small (or the material is soft). Hence a part of the shrinkage occurring in the early stage will generate relatively small stresses. Thus to adopt an equivalent initial strain, -0.35%, for a time dependent analysis (a smaller value than -0.9% as used by Ten Busschen might be reasonable for a time independent analysis).

7.8.2 Prestress state due to matrix shrinkage

After initial loading by a strain of -0.35% and subsequent relaxation of the stress field for one month, the stress distributions as shown in Fig. 7.46 are found. The maximum principal stress as well as the effective stress are shown. Further, in Fig. 7.47, both the maximum principal stress and the minimum

principal stress in the matrix around the centre fibre are drawn. The figure shows that over a relatively long arc, there is a large tensile stress ($90^\circ < \theta < 160^\circ$) while at two positions a large compression stress is found ($\theta = 0^\circ$ & 60°), see Fig. 7.47.

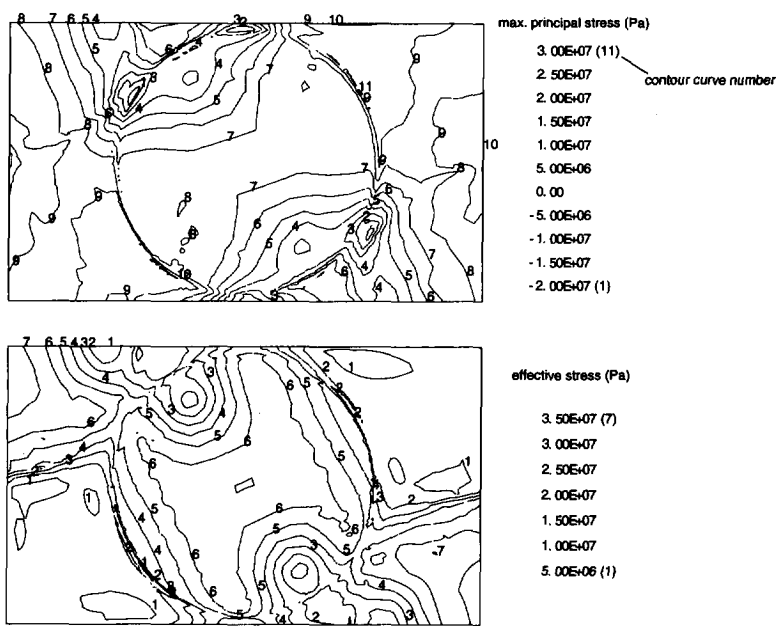


Figure 7.46. Contours of maximum principal stress and effective stress due to initial strain at $t = i$ month

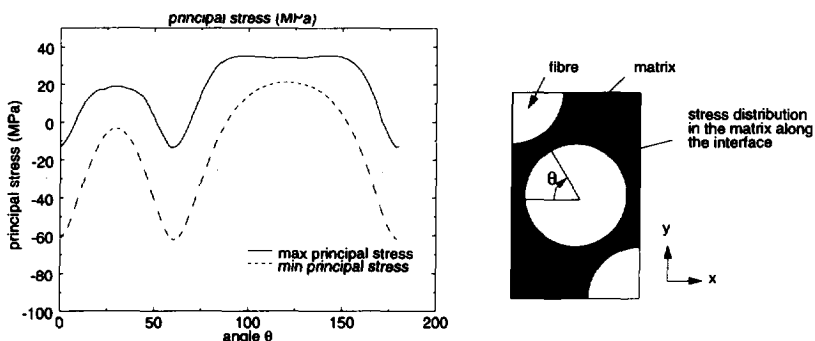


Figure 7.47. Shrinkage induced prestress at $t = 1$ month, numerical model type 1, initial strain 0.35%

7.8.3 Relaxation and creep in the matrix without external loading

The composite usually will not be used immediately after its manufacturing. The products will be stored and transported and will be used after a period of several months to more than a year. Therefore the age of the products may vary in a large range. Hence we need to know how the prestress field in the composite will change during that period of time, since the current prestress field will influence the loading response once it is loaded in application. Fig. 7.48 to Fig. 7.50 illustrate the change of the stress fields and the strain fields after one month of creep/relaxation. Surprisingly the maximum shear stress and the effective stress reduce to about half the initial amplitudes. The strains increased within this period.

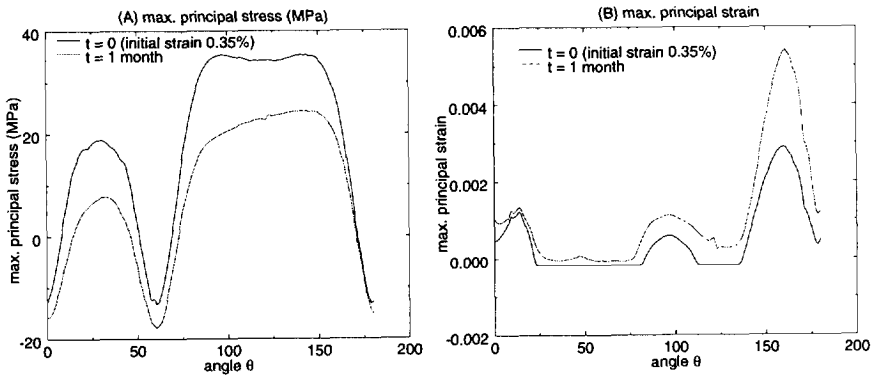


Figure 7.48. Stress change and strain increase due to the relaxation and creep process, starting from an initial strain induced prestress state, 61.8% f_y, numerical model type 1

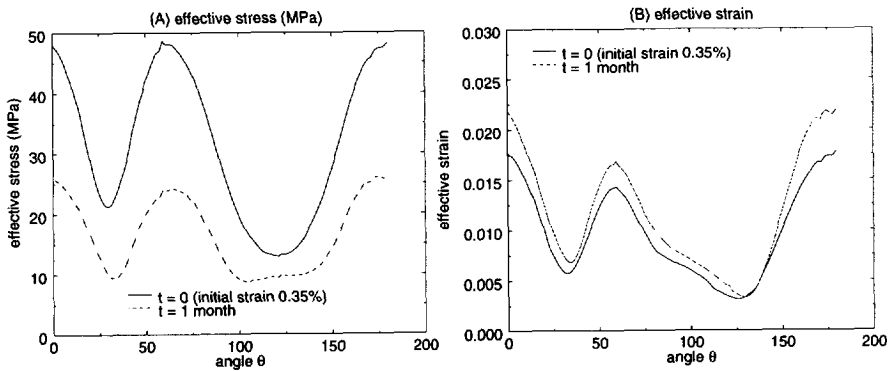


Figure 7.49. Effective stress and strain (same conditions as those in Fig. 7.48)

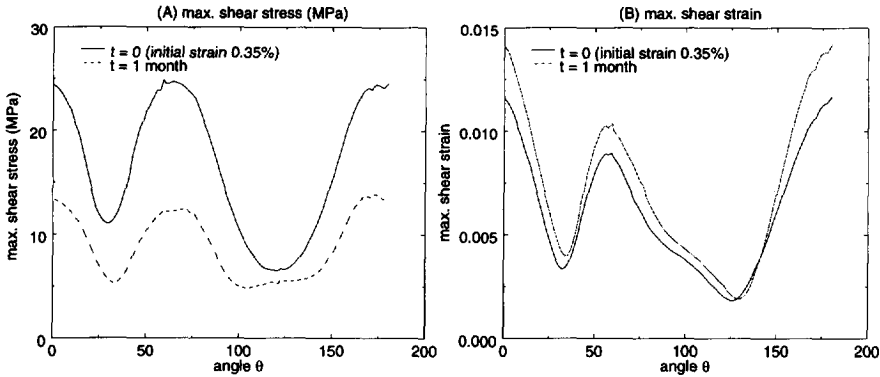


Figure 7.50. Maximum shear stress and strain (same conditions as those in Fig. 7.48)

Fig. 7.51 illustrates a unanimous decline of different stresses of an initially prestressed composite, due to the ongoing creep and relaxation process in the matrix material. An extrapolation of these curves can provide a theoretical prediction that all stresses initiated by shrinkage of the matrix may eventually vanish due to the viscoelastic properties of the matrix. For this case the complete relaxation would take about 4500 years.

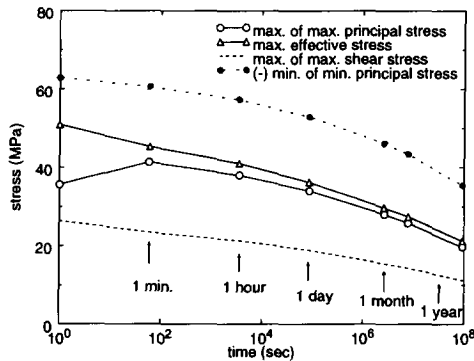


Figure 7.51. Declining stress concentration in the matrix (a case without external load), model type 1, 61.8% f_v , initial strain 0.35%

7.8.4 Influence of prestress on composite creep

When the model cell (type 1, fvf 61.8%) is loaded in different directions, the stress distribution patterns around the fibre are different.

The initial strain influenced results are exhibited in subsequent steps, the comparisons between different loading directions are shown afterwards.

1. X-direction loading

The load situation is demonstrated in the following figure. The stress distributions are presented for the matrix around the interface of the centre fibre, where the angle θ provides the exact positions of the stresses, being presented.

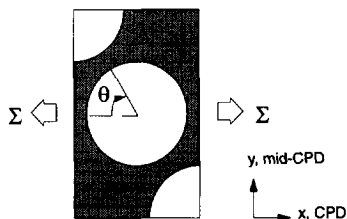


Figure 7.52. Cell model type 1 loaded in CPD, $\Sigma = 24\text{MPa}$

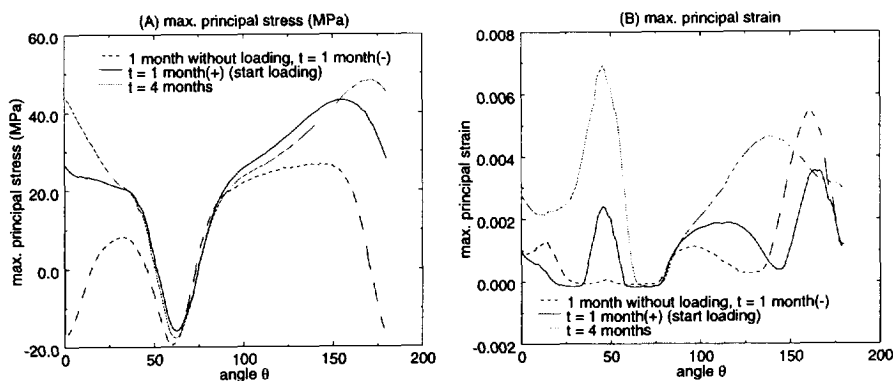


Figure 7.53. Influence of shrinkage on the global creep case. Maximum principal stress and strain, matrix initial strain 0.35%, fvf: 61.8%, global load: 24MPa in CPD

It can be seen from Fig. 7.53 that there is a compression area in the matrix at about $\theta = 60^\circ$, even after application of the tensile loading to the model. On the other hand, from Fig. 7.54, a high peak of

effective stress can be observed in the vicinity of $\theta = 55^\circ$. Due to the fact that the strain continuously increases, this place is likely to show the first matrix failure.

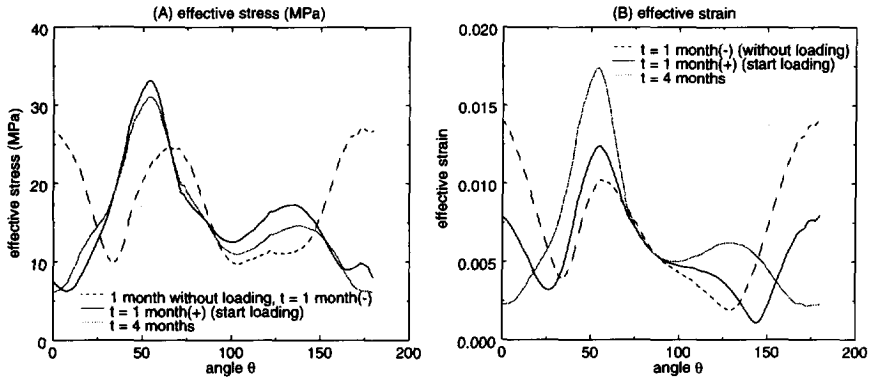


Figure 7.54. Influence of shrinkage on the global creep case. Effective stress and strain. Matrix initial strain 0.35%, f_{vf} 61.8%, global load: 24MPa in CPD

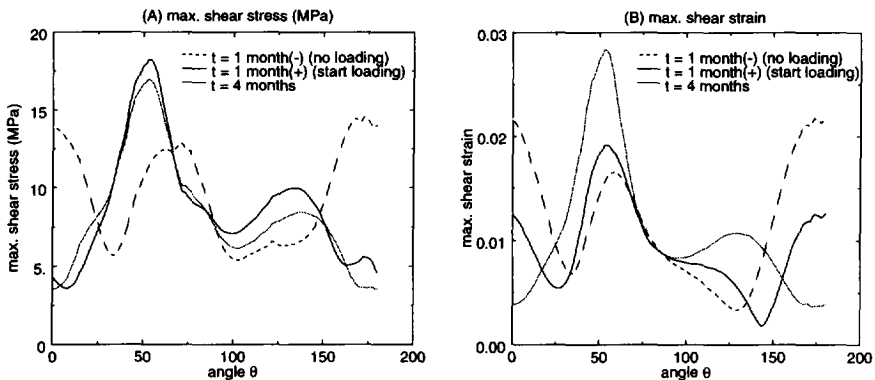


Figure 7.55. Influence of shrinkage on the global creep case. Maximum shear stress and maximum shear strain. Matrix initial strain 0.35%, f_{vf} 61.8%, global load: 24MPa in CPD

2. Y-direction loading

Under a Y-direction or mid-CPD loading, there is a compression area at $\theta = 0^\circ$. Very closely, a effective stress peak locates at $\theta = 170^\circ$.

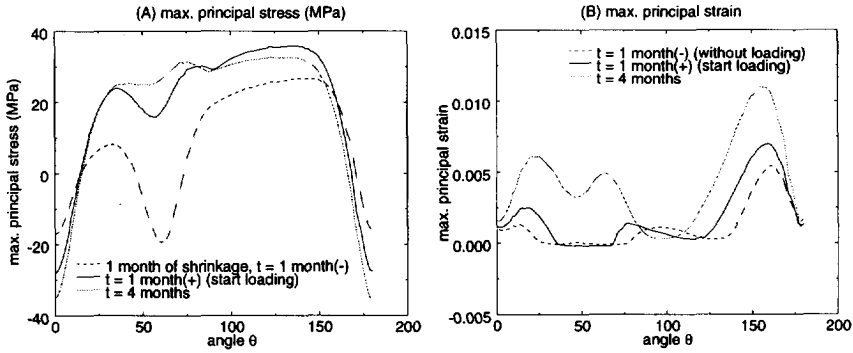


Figure 7.56. Maximum principal stress and strain. Initial strain + mid CPD loading case. Matrix initial strain 0.35%, $f_v f$: 61.8%, load: 24MPa in y-direction

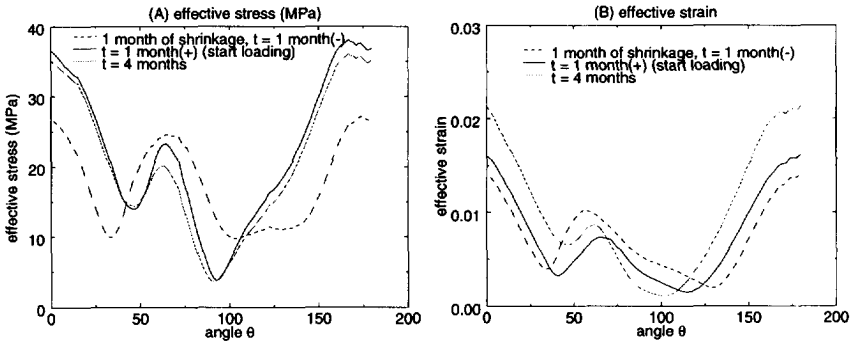


Figure 7.57. Effective stress and strain, for conditions as specified in Fig. 7.56

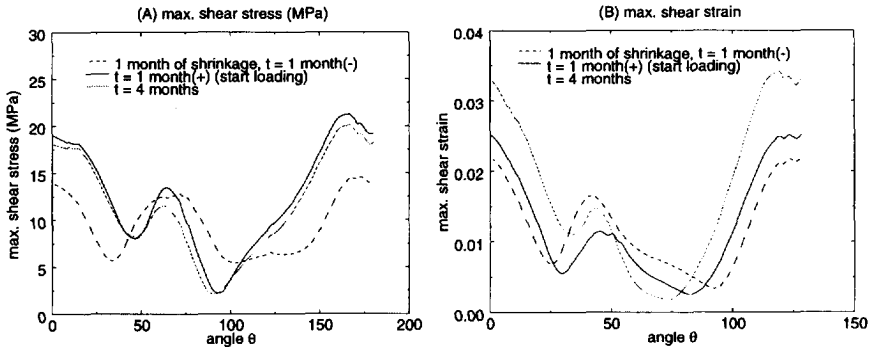


Figure 7.58. Maximum shear stress and strain, for conditions as specified in Fig. 7.56

3. Comparison between different loading directions

The comparisons have shown that the compression areas always exist at the narrowest matrix regions, $\theta = 60^\circ$ (x-dir. loading) and $\theta = 0^\circ$ (y-dir. loading). The maximum of the effective (or of the maximum shear) stress locates in the vicinity of these regions, $\theta = 55^\circ$ and $\theta = 175^\circ$.

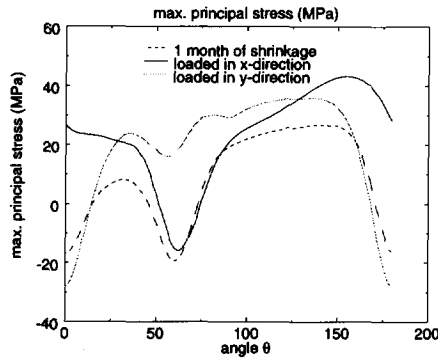


Figure 7.59. Maximum principal stress. Matrix initial strain 0.35%, fvf: 61.8%, load: 24MPa in x- and y-direction respectively

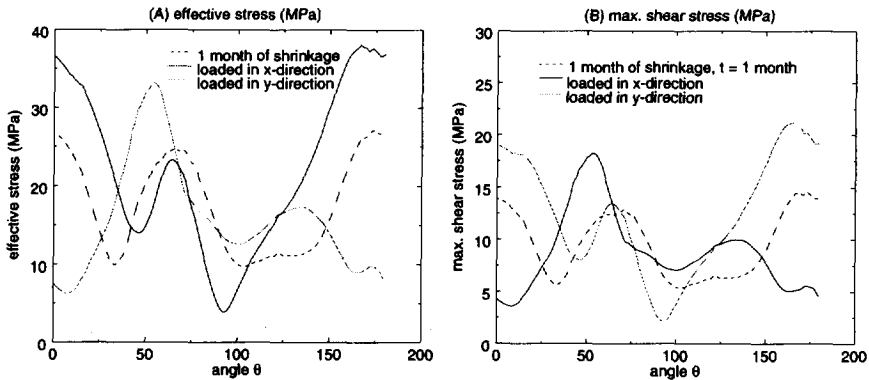


Figure 7.60. Maximum shear stress and effective stress. Matrix initial strain 0.35%, fvf: 61.8%, load: 24MPa in x- and y-direction respectively

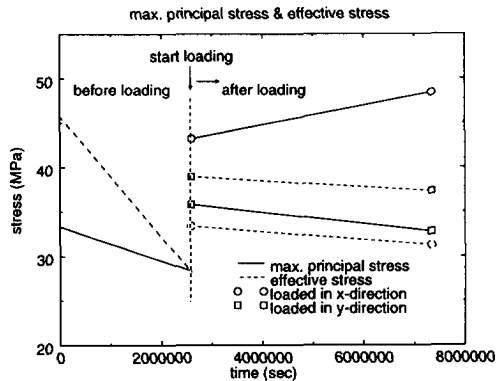


Figure 7.61. Maximum stress before and after loading (linear interpolations between discrete times). Matrix initial strain 0.35%, f_{vf} 61.8%, model type 1

Fig. 7.61 demonstrates the tendency that both the maximums of the maximum principal stress and of the effective stress decline before the loading is being applied. But after loading, the maximum of the maximum principal stress increases with time, if the model is loaded in x-direction. An increasing principal stress at the interface may cause the matrix-fibre debonding.

It is observed that before the loading is being applied, the position of the maxima change with time. But after the application of the loading, these maxima remain on the same positions.

4. Global Strain

The global strain in the transverse direction of UD composites is a measurable quantity, and therefore is one of the limited items which can be used for comparison between theory and experiment. Fig. 7.20 has already shown a comparison between the experimental data and the theory with the cell model type 1. Here the results related to different matrix shrinkage histories and global loading directions are put together. The difference between these theoretical curves is small, see Fig. 7.62. This tells us that the shrinkage gives little influence on the global creep behaviour of UD composites. Although the local distribution and the magnitude of stresses and strains are significantly affected by the matrix shrinkage. In other words, the matrix shrinkage will turn out to be significant, for the cracking and fracture behaviour of composites and hence for the strength in the transverse direction of the composites. However, the matrix shrinkage has little effect on the global stiffness of the composites.

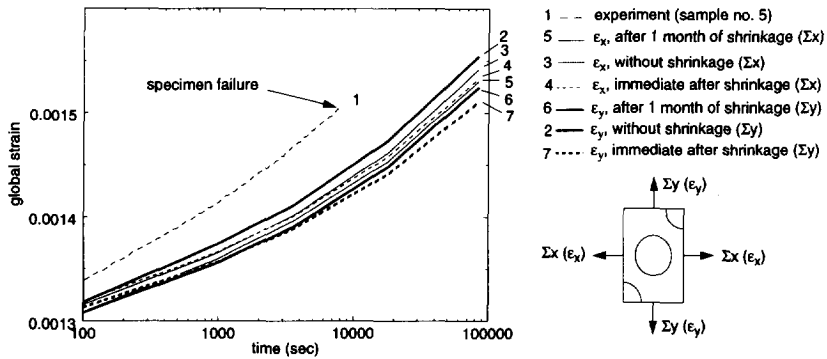


Figure 7.62. Influence from prestress on creep, matrix initial strain 0.35%, f_{fj} : 61.8%, load: 24MPa

5. Stress Evolution in a Prestressed Model Cell

The matrix shrinkage of UD composites may cause a significant change in the stress and strain distributions. Furthermore, the stress and strain fields will redistribute due to the time elapsing and the change in loading. Fig. 7.63–Fig. 7.66 illustrate these time dependent fields.

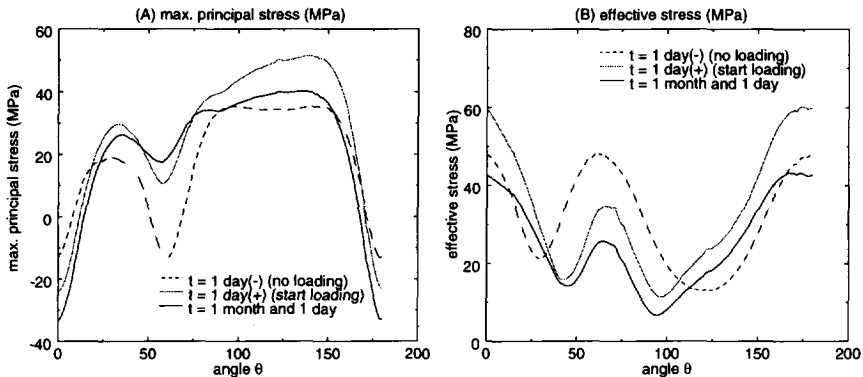


Figure 7.63. Stress Redistribution in Prestressed Composite, numerical model type I, matrix initial strain 0.35%, creep load 24MPa in mid-CPD

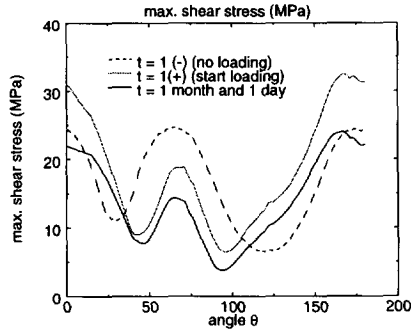


Figure 7.64. Stress Redistribution in Prestressed Composite, numerical model type 1, matrix initial strain 0.35%, creep load 24MPa in mid-CPD

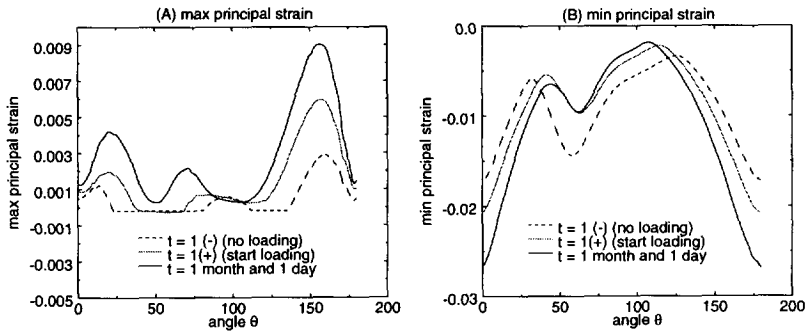


Figure 7.65. Strain Development in Composite Creep, numerical model type 1, matrix initial strain 0.35%, creep load 24MPa in mid-CPD

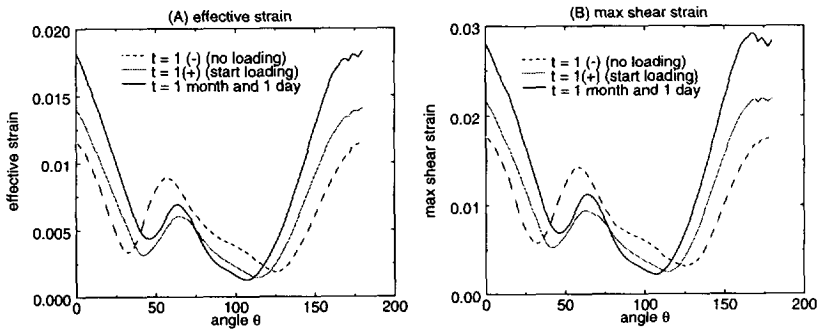


Figure 7.66. Strain Development in Composite Creep, numerical model type 1, matrix initial strain 0.35%, creep load 24MPa in mid-CPD

7.8.5 The Influence of Matrix Initial Strains

Different matrix initial strains are applied to investigate the local stress distributions and the global strains in creep deformation. The numerical work has been done according to the following conditions

numerical cell model type	type 1
fiber volume fraction of the composite	61.8%
aging time of the matrix material	1 month
global constant load and its direction	24 MPa in x-direction
specimen used in experiment	tube # 5
creep time for tests(22°C, r. m. 50%)	1 day

Table 7.5. Test and calculation conditions

In the matrix of the model cell (type 1), the maxima and the minima of the principal stress and the effective stress are listed in the following tables.

initial strain	principal stress (MPa)		effective stress (MPa)	
	maximum	minimum	maximum	minimum
0.0035	37.56	-66.12	56.39	8.142
0.005	60.30	-91.92	74.52	10.35
0.006	73.08	-106.30	81.80	12.47
0.007	84.54	-116.40	82.71	14.49
0.008	94.47	-127.30	86.54	16.38
0.009	104.30	-136.20	88.39	18.32

Table 7.6. Principal stress and effective stress in the model cell (type 1) immediately after the matrix shrinking

When the initial strain is higher, the maximum of the principal stress and the maximum of the effective stress both increase. A modified effective stress is defined as

$$\sigma_e = [(\sigma_1 - \sigma_2)^2 + (\sigma_2 - \sigma_3)^2 + (\sigma_3 - \sigma_1)^2]^{\frac{1}{2}} + 0.34(\sigma_1 + \sigma_2 + \sigma_3), \quad (7.5)$$

This effective stress was suggested by Ten Busschen (1992)^[13] for a failure criterion of the matrix material, where failure occurs for unsaturated polyester resin when

$$\sigma_e > \sigma_{cr} = 153 \text{ MPa}. \quad (7.6)$$

initial strain	modified effective stress (MPa)	
	maximum	minimum
0.0035	69.25	30.16
0.005	103.42	40.85
0.006	121.22	46.12
0.007	133.75	39.83
0.008	145.53	37.56
0.009	154.98	32.70

Table 7.7. Modified effective stress in the model cell (type 1) immediately after the matrix shrinking

In Table 7.7, for the highest initial strain case, the modified effective stress exceeds the criterion, which suggests a local failure due to matrix shrinkage alone. These maximum stresses are presented once again in the following graph:

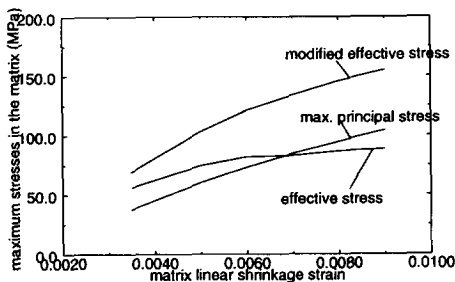


Figure 7.67. The stress maxima in the matrix vs. matrix initial strain

The strength of the interface between the matrix and the fibres is not a subject of this research. But it might be lower than the matrix strength. In that case, even for a lower matrix initial strain, debonding of the interface might occur.

In Fig. 7.69, the specimen failed after about 8000 sec. The comparison shows a larger slope of the test data (or a faster creep rate) compared to the calculated results. Possible reasons are the fact that the model parameters were determined from other specimens; material and/or interface damage most probably occurred during the test (these effects are not described by the computational model). The model does not include these factors. Therefore the model will give a conservative estimation, which means the calculated results should be smaller than the test data and should have a smaller creep rate. However, for higher initial strains, the calculation of the global strain apparently overestimates the measured strain (Fig. 7.69). This suggests that the initial strain used in the calculations should be cho-

sen to be relatively small. Using an initial strain of 0.35% is found not contradictory to what has been discussed above.

Fig. 7.68 gives distributions of the effective stress for two cases with different initial strains. The comparison suggests that the stress distribution patterns are similar except for the amplitudes.

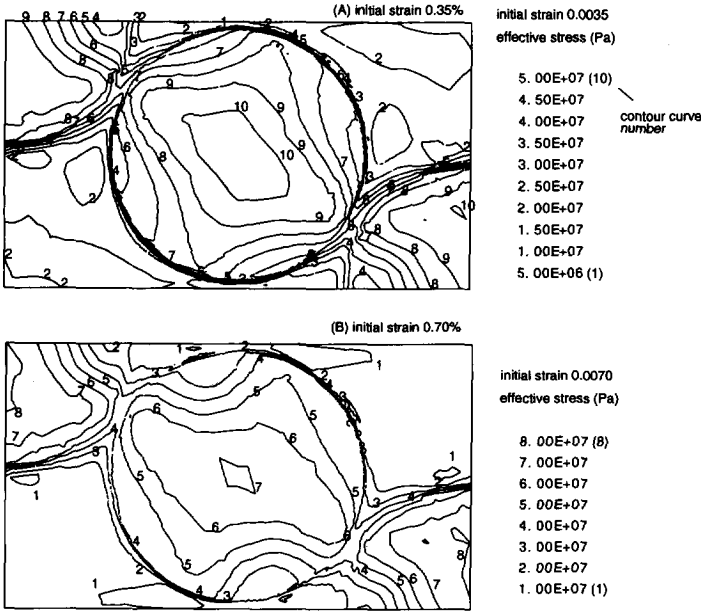


Figure 7.68. Effective stress distribution, numerical model type 1, fvf 61.8%, global load 24MPa in x-dir; the matrix shrinkage was made by an initial strain 0.35% and 0.70% respectively. Application of loading after one month of creep. Pictures show situations directly after loading setup.

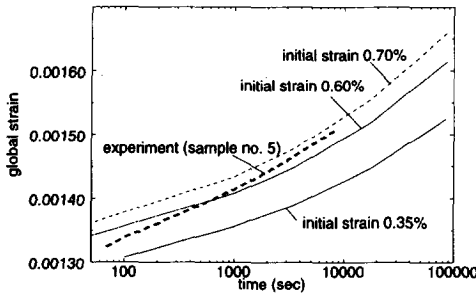


Figure 7.69. Comparison between the numerical results and the experiment results, composite creep in tensile load 24MPa for different matrix shrinkage strains, directly after loading-set-up. For other data see Table 7.5.

7.8.6 Global Loading Level Influence on the Stress Distribution Patterns

Along a half interface, see Fig. 7.70, the maximum principal stress distribution forms a one-peak pattern when the global stress is large. While for the pure shrinkage case and the case of a small global load (10MPa), the stress patterns also show local maxima (peaks).

The change of the distribution pattern can be seen in the effective stress plot as well as in the maximum shear stress plot, see Fig. 7.71. When the global stress is small (10MPa), one of the two local maxima originating from the initial strain influence retreats at the position, $\theta = 175^\circ$, while the other exhibits at the position, $\theta = 70^\circ$. After further increase of the global load, one local maximum disappears (at $\theta = 175^\circ$), while another one is formed (at $\theta = 130^\circ$).

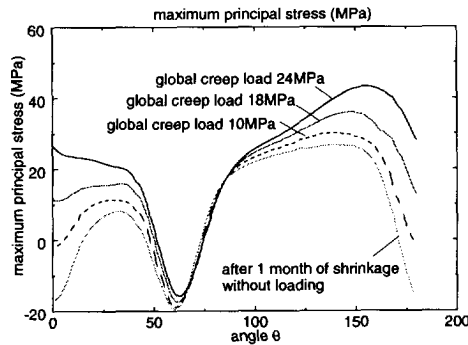


Figure 7.70. Maximum principal stress distribution, fvf 61.8%, type I, one month after initial strain of 3.5% and subsequent creep. Immediate after loading in x-dir.

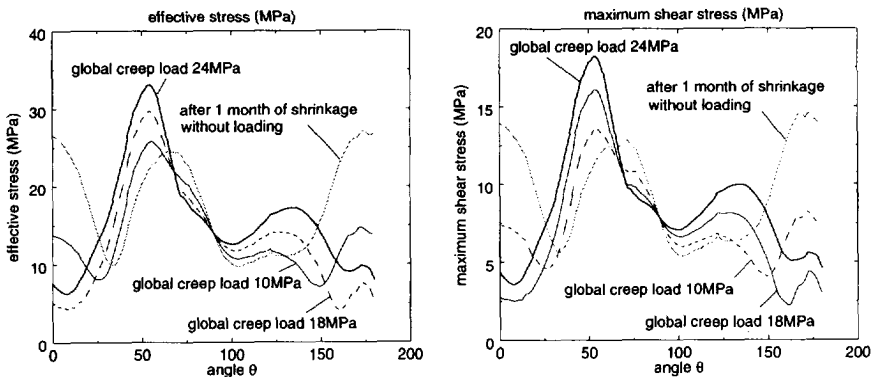


Figure 7.71. Maximum shear stress and effective stress distributions, fvf 61.8%, type I, one month after initial strain of 3.5% and subsequent creep. Immediate after loading in x-dir.

The influence of initial strain on the stress patterns is so large that both the amplitude and the position of the maxima will never be the same compared to the cases without shrinkage (see, *e.g.*, Fig. 7.33 and Fig. 7.34). Hence the shrinkage will contribute not only to a possible earlier initiation of cracking or debonding, but will also influence the initial cracking place, which in turn might evolve a completely different fracture path in the composite.

7.8.7 Stress Fields in the Model Cell

Through numerical simulation, it was found that the global creep deformation is not very sensitive to the local micro-structure of the composite. However, the local stress distributions and stress concentrations are. However the local stress distributions and stress concentrations are quite dependent of the local structure. Next few paragraphs show stress distributions for various models, with and without initial strain influence.

1. 24MPa globally loaded in the *x*-direction

The model was loaded in CPD (the closest packing direction) or *x*-direction, see Fig. 7.72.

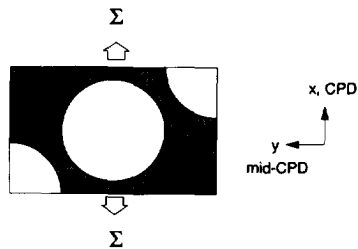


Figure 7.72. Model type 1 loaded in CPD

Stress results with and without initial strain influence are presented in Fig. 7.73 and Fig. 7.74. With or without initial strain influence, the stress distributions are completely different. This suggests that the shrinkage may introduce a different location of crack initiation and a different fracture behaviour.

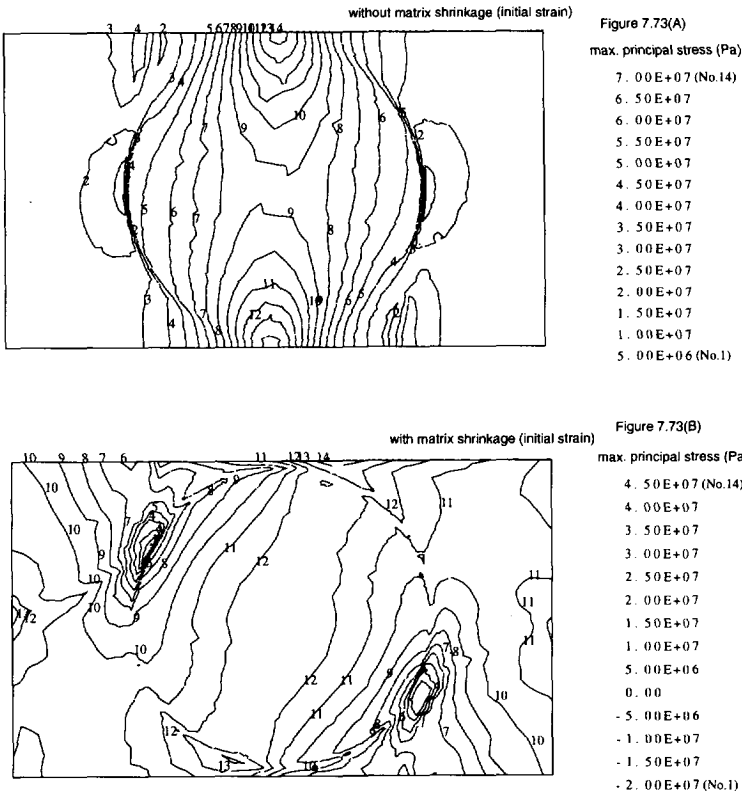


Figure 7.73. Maximum principal stress distribution directly after loading set-up. Numerical model type 1, f_{yf} 61.8%, global load 24MPa in x-dir; matrix shrinkage was initiated by an initial strain of 0.35%, the global load was applied after a month of creep

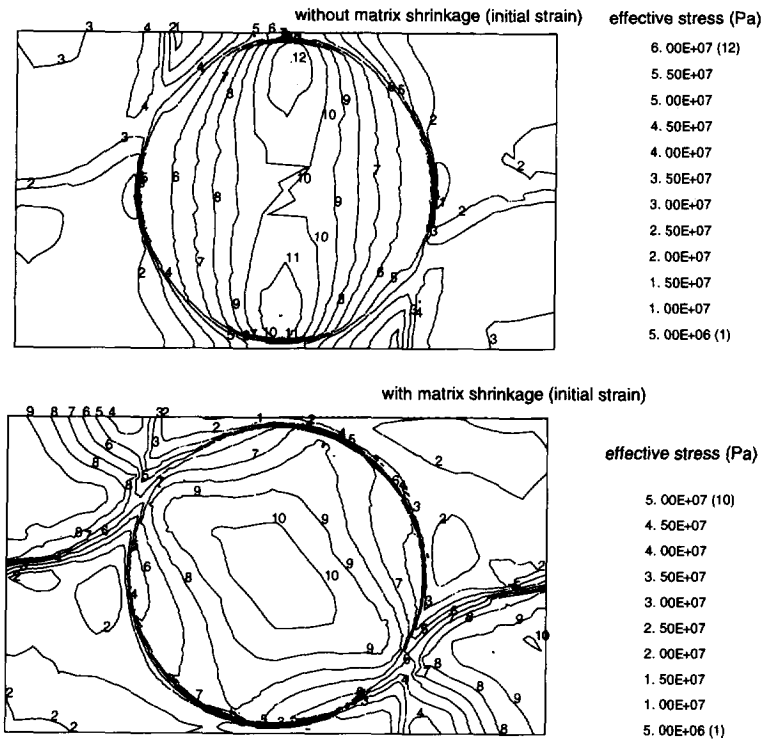


Figure 7.74. Effective stress distribution directly after loading set-up. Numerical model type 1, f_{vf} 61.8%, global load 24MPa in x-dir; matrix shrinkage was initiated by an initial strain of 0.35%, the global load was applied after a month of creep.

2. 24MPa globally loaded in the y-direction

In this section, the model cell is loaded in y-direction, or mid-CPD. Stress results with and without initial strain influence are shown in Fig. 7.76 to Fig. 7.78.

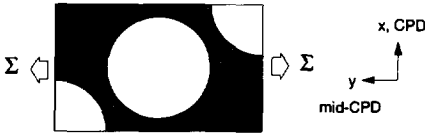


Figure 7.75. Model type 1 loaded in mid-CPD

Again, we have found completely different stress fields due to the initial strain influence.

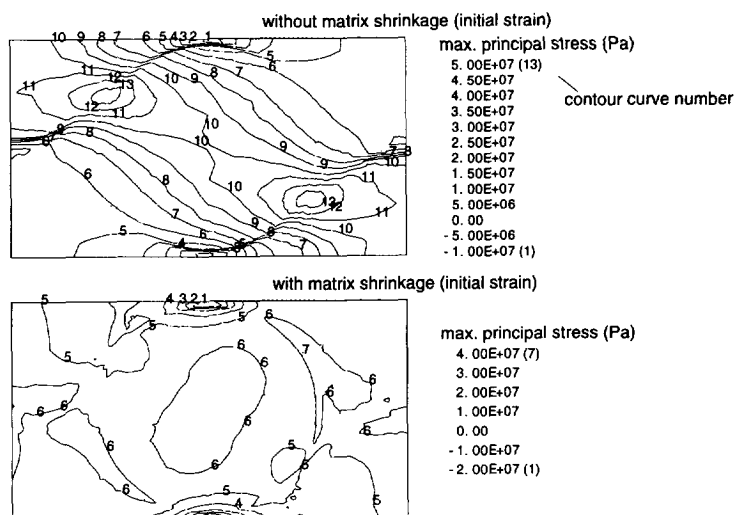


Figure 7.76. Maximum principal stress distribution directly after loading set-up. Numerical model type 1, f_{yk} 61.8%, global load 24MPa in y-dir; matrix shrinkage was initiated by an initial strain of 0.35%, the global load was applied after a month of creep.

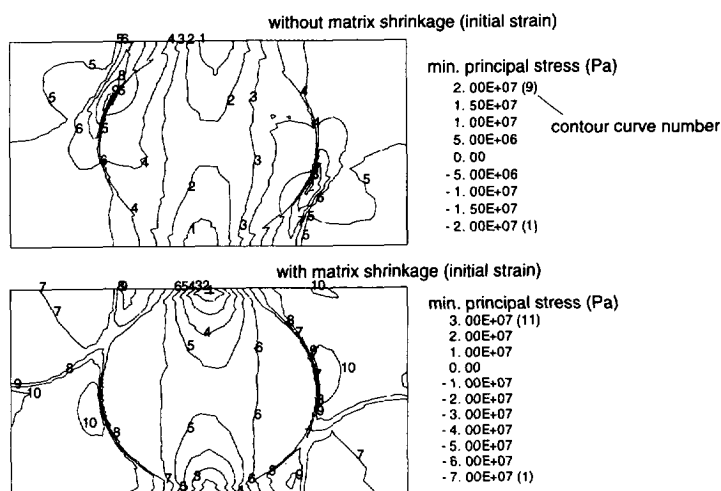


Figure 7.77. Minimum principal stress distribution directly after loading set-up. Numerical model type 1, f_{yk} 61.8%, global load 24MPa in y-dir; matrix shrinkage was initiated by an initial strain of 0.35%, the global load was applied after a month of creep.

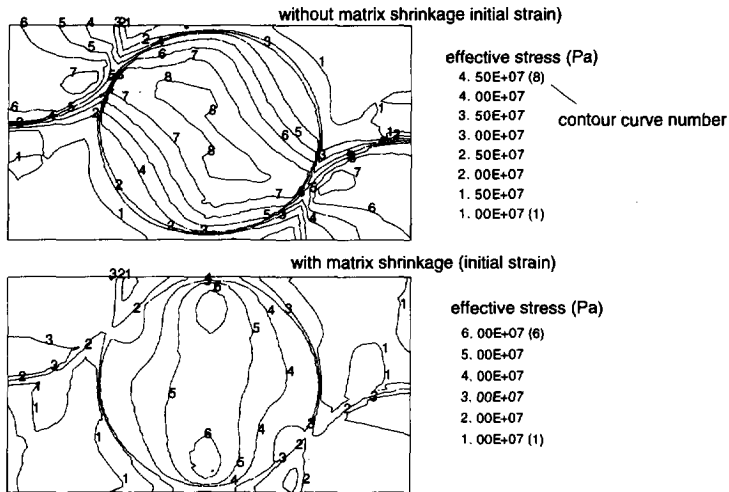


Figure 7.78. Effective stress distribution directly after loading set-up. Numerical model type 1, v_{f0} 61.8%, global load 24MPa in y-dir; matrix shrinkage was initiated by an initial strain of 0.35%, the global load was applied after a month of creep.

7.9 Interphase Influence

No conclusive evidence of the existence of an interphase between fibre and matrix has been found from experimental observations in case of a glass-polyester system. It is still possible that a mechanical weak interphase layer exists (due to entrapped gas, moisture, contaminants, etc.). This layer with lower cohesive properties than their bulk counterparts results at least in reduction in efficiency of load transfer at the interface. The influence of possible interphase behaviour on the local stress fields will be considered here. Some efforts about interfacial effects on the global deformation of the composite have been done by Ten Busschen (1995) by assuming a frictional contact on the interface between fibre and matrix. Here an interphase layer has been assumed in order to examine the possible effect of changed material properties of an interphase on the global creep behaviour.

The influence of the interphase between the matrix and the fibre has been tested numerically by a hexagonal cell model, with a fibre volume fraction of 60%. No experimental results are available. Only the comparisons between numerical results are presented in this section. The mesh for the finite element analysis is presented in Fig. 7.79. The thickness of the interphase is taken to be 4% of the fibre radius. The interphase volume fraction is 4.9%.

There are three situations being considered, without interphase, with a "faster creep interphase" and with a "softer interphase". The "faster creep interphase" has a doubled creep parameter C (defined in

Chapter 2). This suggests a faster creep property of the interphase (doubled creep strain). For a "softer interphase" the Young's modulus of the interphase is taken to be 20% of that of the matrix itself.

The results have shown that when a softer interphase exists, the effective strain (defined in Eq (7.3)) will be more concentrated in the interphase, see Fig. 7.80. While for the effective stress distribution, the three different interphases show little differences, see Fig. 7.81.

However, the maximum modified effective stresses, defined in Eq (7.4), yet show relevant differences between different types of interphases (see Table 7.8 and Table 7.9). Some phenomena can be observed from the tables,

1. In both matrix and interphase (if this exists) the maximum modified effective stresses decline during the relaxation period before loading set up and rise during the global creep stage after set up of the loading;
2. The existence of the interphase, for both cases, will cause a difference in the maximum modified effective stress;
3. With one exception only, the maximum modified effective stress is lower in the interphase than in the matrix.

Max. modified effective stress in matrix (MPa)	shrinkage start	after one month	loading start	after one month
without interphase/interface	47.00 (#2554)	31.53 (#3050)	53.72 (#2915)	59.35 (#2106)
with an easier creep interphase	46.95 (#2379)	26.70 (#2557)	50.01 (#2548)	56.02 (#2861)
with a softer interphase	48.64 (#2376)	27.87 (#2559)	52.13 (#2861)	54.34 (#2861)

Table 7.8. The maximum effective stress in the matrix for different interphase conditions. Numerical results for a hexagonal cell, fibre volume fraction 60%, matrix and interphase volume shrinkage 1.05% (i.e., initial strain 0.35%), loading started after one month: 24MPa in CPD.

Max. modified effective stress in interphase (MPa)	shrinkage start	after one month	loading start	after one month
with an easier creep interphase	41.42 (#3002)	22.61 (#3050)	50.11 (#2912)	52.44 (#2877)
with a softer interphase	11.10 (#2074)	11.00 (#3050)	45.10 (#2125)	48.10 (#2128)

Table 7.9. The modified maximum effective stress in the interphase for different interphase conditions. Numerical results by a hexagonal cell, fibre volume fraction 60%, matrix and interphase volume shrinkage 1.05% (i.e., initial strain 0.35%), loading started after one month: 24MPa in CPD.

In Table 7.8 and Table 7.9, the numbers within parentheses indicate the element numbers. The change of these numbers suggests a relocation of the stress concentration.

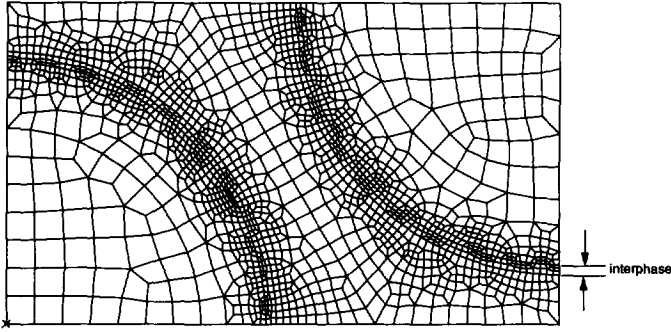


Figure 7.79. The mesh for a hexagonal cell with an interphase, the interphase layer contains two or three elements in the thickness direction

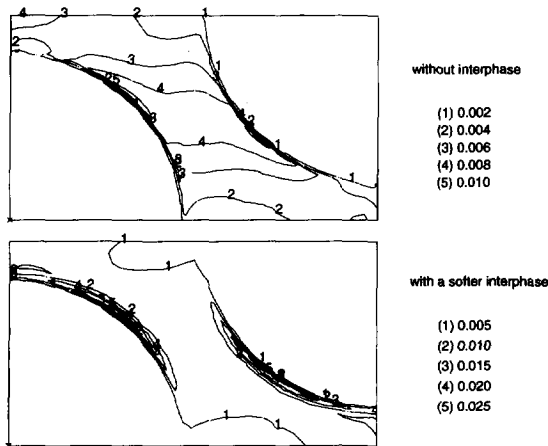


Figure 7.80. Effective strain distribution after one month of loading (matrix initial strain 0.35%, without external loading stress/strain redistribution for one month subsequently, load application (24MPa in CPD) and again stress/strain redistribution for another month.

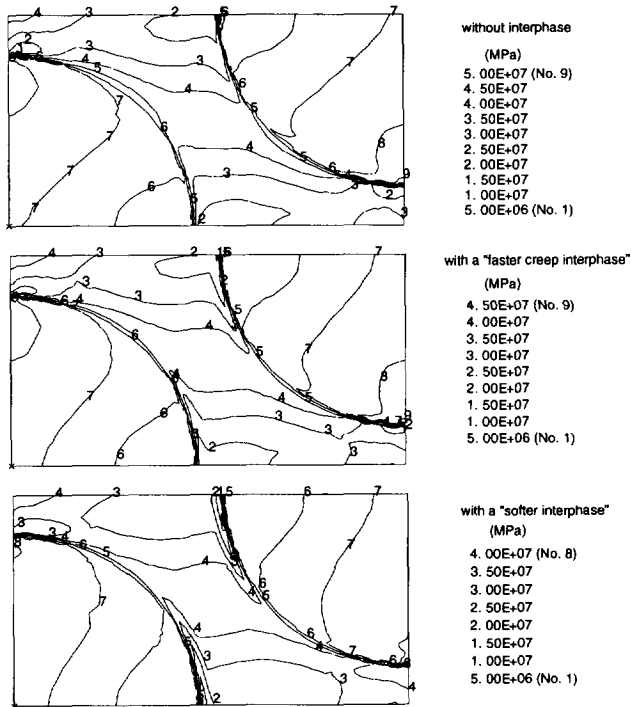


Figure 7.81. Effective stress distribution after one month of creep loading (matrix initial strain 0.35% without external loading stress/strain redistribution for one month subsequently, load application (24MPa in CPD) and again stress/strain redistribution for another month.

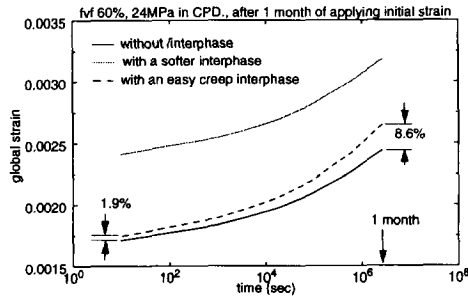


Figure 7.82. Global strains for different interphase conditions, numerical results by a hexagonal cell, fibre volume fraction 60%, matrix and interphase have initial strain of 0.35%, the global load, 24MPa CPD, was applied after one month of creep

Fig. 7.82 demonstrates that the influence of two different interphases on the global creep deformation. For a "softer interphase", the global creep deformation is mainly shifted upwards. But for a "faster creep interphase", an apparent acceleration of the global creep can be seen in Fig. 7.82, from 1.9% difference at 10 sec. to 8.6% at 1 month.

7.10 Conclusions

The fibre packing geometry plays an important role in the transverse creep simulation of unidirectional composites. After establishing an accurate matrix stress-strain relationship (at least under a mild stress range), we are able to examine the creep behaviour of traditional hexagonal and rectangular types of fibre packing geometry by means of a finite element approach and then to compare the results with experimental data. The comparison shows that the global strains from the calculation are always overestimated by these traditional forms of fibre packing geometry. The rectangular packing reveals a severe anisotropic property, not leading to an appropriate simulation of reality. The overestimation of the strains give us evidence that the uniform fibre distribution is an over-simplification of the fibre packing geometry. In reality, the fibres are distributed randomly and non-uniformly. There are fibre-rich regions and matrix-rich regions which play different roles in the deformation. The matrix-rich regions contribute to a major part of the global strain while the fibre-rich regions possess the highest stresses. Therefore taking into account the influence of fibre-rich regions and matrix-rich regions can provide not only more accurate global deformation predictions, but also a better prediction of the local stress field of UD composites. We have developed two different types of fibre packing geometry, which are locally non-uniform but globally still periodic. The advantages of these types of geometry include simplicity for calculation, local non-uniform distribution of the two constituents and (almost) global isotropic properties. The comparison between theory and experiment for the global strain shows a satisfactory model description.

The non-uniform fibre packing geometry will result in a higher stress concentration within the matrix as well as within a possible fibre-matrix interphase. On the other hand, a high fibre volume fraction and eventually contact of fibres will also enhance the stress concentration. Some calculations have been done for a random packing model, in Section 7.7, and for other types of cell models with different fibre volume fractions.

With or without matrix shrinkage or initial strain, the global stiffness of composites hardly changes. But a pre-shrunk composite exhibits a higher stress concentration and completely different stress and strain distributions. Hence the shrinkage does have its influence on the local stress fields and consequently in the initiation and development of crack behaviour, but not significantly in the global transverse behaviour of composites if the crack initiation does not yet occur.

The manufacturing of a composite with a "softer" or a "faster creep interphase" can be helpful for the reduction of the stress concentration within the matrix and within the interphase.

Conclusions

8.1 General Conclusions

This thesis presents the research results in three aspects:

- A. a constitutive model for an unsaturated polyester resin;
- B. the numerical implementation of the model into an FEM package;
- C. the transverse creep of a unidirectional unsaturated polyester/glass fibre composite.

8.1.1 A constitutive model for an unsaturated polyester resin

A time-dependent nonlinear model has been established on the basis of a theory, due to Schapery. The model has been modified and improved in order to have a better description of the studied material.

The conclusions are

1. *The kernel function of Schapery's model should be chosen to be an exponential function, Eq (2.9) instead of the usual power law. The exponential function provides a more accurate description of the creep behaviour of the unsaturated polyester. This is especially true when predicting long-term behaviour where physical ageing effects are important.*

2. *In the general three dimensional model, two constants are presented, the instantaneous Poisson's ratio and the creep Poisson's ratio. The constancy of the creep Poisson's ratio prevents a difficult description of a time/deformation dependent Poisson effect. A testing method has been presented for the measurement of the creep Poisson's ratio, Section 4.3.3.*
3. *Physical ageing is incorporated into the model by a time-shifting effect, see Section 2.3.5. The shifting factor has been measured through experiments, Section 3.1.*
4. *The model parameters have been analysed leading to a better understanding of the viscoelastic theory. Specific conclusions are summarized in Section 3.2.7.*
5. *A simplified model, with only two nonlinearizing model parameters, has been found accurate enough for the studied material. The model is restated in Section 5.2.1 and Section 5.3.1. Its discretized form for FEM analysis is presented in Section 6.2.2.*

8.1.2 Numerical implementation of the model into an FEM package

The 3D model has been implemented into an FEM package (DIANA). The exponential series Eq (5.42) has been used to replace the exponential function Eq (2.9). By this technique, the numerical scheme contains only the variables of the previous time step and the present time step. This therefore avoids the storage of all the information of the stress history for evaluation of the convolution integral of the model.

1. *The DIANA simulation has sufficient accuracy for short-term and physical ageing influenced long-term creep (Section 5.3), for the cyclic loading situation (Section 5.3), for a 2D stress state of a plate with a circular hole (Section 6.2), and for a biaxial loading case (Section 6.3).*
2. *The numerical method has adequate convergent speed, especially for the creep calculation.*
3. *The relaxation simulation has also been checked indirectly. In the case of a plate with a circular hole, Section 6.2, stress relaxation occurs at the edge of the hole. Due to the fact that the comparison of the strain between calculation and experiment exhibits a good agreement, the relaxation process is appropriately simulated.*

8.1.3 Transverse creep of a unidirectional polyester/glass fibre composite

The modelling of transverse creep of a unidirectional composite in this thesis has been concentrated on two aspects: the study of the fibre packing geometry in the numerical simulation and the influence of the initial strain introduced by matrix shrinkage, Section 7.8. This initial strain is a lumped parameter for underlying causes as matrix cure shrinkage, difference in thermal expansion between fibre and matrix, etc. The interphase influence, Section 7.9, has been touched very briefly due to a lack of experimental information. The conclusions of this study are as follows.

1. *Two special types of fibre packing geometry are presented. A new fibre packing geometry yields quite a good replacement model for the random packing which is present in reality, Section 7.5.*
2. *By means of the new fibre packing geometry, the global strain is successfully calculated in creep cases. The local stress strain fields and their changes with time are presented in Section 7.6.*
3. *The initial strain due to matrix shrinkage changes the local stress and strain fields completely, but the global strain does not differ much from the case without initial strains. The stress field will be relaxed after a period of time. The initial strain generally causes a higher stress concentration.*
4. *The case of a 'softer' or a 'faster creep interphase' has shown a tendency of reducing the stress concentration in a unidirectional composite, Section 7.9.*

8.2 Limitation and Recommendation

1. *The theory presented in this thesis is a nonlinear viscoelastic theory. When this theory is applied to the material studied, the assumption of elasticity is adopted, i.e. no plastic or permanent deformation due to external loading exists. Future research might be directed to higher stress levels, where plastic deformation is more important.*
2. *A possible effect of hydrostatic stress has not been included in the model, i.e. coupling is governed by the effective stress which is equivalent to the Von Mises equivalent stress. Experimental results show that there is a difference between the tensile behaviour and the compression behaviour of unsaturated polyester. This is usually considered an effect of hydrostatic stress.*
3. *The compressive behaviour of unsaturated polyester-resin has not been considered in this study. The compressive behaviour is generally different from the tensile behaviour for polymers.*
4. *The theory has been verified through experiments in a mild range of stress levels. For higher stress levels, close to the failure point, polymers may behave strongly nonlinear and stress/deformation dependent.*
5. *The stress-erased or deformation-erased ageing effect has been assumed negligible in this model.*
6. *Contacting fibres and other initial cracks are not considered in this study. The composite studied is assumed to be undamaged and without defects in matrix, fibre and interface.*
7. *The initial strain concept used represents an oversimplification of the matrix shrinkage process. The chemical reaction or polymerization of matrix material, an unsaturated polyester resin, causes a volume shrink. However, uncured resin behaves differently and its relaxation time is*

much shorter than for a cured resin. Therefore during the curing process, the stress is being built up and relaxed at the same time. The complex process is simplified in this work as a sudden shrinkage which takes no time. This simplification may bring errors in the stress/strain fields. A separate research is needed for understanding the coupled chemical-mechanical process in reality.

8. *In the future work, the influence of moisture absorption for both resin material and composite should be considered especially for a long-term prediction.*

Future work should be devoted in considering and improving any of these above-mentioned items.

References

- ¹ Aboudi, J. (1982), 'A Continuum Theory for Fibre-Reinforced Elastic-Viscoplastic Composites', *Int. J. Eng. Sci.*, Vol. 20, pp. 605-621
- ² Aboudi, J. (1989), 'Micromechanical Analysis of Composites by the Method of Cells', *Appl. Mech. Res.*, Vol. 42, No. 7, pp. 193-221
- ³ Aboudi, J. (1990), 'Micromechanical Characterization of the Nonlinear Viscoelastic Behaviour of Resin Matrix Composites', *Composites Sci. & Tech.*, Vol. 38, pp. 31-386
- ⁴ Achenbach, J. D. and H. Zhu (1989), 'Effect of Interfacial Zone on Mechanical Behaviour and Failure of Fibre-Reinforced Composites', *J. Mech. Phys. Solids*, Vol. 37, No. 3, pp. 381-393
- ⁵ Achenbach, J. D. and H. Zhu (1990), 'Effect of Interphases on Micro and Macromechanical Behaviour of Hexagonal-Array Fibre Composites', *J. Appl. Mech.*, Vol. 57, pp. 956-963
- ⁶ Adams, D. F. (1973), 'High Performance Composite Materials for Vehicle Construction: An Elastic-Plastic Analysis of Crack Propagation in a Unidirectional Composite', *Report R-1070-PR*, The Rand Corporation, Santa Monica, California
- ⁷ Adams, D. F. (1987), 'A Micromechanics Analysis of the Influence of the Interface on the Performance of Polymer-Matrix Composites', *J. Reinforced Plastics and Composites*, Vol. 6, pp. 66-88
- ⁸ Boer, H. De (1993), 'De Invloed van Chemische en Fysische Veroudering op Vervormingen' (in Dutch), *Report LTM-994*, Laboratory for Engineering Mechanics, Delft University of Technology
- ⁹ Boyle, J. T. and J. Spence (1983), *Stress Analysis for Creep*, Butterworth & Co. (Publishers) Ltd.
- ¹⁰ Brockenbrough, J. R., S. Suresh and H. A. Wienecke (1990), 'Deformation of Metal-Matrix Composites with Continuous Fibres: Geometrical Effects of Fibre Distribution and Shape', *Acta Metall. Mater.*, Vol. 39, No. 5, pp. 735-752
- ¹¹ Brouwer, R. (1986), *Nonlinear Viscoelastic Characterization of Transversely Isotropic Fibrous Composites under Biaxial Loading*, Ph. D. Dissertation, Free University of Brussels, Belgium
- ¹² Busschen, A. Ten (1990), 'Micromechanical Modelling of Unidirectional Glass Fibre Reinforced Polyester: Effect of Matrix Shrinkage', *Proc. Euromech-269-Colloquium*, ed. A. Vautrin, Dec. 1990, St. Etienne, France
- ¹³ Busschen, A. Ten (1992), 'Mechanisches Verhalten von Polyester' (in German), private communication
- ¹⁴ Busschen, A. Ten (1995),

- ¹⁵ Busschen, A. Ten, J. H. M. Kuypens and H. R. R. van Roosmalen (1989), 'Creep Experiments on Synolite 593-A-2', *Report LTM-894*, Laboratory for Engineering Mechanics, Delft University of Technology
- ¹⁶ Christensen, R. M. and K. H. Lo (1979), 'Solutions for Effective Shear Properties in Three Phase Sphere and Cylinder Models', *J. Mech. Phys. Solids*, Vol. 27, pp. 315-330
- ¹⁷ Crane, D. A. and D. F. Adams (1981), 'Finite Element Micromechanical Analysis of Unidirectional Composite Including Longitudinal Shear Loading', *Report UWME-DR-101-101-1*, Department of Mechanical Engineering, University of Wyoming
- ¹⁸ Findley, W. N., J. S. Lai and K. Onaran (1976), *Creep and Relaxation of Nonlinear Materials with an Introduction to Linear Viscoelasticity*, North-Holland Publishing Company
- ¹⁹ Foye, R. L. (1966), 'An Evaluation of Various Engineering Estimate of the Transverse Properties of Unidirectional Composites', in *Advanced Fibrous Reinforced Composites, 10th National SAMPE Symposium*, pp. G-31 - G-42
- ²⁰ Gopalakrishnan, K. S., A. M. Neville and A. Ghali (1969), 'Creep Poisson's Ratio of Concrete Under Multiaxial Compression', *Journal of the American Concrete Institute*, Title No. 66-90, pp 1008-1019
- ²¹ Green, A. E. and R. S. Rivlin (1957), *Arch. Rat. Mech. Anal.* Vol. 1, pp. 1-21
- ²² Green, A. E. and R. S. Rivlin (1960), *Arch. Rat. Mech. Anal.* Vol. 4, pp. 387-404
- ²³ Green, A. E., R. S. Rivlin and A. J. M. Spencer (1959), *Arch. Rat. Mech. Anal.* Vol. 3, pp.82-90
- ²⁴ Haan, J. W. de (1992), 'Bepproeven van Glasvezelversterkte Polyesterbuizen' (in Dutch), *Rapport LTM-971*, Laboratory for Engineering Mechanics, Delft University of Technology
- ²⁵ Hadley, D. W. and I. M. Ward (1975), *Reports on Progress in Physics*, Vol. 38, pp. 1143-1215
- ²⁶ Hashin, Z. (1979), 'Analysis of Properties of Fibre Composites with Anisotropic Constituents', *ASME J. of Appl. Mech.*, Vol. 46, pp. 543-550
- ²⁷ Henriksen, M. (1984), 'Nonlinear Viscoelastic Stress Analysis - A Finite Element Approach', *Computer & Structures*, Vol. 18, No. 1, pp 133-139
- ²⁸ Lamers, H. (1989), 'Long-term Creep and Physical Aging of Polymeric Composites', *TNO-report: 425/89*
- ²⁹ Leaderman, H. (1943), *Elastic and Creep Properties of Filamentous Materials and Other High Polymers*, The Textile Foundation, Washington, D.C.
- ³⁰ Lockett, F. J. (1965), *Int. J. Eng. Science*, Vol 3, pp. 59-75
- ³¹ Lou, Y. C. and R. A. Schapery (1971), 'Viscoelastic Characterization of a Nonlinear Fiber-Reinforced Plastic', *J. Composite Materials*, Vol. 5, pp. 208-234
- ³² Press, W. H., B. P. Flannery, S. A. Teukolsky and W. T. Vetterling (1989), *Numerical Recipes*, Cambridge University Press, Cambridge
- ³³ Rabotnov, Y. U. (1980), *Elements of Hereditary Solid Mechanics*, Mir Publishers, Moscow
- ³⁴ Rendell, I. W., K. L. Ngai, G. R. Fong, A. F. Yee and R. J. Bankert (1987), 'Nonlinear Viscoelasticity and the Yield: Application of a Coupling Model', *Polymer Eng. & Sci.*, Vol. 27, No. 1, pp. 2-15
- ³⁵ Ronald, P. N., R. J. Bankert, E. S. Russell, G. A. Smith and P. K. Wright (1991), 'Micromechanical Modeling of Fibre/Matrix Interface Effects in Transversely Loaded SiC/Ti-6-4 Metal Matrix Composites', *J. Composites Technology & Research, JCTRE*, Vol. 13, No. 1, pp. 3-13
- ³⁶ Rooijackers, H. F. L. (1988), *A Numerical Implementation of the Schapery Model For Nonlinear Viscoelasticity*, Ph. D. Dissertation, Eindhoven University of Technology, The Netherlands

- ³⁷ Ross, A. D. (1964), 'Experiments on the Creep of Concrete Under Two-Dimensional Stressing', *Magazine of Concrete Research*, Vol. 16, No. 46, pp. 12-30
- ³⁸ Schapery, R. A. (1969), 'On the Characterization of Nonlinear Viscoelastic Materials' *Polymer Eng. & Sci.*, Vol. 9, No. 4, pp 295-310
- ³⁹ Silenka Manual (1990), Introduction to Glass Fibre Composites, Silenka bv, Hoogezand, The Netherlands, Table 2 and Table 3
- ⁴⁰ Sottos, N. R., R. L. McCullough and S. I. Guceri (1989), 'Thermal Stresses due to Property Gradients at the Fibre/Matrix Interface', in *Mechanics of Composite Materials and Structures*, ASME, pp. 11-20
- ⁴¹ Sterrett, T. and E. Miller (1988), 'An Evaluation of Analytical Expressions for the Representation of Plastic Creep Data', *J. of Elastomers and Plastics*, Vol. 20, pp. 346-362
- ⁴² Struik, L. C. E. (1978), *Physical Aging in Amorphous Polymers and other Materials*, Elsevier Sci. Publ., Amsterdam
- ⁴³ Struik, L. C. E. (1990), *Internal Stress, Dimensional Instabilities and Molecular Orientations in Plastics*, John Wiley & Sons Ltd., England, p. 31
- ⁴⁴ Toutenhoofd, V. (1993), 'Onderzoek naar Kruip in Vezelversterkt Polyester', *Report LTM-975*, Laboratory for Engineering Mechanics, Delft University of Technology
- ⁴⁵ Tuttle, M. E. and H. F. Brinson (1986), 'Prediction of the long term creep compliance of general composite laminates', *Exp. Mechanics*, March 1986, pp. 89-102
- ⁴⁶ Ward, I. M. and E. T. Onat (1963), 'Non-linear Mechanical Behaviour of Oriented Polypropylene', *J. Mech. Phys. Solids*, Vol. 19, pp. 201-214
- ⁴⁷ Zhang, L. (1992), 'Time-Dependent Behavior of Polyester', *Report LTM-975*, Laboratory for Engineering Mechanics, Delft University of Technology
- ⁴⁸ Zhang, L. (1993a), 'Aging Phenomena of Polyester', *Report LTM-996*, Laboratory for Engineering Mechanics, Delft University of Technology
- ⁴⁹ Zhang, L. (1993b), 'Poisson's Ratios in Viscoelasticity', *Report LTM-999*, Laboratory for Engineering Mechanics, Delft University of Technology
- ⁵⁰ Zhang, L. (1993c), 'An Application of a Simplified Nonlinear Viscoelastic Model', *Report LTM-1001*, Laboratory for Engineering Mechanics, Delft University of Technology
- ⁵¹ Zhang, L. (1993d), 'Implementation of Nonlinear Viscoelasticity in DIANA', *Report LTM-1006*, Laboratory for Engineering Mechanics, Delft University of Technology
- ⁵² Zhang, L. and L. J. Ernst (1993), 'A Three Dimensional Model for Nonlinear Viscoelasticity', *Topics in Applied Mechanics*, eds. J. F. Dijkman and F. T. M. Nieuwstadt, Kluwer Academic Publisher, pp. 253-260
- ⁵³ Zywickz, E. (1986), *Local Stress and Deformation Due to Fabrication and Transverse Loading in an Ideal Continuously Reinforced Graphite/Aluminum Metal Matrix Composite*, M. Sc. Thesis, Department of Mechanical Engineering, MIT

Appendix

Total differential

The total differential of Eq (5.8) is

$$d\epsilon_i = g_0 J_0 S_{ij} d\sigma_j + J_0 S_{ij} \sigma_j dg_0 + S_{ij}^c dg_1 \int_0^t \frac{\Delta J}{d\tau} (g_2 \sigma_j) d\tau + S_{ij}^c g_1 d \int_0^t \frac{\Delta J}{d\tau} (g_2 \sigma_j) d\tau. \quad (A-1)$$

The differential in the last term of the right hand side of Eq (A-1) can be written as

$$d \int_0^t \frac{\Delta J}{d\tau} (g_2 \sigma_j) d\tau = \left[\Delta J \frac{d}{d\tau} (g_2 \sigma_j) \right] \Big|_{\tau=t} dt + \int_0^t \frac{d}{d\tau} (g_2 \sigma_j) d(\Delta J) d\tau. \quad (A-2)$$

Since $\Delta J(\psi - \psi')|_{\tau=0} = \Delta J(0) = 0$, the first term on the right hand side of Eq (A-2) is zero.

$$\begin{aligned} d(\Delta J) &= d \sum_p J_p \left(1 - e^{-\lambda_p(\psi - \psi')} \right) = \sum_p J_p d \left(1 - e^{-\lambda_p(\psi - \psi')} \right) = \sum_p J_p d \left(-e^{-\lambda_p(\psi - \psi')} \right) = \\ &= \sum_p J_p \left(-e^{-\lambda_p(\psi - \psi')} \right) (-\lambda_p) d\psi = \sum_p J_p \lambda_p e^{-\lambda_p(\psi - \psi')} \left[d \int_0^t \frac{d\tau'}{\left(\frac{t_e + \tau'}{t_e} \right)^\alpha a_\sigma(\tau')} \right] = \\ &= \sum_p J_p \lambda_p e^{-\lambda_p(\psi - \psi')} \left[\frac{dt}{\left(\frac{t_e + t}{t_e} \right)^\alpha a_\sigma(t)} \right] \end{aligned} \quad (A-3)$$

Eq (A-2) becomes

$$\begin{aligned}
 \int_0^t \Delta J \frac{d}{d\tau} (g_2 \sigma_j) d\tau &= \left(\frac{t_e + t}{t_e} \right)^\alpha \frac{dt}{a_\sigma(t)} \int_0^t \sum_p J_p \lambda_p e^{-\lambda_p(\Psi - \Psi')} \frac{d}{d\tau} (g_2 \sigma_j) d\tau = \\
 &= \left(\frac{t_e + t}{t_e} \right)^\alpha \frac{dt}{a_\sigma(t)} \sum_p J_p \lambda_p \int_0^t e^{-\lambda_p(\Psi - \Psi')} \frac{d}{d\tau} (g_2 \sigma_j) d\tau
 \end{aligned} \quad (\text{A-4})$$

An intermediate variable is introduced

$$\theta_j^p(t) = \int_0^t e^{-\lambda_p(\Psi(t) - \Psi(\tau))} \frac{d}{d\tau} (g_2 \sigma_j) d\tau, \quad (\text{A-5})$$

Eq (A-4) is then

$$\int_0^t \Delta J \frac{d}{d\tau} (g_2 \sigma_j) d\tau = \left(\frac{t_e + t}{t_e} \right)^\alpha \frac{dt}{a_\sigma(t)} \left(\sum_p J_p \lambda_p \theta_j^p \right). \quad (\text{A-6})$$

The integral in the third term on the right hand side of Eq (A-1) can also be written by means of the variable in Eq (A-5),

$$\begin{aligned}
 \int_0^t \Delta J \frac{d}{d\tau} (g_2 \sigma_j) d\tau &= \int_0^t \sum_p J_p \left(1 - e^{-\lambda_p(\Psi - \Psi')} \right) \frac{d}{d\tau} (g_2 \sigma_j) d\tau = \\
 &= \int_0^t \sum_p J_p \frac{d}{d\tau} (g_2 \sigma_j) d\tau - \int_0^t \sum_p J_p e^{-\lambda_p(\Psi - \Psi')} \frac{d}{d\tau} (g_2 \sigma_j) d\tau = \\
 &= (g_2 \sigma_j - g_2^0 \sigma_j^0) \sum_p J_p - \sum_p J_p \theta_j^p
 \end{aligned} \quad (\text{A-7})$$

Rewrite Eq (A-1) in terms of Eq (A-6) and Eq (A-7),

$$d\epsilon_i = g_0 J_0 S_{ij} d\sigma_j + J_0 S_{ij} \sigma_j d g_0 + S_{ij}^c \left[(g_2 \sigma_j - g_2^0 \sigma_j^0) \sum_p J_p - \sum_p J_p \theta_j^p \right] d g_1 + \left(\frac{t_e + t}{t_e} \right)^\alpha \frac{S_{ij}^c g_1}{a_\sigma} \left(\sum_p J_p \lambda_p \theta_j^p \right) dt. \quad (\text{A-8})$$

Further, the last term in Eq (A-8) is dissolved by the relation of θ_j^p

$$\theta_j^p(t) = e^{-\lambda_p d\Psi(t)} \theta_j^p(t - dt) + d(g_2 \sigma_j(t)) \Lambda_p(t), \quad (\text{A-9})$$

where

$$\Lambda_p(t) = \frac{1 - e^{-\lambda_p d\Psi(t)}}{\lambda_p d\Psi(t)}. \quad (\text{A-10})$$

Hence

$$\theta_j^p(t) = e^{-\lambda_p d \Psi(t)} \theta_j^p(t-dt) + (\sigma_j dg_2 + g_2 d\sigma_j) \Lambda_p(t), \quad (\text{A-11})$$

$$\sum_p J_p \lambda_p \theta_j^p(t) = \sum_p J_p \lambda_p e^{-\lambda_p d \Psi(t)} \theta_j^p(t-dt) + \sigma_j \left(\sum_p J_p \lambda_p \Lambda_p(t) \right) dg_2 + g_2 \left(\sum_p J_p \lambda_p \Lambda_p(t) \right) d\sigma_j \quad (\text{A-12})$$

and

$$\begin{aligned} \left(\frac{t_e + t}{t_e} \right)^\alpha \frac{S_{ij}^c g_1}{a_\sigma(t)} \left(\sum_p J_p \lambda_p \theta_j^p(t) \right) dt &= \left(\frac{t_e + t}{t_e} \right)^\alpha \frac{S_{ij}^c g_1}{a_\sigma(t)} \sigma_j \left(\sum_p J_p \lambda_p \Lambda_p(t) \right) dt dg_2 + \\ &+ \left(\frac{t_e + t}{t_e} \right)^\alpha \frac{S_{ij}^c g_1}{a_\sigma(t)} g_2 \left(\sum_p J_p \lambda_p \Lambda_p(t) \right) d\sigma_j dt + \left(\frac{t_e + t}{t_e} \right)^\alpha \frac{S_{ij}^c g_1}{a_\sigma(t)} \sum_p J_p \lambda_p e^{-\lambda_p d \Psi(t)} \theta_j^p(t-dt) dt \end{aligned} \quad (\text{A-13})$$

Reformulation of Eq (A-8) yields,

$$\begin{aligned} de_i &= \left[g_0 J_0 S_{ij} + \left(\frac{t_e + t}{t_e} \right)^\alpha \frac{S_{ij}^c g_1 dt}{a_\sigma(t)} g_2 \left(\sum_p J_p \lambda_p \Lambda_p(t) \right) \right] d\sigma_j + J_0 S_{ij} \sigma_j dg_0 + S_{ij}^c \left[\left(g_2 \sigma_j - g_2^0 \sigma_j^0 \right) \sum_p J_p - \sum_p J_p \theta_j^p \right] dg_1 + \\ &+ \left(\frac{t_e + t}{t_e} \right)^\alpha \frac{S_{ij}^c g_1 dt}{a_\sigma(t)} \sigma_j \left(\sum_p J_p \lambda_p \Lambda_p(t) \right) dg_2 + \left(\frac{t_e + t}{t_e} \right)^\alpha \frac{S_{ij}^c g_1}{a_\sigma(t)} \sum_p J_p \lambda_p e^{-\lambda_p d \Psi(t)} \theta_j^p(t-dt) dt \end{aligned} \quad (\text{A-14})$$

Consider the total derivative $dg_0 = \frac{\partial g_0}{\partial \sigma_i} d\sigma_i$, $dg_1 = \frac{\partial g_1}{\partial \sigma_i} d\sigma_i$ and $dg_2 = \frac{\partial g_2}{\partial \sigma_i} d\sigma_i$, Eq (A-14) becomes

$$d\epsilon_i = D_{ij}^{-1} d\sigma_j - \left(D_{ij}^{-1} C_j \right) dt. \quad (\text{A-15})$$

Samenvatting

Om het lange-duur-tijdsafhankelijke gedrag van in n richting versterkte polymere matrix-composieten micromechanisch te berekenen, is een constitutief model voor het matrix-materiaal noodzakelijk. Dit model dient het mechanische gedrag van het matrix-materiaal adequaat te beschrijven. Een driedimensionaal model gebaseerd op een niet-lineaire viscoelastische theorie werd opgezet, waarbij de verouderingseffecten en het kruip-dwarscontractie-effect werden verdisconteerd. Dit model is vervolgens geïmplementeerd in een eindige-elementenpakket. Een serie experimenten, waaronder biaxiale en cyclische testen, werd uitgevoerd. Experiment en theorie vertonen een uitstekende overeenkomst.

Vervolgens wordt dit matrix-materiaalmodel gebruikt voor het simuleren van het kruipgedrag van de composiet. De vezelverdeling bleek zowel voor het lokale spanningsveld alsook voor de globale vervorming een belangrijke rol te spelen. De traditioneel gebruikte uniforme hexagonale en rechthoekige vezelverdelingen bleken niet geschikt om het mechanische gedrag van de in een richting versterkte composiet te beschrijven. Door rekening te houden met een niet uniforme vezelverdeling, met vezelrijke en matrixrijke gebieden, kan de globale kruipvervorming beter beschreven worden. In een verbeterde aanpak worden een tweetal speciale periodieke vezelverdelingen voorgesteld. Het betreft hier verdelingen die, hoewel periodiek, lokaal toch niet-uniform zijn. Deze verdelingen leiden tot celmodellen, die eenvoudig gebruikt kunnen worden voor numerieke berekeningen. Vergeleken met testgegevens blijken de nieuwe celmodellen tot betere resultaten te leiden dan de traditionele modellen. In dit proefschrift is voor het eerst het fenomeen van spanningsherverdeling in de matrix en de vezels als gevolg van tijdsafhankelijke vervorming uiteengezet. De door matrixkrimpgenitierde voorspanningstoestand is eveneens onderzocht en met name diens invloed op het lokale spanningsveld en de globale kruipvervorming.

Curriculum Vitae

The author, Zhang Li, was born in Shanghai, China, on 6th July 1961. He started his school life in September 1968 at the 3rd Primary School of An-Fu (peace and happiness) Road in Shanghai. In February 1975, he entered Li-Ming (dawning) High School in Shanghai, just one hundred yards from his home. In July 1979 he graduated as the best student in Li-Ming High School and, in September, fluently enrolled in Department of Engineering Mechanics, Shanghai Jiao Tong University, as a freshman. He was entitled as the Bachelor of Science in Engineering in this Department on 10th July 1983 and the Master of Science in Engineering on 25th March 1986 respectively. The subject was engineering mechanics, emphasized in applied fluid mechanics.

After six and half years college studies, in March 1986, he became for the first time a researcher and a part-time lecturer in Department of Chemical Engineering, East China University of Chemical Technology, Shanghai. The research activities included Laser-Doppler Velocimeter technique, fluid mixing quality and injection moulding phenomena.

In November 1989, he gave up his job in Shanghai and came to Europe through a long journey by train to pursue his further education. During the period between November 1989 and August 1990, he was a participant of a postgraduate program at International Institute for Hydraulic and Environmental Engineering (IHE), Delft, The Netherlands, under the supervision of Prof. Dr. M. B. Abbott. After achieving a hydraulic engineering diploma in this institution, he started his Ph.D. research immediately as an Assistant in Opleiding (AIO) in Laboratory for Engineering Mechanics and Fibre Technology, Faculty of Mechanical Engineering and Marine Technology, Delft University of Technology, Delft, The Netherlands, under the supervision of Prof. Dr. Ir. L. J. Ernst. The research topics included long-term behaviour and nonlinear viscoelastic properties of polyester and the micromechanics of glass fibre reinforced polymers.

Since August 1994, he has joined Philips Research Laboratories in Eindhoven as a research staff member in the group of Transport Phenomena, directed by Dr. P. E. Wierenga. His current research involves thermomechanical properties of glass and numerical simulation of glass moulding.